Traveling-wave photomixers for sub-THz and THz generation

Charbel Tannoury

École doctorale no 632: ENGSYS Sciences de l'ingénierie et des systèmes

THÈSE

pour obtenir le grade de docteur délivré par

L'université de Lille

Spécialité : Electronique, photonique

présenté et soutenue publiquement le 13 juin 2023 par

Charbel Tannoury

Institut d'Electronique de Microélectronique et de Nanotechnologie (IEMN)

Traveling-wave photomixers for sub-THz and THz generation

Photomélangeurs distribués pour la génération d'onde sub-THz et THz

devant le jury composé de:

Rapporteures :

HDR Prof. Florence Podevin Laboratoire TIMA, Université Grenobles Alpes

HDR Dr. Juliette Mangeney Laboratoire de physique de l'ENS - LPENS

Examinateurs :

DR CNRS Dr. Jean-Francois Lampin IEMN, Villeneuve d'Ascq

Dr. Vincent Magnin IEMN, Université de Lille, Villeneuve d'Ascq

Dr. Frederic Van Dijk Laboratoire III-V, Paris

Président du jury : Dr. DR CNRS Patrick Mounaix LOMA, Université de Bordeaux

Directeur : HDR CNRS Dr. Emilien Peytavit IEMN, Villeneuve d'Ascq

A mes parents

And so on and so on …

- *Slavoj Žižek*

Remerciements

Je tiens à exprimer mes sincères remerciements à toutes les personnes qui ont contribué à la réalisation de ce travail de thèse. Tout d'abord, je suis reconnaissant envers mon directeur de thèse, Emilien, pour son engagement exceptionnel en dépit des difficultés liées à la pandémie de COVID-19. Sa patience et sa bienveillance ont été une source de motivation constante tout au long de ces années de recherche. Je le remercie également pour les expériences inestimables qu'il m'a transmises, notamment dans le domaine de la technologie en salle blanche, qui est devenu une véritable passion pour moi. Travailler avec Emilien a été un plaisir et une expérience enrichissante.

Je tiens également à remercier Jean-François pour les informations précieuses qu'il m'a partagé lors de nos manips ensemble. Je n'oublie pas non plus les discussions intéressantes avec Romain sur des sujets sociaux et politiques, ainsi que ses conseils avisés pour mon projet professionnel. Je suis également reconnaissant envers l'équipe d'ingénieurs et de personnel de l'IEMN qui ont contribué à la fabrication et à la caractérisation du composant. Tout d'abord, je tiens à remercier Funaki pour ses conseils importants sur la fabrication du composant, sans lesquels ce travail n'aurait pas été possible en trois ans. J'aimerais également citer François pour sa disponibilité à toute épreuve sur le masqueur électronique, même les weekends. Je suis reconnaissant envers tous les membres de l'équipe de la salle blanche, y compris Saliha, Christophe, Timothé, Dmitri, Marc, Annie, Isabelle, Pascal, David et tous les autres que j'ai eu la chance de rencontrer. Je remercie également chaleureusement l'équipe de caractérisation, composée de Sylvie, Etienne, Sophie et Vanessa.

J’ai eu la chance de rencontrer de nombreux collègues à l'IEMN qui sont devenus des amis. Giuseppe, Mickael, Quyang, Théo, Mélanie, Elias, Roudy, Alexandra, Victor, Hugo, Chiara, Carlos et Akash, je vous remercie pour les bons moments passés ensemble et vous souhaite bon courage pour la suite de vos travaux.

Enfin, je tiens à remercier toutes les personnes qui ont été à mes côtés depuis mon arrivée en France en 2017 et qui m'ont permis de m'intégrer et de me sentir chez moi. Je

tiens particulièrement à citer Julien, Marine, Quentin, Grégory, Theodore, Marie, Nicolas, Anaïs et Isabelle. Je n'oublie pas non plus mon ami d'enfance, Dimi, avec qui j'ai parcouru un chemin similaire, du petit village de Kaa el Rim au Liban jusqu'à l'université à Beyrouth, puis maintenant à Lille. Je suis également reconnaissant envers Rita et Michel, que je considère comme mes parents en France, pour leur aide précieuse depuis mon arrivée dans ce pays et jusqu'à présent. Je ne pourrai jamais leur être assez reconnaissant. Avant de conclure, je souhaite remercier ma compagne Pauline, qui a toujours été présente pour moi et qui a partagé les hauts et les bas de ce parcours avec moi. Je la remercie tout particulièrement pour son soutien durant la longue phase de rédaction qui n'a pas été facile. Enfin, je dédie ce manuscrit à mes parents Edward et Sanaa, qui sont au Liban. Sans leur soutien inconditionnel et leur encouragement permanent, je ne serais pas là où je suis aujourd'hui. Je tiens également à remercier mon frère Antonio et mes sœurs Margo, Yara et Mariam, qui ont toujours été présents pour me soutenir et s'enquérir de mes avancées dans ce projet.

Abstract

Photomixing is an optical to THz conversion technique that involves the interaction of two optical fields of different frequencies in a photoconductive material, resulting in the generation of a THz electromagnetic wave at the frequency difference between the two optical sources. One of the significant advantages of photomixing is its broadband operation, which allows for the generation of THz radiation with a wide range of frequencies. Moreover, photoconductive materials can be easily integrated into small and portable devices, making it possible to create compact and highly efficient THz sources. The use of photoconductive material is attributed mainly to its large photoconductivity and to the short carrier lifetime of the material and, in part, to the device's design. State of the art photomixers are micrometer sized devices that are vertically illuminated and mainly limited by the maximum incident optical power due to the small size of their active region. The latter is necessary in order to minimize their well-known frequency limitation related to capacitance defined by the electrode size. Traveling wave photomixers is another type of photomixers that allows to overcome the capacitance limitation of the vertically illuminated devices due their distributed structure. In addition to the carrier lifetime's fundamental limitations of photomixers, the traveling-wave photomixers are limited by the mismatch between the THz refractive index and the optical group index. Herein, we introduce a novel concept for traveling-wave photomixers based on low temperature grown Gallium Arsenide capable of handling high optical powers reaching the watt level for wavelengths of both 780 nm and 1550 nm due to its larger active region reaching the 1 mm length. Moreover, this new design enables an easy adjustment of both indices, leading to a better matching. Ultimately, the findings of this manuscript demonstrate that it is feasible to fabricate a traveling-wave photomixers allowing both high optical power handling and plausible index matching allowing for these photomixers to compete with vertically illuminated photomixers and even overcome their limitations.

Résumé

Le photomélange est une technique de conversion d'onde optique en onde THz qui implique l'interaction de deux sources optiques de fréquences différentes dans un matériau photoconducteur, ce qui entraîne la génération d'une onde électromagnétique THz à la différence de fréquence entre les deux sources optiques. L'un des principaux avantages du photomélange est son fonctionnement à large bande, qui permet de générer un rayonnement THz dans une large gamme de fréquences. En outre, les matériaux photoconductifs peuvent être facilement intégrés dans des dispositifs petits et portables, ce qui permet de créer des sources THz compactes et très efficaces. L'utilisation de matériaux photoconductifs est principalement attribuée à leur grande photoconductivité et à la courte durée de vie des porteurs du matériau et, en partie, à la conception de l'appareil. Les photomélangeurs actuels sont des dispositifs de la taille micrométrique qui sont éclairés verticalement et sont principalement limités par la puissance optique incidente maximale en raison de la petite taille de leur zone active. Cette dernière est nécessaire pour minimiser la limitation de fréquence bien connue liée à la capacité définie par la taille de l'électrode. Les photomélangeurs distribués sont un autre type de photomélangeurs qui permettent de surmonter la limitation de capacité des dispositifs à éclairage vertical grâce à leur structure distribuée. Outre les limites fondamentales de la durée de vie des porteurs, les photomélangeurs distribués sont limités par le décalage entre l'indice de réfraction THz et l'indice du groupe optique. Nous présentons ici un nouveau concept de photomélangeurs distribués basé sur de l'arséniure de gallium épitaxié à basse température, capable de gérer des puissances optiques élevées atteignant le niveau du watt pour des longueurs d'onde de 780 nm et 1550 nm grâce à sa plus grande zone active atteignant une longueur de 1 mm. En outre, cette nouvelle conception permet un ajustement facile des deux indices, ce qui conduit à une meilleure adaptation entre ces indices. En fin de compte, les résultats de ce manuscrit démontrent qu'il est possible de fabriquer un photomélangeur distribué permettant à la fois de gérer une puissance optique élevée et une adaptation d'indice plausible, ce qui permet à ces photomélangeurs de rivaliser avec les photomélangeurs à illumination verticale et même de surmonter leurs limites.

Abstract for the general public

THz sources based on the photodetection of an optical beat of two laser lines by an ultrafast photodetector, also called photomixer, are very promising because they operate at room temperature, are compact, and above all, can be tuned over frequency ranges reaching the THz level. They are thus perfectly adapted to THz molecular spectroscopy systems for the study of materials, the earth, the sciences of the universe or biological systems. In this work, we developed a travelling wave photomixer capable of handling high optical powers reaching the watt level due to its large active region. Overall, this work proves the feasibility of a photomixer capable to overcome the limitations of vertically illuminated photomixers due its distributed structure and to its 100 times larger active region.

Résumé pour le grand public

Les sources THz basées sur la photodétection d'un battement optique de deux lignes laser par un photodétecteur ultrarapide, également appelé photomélangeur, sont très prometteuses car elles fonctionnent à température ambiante, sont compactes et, surtout, peuvent être accordées sur des gammes de fréquences atteignant le niveau THz. Ils sont donc parfaitement adaptés aux systèmes de spectroscopie moléculaire THz pour l'étude des matériaux, de la terre, des sciences de l'univers ou des systèmes biologiques. Dans ce travail, nous avons développé un photomélangeur distribué capable de gérer des puissances optiques élevées atteignant le niveau du watt grâce à sa grande région active. Dans l'ensemble, ce travail prouve la possibilité de fabriquer un photomélangeur capable de surmonter les limitations des photomélangeurs à éclairage vertical grâce à sa structure distribuée et à sa région active 100 fois plus grande.

Contents

Introduction:

Science and technologies based on THz electromagnetic radiation are sometimesconsidered as a recent topic with respect to other domains of physics. However, the research in this domain seems to have its origins from the radio wave discovery by H. Hertz in 1886. The development of experimental techniques to generate THz radiations, known back then as sub-millimeter waves or far infrared radiation, started in the early 1920's. However, it is true that in the last 30 years, this topic has developed at a high rate because of new potential applications in real and everyday life. One good reason for this fast evolution, is the development of laser-based terahertz time-domain spectroscopy in the 1980s and the 1990s. Nowadays, THz technologies have become prevalent in the research community especially for projects related to governments. On the other hand, THz radiation have several potential applications like biomedicine, food, security, telecommunication *etc*.

The focus of this study is on photoconductors and their role in the generation and detection of THz radiation. The first chapter introduce the THz frequency domain and its various applications, followed by a discussion on continuous wave THz sources and coherent THz detectors. The last part of this chapter will be dedicated to photonics and its role in THz generation via photomixing and THz detection via heterodyne mixing. In the second chapter, traveling wave photomixers will be discussed, including a comparison between their limitations and those of vertically illuminated photomixers, leading to the presentation of a new design for a traveling wave photomixer that is compatible with 780 nm and 1550 nm wavelengths. Chapter 3 and 4 will cover the design, simulation, fabrication, and characterization of this device at those wavelengths respectively.Overall, this work represents a significant advancement in photoconductor engineering for THz generation and detection.

Chapter 1: Introduction to the THz domain

1. Introduction to the THz domain

1.1. THz frequency band

Historically, the THz frequency domain is considered as the last unexplored region of the electromagnetic spectrum due to the difficulty of generation and detection of these waves. However, for a couple of recent decades, THz science and technology have been shown a rapid growth. Figure 1.1 shows the electromagnetic spectrum from the ultraviolet (UV) to the radio wavelength region. The THz region is defined here as the interval of frequencies ranging from 0.1 THz to 10 THz (30 µm to 3000 µm)[1].In this frequency range, the electromagnetic waves interact mainly with the molecular structure of the material.Figure 1.1, shows only the THz molecular interaction with solid phase of the material which is associated to lattice vibrations and intraband transitions.In gas phase, transitions happen between rotational energy levels for small molecules and vibrational energy levels for large molecules.

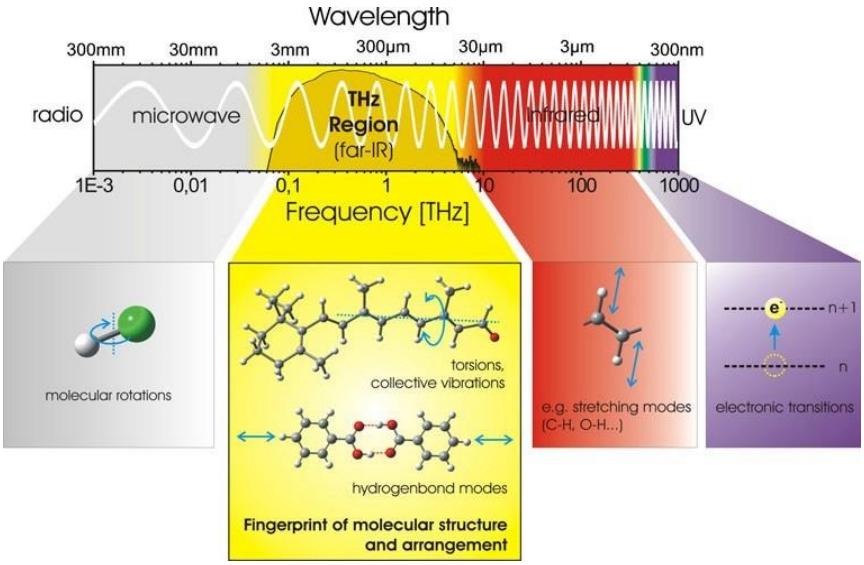

Figure 1.1: The electromagnetic spectrum showing the corresponding molecular excitations [2]. The dark yellow area (0.1 THz to 5 THz) is frequently used for THz imaging and spectroscopy

1.2. THz and sub THz applications

1.2.1. Space applications

The first application for the THz and sub-THz domains was in astronomy. The reason behind this is that THz waves can pass through dust clouds surrounding a star

forming region. This enable the gathering of important information about the universe formation [3]. In fact, more than fifty percent of the interstellar matter is mainly formed from hydrogen gas. This hydrogen gas in its molecular form is concentrated in extensive molecular and dust cloud complexes. These clouds absorb approximately half of the available stellar energy spreading throughout our galaxy and then re-radiate it within the millimeter, THz and sub-THz range, this is why it is important to have very good detectors in this frequency range. NASA's Cosmic Background Explorer (COBE) is a good example. COBE was a satellite that operated between 1989 and 1993 in the frequency range 1-100 GHz. It was assigned to observe both interstellar and extragalactic regions. Its goal was also to investigate the cosmic microwave background radiation (CMB) of the universe and provide measurements that would help shape our understanding of the cosmos.

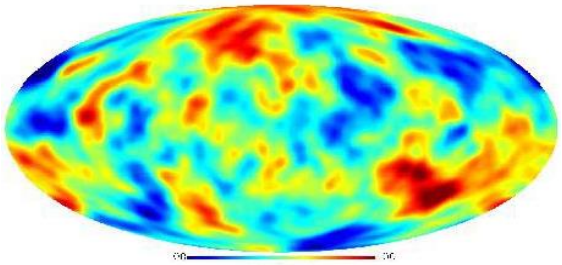

Figure 1.2: THz observation of the cosmic microwave background. (COBE resolution)[3]

Planetary and cometary observation is another major space application for THz detectors. The main idea here is to study the atmospheric dynamics of planets and the composition ofsmallbodies(asteroids, moons and comets)in order to improve the understanding ofour own atmosphere and to collect more information about the origins and evolution of our solar system.Nowadays,landers or orbital remote sensing instruments are the best to collect data on the composition, temperature, pressure and gas velocity (winds) because the collected information will be unaffected by dust and sunlight conditions. MIRO (Microwave Instrument for the Rosetta orbiter) the first instrument of this kind is a good example. The abundance and temperature of volatile substances like water, ammonia and carbon dioxide could be detected by MIRO via their microwave emissions. The 30 cm radio antenna along with the rest of the 18.5 kg instrument was built by NASA's Jet

Propulsion Laboratory with international contributions and operated in the frequency range 190-670 GHz[3].

1.2.2. Security and defense

THz electromagnetic waves experience low propagation loss in many materials that are opaque in the visible region such as clothing, plastics, glass and paper. These materials have relatively low loss to frequencies as high as 1 THz and knowing that the THz waves are highly reflected by ceramic and metallic bodies, this gives the opportunity to detect weapons and explosives. It explains why there isnow a considerable interest for using THz imagery and sensing for security purposes. Figure 1.3 shows an illustration of THz imagery identifying a hidden weapon. THz techniques give also the possibility to distinguish between explosives and drugs because of the difference in the absorption spectrum of these two materials.

Figure 1.3: Illustration of a detected weapon by THz imagery [4].

In Figure 1.4is shown the imaging and spectral analysis of a mail bomb mockup. The scanned image is a false color image which helps in resolving the details (microprocessor, RFID-card, various electronic components, post stamp). The insets give spectral information about the constituents of the two bags inside the envelope (here lactose and salicylic acid). The picture was obtained at a detection speed of 40 pixels per second. It is important to mention that the spectral information of each pixel is recorded. However, some areas of the scanned body can be more interesting than others. Therefore, the quality of the spectrum can be enhanced by averaging the spectra of this specific area.

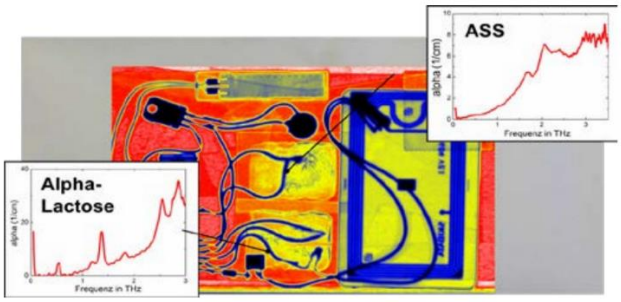

Figure 1.4: False color transmission image of a mail bomb mockup. Insets show the spectral analysis of the bags detected in the envelope [5].

Moreover, in this domain, some companies have commercialized products working in the millimeter and micro-wave range. For example, MC2 technologies produces a passive millimeter wave camera (MM-Imager 90) that is used for the detection of hidden objects under clothes. Knowing that the camera doesn't emit any radiation, it is interesting to note that it could scan bodies at less than 2 m for short distance use and it can also be used for objects farther than 10 m.

1.2.3. Wireless THzcommunications

In the recent years, the fast increase of wireless devices and the rising number of free space communication serviceshave resulted in a dramatic risein thedemand for spectral bandwidth along with the requirement for high data rate transmission.Within the next ten years and beyond, wirelessTbit/s communications systems and the supporting backhaul network infrastructure are expected to become the main technology trend. THz radiation is envisioned as one of the possible resources to be utilized for wireless communications in networks beyond 5G.Since it is the last explored region of the electromagnetic spectrum, it is possible touse a modulated THz carrier for the transmission of the data [6]. The aim of using THz links is to have fast and high data rate transmission between two stations or between stations and users. For example, users that are living in regions which are difficult to access (mountains, islands) should be connected with high data rates upto 10 Gbit/sper user. This is considered as a costly project if done by fiber optic links. THz could serve as an extension for the stations. It could also be used for communication between relatively close users as a connection between tablets and mobile phones in indoor communication assuring beyond 5G telecommunication.Figure

1.5 from [6] presents a promising architecture of a THz telecommunication system. The THz carrier at 400 GHz is generated by beating two optical lines at 194 THz and 193.6 THz. The amplitude of one of the optical lines is modulated by a conventional telecommunications modulator widely used today in fiber-optic networks, driven up to 46 Gbps. After optical amplification in an erbium-doped fiber amplifier (EDFA), the signal is injected in the photomixer which realizes the photonic-to-THz conversion. The coherent detection system is composed of a subharmonic mixer (SHM) feed by WR 2.2 canonical horn.

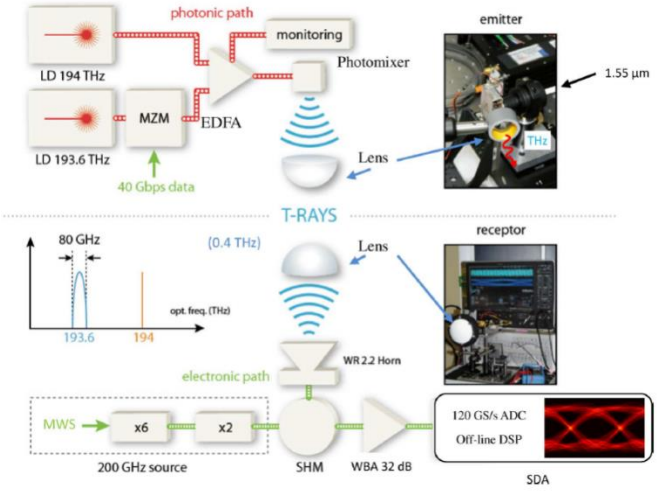

Figure 1.5: THz transmission setup. In red: photonic path with lasers diodes (LD), modulation (MZM) andoptical amplifier (EDFA). In blue: The T-rays are controlledwith two polymer lenses. In green: electronicreception using a microwave source (MWS), a mixer (SHM), a wideband amplifier (WBA 32 dB). Atreceiver, thedata is captured by a 120 GS/s ADC inside a 45-GHz real-time serial data analyzer (SDA)[6].

1.2.4. Biomedical applications

Since THz interactions happen only with the molecular state of matter and is considered non-ionizing,therefore they are recognized as a good candidate for medical imaging for both screening and diagnostic purposes. Knowing that it is highly absorbed by hydrogen bonds and N-H bonds present in water and protein respectively, it represents an interesting method to measure the changes of water content or blood flow due to the presence of a disease.However, it has also been proven that the origin behind the contrast between healthy and diseased tissues in THz region is not only due to changes in water content[7]. THz waves also could be used in biology for biomolecule sensing.As matter of fact, there are several methods to realize THz imaging. For example, in [8]they used a

THz Time Domain Spectroscopy imaging system (THz-TDS) to image a tumor of a colorectal cancer. Figure 1.6 shows the experimental setup of the THz-TDS imaging technique based on the conventional TDS technique[9]. The reflection characteristics of colorectal cancer were measured. It is important to note that the samples were non-stained-blocks of tissue prepared by formalin fixation and paraffin embedding.

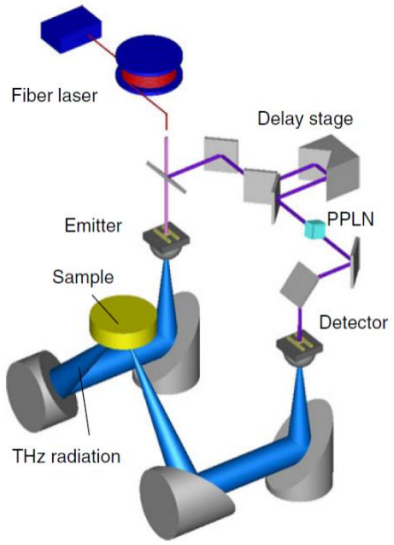

Figure 1.6: Experimental setup of the THz imaging system [7].

Figure 1.7 shows the reflectance spectra calculated from THz-TDS measurement data of tumor area and normal area. It is clear that the tumor area shows a higher reflectance spectrum from the normal area. This is attributed to the fact that the water content or the density of the cell nucleus are higher in a tumor than in a normal tissue.

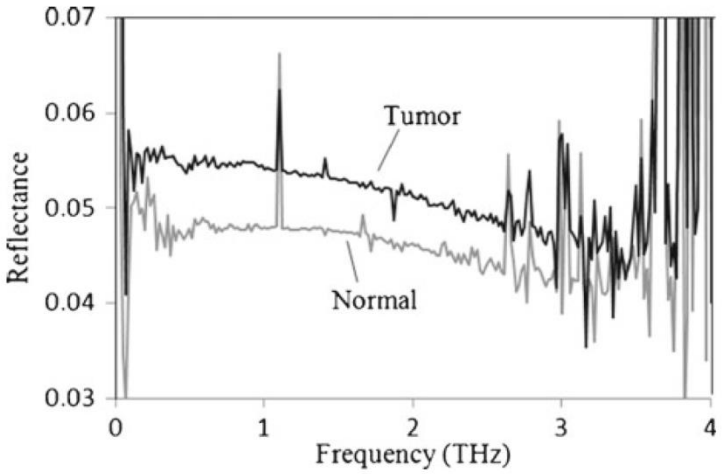

Figure 1.7: Reflectance of paraffin embedded colorectal tissues calculated from THz-TDS measured data.

In conclusion, THz technology has shown great potential in various biomedical applications. Its ability to penetrate non-conducting materials such as tissues, coupled with its non-ionizing nature, make it a promising tool for non-invasive imaging and diagnosis of diseases. Overall, the continued development of THz technology has the potential to revolutionize the field of biomedicine and improve healthcare outcomes.

1.2.5. Nondestructive testing

THz waves possess the unique ability to effectively traverse numerous materials including paper, vinyl, plastics, textiles, ceramics, semiconductors, lipids, and certain types of powders. In contrast to X-rays, THz waves have a limited penetration depth, indicating that their optical characteristics are moderately absorbent and moderately transparent. This quality of THz waves to partially absorb while passing through packaging materials makes it a highly desirable option for noninvasive and nondestructive inspections in various industries. THz wave technology has been widely employed for nondestructive testing, making it the initial industrial application for THz waves. Although the applications mentioned in earlier sections are still only potential applications in the industry, they have already been studied by various government agencies and research communities. For example, Teraview, a UK-based company, has developed the first commercially available THz sensor that measures film thickness in a nondestructive manner [10]. Figure 1.8 has been extracted from the video provided in reference [10].

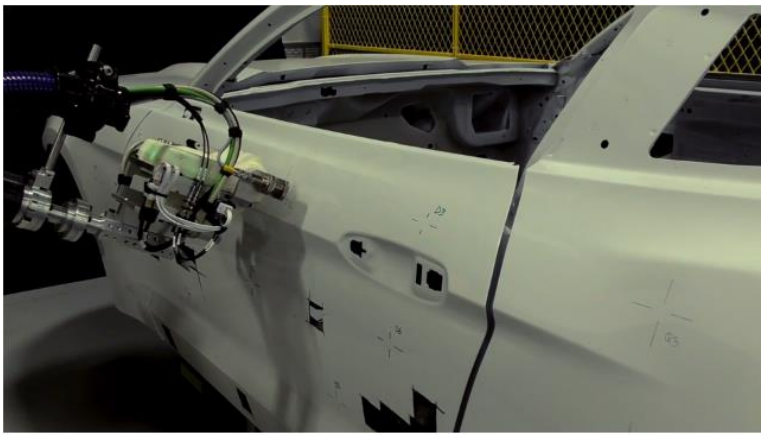

Figure 1.8: Teraview THz sensor integrated to a robot arm measuring the paint thickness on a vehicle [10].

The sensor is integrated to a robot arm that measures paint thickness of vehicles as seen in Figure 1.8. Typically, a vehicle has 4 layers of paint (electrocoat, primer, basecoat and clearcoat) The THz radiation passes the boundary between these layers and part of the signal is reflected back to the receiver. By measuring the time of flight of the signal, the thickness of the paint is calculated. The sensor could measure a minimum thickness of 5 µm with a 1.5 µm accuracy knowing that these values could change slightly depending on the paint. The spot size is between 1 and 2 mm and the measurement time takes 2 to 4 seconds per point (acquisition and analysis). The measurement should be done at 50 mm ± 0.75 mm from the surface. If the measurement is done handheld, the sensor provides real-time position feedback. If mounted on a robot arm, it requires angular positioning to within ±1° of normal incidence.Figure 1.9 shows a summary of all the potential applications presented above. In the following, promising THz sources for these applications will be discussed.

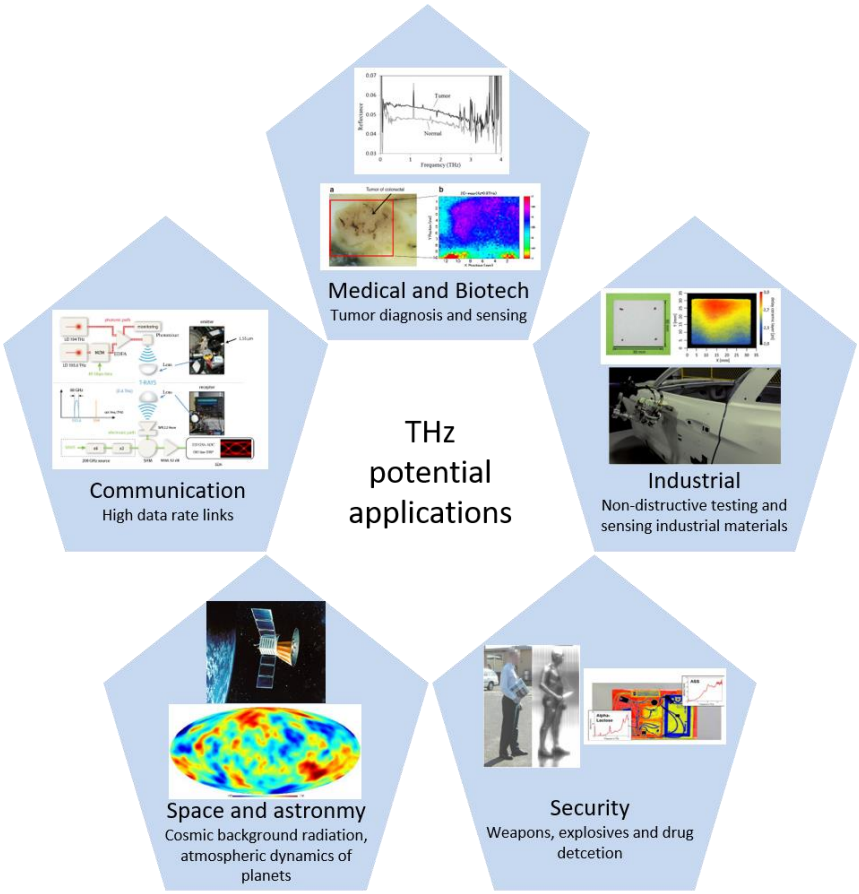

Figure 1.9: THz potential applications. The lower figure in the medical and biotech applications panel shows a photo of a tumor and its THz scanning in a color map [9]. The upper figure in the industrial applications panel is an image of a ceramic plate and its THz scanning shown in a color map [5]. The upper figure in the space and astronomy applications panel is an image the COBE [11].

1.3. Continuous-Wave THz sources

Since the THz frequency range lies between the far infrared and microwave regions, it can be generated through electronic or photonic techniques such as frequency multiplication or nonlinear generation. Alternatively, THz radiation can be directly produced through vacuum sources, solid-state sources, or gas lasers. THz sources can be continuous wave (cw) or pulsed, depending on the generation technique used. Pulsed THz sources are typically generated using pulsed optical sources, while cw lasers produce narrowband THz radiation. Femtosecond laser pulses, on the other hand, generate broadband THz spectra.In spectroscopy, cw THz sources offer high resolution, while pulsed sources offer high bandwidth but with lower frequency resolution. A cw source

requires more measurement time to achieve the same bandwidth as a pulsed source. In imaging, cw THz wave techniques are generally preferred for their lower cost, simplicity, and higher scanning speed. However, pulsed THz imaging systems provide more information such as electric field magnitude, depth of scattering centers, optical path length, absorption spectrum, phase, and pulse shape.To summarize, the selection of a THz source is dependent on the specific application, with cw sources providing simplicity and adaptability and pulsed sources offering wider bandwidth and more information. Since the focus of this thesis is on sources based on cw laser sources, table Table 1-1 shows a brief comparison between a variety of different cw THz sources that are presented in details below.

Sources	Price	Size	Material Scarcity	Cooling Necessity	Tunability	Output Power above 1 THz	Fabrication complexity
Electronic frequency multipliers	Low	Compact	Low	No	Limited	Low	Low
RTD oscillators	Low-Moderate	Compact	Low	No	Limited	Low	Low
Si IMPATT oscillators	Low	Compact	Low	Yes	Limited	Low	Moderate
InP Gunn oscillators	Moderate-High	Compact	Moderate	Yes	Limited	Moderate	Moderate
Nonlinear optical down-conversion	Low	Compact-Moderate	Moderate	No	Wide	Low	Moderate
THz QCLs	Low-Moderate	Compact-Moderate	Moderate	Yes	Moderate	High	High
Gas lasers	High	Large	Moderate	Yes	Limited	High	High
BWO tubes	High	Large	Moderate	Yes	Wide	High	High
Photomixers	Low	Compact	Low	No	Wide	Moderate	Low

Table 1-1: Comparison between different cw THz sources based on their price, size, material scarcity, cooling necessity, tunability,output power above 1 THz and their fabrication complexity.

1.3.1. THz sources based on Electronics oscillators

These sources are generally based on diodes presenting a negative differential resistance $\left(\frac{dI}{dV} < 0\right)$ coupled to electromagnetic resonator. These sources emit in the sub-THz and the THz region with powers of some tens of µW at 1 THz and some hundreds of mW in the millimeter range. In the following sub-sections, we present the IMPATT diode, the RTD and the Gunn diode.

- An IMPATT diode is a high-power negative differential resistance device that operates based on the impact ionization avalanche breakdown effect. It consists of a p-n junction and an intrinsic high resistivity layer. When a reverse bias above a certain threshold value is applied, an avalanche breakdown occurs due to impact ionization, leading to the concentration of a large number of carriers in the avalanche region. An AC signal just below the breakdown threshold is then applied to generate electromagnetic radiation. The carrier concentration attains its maximum value when the AC signal goes back to its average value, resulting in a 90° phase shift. The diode length is chosen to introduce a further 90° phase lag and generate negative differential resistance, which is sustained by an external resonant circuit to generate electromagnetic waves. High-frequency and high-power IMPATT sources are limited by heat generation and dissipation in the device. Wide-band-gap (WBG) semiconductors such as SiC and GaN are a promising option for realizing high-power, high-frequency IMPATT devices due to their intrinsic material properties. Nowadays, IMPATT devices are used in various applications such as microwave and mm-wave communication systems, high power RADARs, missile seekers, and defense systems. However, they are still not considered compatible with THz applications due to the lack of high output power at high frequencies and small tunability. A commercial sub-THz source produced by TeraSense is an example of an IMPATT sources that can produce power ranging from 80 to 400 mW at 100 GHz and a power of 10 mW at 300 GHz with a linewidth of 1 MHz [12].

-In 1962, John Battiscombe Gunn discovered the Gunn effect, which led to the invention of the Gunn diode, the first low-cost source of microwave power that did not require vacuum tubes. Gunn diodes, made of III-V materials like GaAs and InP, are commonly used in radio communications, military and commercial radar sources for frequencies less than 0.3 THz. Gunn diodes are composed of a uniformly n-doped III-V material sandwiched between heavily doped regions at each terminal. Figure 1.10 (a) shows the energy band diagram variation due change in the orientation of GaAs. When electrons pass from the Γ-valley to the L-valley due to an increase in bias voltage, they experience a high effective mass and low mobility, leading to negative differential resistance and current reduction as shown Figure 1.10 (b). This effect results in ac current oscillations at the contacts and emission of electromagnetic radiation. THz frequency capabilities of

Gunn diodes are limited by the rate of electron intervalley transfer and the breakdown electric field. However, the use of GaN with increased electrical strength and reduced electron-transfer time constants offers the possibility to increase frequency and power-capability. Recent research shows promising results for GaN Gunn diodes in the THz region [13], offering an output greater than 10 mW at selected target frequencies and a range of fundamental frequencies between 0.1 THz and 0.7 THz.

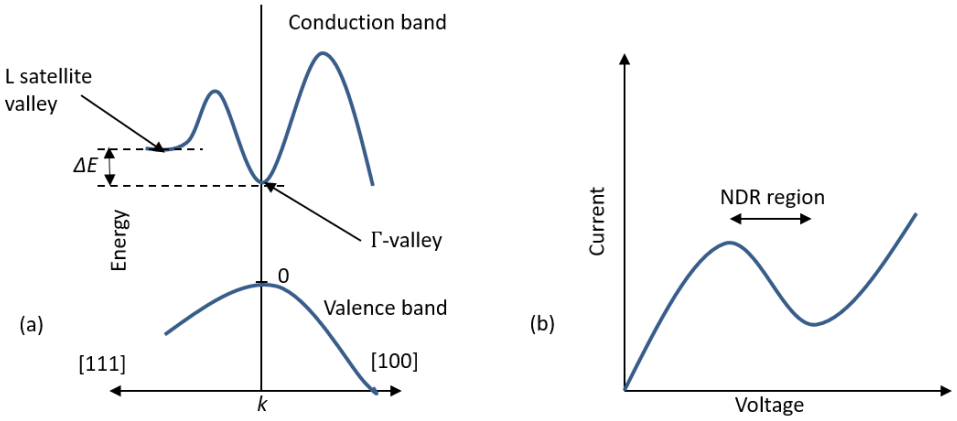

Figure 1.10: (a) Energy diagram variation due change in the orientation of GaAs. It shows the Γ-valley and the L-valley. (b) current-voltage characteristic curve showing the NDR region.

-Resonant tunnel diodes (RTDs) have been studied since the 1950s, and a theoretical analysis of practically realizable semiconductor-heterostructure RTDs was presented in 1973 [14], followed by an experimental demonstration in 1974 [15]. Resonant tunnel diodes (RTD) consist of layers of undoped material leading to the creation of quantum wells between two thin barriers. Quasi-bound, or resonant, energy states are formed in the quantum wells. Resonant tunneling through the double-barrier structure happens when an energy level in the quantum well is close to the energy of the electrons in the conduction band. This tunneling effect gives rise to a peak in the current-voltage characteristic curve. As the bias voltage increases and passes the resonance peak, the current starts to decrease exhibiting an NDR. RTDs need an external resonant circuit to generate electromagnetic waves. An important parameter for high-performance NDR devices is the current peak to valley ratio (PVR), which should be high for maximizing device dynamics. However, increasing peak current densities through techniques such as increased doping or reduced barrier thickness may decrease PVR by increasing the valley current and power consumption due to leakage current. RTDs operate at room temperature and can reach up

to 2 THz, with output power reported in the range of 0.4-10 μW. Although RTDs are promising candidates for THz generation, their resonators and antennas are still simplistic and not efficient, and further developments are needed to optimize their performance.

1.3.2. Electronic frequency multipliers

In the early 1960s, the notion of producing microwaves and millimeter waves through the utilization of frequency multipliers became increasingly prevalent. Subsequently, frequency multipliers were extensively employed in numerous applications, including but not limited to military radios, radar, electronic countermeasures (ECM), and test instrumentation.The operation of an electronic frequency multiplier is based on capacitance or/and conductancenonlinearities existing in a Schottky diode.These nonlinearities can be used to produce harmonics of a RF input signal and thus generating power at multiple integers of the initial input power. However, instead of generating a comb of harmonics, it is possible to concentrate the spectral content in a chosen harmonic. To generate THz waves, a chain of multipliers needs to be coupled to an output oscillator (IMPATT, RTD, Gunn diode, etc) or a microwave synthesizer.Moreover, like all other sources, this source presents several limitations leading to low efficiency especially at high frequencies. The limitations can generally be divided into two distinct types. The first is related to the intrinsic physical limitations of Schottky diodes (high transition time, high capacitance and impedance) leading to low conversion efficiencies (0.5-30%) [16]. The second set of limitations can be categorized as practical limitations related to the way a particular frequency multiplier circuit will be physically implemented and used. In fact, the input and output coupling property of the device is an important criterion for any successful design. In reality at high frequencies it is difficult to provide a purely reactive match to the device for maximum coupling efficiency.

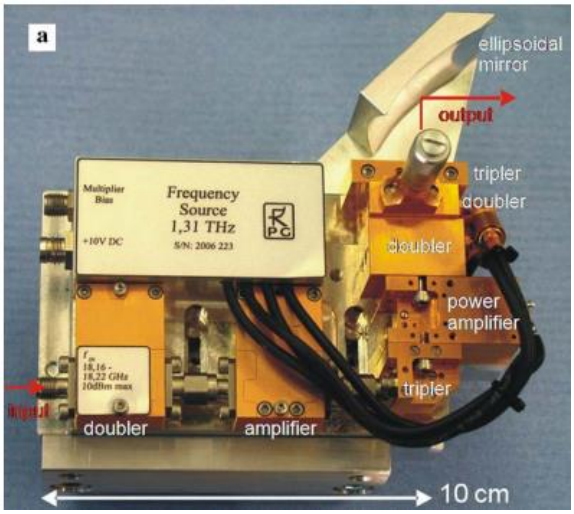

Figure 1.11: Multiplier chain generating a narrow-bandwidth THz wave [17].

A good example of a multiplication chain generating THz wave is shown in reference [17]. Figure 1.11 shows a multiplication chain generating a narrow-bandwidth THz wave. The input source is a commercial microwave synthesizer providing 8 dBm at 18.2 GHz. The cascaded chain of multipliers consists of a frequency doubler, an amplifier, a tripler, a power amplifier at 109 GHz, two doublers, and a final tripler. This results in a total multiplication factor of 72 (72nd harmonic) leading to a 1.31 THz output frequency. The maximum output power is 2.5 µW with a narrow bandwidth of 40 GHz.

As a conclusion, at low frequencies (< 100 GHz) electronic sources are the perfect choice for high output power, however in the THz range efficient and > mW power generation is still a challenge. To eliminate important losses, there is a high necessity to reduce time constants and capacitance which only can be achieved by small area devices. The fabrication and cooling of such electronic devices is also one of the biggest challenges to upgrade these devices.

Moreover, Injection-locked frequency multipliers based on silicon offer a promising approach for efficient and compact terahertz (THz) generation. Such devices could reach the µW level in the J-band (220 GHz-325 GHz) [18] and represent a good competitor for the multipliers previously mentioned. These devices leverage the integration potential and compatibility of silicon with existing technologies, resulting in significant advantages over traditional frequency multipliers. The compact integration capability allows for multiple components on a single chip, facilitating seamless integration with other

functionalities. Compatibility with silicon-based electronics and photonics platforms ensures improved performance and functionality. Furthermore, silicon's wide availability and cost-effective fabrication processes make these sources economically viable. They exhibit high efficiency, enabling strong THz signals for imaging, sensing, and spectroscopy applications.

1.3.3. Vacuum THz sources

In the early 1950s, the first high power (mW range at 1 THz) Vacuum Electronic Device (VED) was manufactured in France offering a limited electronic tunability of 10% [19]. The late 1950s witnessed the development of high power gyrotrons which are a class of VEDs that generates highly coherent microwaves. In the late 1990s, both the U.S and Russia introduced these devices as a weapon. Due to their high-power generation (10-100 MW), VEDscan burn out an unprotected receiver's frontend. Today, VEDs are considered the first reference for high power generation at radio and microwave frequencies and they are mostly used in applications such as industrial radio frequency heating, particle accelerators, and broadcast transmitters. VEDs principle consists in converting a stored electrical energy into a kinetic energy by accelerating a beam of electrons. This kinetic energy is then converted into electromagnetic field energy by the aid ofelectromagnetic guides or cavities defined as interaction zone or circuit. An example of VEDs is the Backward Waves Oscillator (BWO). In BWO,electrons are generated accelerated then focalized by magnets on the anode. The interaction happens when the electron velocity is approximately equal to the phase velocity of the THz electromagnetic wave.In most of the cases, the highest attainable frequency depends on two important criterias. The first criteria is related to the technological fabrication process. In fact, to minimize power dissipation, conducting surfaces should have perfect surface quality with low impurity concentrations, low surface roughness and moderate grain size. The second criteria is related to the theoretical scaling relation $P \propto 1/(\text{frequency})^2$[20] whichis related to the damage threshold of the device caused by the generated high power densities. As a result, the output power is decreased in order to prevent device deterioration. In the THz range,VED sources range from 0.2 THz to 1 THz having an output power between 10 mW and 1 MW[21]. Even though, VEDs are the THz source with the highest output power,

they are still not compatible with THz application since they are considered expensive and could be replaced by semiconductor sources with lower footprint and better tunabilty.

1.3.4. THz quantum cascade lasers

Quantum cascade lasers were first introduced in 1970 by Esaki and Tsu [22]. They fabricated the first one-dimensional periodic potential multilayer by periodically varying the composition during epitaxial growth (superlattice). Later the first QCL was demonstrated at Bell laboratories by Faist et al [23] in 1994. QCLs were first used in the mid-infrared range, but since 2002, they have also been utilized in the THz range.[24]. QCLsare compact semiconductor sources based on superlattice materials created by using multilayered heterostructures of III-V compounds semiconductors. Stimulated emission is generated from the transitions between electronic subbands formed in a series of quantum wells. By 'cascading' several such active regions together, the injected electron undergoes numerous lasing transitions as they pass through the device. So, the characteristics of the laser can be chosen through the engineering of the band structure and the semiconductor superlattice. Figure 1.12 is a conceptual representation of the conduction band of a heterostructure QCL laser. It shows numerous lasing transition due to the presence of polarized quantum wells

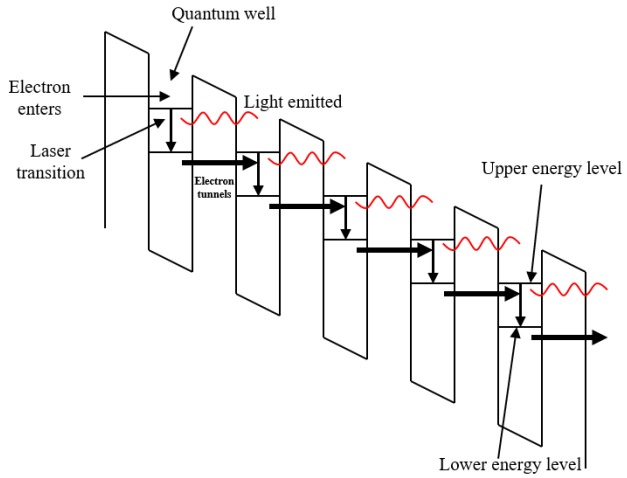

Figure 1.12: Shcematic representation of the conduction band of a heterostructure QCL laser.

Ref.	*Frequency(THz)*	*Output power(mW)*	*Temperature(K)*	*Year*
[25]	3.7	5	121	2016
[26]	3.41	0.014	293	2016
	2.06	0.0006	293	2016
[27]	3.57	0.08	293	2016
[28]	3.09	0.1	15	2016
[29]	3.1	1	-	2010
[30]	3.4	1010	10	2014
[31]	3.87	-	120	2017
[32]	3.4	103	20	2012

Table 1-2: Review on THz QCLs **[33]**.

QCLs have brought a revolutionary change in the development of MIR sources, demonstrating remarkable performance with multi-Watt output power at room temperature.CW QCLs have achieved significant wall-plug efficiencies of up to 21% at room temperature, covering a wide spectral range of 2.7-25 μm [34]. Pulsed QCLs have also exhibited remarkable performances over the range of 1-5 THz, resulting in peak output power higher than 1 W [35]. However, in the THz region, QCLs operate at low temperatures [36], requiring cryogenic cooling. This phenomenon can be attributed to the fact that at room temperature, the energy of thermal agitation allows the filling of higher energy levels, thus preventing population inversion. Table 1-2presents the performance of some QCLs in the THz region. The highest operation temperature was achieved using a design with a three-quantum-well resonant depopulation THz QCL, utilizing GaAs/$Al_{0.15}Ga_{0.85}As$ grown on GaAs substrates. It has been shown that the performance of these devices is limited by two significant factors: optical phonon scattering of thermal electrons, which dominates at shorter wavelengths, and parasitic current, which dominates at longer wavelengths [37]. Despite the limitations in operating temperature, QCLs currently generate the highest THz output power among all solid-state sources and remain one of the best candidates for THz applications.

1.3.5. THz sources based on difference frequency generation (DFG)

DFG THz sources are one of many types of non-linear optic THz sources. In such devices the optical phenomena resulting from the interaction between electromagnetic fields and electrons in a medium lead to electron acceleration and radiation. In the linear optical regime, electron oscillations are proportional to the optical field, while in the non-linear regime, strong optical fields cause non-linear electron oscillations at different frequencies.However, in the non-linear regime, the external optical field is exceedingly strong, and the electron oscillation is no longer linear. As indicated in equation (1.3.1), the relationship between the external electric field and the polarization of the field is non-linear.

$$\vec{P} = \varepsilon_0 \chi^{(1)} \vec{E} + \varepsilon_0 \chi^{(2)} \vec{E}\vec{E} + \varepsilon_0 \chi^{(3)} \vec{E}\vec{E}\vec{E} + \ldots \qquad (1.3.1)$$

In this scenario, the non-centrosymmetric medium used (such as GaAs, ZnTe, or LiNbO3) only considers the second-order nonlinearity ($\chi^{(2)}$). Depending on the orientation of the medium, the second-order nonlinearity can produce either sum frequency generation (SFG) or difference frequency generation (DFG). In a DFG experiment, a non-centrosymmetric crystal is excited by two laser beams that are spatially overlapped and have slightly shifted radial frequencies ω_1 and ω_2. This results in the generation of a THz wave with a radial frequency $\omega_{THz} = |\omega_1 - \omega_2|$. Figure 1.13 (a) illustrates the input frequencies and the non-centrosymmetric crystal generating the difference frequency. Figure 1.13 (b) displays energy band diagram transitions that correspond to DFG phenomena.

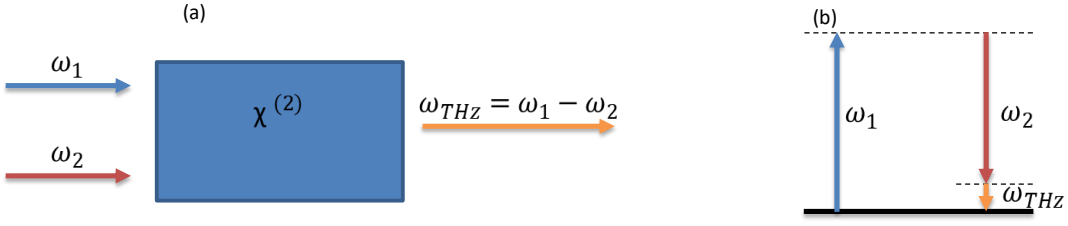

Figure 1.13: (a) Simplified depiction of a DFG phenomenon in a non-centrosymmetric crystal and(b) Energy-level diagram for DFG showing the THz generated wave.

Achieving efficient THz generation requires phase matching between the THz generated wave and the optical sources, but perfect phase matching is not possible due to the normal dispersion of materials that are lossless in the range of ω_1, ω_2 and ω_{THz} (where the effective index increases with frequency). Therefore, the technique of quasi-phase matching [38]is typically employed, which involves fabricating a periodically poled material where the orientation of one of the crystalline axes, usually the c axis of a ferroelectric material, is inverted periodically within the material. This periodic inversion compensates for the wavevector mismatch, allowing the field amplitude to grow monotonically with propagation distance, although not as rapidly as in perfectly phase-matched interactions. Regarding performance, reference [39]is a good example where they report a cw single-frequency THz laser emitting at 1.9 THz with a linewidth of less than 100 KHz and an output power exceeding 100 µW. The THz source is generated through a parametric difference DFG in a nonlinear crystal located in an optical enhancement cavity. Two single-frequency vertical-external-cavity lasers with emission wavelengths of 1029.2 nm and 1036 nm ($\Delta\lambda$ = 6.8 nm) and 1 W output power each are used as pumping sources. The lasers are phase-locked to an external cavity to reduce phase losses in the output THz source. This THz source could be utilized as a local oscillator to drive a receiver in astronomy applications.

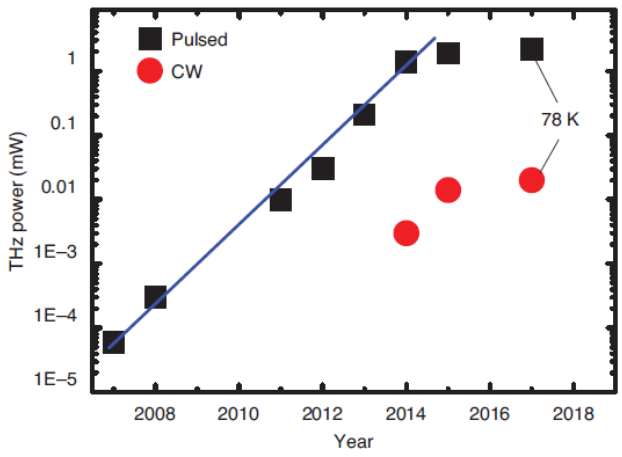

Figure 1.14: Timeline for the output powerimprovement of THz DFG-QCL**[40]**. The data of pulsed sources correspond to the peak output powers.

In recent years, the development of THz DFG-QCLs has emerged as a promising nonlinear THz source. These devices exploit the powerful and room temperature operation characteristics of mid-IR QCLs to generate THz via DFG. By generating two mid-IR lines at $\omega_1$andω_2, these lines act as a pump to emit a THz frequency through DFG. THz DFG-QCLs are currently the only electrically pumped monolithic semiconductor sources operating at room temperature in the range 1-6 THz. Recent improvements in giant second order susceptibility medium and phase matching have led to significant advances in performance, including narrow-linewidth single-mode terahertz emission that is tunable from 1 to 6 THz with peak output powers reaching the mW level in pulsed mode. Figure 1.14 illustrates the rapid improvement in output power over the last decade. However, these devices still have limitations such as low wall plug efficiency and narrow tunability, which make it challenging to meet the requirements for many THz applications. Nonetheless, ongoing research continues to show promising advancements for THz DFG-QCLs.

1.3.6. Far infrared gas lasers

In 1963, A. Crocker et al. [41] demonstrated the first stimulated far-infrared emission with watts of power from a pulsed electrical discharge in water vapor, which was a milestone in the history of terahertz (THz) stimulated emission in a molecular gas. Subsequently, the first optically pumped CO_2 far-infrared (far-IR) laser was demonstrated in 1970. In the following two decades, a spectrum of far-IR lines was discovered, which are currently used in various applications, such as terahertz spectroscopy, terahertz imaging, and fusion plasma physics diagnostics. The basic design of these lasers follows that of a typical laser, comprising a cavity and a gain medium consisting of molecular gases such as CH_3F, CH_3OH, NH_3, and CH_2F_2[42]. The laser emission occurs when the molecular gas is pumped either electrically or optically at room temperature and low pressure, leading to population inversion between the rotational levels of an excited vibrational state of the molecule that is nearly empty at room temperature. Typically, this type of laser is pumped by an infrared CO2 laser, and lasing occurs from different transition frequencies covering the THz range by changing the CO2 laser wavelength. These lasers typically operate at low pressures (< 0.1 Torr) with cavities of around 1 meter long, producing up to 100 mW output power, depending on the rotational transitions

involved. However, compared to other THz sources, this source offers limited tunability since the output THz frequency is determined solely by precise transitions in the CO2 molecules.

Summary for cw THz sources

A. Pagies et al. [43]were the first to use a QCL instead of aCO_2 laser to pump a NH_3 (ammonia) gas laser.The authors demonstrate the continuous-wave generation of ten laser lines around 1 THz. A power of 34 μW is measured at 1.07 THz, with a very low threshold of 2 mW and a high differential efficiency of 0.82 mW/W. The generated laser lines exhibit a linewidth lower than 1 MHz, as determined from spectrum measurements.The use of QCLs as a pumpis way better than CO_2 laserssince they give the possibility to excite more transition lines due to theireasy and larger tunability. In reference [44],by using an optimized structure, they demonstrateda ML (molecular laser) emissionof 1 mW at 1.1THz in continuous wave. For future research, the results in ref.[43] and[44] could reintroduce the use of optically pumped far-infrared gas lasers as a compact and powerful continuous THz sources.

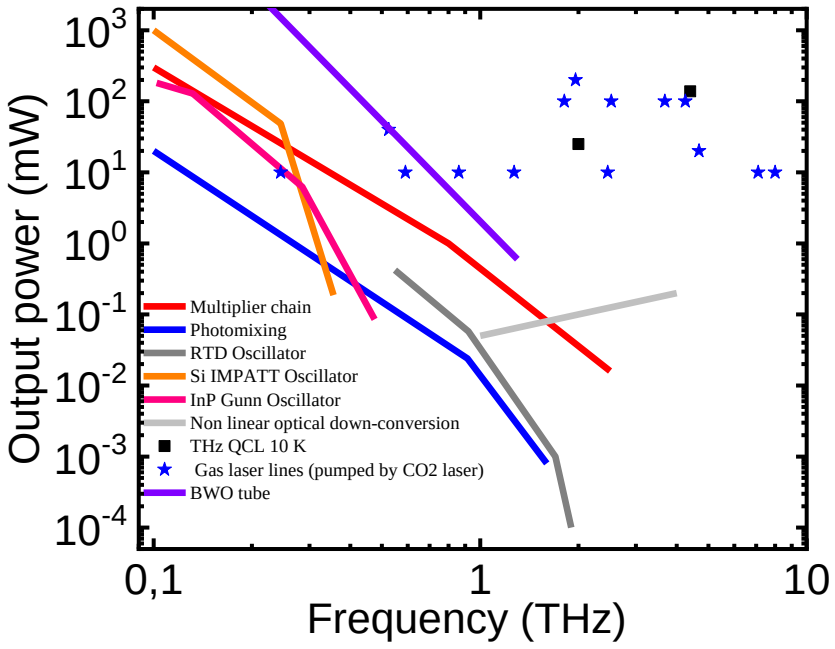

Figure 1.15: State of the art of the output power for cw THz sources.

Figure 1.15 shows a state of the art of the output power for the cw THz sourcespresented above. All the results in this figure are obtained at room temperature except for the THz QCLs (at 10 K). It is clear that the sources having the highest output power are CO_2 gas lasers and BWOs. However, these two sources are considered less practical than the other sources since they present several important limitations. For example, a BWO needs a permanent water-cooling system and a magnetic field higher than 1 T. Additionally, they are considered quite costly compared to the other sources. Furthermore, the CO_2 gas lasers are considered too bulky and could not emit on some frequency points. For this reason, a lot of research is being done to improve the other sources or to reduce the limitations of these two high power sources. It is important to mention that photomixing is the only cw source existing in Figure 1.15that was not described in this section. It is discussed in detail below since it is the main concern ofthis work.

1.4. THz sources based on optical mixing of laser tones: Photomixing

In the early 1960s, the mixing of two laser frequencies by using a detector presenting a quadratic response in amplitude of the incident EM wave, has been investigated to measure the spectral purity of lasers [45]. Brown et al. [46] were the first to report the production of cw waves in the THz frequency range using a technique they named "Photomixing". Their method involved mixing two cw Ti:Sa lasers in an ultrafast photodetector that was coupled to a wideband antenna. Since then, the term Photomixing has referred to the generation of cw THz waves by illuminating an ultrafast photodetector (called Photomixer) with an optical beating note produced by the superposition of two laser tones. The beating signal at ω_B is the difference between the slightly shifted angular frequencies ω_1 and ω_2 of the two lasers. The internal photoelectric effect, described later induces the oscillation of the photocarrier density at the beat frequency, which in turn generates an oscillating electrical photocurrent at the same frequency when driven by a static electric field. When connected to a suitable load such as a planar antenna, the device emits a THz wave with the beat angular frequency ω_B. Photomixer devices can be divided into two categories: lumped-element devices and traveling wave devices. In this section, we will only discuss lumped-element devices, which have been extensively studied in the

past. Traveling wave devices will be introduced and compared to lumped-element devices in the following chapter.

Two types of lumped-element photomixers exist: 1) photoconductive devices which are based on Metal-Semiconductor-Metal (MSM) structures using interdigitated electrodes as shown in Figure 1.16 (a) and (b) and 2) photodiodes such as pin and UTC-PD (Uni-Traveling-Carrier photodetectors).Figure 1.16 (c) shows a representation of a pin photodiode. MSM photoconductors are top illuminated devices consisting of a photoconductive material presenting a sub-picosecond carrier lifetime (induced mainly by deep energy level defects incorporated in the semiconductor material) electrically biased through metallic electrodes forming Schottky contacts.Pin devices consist of a thin intrinsic (I) layer sandwiched between heavily doped p-type (P) and n-type (N) layers, forming apindiode. When the device is illuminated with optical beating, electron-hole pairs are generated within the intrinsic layer, and carriers undergo drift motion towards their respective electrodes under the influence of the built-in electric field. The application of a bias voltage induces an electric current that flows through the device and results in a periodic density modulation of the carriers within the intrinsic layer which generates THz radiation through photomixing.

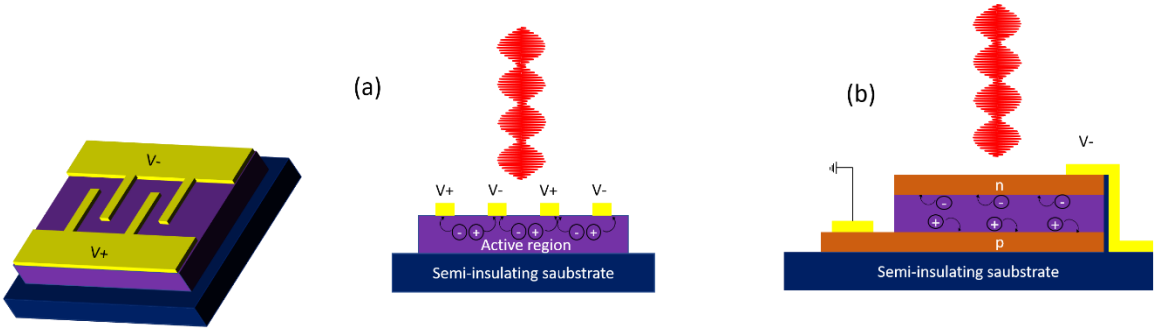

Figure 1.16:(a) Top and cross-sectional view of an interdigitated photomixer structure. (b) cross-section view of the pin structure. In the two configurations the V+ and V- denote the bias voltage.

1.4.1. Photomixing principle

As mentioned in the previous section, photomixing is based on the photodetection of the optical beatnote produced by the superposition of two cw lasers of same polarization and slightly shifted angular frequency. From a mathematical point of

view, we will assume that the propagation direction of the beating source is along the *z*-axis so the electric field of one laser can be written as

$$\overrightarrow{E_l}(z,t) = E_l\, cos(\omega_l t - k_l z + \phi_l)\overrightarrow{e_x}$$

Assuming that $\omega_2 < \omega_1$ the energy flux density of the superposition of the two fields is:

$$\begin{aligned}
\left|\vec{S}(z,t)\right| &= \left|\vec{E}(z,t) \times \vec{H}(z,t)\right| \\
&= Y_0 \vec{E}^2(z,t) \\
&= Y_0 \left(\vec{E}_1(z,t) + \vec{E}_2(z,t)\right)^2 \\
&= Y_0\, {E_1}^2\, cos^2(\omega_1 t - k_1 z + \phi_1) + Y_0\, {E_2}^2 cos^2(\omega_2 t - k_2 z + \phi_2) \\
&+ Y_0 E_1\, E_2 cos\big((\omega_1 + \omega_2)t - (k_1 + k_2)z + \phi_1 + \phi_2\big) \\
&+ Y_0 E_1\, E_2\, cos\big((\omega_1 - \omega_2)t - (k_1 - k_2)z + \phi_1 - \phi_2\big) \qquad (1.4.1.1)
\end{aligned}$$

$Y_0 = \sqrt{\varepsilon_0 / \mu_0}$ represents the admittance of free space

From the energy flux density, it can be inferred that there exist four distinct components: namely, the laser frequencies $\omega_1$and ω_2, the combined sum frequency $\omega_1 + \omega_2$, and the difference frequency referred to as the beat frequency $\omega_B = \omega_1 - \omega_2$. In order to facilitate detection by the photomixer, the beat frequency is chosen such that its magnitude is sufficiently small. Conversely, the sum frequency and the laser frequencies possess magnitudes exceeding the photomixer's cutoff frequency, and therefore only their temporal average can be detected. Consequently, the detected energy flux density is:

$$\left|\vec{S}(z,t)\right| = \frac{Y_0}{2}(E_1^2 + E_2^2) + Y_0 E_1 E_2 cos\big((\omega_1 - \omega_2)t - (k_1 - k_2)z + \phi_1 - \phi_2\big) \quad (1.4.1.2)$$

This equation can be separated into two distinct components. The first component is the linear "dc" part, which is comprised of the sum of the intensities of the two lasers. The second component is the modulated part, which is proportional to the product of $Y_0 E_1 E_2$. The dc part generates a dc current in the circuit, which can contribute to heating and potential damage of the device. The modulated part represents the beating effect, where the beating frequency ω_B is determined by the difference between the angular frequencies of the two lasers ($\omega_B = \omega_1 - \omega_2$). For the sake of simplicity, we will consider $E_1 = E_2 = E_0$ and $\phi_1 - \phi_2 = 0$. As a result, the energy flux density can be simplified and written as the following:

$$\left|\vec{S}(z,t)\right| = Y_0 E_0^2\{1 + cos\big((\omega_1 - \omega_2)t - (k_1 - k_2)z + \phi_1 - \phi_2\big)\} \quad (1.4.1.3)$$

1.4.2. Photoconductive devices

In this part, a detailed study will be done from a theoretical point of view on the photoconduction physical phenomena. Let us assume a given type of photoconductive material (here only electrons are considered in the equations) having a thickness *d*, a width *w*, and a length *l* and let us consider an optical beam perpendicularly incident on the upper surface of the medium which biased though contact electrodes as shown in Figure 1.17. As a result of high carrier density and the presence of an electric field, a photocurrent flows between the two electrodes.

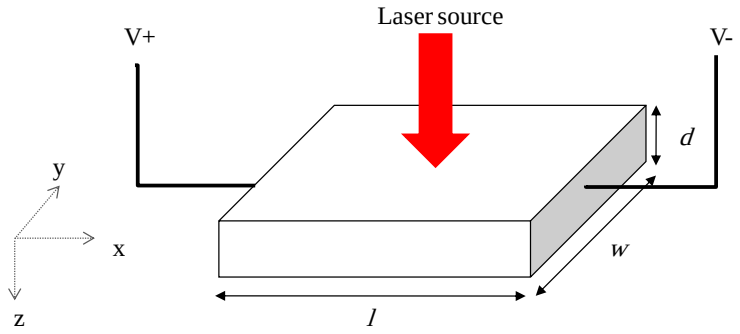

Figure 1.17: Geometry of a simplified photoconductor showing its dimensions.

Photons are absorbed in a semiconductor following the Beer-Lambert Law: $I(t,z) = (1-R)I_0(t)e^{-\alpha z}$.where R is the reflectance and α is the absorption coefficient of the material.$I_0(t)$ is the intensity of light at $z = 0$which is equal to $\left|\vec{S}(z=0,t)\right|$. If the optical power$P_{opt}$ is distributed equally on the semiconductors surface $I_0(t)$ can be written as $I_0(t) = \frac{P_{opt}(t)}{A}$ where $A = wl$ is the surface of the semiconductor.

The density of the generated carriers is given by

$$\begin{aligned} \mathrm{g}(z,t) &= -\frac{1}{h\nu}\frac{\partial I(z)}{\partial z} \\ &= \frac{1}{h\nu}\alpha I_0(t)(1-R)e^{-\alpha z} \\ &= \frac{Y_0 {E_0}^2 \alpha(1-R)e^{-\alpha z}}{h\nu}(1+cos(\omega_B t)) \end{aligned} \qquad (1.4.1.4)$$

Where $h\nu$is the energy of one photon. The electron density in the semiconductor $n(\vec{r},t)$ can be calculated based on the continuity equation:

$$\frac{\partial n(\vec{r},t)}{\partial t} = g(\vec{r},t) - \frac{n}{\tau} + \frac{1}{e}\nabla\vec{J}(\vec{r},t) \qquad (1.4.1.5)$$

The ratio $\frac{n}{\tau}$ represents the recombination/trapping rate of free carriers, with τ indicating the carrier lifetime of the material. The current density $\vec{J} = \vec{J}_{diff} + \vec{J}_{drift}$ is composed of both diffusion and drift currents, where $\vec{J}_{diff} = -eD\vec{\nabla}n$ and $\vec{J}_{drift} = -ne\vec{v} = ne\mu\vec{E}$, with $\vec{E}$ being the electric field and μ the mobility. It is assumed that the charge neutrality is maintained throughout the device. Due to the short lifetime of the photoconductive material, which is on the order of $\tau \approx 1$ ps, the diffusion current is negligible when compared to carrier trapping. Under conditions of negligible current or low electric fields, the impact of drift current on $\frac{\partial n(\vec{r},t)}{\partial t}$ be disregarded. Conclusively, the continuity equation will be expressed of the following form:

$$\frac{\partial n(\vec{r},t)}{\partial t} = g(\vec{r},t) - \frac{n(\vec{r},t)}{\tau} \qquad (1.4.1.6)$$

Equation(1.4.1.6)can be solved analytically by replacing $g(\vec{r},t)$ from equation (1.4.1.4) which leads to the following general solution

$$n(z,t) = n_0(z,t)\left[1 + \frac{\cos\left(\omega_B t + \operatorname{atan}(\omega_B t)\right)}{\sqrt{1+(\omega_B\tau)^2}}\right] \qquad (1.4.1.7)$$

Where $n_0(z,t) = \frac{Y_0 E_0^2 \tau\alpha(1-R)e^{-\alpha z}}{h\nu}$

Let τ_{tr}be the transit time of a carrier moving from one electrode to another. In general, τ_{tr} depends on the position of creation of carriers and the bias field strength. Here we will presume that the carriers pass a length *l*leading to $\tau_{tr} = \frac{l}{v} = \frac{l}{\mu E}$. Let us also define $\gamma = \frac{\tau}{\tau_{tr}}$as the ratio between the carrier life time and the carrier transit time. It is known as the photoconductive gain and it depicts the number of electrons that are collected by the electrodes per an absorbed photon.

The photocurrent I_p is calculated through the simplified definition of the current density$j = n(z)ev$

$$I_p = \int_0^w \int_0^d j dz\, dy$$

$$= evw \int_0^d n(z) dz$$

$$= e.v.w.n(d,t)\left[1 + \frac{cos\left(\omega_B t + atan(\omega_B t)\right)}{\sqrt{1+(\omega_B\tau)^2}}\right] \qquad (1.4.1.8)$$

For a clearer representation of I_p ,let $\eta_{opt} = (1-R)(1-e^{-\alpha d})$, and $P_{opt} = AI_0 = wlY_0{E_0}^2and\theta = atan(\omega_B t)$. Finally, the photocurrent could be written of the following form

$$I_p = \frac{e}{h\nu}\gamma\eta_{opt}P_{opt}\left[1 + \frac{cos\left(\omega_B t + \theta\right)}{\sqrt{1+(\omega_B\tau)^2}}\right] \qquad (1.4.1.9)$$

The previous equation describes the current in a photoconductor without a load, however in reality the generated THz power is dissipated in a load such as an antenna. It can also be coupled to a power meter or a spectrum analyzer through contact probes. In most of

the cases the impedance of such instruments is real and is around 50 ohms. The whole setup of coupling a photogenerated current to a load can be modeled in the circuit shown in Figure 1.18. The photoconductor is represented by a photoconductance $G(t)$ in parallel to a capacitance C which is biased by a source at V_b. At the output, the current $I(t)$ is dissipated in the load having a conductance G_L. In order to filter the higher orders of ω_B, an LC resonator was placed in the circuit.

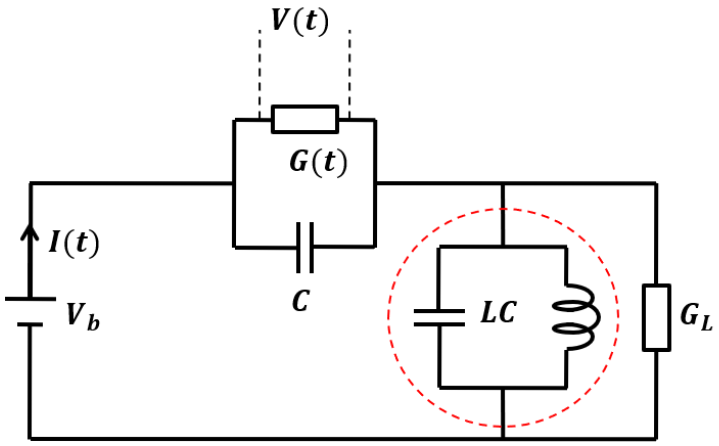

Figure 1.18: Circuit model of a photoconductor considering the LC resonator which filters all the harmonics except $\boldsymbol{\omega_B}$

For better circuit analysis, let us calculate the photoconductance $G(t)$ which is the ratio between the calculated current I_p and the voltage V:

$$G(t) = \frac{I_p}{V} = \frac{e}{hV\nu}\gamma\eta_{opt}P_{opt}\left[1 + \frac{cos\,(\omega_B t + \theta)}{\sqrt{1 + (\omega_B\tau)^2}}\right] \qquad (1.4.1.10)$$

For a sufficient low voltage and in constant mobility regime $\nu = \mu E = \mu V/l$, $\tau_{tr} = \frac{l}{\nu} = \frac{l^2}{\mu V}$ and $\frac{\partial G}{\partial V} = 0$. In this case $G(t)$ is of the following form:

$$G(t) = G_0 + G_1\,cos\,(\omega_B t + \theta) \qquad (1.4.1.11)$$

where G_0 is defined as $\frac{e\mu\tau}{h\nu l^2}\eta_{opt}P_{opt}$ and represents the dc photoconductance and $G_1 = \frac{G_0}{\sqrt{1+\omega_B{}^2\tau^2}}$ is the amplitude of modulation of the photoconductance. In the follow, in order to simplify the calculations, we will set θ to 0. If we consider that all the harmonics of ω_B are filtered we can write the voltage and the current across the photoconductor as follows:

$$V(t) = V_{dc} + V_{ac}\,cos\,(\omega_B t + \delta) \qquad (1.4.1.12)$$

$$I(t) = I_{dc} + I_{ac}\, cos\, (\omega_B t + \delta) \tag{1.4.1.13}$$

Where δ is the phase delay and will be defined later The relation between the voltage and the current across the photoconductor will be of the following form:

$$I(t) = G(t)V(t) \tag{1.4.1.14}$$

By using the complex notation as follows: $V_{ac} co\, s(\omega_B t + \delta) = Re\{v_{ac}(\omega_B) e^{j\omega_B t}\}$, $I_{ac} co\, s(\omega_B t + \delta) = Re\{i_{ac}(\omega_B) e^{j\omega_B t}\}$ etc. and based on equation (1.4.1.14) the following can be calculated:

$$I_{dc} = V_{dc} G_0 + \frac{1}{2} V_{ac} G_1 cos\, (\delta) \tag{1.4.1.15}$$

$$i_{ac} = G_0 v_{ac} + G_1 V_{dc} \tag{1.4.1.16}$$

After that the current Kirchhoff's law is applied resulting in the following written in the complex notation:

$$-G_L v_{ac} = i_{ac} + jC\omega_B v_{ac} \tag{1.4.1.17}$$

Finally, V_{ac} and δ are calculated:

$$V_{ac} = V_{dc} \frac{G_1}{\sqrt{(G_0 + G_L)^2 + (C\omega_B)^2}} \tag{1.4.1.18}$$

$$\delta = \pi - atan\left(\frac{C\omega_B}{G_0 + G_L}\right) \tag{1.4.1.19}$$

Additionally, the LC resonator short-circuits G_L at $\omega = 0$. As a result, one can conclude from the resulting circuit that $V_{dc} = V_b$.

Now that all the parameters are well defined, the generated THz power can be written of the following form:

$$P_{THz} = \frac{1}{2} G_L {V_{ac}}^2 \tag{1.4.1.20}$$

In general, the load admittance is not purely conductive where $Y_L = G_L + jB_L$. Now if V_{ac}, G_1 and Y_L are replaced in P_{THz} equation (1.4.1.20) will be of the following from:

$$P_{THz} = \frac{{V_b}^2 {G_0}^2}{2} \frac{G_L}{[(G_0 + G_L)^2 + (\omega_B C + B_L)^2](1 + {\omega_B}^2 \tau^2)} \qquad (1.4.1.21)$$

For a maximum power dissipation, a perfect impedance matching is needed, i.e $G_0 = G_L$ and $B_L = -\omega_B C$. However, in practical cases B_L is considered 0 and $G_0 \ll G_L$ which leads to the well-known expression of P_{THz} popularized by E. Brown and coworkers [47]:

$$P_{THz} = \frac{{I_{dc}}^2}{2} \frac{R_L}{[1 + (\omega_B R_L C)^2](1 + {\omega_B}^2 \tau^2)} \qquad (1.4.1.22)$$

R_L is the load resistance and is defined by $1/G_L$ and is equal to 50 ohms in most of the electronic instruments such as power meters and spectrum analyzers. Equation (1.4.1.22) shows clearly the two cut-off frequencies related to the device capacitance (f_{RC}) and carrier lifetime (f_τ).

In this context, a hypothetical scenario is considered where the capacitance is assumed to be negligible ($C = 0$), and the device performance is solely dependent on the carrier lifetime. The frequency response of such a system is illustrated in Figure 1.19 (b) for various lifetimes within the frequency range of 0-500 GHz. Active regions of photoconductors often employ semiconductors such as LT-GaAs, which exhibit low carrier lifetimes (sub-picosecond) and high dark resistivity resulting in lifetime cut-off frequencies above 300 GHz. However, in reality, the capacitance of a photoconductor cannot be ignored and can be quantified by the following equation:

$$C = \frac{s\varepsilon}{l}$$

where l represents the interelectrode spacing, s denotes the electrode surface area, and ε is the dielectric constant of the semiconductor. Figure 1.19 (a) presents a more realistic scenario where the lifetime is fixed at 100 fs, and the RC roll-off is shown for different capacitance values. Thus, it can be concluded that for optimal performance in photomixers utilized for THz generation, sub-picosecond lifetimes and electrode configurations resulting in capacitance values lower than 10 fF are ideal.

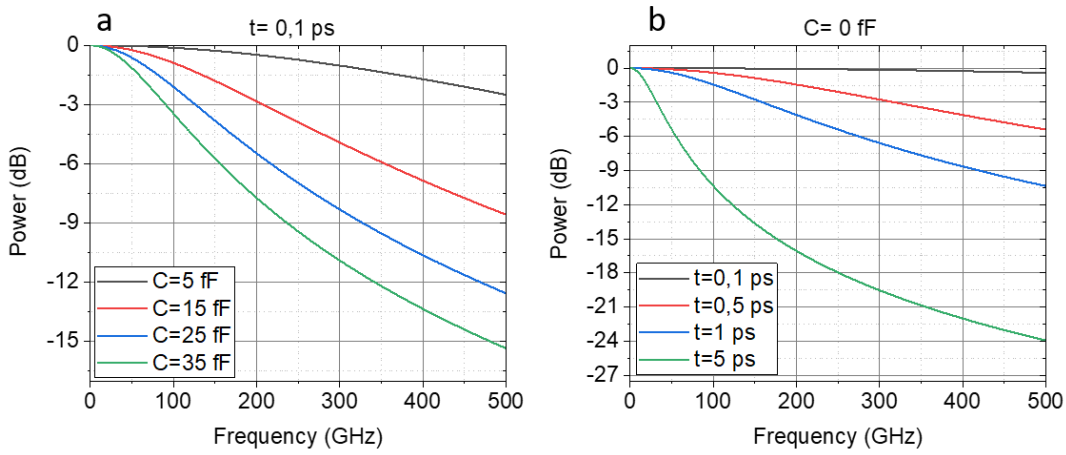

Figure 1.19: Generated power by a hypothetical photomixer in the frequency range 0-0.5 THz. (a) Frequency response dependence on the capacitance for a lifetime of 0.1 ps. (b) Frequency response dependence of the lifetime for an ideal case where C=0.

1.4.3. Photodiodes

PIN structure: As previously mentioned, another type of semiconductor device that can be utilized as a photomixer is the pn junction photodiode. When photons generate electron-hole pairs within the depletion region of a pn junction, the built-in potential accelerates the electrons and holes towards the electrodes, resulting in a photocurrent. However, p-n homojunctions with constant doping in the p and n regions are not very efficient photodiodes. At high doping concentrations, the depletion region where carrier transport is efficient (drift) becomes narrow, and only a small portion of the incoming light can be absorbed in or close to the depletion region. Lower doping concentrations increase the depletion region width, but also make it more difficult to form low resistance ohmic contacts. The principal difficulties of p-n junctions for photodetectors can be addressed by introducing an intrinsic layer between the p and n regions. Pin diodes enable high doping concentrations for low resistance ohmic contacts, independent of the intrinsic layer width. The intrinsic layer should be wide enough to absorb most of the incoming radiation and reduce the capacitance of the device, but it should also be as narrow as possible to decrease the transit time of the charge carriers. Minority carriers that are generated in the doped regions diffuse until they reach the intrinsic region, where they are efficiently accelerated by the electric field. The doped regions of pin diodes are usually fabricated from a material with a larger bandgap than the photon energy at the operating

wavelength. Light absorption and the generation of charge carriers only take place in the intrinsic region, where the electric field efficiently separates the charge carriers. The frequency response of pin diodes has an RC-roll-off similar to that of photoconductors. Recombination of photogenerated charge carriers is negligible, and the frequency response is determined by the transit time rather than the carrier lifetime, as in the case of photoconductors. The pin photodiodes are not suitable for THz photomixing because the low drift velocity of holes in most III-V semiconductor materials results in a low intrinsic frequency bandwidth and a low saturation current due to the space charge accumulation in the intrinsic layer, which screens the bias field.

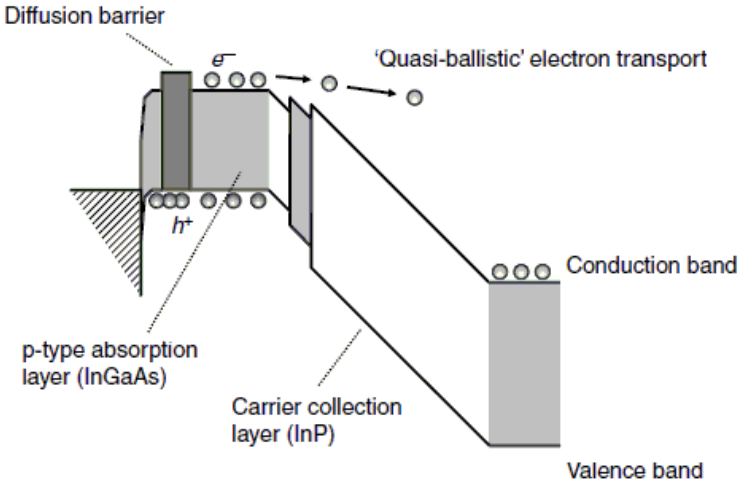

Figure 1.20: Schematic band diagram of a UTC-PD**[48]**

UTC-PD structure: In 1997, researchers from the NTT laboratory proposed UTC-PD to overcome the limitations of InP/InGaAs pin photodiodes in terms of frequency response and photocurrent saturation [49]. UTC-PD's have a pin diode-like structure in which light absorption and carrier collection occur in two distinct regions, as illustrated inFigure 1.20. The heavily p-doped InGaAs absorption layer results in a frequency response that is no longer limited by the transit time of low-saturation velocity holes in InGaAs, but by the motion of electrons in the InGaAs absorption and InP collection layer. A blocking layer ensures that electrons only diffuse/drift towards the InP collection layer, where they drift across at their overshoot drift velocity. Additionally, the photocurrent saturation level is

improved due to the reduction of the space charge effect in the collection layer induced mainly by the slow holes in the pin photodiodes.

1.5. Coherent THz detectors

Coherent detectors are devices used to measure the amplitude and phase of electromagnetic waves. In most of the cases except in electro-optic sampling, these detectors operate using mixing between two radiations. The principle of detection by mixing two radiation is based on combining the THz frequency f_{THz} with a reference frequency generated by a 'local oscillator' of frequency f_{LO}. The local oscillator sources are often solid-state or gas lasers. The THz frequency and the local oscillator frequency are combined in a non-linear mixer that bring out frequency components corresponding to the sum frequencies ($f_{THz} + f_{LO}$) as well as the difference frequency ($f_{THz} - f_{LO}$). The former represents the upconversion of the THz signal and the latter corresponds to the downconversion of the THz signal. The difference frequency is usually called 'intermediate frequency' (IF) and is proportional to the original THz signal. These mixers can be divided to two types: photoconductive mixers and electronic based mixers. For example, well-known electronic based mixers are heterodyne receivers incorporating Schottky diode mixers. The latter are powered by local oscillators based on multiplier chains which enabled the realization of THz sensors with fW-level sensitivity operating at room temperature [50][51]. These electronic devices have been developed primarily for applications in astronomy, earth, and planetary science [52], and have demonstrated promising results. In addition to the aforementioned electronic devices, there have been several studies carried out in recent years on photoconductive devices as THz sources and detectors. These investigations have been facilitated by the continuous improvement of near-infrared laser sources operating at wavelengths ranging from 780 to 1550 nm. Currently, laser-driven sources and detectors play a pivotal role as key components in commercial THz spectrometers [53][54], and they are driving the progress towards high data rates in THz wireless communications by serving as a bridge between optical fibers and wireless communication technologies [55]. In the following we will emphasize on optoelectronic mixing using photoconductive devices for THz detection.

- Optoelectronic mixing: heterodyne detection, downconversion

In the realm of photonic-based detection of continuous THz waves, frequency mixing is also employed. In this approach, the input THz wave is down-converted to an intermediate frequency f_{IF} using a photoconductor that is illuminated by an optical signal that has been modulated at a frequency f_{LO}, satisfying the previously presented condition $f_{IF} = |f_{THz} - f_{LO}|$. This detection process is generally called heterodyne detection. Specifically, in this scenario, the detection scheme could be referred to as homodyne detection [56], if the same optical beat note of two slightly detuned laser lines is utilized for the generation and detection of THz radiation, with f_{THz} being equal to f_{LO}. As a result, the only detected signal at the output is the dc current.

Frequency sampling:

Mixing can also be achieved using a pulsed laser system as LO instead of a modulated cw source. In this case the mixing happens between the THz frequency f_{THz} and the repetition frequency of the pulsed laser f_{rep}. Knowing that there will be a comb of n integer number of f_{rep}, optoelectronic mixing happens between the THz wave and each f_{rep} component resulting in $f_{IF} = |f_{THz} - nf_{rep}|$. In other words, the optical pulses act as an ON switch for the photoconductive device allowing the transmission of samples of the THz wave. This is generally referred to frequency sampling. Sampling is one essential function in analog to digital conversion. In order to realize frequency sampling, basic rules should be followed. The Shannon principle states that in order not to lose information when sampling a signal, the sampling frequency must be at least twice the highest frequency component in the signal to be sampled ($f_s \geq 2f_{max}$) where f_{max} is the maximum frequency in the RF or THz frequency band to be sampled and f_s is the sampling frequency which is a well-chosen multiple of f_{rep} in order to validate the Shanon principle.

Frequency sub-sampling:

As telecommunication systems incorporate higher frequency bands, the need for increased sampling frequencies arises. However, beyond 10 GHz, obtaining a stable sampling signal for high quality sampling poses a significant challenge [57]. Nonetheless, it is feasible to sample signals on a high carrier frequency with a lower sampling frequency, given specific conditions. This approach is applicable when the objective is to

reconstruct the signal modulated onto the high-frequency carrier, rather than the real-time domain signal. In such cases, the modulation has a frequency bandwidth that is a fraction of the carrier frequency. After sampling, replicas of the RF frequency are generated in the frequency ranges known as Nyquist zones [58] shown in Figure 1.21. These zones represent portions of the spectrum with frequency limits ranging from $n\frac{f_{rep}}{2}$ to $(n+1)\frac{f_{rep}}{2}$. As a result, a comb of IF frequencies are measured at the output. This method of sampling is referred to as sub-sampling or bandpass sampling. When selecting the optimal sampling frequency f_{rep}, certain rules must be considered [59]. The bandwidth of the frequency to be sampled BW should be at most equal to the half of the repetition frequency, ($BW \leq \frac{f_{rep}}{2}$).

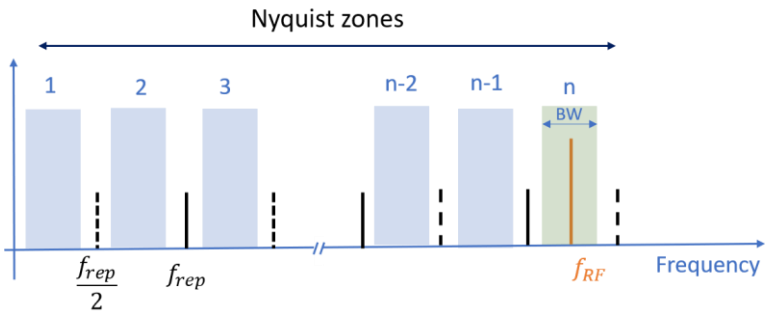

Figure 1.21: Representation of the Nyquist zones in the frequency domain.

In the course of this thesis, part of the work concerned THz detection by heterodyne-mixing in photoconductive devices. The main subject was the fabrication and characterization of plasmonic micro-cavity photodetectors based on iron doped InGaAs. The results of this work are not presented in this manuscript however some details about the research realized on these devices will be presented in the PhD defense presentation.

Conclusion

This chapter has discussed several promising technologies that have potential applications in the THz and sub-THz frequency range. The impact of these technologies on our society could be significant. However, the current generation and detection capabilities of THz sources are still considered insufficient due to the need for unbulky, low-cost, and efficient THz sources/detectors. Optoelectronic THz technology has played an increasingly important role in recent years in improving the miniaturization and optimization of THz sources and detectors. Therefore, this chapter has provided a comprehensive review of THz sources and detectors, with a particular emphasis on optoelectronic devices, especially the photoconductive structure. It is noteworthy to precise that in this chapter we did not show the state of the art of photomixers since it will be presented inchapter 2 that discusses in details the photomixers which represent the main subject of this thesis

Chapter 2: Traveling Wave Photomixers

Introduction:

The primary focus of this chapter pertains to the generation of THz radiation through the process of photomixing, utilizing a Traveling-Wave (TW) photodetector. Firstly, the concept of TW-photomixers will be introduced, highlighting the constraints of such devices and their superiority over lumped-element photomixers. After that, a comprehensive overview of continuous-wave THz sources based on photomixing will be presented allowing the performance evaluation of existing lumped element and TW-photomixers. Subsequently, a novel design of a TW-photomixer will be introduced, which proposes a modified structure to optimize photomixing in such devices. This concept consistsin integrating a dielectric waveguide platform on a photoconductive membrane having coplanar waveguide. Subsequenctly a theoretical framework describing photoconductive TW-photomixers will be presented, along with an electrical circuit model for theoretical modeling purposes. The model will then be utilized for experimental measurements.

2. Traveling-Wave photomixers

In 1990, the concept of a Traveling wave (TW) photomixer was first proposed [60]to go beyond the bandwidth-efficiency limits of conventional photomixers. In the following years multiple theoretical and experimental studies started to be published.To define a traveling wave device, one should consider two or more distinct waves, optical, electrical, acoustical or other which propagates and interacts through the interface of their respective waveguides. A TW-photomixer consists mainly of a waveguide for the optical beatnote and metallic waveguides (CPW, CPS) for the THz wave. These metallic waveguides act also as biasing electrodes for the photomixer.Similarly to the lumped-element devices,there arealsotwo configurationsforTW-photomixers: the photodiode TW-photomixer and the photoconductive MSM-TW-photomixer. The basic design of a TW-photomixer is shown in Figure2.1 (a). It shows asemiconductor ridge waveguide for the optical beat note. The carriers are collected through the electrodes that possess a coplanar waveguide design. It can be seen in Figure 2.1 (b) that the beatnote is absorbed gradually along the ridge and at the same time the THz power will increase gradually along the device. This is a conceptual representation and in reality, there are different challenges to achieve efficient generation. They will be discussed in detail in the following section.It should be noted that TW-photomixerscan be configured through various forms such as periodic TW-photomixerss or velocity matched distributed photomixers (VMDP)[61].In these cases, the active region is periodically structured above the optical waveguide. In the following we will detail the theory of TW-photomixers and will present a review on this device over the past couple of years and finally a state of the artof the TW-photodetectors and the lumped element devices for THz generation by photomixing.

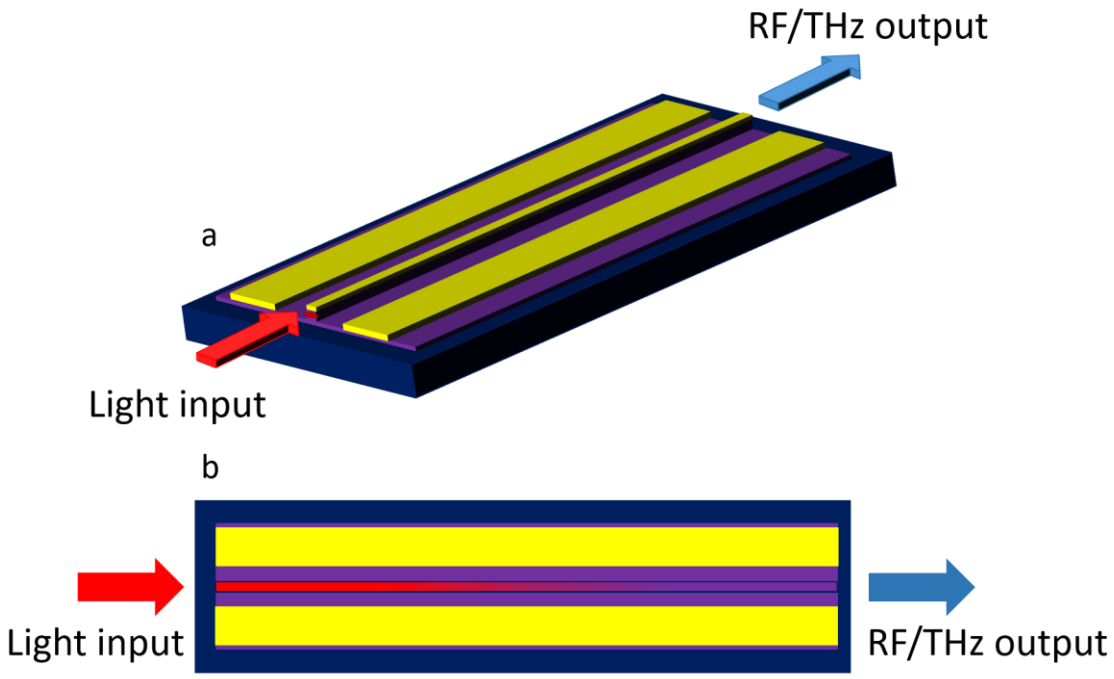

Figure 2.1: (a) Schematic representation of a traditional TW-photomixer. (b) Top view of a TW-photomixer showing the absorption of the optical input along the device resulting in the RF/THz generation.

2.1. Theory of TW-photomixers

In the realm of distributed photomixers, it is crucial to consider two important factors. Firstly, the THz output power reaches its highest value when the group velocity of the optical beating source is equivalent to the phase velocity of the generated THz source.Secondly, the THz output power is around 6 dB lower compared to lumped-element photomixers with the same photocurrent.

In order to gain a general comprehension of the significance of phase matching in distributed photomixers, we can draw an analogy to the phase matching observed in second-order non-linear generation processes ($\chi^{(2)}$)to satisfy the momentum conservation law:

$$k_1 - k_2 = k_{THz} \tag{2.1.1}$$

where k_1 and k_2 are the optical propagation constants of the laser sources and k_{THz} is the propagation constant of the generated THz wave. If we divide by the THz frequency ($\omega_{THz} = \omega_B = \omega_1 - \omega_2$) and considering that the dispersion is linear over the frequency range between the two optical sources we get:

$$\frac{k_1 - k_2}{\omega_1 - \omega_2} = \frac{\Delta k}{\Delta \omega} = \frac{1}{d\omega/dk} = \frac{k_{THz}}{\omega_{THz}} \tag{2.1.2}$$

which can be reduced to:

$$v_g = v_{THz} \tag{2.1.3}$$

where v_g is optical group velocity and v_{THz} is the THz wave phase velocity.

To comprehend the reason behind the 6-dB decrease in THz output power, it is helpful to conceptualize the device as a current source with an active area that feeds currents to a load. When the electrical wavelength is considerably larger than the active area's length, all the generated currentsare in phase and add up in the load. Nevertheless, when the electrical wavelength is comparable in length to the active area, we should consider that each point along the device is a current source coupled to a THz waveguide leading to modulated currents propagating forward and backward. Since phase matching with a propagating optical beatnote is only possible in one direction,only half of the current (-3 dB) can be dissipated in the load at best, resulting in a quarter of the power (-6 dB) being dissipated as THz.

- **Simplified model for a TW-photomixer**

In this sub-section we will present a simplistic model of a TW-photomixer in order to show the effect of velocity mismatch and the 6 dB TW signature. We will neglect the THz propagation losses and the frequency roll-off that originates from the carrier lifetime. We will consider a TW-photomixer based on a coplanar waveguideof length L and characteristic impedance Z_c. We assume that the absorption coefficient$\alpha_o$in the optical waveguide is a function of z such that the photocurrent amplitudegenerated along the path of the optical beam is constant along the photodetector:

$$-\frac{d|P_{ac}(z)|}{dz} = \frac{P_0}{L} \tag{2.1.4}$$

This is practically possible and will be presented in the following chapter. As it will be demonstrated in part 2.4, the THz current generated in z can be expressed as follows [62][63]:

$$dI_{ac}(z) = Je^{-jk_o z}dz \qquad (2.1.5)$$

Where $k_o = n_g \omega_b c$ and J depends on the input power and the photomixer's properties. Here we will consider two device configurations: 1) A device which is closed at its both ends with a perfect matched resistor ($R = Z_c$) (Figure 2.2 (a)) and 2) A device which is perfectly matched only at the output (Figure 2.2 (b)).

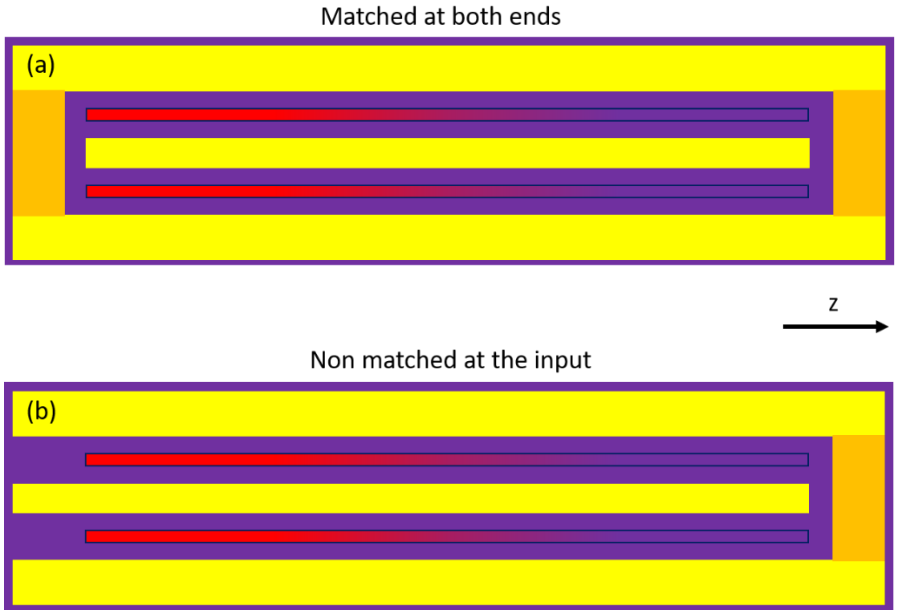

Figure 2.2:(a)Representaion of a CPW matched at both ends and (b) a CPW only matched at the output.

– **Match resistor at both ends**

If we are focused on the power dissipated only in the output resistor, we can consider only the forward waves at the output of the device ($z = L$). The forward THz current created in z_0, $\frac{1}{2}dI_{ac}(z)$ travels without loss, on the CPW guide at a phase velocity $v_{THz} = c/n_{THz}$ and a wavelength number k_t and give a contribution to the total output current $dI_{ac\_L}(z)$:

$$dI_{ac\_L}(z) = \frac{1}{2}dI_{ac}(z)e^{-jk_t(L-z)} \qquad (2.1.6)$$

the total current at the output I_{total} is:

$$I_{total} = \int_0^L dI_{ac\_L}(z) = \frac{1}{2} J e^{-jk_t L} \int_0^L e^{j\Delta k\, z} dz$$

$$= \frac{1}{2} L J e^{-jk_t L} e^{-jL\Delta k/2} \frac{\sin L\Delta k/2}{L\Delta k/2} \qquad (2.1.7)$$

with $\Delta k \equiv k_t - k_o = \frac{\omega_b}{c}(n_{THz} - n_g)$. The THz output power P_{THz}delivered to the load Z_c is then given by $P_{THz} = 1/2\, Z_c |I_{total}|^2$ whose maximum $P_{mf} = 1/8\, Z_c |LJ|^2$ is obtained when Δk=0. As already explained earlier, only a quarter (-6 dB) of the power obtained as compared with a lumped device exhibiting the same dc-photocurrent $P_{ld} = 1/2\, Z_c |LJ|^2$. Furthermore, the loss induced by the phase mismatch $L_{\Delta\varphi}$is thus identical to the one experienced in THz emission based on non-linear process:

$$L_{\Delta\varphi} = \frac{P_{THz}}{P_{mf}} = \left| \frac{sin\, L\Delta k/2}{L\Delta k/2} \right|^2 \qquad (2.1.8)$$

– **Match resistor at the output**

If we assume an open circuit at the device input ($Z_{input} \approx +\infty$), we have to add the backward photocurrent waves after they have been reflected at the input, hence the contribution of the photocurrent generated between *z* and *z+dz* to the total output becomes:

$$dI_{ac\_L}(z) = \frac{1}{2} dI_{ac}(z) e^{-jk_t(L-z)} + \frac{1}{2} dI_{ac}(z) e^{-jk_t(L+z)} \qquad (2.1.9)$$

And the total current at the output I_{total} is given by:

$$I_{total} = \frac{1}{2} L J e^{-jk_t L} \left(e^{jL\Delta k/2} \frac{\sin L\Delta k/2}{L\Delta k/2} + e^{-jL\Sigma k/2} \frac{\sin L\Sigma k/2}{L\Sigma k/2} \right) \qquad (2.1.10)$$

with $\Sigma k \equiv k_o + k_t = \frac{\omega_b}{c}(n_g + n_{THz})$. From the equation above we can consider that half of the current propagated towards the output and the other half propagates towards the input.

Finally, the THz power can be calculated from equation (2.1.10). Note that this equation represents the realistic design of the proposed TW-photomixer that will be presented later. We will now study in detail the 6-dB roll-off of such devices.Figure 2.3shows the

frequency dependence of the THz power provided by a lossless ($\alpha_t = 0$) 1-mm-long TW photomixer normalized to the power provided by a hypothetical lumped device (size <<λ_{THz}) at equal photocurrent level. We show the two first frequencies f_{t1}, f_{t2} at which the 6 dB-power penalty occurs, which can be calculated analytically and are inversely proportional to $L(n_g + n_{THz})$ as detailed inequation (2.1.10). If the lifetime related frequency roll-off is neglected, a photoconductor working in a TW regime should thus exhibit a frequency response presenting the 6-dB roll-off at frequencies close to f_{t1}, f_{t2} followed by a plateau-like response.

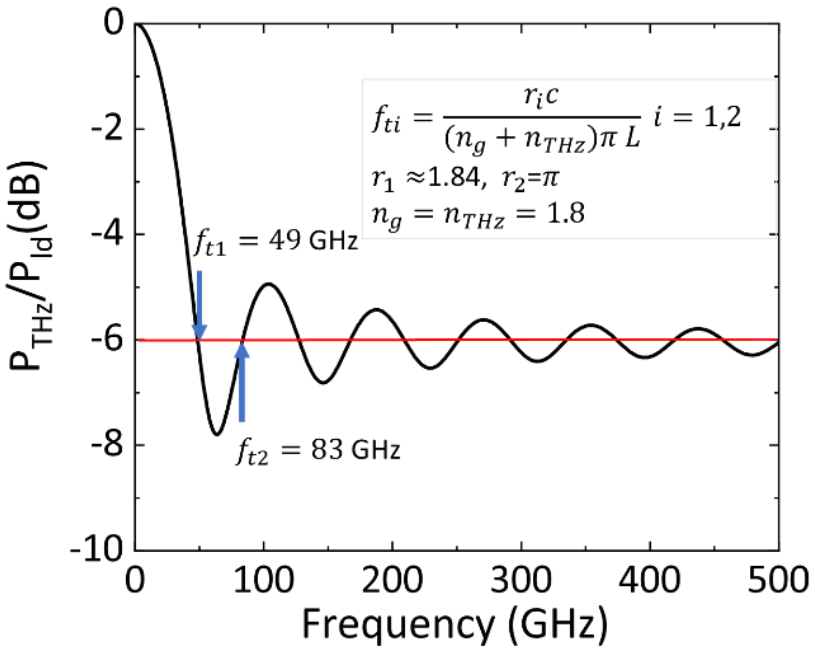

Figure 2.3: Theoretical power provided by lossless 1-mm-long TW photomixer ($\boldsymbol{\alpha_t = 0}$) normalized to the power provided by a perfect (no RC cut off frequency) lumped device $\boldsymbol{P_{THz}/P_{ld}}$. Here is assumed a linear absorption of the optical power. In the inset are shown the analytic expression of $\boldsymbol{f_{t1}, f_{t2}}$ as demonstrated

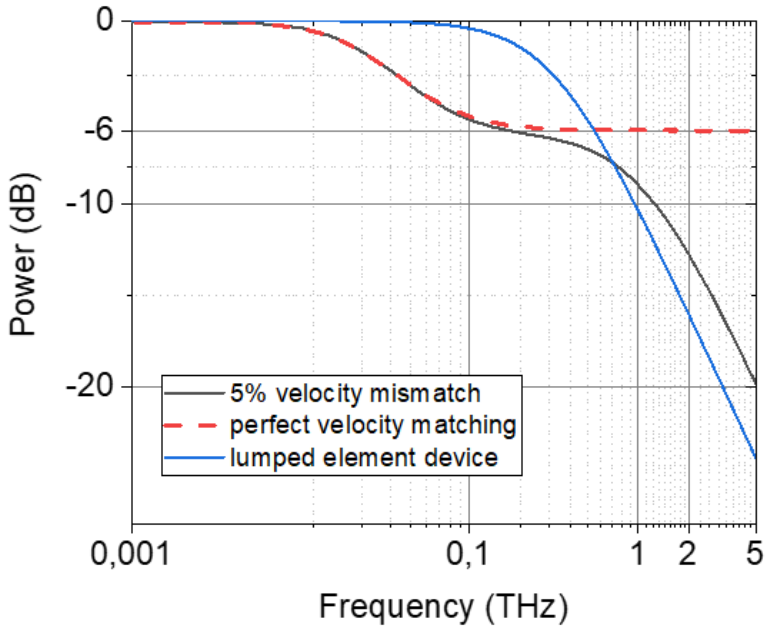

Figure 2.4: Bandwidth plots of both lumped-element and (velocity matched and non-velocity matched) TW-photomixers. The two kinds of photomixers are considered functioning at the same photocurrent however the carrier lifetime effects are neglected and the capacitance of the lumped-element photomixer is considered 10 fF.

Figure 2.4 shows the frequency response at the output of a TW-photomixer matched only at the output and having a perfect velocity matching (dashed red), a 5% velocity mismatch (black) and the frequency response of a lumped element photomixer (blue) having the same dc photocurrent of the TW-photomixers. A capacitance of 10 fF is defined based on the capacitance of a typical photomixer having interdigitated electrodes. Note that the frequency response of the TW-photomixer in Figure 2.4 was calculated based on a realistic model that will be detailed later in this chapter. In this model we consider an infinite device length (physical length >> absorption length) resulting in no ripples in the response since there is no interference with a reflected THz wave from the input. Note that the index mismatch is defined as $\frac{\Delta n}{n_{THz}} = \left(1 - \frac{n_g}{n_{THz}}\right)$. It is clear that a TW-photomixer can overcome the the RC limitation of a traditional lumped element photomixer only if there is a perfect velocity matching between the THz wave and the optical beatnote.

2.2. CW photomixers: State of the art

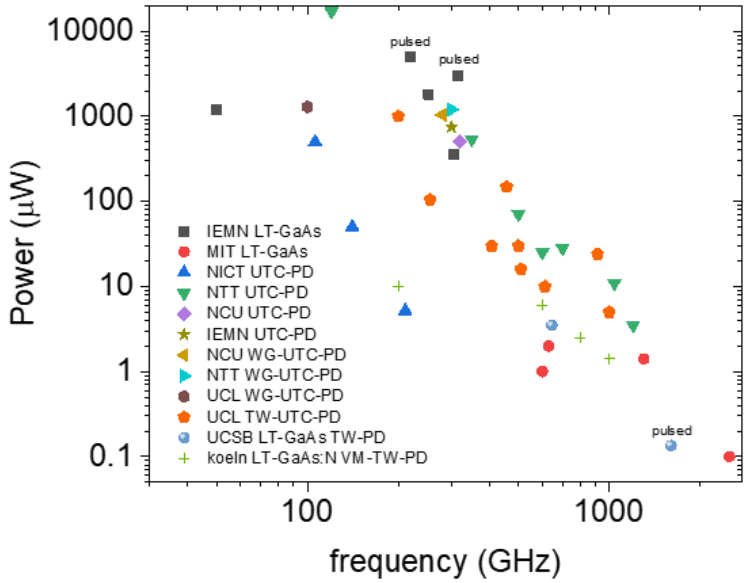

Figure 2.5: State of the art of the photomixing sources. For LT-GaAs MSM structures, MIT results are from the following reference **[64]**, IEMN results are from reference**[65]**, **[66]** (pulsed) and **[67]**. For UTC structures, NICT results are from reference **[68]** (large bandwidth from 10 MHz to 110GHz), NTT results are from reference **[69]**, **[70]**,**[71]** and **[72]**. IEMN results are from ref. **[73]**. NCU results are from ref. **[74]**. For WG-UTC, NTT results are from ref. **[75]**. UCL results are from ref. **[76]**. For TW-UTC, UCL results are from ref. **[77]** and **[78]**. For LT-GaAs TW-PD, UCSB results are from ref **[79]** and **[80]** (pulsed). For VM-PD, Uni-Koeln results are from ref **[81]**.

Figure 2.5 shows the state of the art in output power of different configurations of photomixers which are divided into two main designs: the lumped-element photomixers (MSM and pin structures) and the traveling-wave photomixers. In most of the cases, the lumped-element photomixers are vertically illuminated but in some cases, they are horizontally illuminated through an integrated waveguide. The MSM was the first to be proposed for photomixing in low temperature grown GaAs (LT-GaAs) in MIT by Brown et al [82]. This design was initially introduced featuring interdigitated electrodes on the LT-GaAs layer as shown in Figure 1.16 (a). The performance of these traditional structures is dependent on the design of the interdigitated electrodes (electrode spacing, electrode width and overall size of the active area). The photoresponse of these MSM interdigitated photomixers is relatively low (0.005 A/W [83]) due to low photoconductive gain. Peytavit and coworkers[67] upgraded these devices to photoresponses up to 0.14

A/W which resulted in a state of the art output power reaching 1.8 mW at 252 GHz. The photoconductive gain was increased thanks to aresonant Fabry-Perot cavity. As for the pin structures, as already mentioned in the previous chapter, UTC-PD were first developed by NTT in the late 1990s for communication purposes. The aim of these devices was to increase the photoresponse andthe saturation currentof traditional pin devices. In such devices thefrequency response is no longer limited by the transit time of low-saturation velocity carriers (holes). As seen in Figure 2.5, a UTC developed by NTT reached 17 mW at 120 GHz however, above 300 GHz lumped-element photomixers are still under the µW level. These devices are still limited by the trade-off between the reduction of their size to minimize their capacitance and the sufficient photocurrent needed to generate high THz power.

In 1990, an alternative device based on traveling wave (TW) was proposed by Taylor et al [60]. As explained before, the central idea of a TW photomixer is to bypass the parasitic RC constant of the corresponding lumped-element capacity by distribution of the beat signal generation along a transmission line. These structures which exists also in a periodic configuration (VMPD) [84][85][86][87] combine controlled impedance lines with long absorption regions allowing high saturation optical powers. They exist in both MSM andUTC-PD configuration, however MSM configurations are preferable due to their superior microwave guiding structure and the low carrier lifetime of LT-GaAs [88][89]. As for their output power, till now there are no significant results. At the university of Cologne in Germany, Michael et al. [81] reported µW level output powers (10 µW at 200 GHz and 1.4 µW at 1000 GHz) from VMDPs using ion-implanted GaAs. In pulsed mode, at the UCSB (University of California, Santa Barbara), Shi et al. [80] reported 0.135 µW of average THz output power at 1.6 THz. This corresponds to 1.63 mW THz peak output power. Generally, these devices were based on standard III-V semiconductor optical waveguides coupled to pin or MSM photodetector structures whose metallic contact electrodes define also a microwave coplanar waveguide (CPW). This design leads to a large mismatch between the group index of the optical mode (n_g~3.3 in III-V semiconductors) and the refractive index of the CPW fundamental propagation mode (n_g~2.7). Furthermore, doped layers (pin) and reduced inter electrode spacing required for the embedded photoconductor lead to propagation losses often [90] larger

than 10 dB/mm beyond 100 GHz. In addition, it is well known that CPW on bulk substrate suffer from radiation losses increasing as the frequency cubed avoiding any practical use of this waveguide for length >100 µm at frequency above 1 THz [91]. This explained mostly why the active length of these photodetectors, with the exception of that one studied in [92], equal to the optical absorption length is often lower than 50 µm. In the frequency range considered (< 500 GHz), these photoconductors are not really distributed and their limited size avoid any significant increase of their power dissipation and saturation photocurrent capabilities. In [92], the authors take advantage of the n-doped contact layer of the pin junction to design a slow wave waveguide (n~3), mixed between a CPW and a microstrip waveguide. However, the thickness of the intrinsic semiconductor layer (1.2 µm) used in the pin structure leads to a cut-off frequency related to the electron transit time not compatible with THz operation. A cut-off frequency below 5 GHz has been measured on a 1.25-mm-long device. Again, there is no convincing evidence of travelling wave operation here since the frequency response of this device has been characterized only up to 10 GHz. As a matter of fact, the only TW photodetectors showing very promising results as THz photomixers were based on vertical illumination and not on integrated optical waveguide. The phase-matching was then achieved by tuning the incidences angles of the two free space laser beams[93]. Elliptical spots were thus needed limiting the active length at a value of approximately 200 µm.

-Conclusion: In summary, we should expect that the performance of a TW-photomixersurpasses that of a lumped-element photomixer due to the guiding structure of its electrodes, which enables it to avoid the $(\omega_B R_L C)^{-2}$frequency roll-off limitation. Furthermore, TW-photomixers can handle higher optical power levels than lumped-element photomixers because of their larger active area. Despite these advantages, the output power of TW-photomixers is still limited because of the challenge of achieving optimal matching between the optical group velocity and the THz phase velocity. Additionally, the frequency cutoff in pin structures is linked to the carrier transit time, which necessitates closely spaced electrodes that cause substantial propagation losses at high frequencies. In the following section, a new approach for TW-photomixers will be presented, which enhances the velocity matching conditions.

2.3. TW-photomixer based on an optical dielectric waveguide: concept and design

The primary objective of this section is to introduce a new concept of TW-photomixers, which enablessimple tuning of the index matching between the two waves.The proposed design features separate waveguides for each wave, with a silicon nitride/silicon oxide (Si_3N_4/SiO_2) waveguide platform for the optical wave and a coplanar waveguide (CPW) for the THz wave. Figure 2.6 shows a schematic representation of the proposed TW-photomixer. The dielectric waveguide is integrated above a photoconductive bulk layer or membrane between the electrodes of the CPW. The evanescent coupling between the dielectric waveguide and the active region allows for distributed optical absorption, resulting in the generation of THz waves that propagates in the CPW and is either dissipated in a load (spectrum analyzer/powermeter) or emitted through THz antennas at the end of the device.The index matching can be easily adjusted by modifying the dimensions of either waveguides. In the dielectric waveguide,the optical mode confinement can be modified by altering the Si_3N_4 core width which affects the mode overlap with the cladding and the active region. As a result, multiple optical properties of the optical mode are varied, including the effective index, group index, effective area, and the absorption in the active region and the surrounding. Similarly, based on the transmission line theory, the refractive index of the propagating mode in coplanar waveguides can be adjusted by varying the width of the central strip (Appendix B).

A well-known material for THz generation is the LT-GaAs (Low Temperature grown Gallium Arsenide). The growth of LT-GaAs is typically carried out using molecular beam epitaxy (MBE). During the growth process, the LT-GaAs layer is deposited at a low temperature (typically around 200-300°C) to produce a material with a high density of defects such as dislocations and point defects. These defects are necessary to achieve the desired material properties, such as dark resistivity and fast response time. After the growth process, the LT-GaAs layer is annealed at a higher temperature (typically around 600-700°C) to reduce the number of defects in the material. Annealing helps to heal the defects and improve the material's crystalline quality, resulting in improved electrical and optical properties. LT-GaAs played a key role in the advancement of MSM-

photomixers for THz generation. Conclusively, it will be used as the photoconductive layer of the TW-photomixer. For more information about LT-GaAs, AppendixA presents an overview on the material. The LT-GaAs will be transferred to a high-resistivity silicon substrate, which offers superior thermal and mechanical properties compared to a GaAs substrate. Additionally, by etching the silicon under the coplanar waveguides, a membrane can be realized allowing a partial propagation of the THz wave in air resulting in an overall reduction of the THz refractive index which allows it to approach the low group index in the dielectric waveguide. Membrane-supported CPW have significantly lower propagation losses in the THz range compared to CPW on a bulk substrate due to their low radiation losses and lower effective index [94]–[96].Overall, the creation of a membrane would enable the fabrication of devices with a length reaching 1 mm, capable of absorbing high optical powers up to the watt level. Subsequently, the viability of these membranes will be demonstrated and analyzed. The devices will be designed to work with both 780 nm and 1550 nm wavelength illumination, with LT-GaAs being used in both cases.

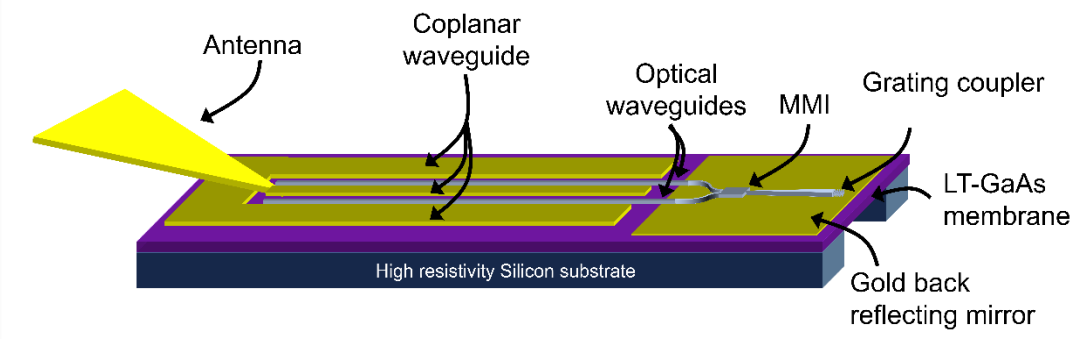

Figure 2.6: Conceptual representation of the proposed TW-photodetector showing the dielectric and the coplanar waveguides. The optical beating is coupled through a grating coupler into a SiO_2/Si_3N_4 waveguide platform. The optical mode is split into two modes by the aid of MMI (multimode interferometer). The two modes enter between the slit of the CPW and are absorbed gradually in the LT-GaAs resulting in the generation of THz waves that can be emitted by an Antenna at the output

Regarding the optical coupling to the active region, there are three main methods in photonics. The first approach (Figure 2.7 (a)), which is the most prevalent, is based on edge coupling and involves integrating a tapered structure at the beginning of a planar waveguide. The taper's dimensions are sufficiently large, comparable to the fiber core's size, resulting in a significant overlap between the modes of the two structures, thereby

enabling efficient coupling. These couplers are intrinsically broadband and exhibit a coupling loss lower than 1 dB per facet [97]. However, achieving high-efficiency coupling often requires precise end facet cleaving and fiber alignment. The second method (Figure 2.7 (b)), grating couplers, is a surface-based coupling technique that utilizes diffraction gratings patterned directly on the Si_3N_4 core. This approach is narrowband since it relies on light diffraction. A significant advantage of this method is that it allows higher optical power to be coupled to the waveguide through large-area grating couplers without leading to thermal destruction. The third method ((Figure 2.7 (c)), which is less well-known, relies on evanescent-field coupling from a single-sided conical tapered fiber and a tapered planar waveguide. The conical shape of the fiber ensures that the electromagnetic field intensity increases as the fiber is tapered, leading to a stronger evanescent field at the tapered end. The tapered waveguide, on the other hand, is designed to match the mode profile of the fiber, ensuring maximum overlap between the fiber and waveguide modes. Even though this technique results in low coupling losses, the coupling efficiency is highly dependent on the gap distance between the fiber and the waveguide, making alignment critical. Table 2-1 summarizes the advantages and disadvantages of each technique.

	Grating	**Edge-coupling**	**Evanescent field**
Fiber direction	Out of plane	In plane	In plane
Bandwidth	Limited	Wide	Wide
Polarization dependence	Poor	Good	Good
SMF mode matching	Good	Poor	Good
Number of alignments	1	1	2
Handling	Good	Poor	Poor

Table 2-1: Summary on the advantages and disadvantages of three coupling techniques: Grating coupler, Edge coupling and Evanescent coupling.

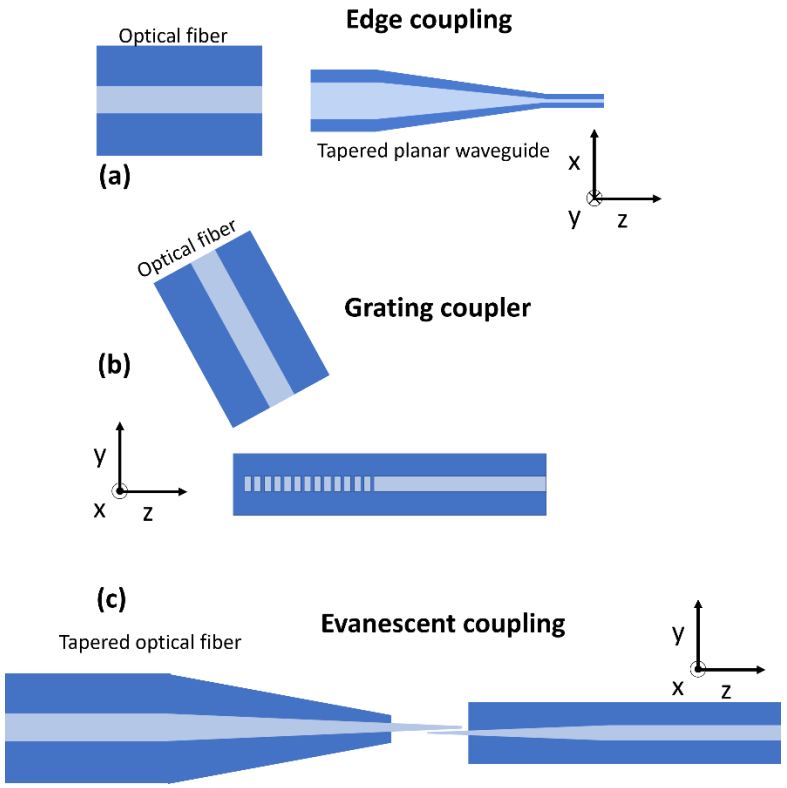

Figure 2.7: Representation of the three fiber coupling techniques: (a) edge coupling, (b) coupling though a diffraction grating and evanescent coupling between a tapered optical fiber and a tapered planar waveguide.

Owing the fact that we aim to pump the device up to the watt-level and since we are working on a proof of concept and we need a fast and simple fabrication process that is easy to characterize, we chose to use a grating as the optical coupler for the device.Figure 2.8 illustrates the grating design integrated into the TW-photomixer. The grating and core of the planar waveguide are made of silicon nitride and are surrounded by a silicon oxide cladding. In a basic grating model, where the design of the grating consists on periodically notching a rectangular core surrounded with a cladding material(Figure 2.7 (b)), coupling losses are around 3 dB as shown in the state of the art presented in AppendixC. In order to enhance the coupling efficiency,and reach coupling losses under 3 dB,a thin layer of gold is deposited under the grating coupler acting as a back reflector. The key dimension here is the thickness of the lower SiO_2 cladding. For a well-defined thickness the reflected light will interfere constructively with the incoming light resulting in higher coupling efficiency. The optical beating then travels through an adiabatic taper, towards the active

region. We will provide more details on the simulation model and experimental results later, but for now we will focus only on the device design.

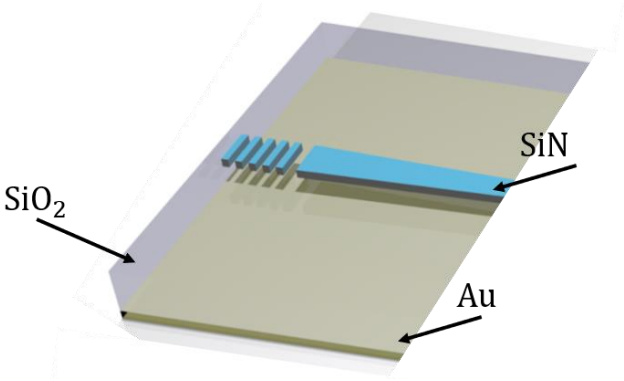

Figure 2.8: Schematic representation of the grating coupler design

In order to couple to the uneven mode of the CPW, the photocurrent should be generated between the electrodes. This is possible only if the dielectric waveguide is integrated between the electrodes resulting in optical absorption in the active region. In order to realize this, devices as directional couplers [98][99], asymmetric Y-junctions[100], Mach-Zehnder interferometers (MZI)[101] and Multimode interferometers[102] can be employed. Directional couplers have been identified as being particularly vulnerable to fabrication errors. Conversely, asymmetric Y-branches and Mach-Zehnder interferometers (MZIs) are typically long and have high insertion losses, exceeding 1 dB. However, devices utilizing multimode interference (MMI) are capable of generating compact and low loss wavelength multi/demultiplexers that exhibit greater tolerance to fabrication errors when compared to directional couplers[103]. An MMI is a type of optical interferometer that can operate with multiple modes of light simultaneously. In a 1×2 MMI, the interferometer has a single input port and two output ports. This configuration allows the interferometer to split incoming light into two separate paths, which can then be used for various optical measurements or manipulations. MMI interferometers are often used in applications such as telecommunications and biosensing, where their ability to operate with multiple modes of light can provide significant advantages over traditional interferometers. In our case, the MMI is used to split the fundamental mode in two equal-powered modes. The coupling structure composed of the grating coupler and the MMI is shown in Figure 2.9.

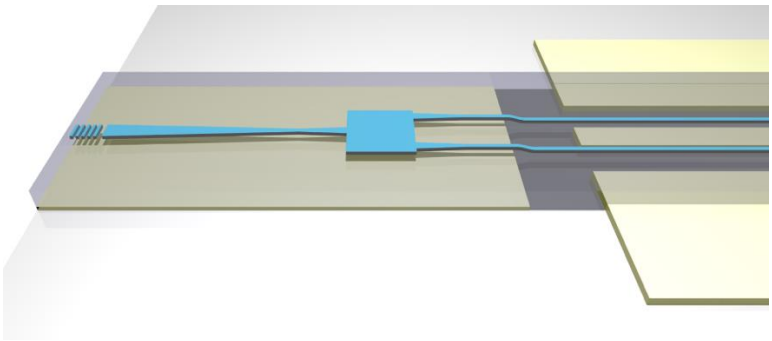

Figure 2.9: Schematic representation of the coupling structure showing the grating coupler and the MMI.

Concerning the heat management of the membrane, GaAs membranes have been commonly used in the final stages of Schottky-based terahertz (THz) multipliers and mixers[104], where the dissipated power is typically low and thermal management is not a significant concern. However, in this particular case, it is expected that the heating power density (resulting from both joule heating and optical absorption) will be around 2 W/mm, which is significantly higher than usual. To ensure that the maximum working temperature does not exceed 100°C and assuming that the silicon bulk remains at room temperature, it is necessary to have a thermal resistance per unit length (R_l^{th}) not greater than 100 K/(W.m), as shown inFigure 2.10. Based on a simplified one-dimensional thermal model and neglecting thermal boundaries, the thermal conductivities of LT-GaAs and gold layers ($\sigma_{LT-GaAs}^{th}$ = 25 W/(m·K) and σ_{Au}^{th}=317 W/(m·K)) [105] were used to estimate R_l^{th}. By considering dimensions of the order of tens of micrometers, it is possible to show that R_l^{th}<100 K/(W.m) as long as the difference between the membrane width (w_m) and the total width of the coplanar waveguide (w_{CPW}), denoted byδw, is less than 2.5 µm. This is due to the significantly better thermal conductance of the gold layer compared to that of the LT-GaAs layer. Therefore, it is essential to have membranes with limited widths to handle power levels of the order of watts in devices of millimeter-scale dimensions. Later we will describe the technological process used to obtain membranes with transverse dimensions (w_m) less than 100 µm, which are suitable for their application. Thus far, we have established the concept of the new TW-photomixer. In the following section, we will present a realistic optoelectronic model of a TW-photomixer that will be applied later to experimental results.

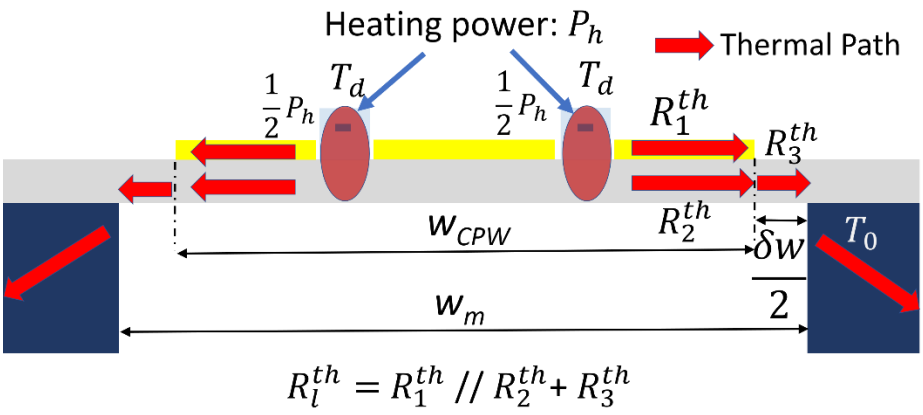

Figure 2.10: Thermal model of the traveling-wave photomixer.

2.4. Optoelectronic model

In order to quantify the physical parameters of a fabricated device, we will present an optoelectronic model of the TW-photomixer. The first part represents a model of the beatnote, then the photocurrent source and finally a circuit model of a full device considering THz propagation losses, lifetime frequency roll-off and the velocity mismatch.

-Optical source model: Since the optical wave propagates and gets absorbed in the active region, we will consider that the fundamental mode has a propagation constant $\beta(\omega)$ and absorption coefficient α_0 representing the absorption in the active region. If we consider two cw lasers slightly shifted in frequency with ω_1 and ω_2 the angular frequencies of the two lasers and $\omega_b = \omega_1 - \omega_2$ the beatnote frequency. The two lasers are considered identical and their polarization and output power ($P_0/2$) are the same. The optical power detected by a photodetector can be expressed by [106]:

$$P(z,t) = P_0[1 + cos(\omega_b t - (\beta(\omega_1) - \beta(\omega_2))z)]e^{-\alpha_0 z} \qquad (2.4.1)$$

As it is clear, the energy component related to $\omega_1 + \omega_2$ is not present since it is much larger than the photoconductor cut-off frequency and is cancelled due to time averaging. By using a Taylor expansion of the optical mode dispersion curve, we obtain:

$$\beta(\omega_1) - \beta(\omega_2) = \frac{d\beta}{d\omega}(\omega_1 - \omega_2) = \frac{1}{v_g}(\omega_1 - \omega_2) = \frac{n_g}{c} \quad (2.4.2)$$

where v_g (n_g) the group velocity(index) of the optical mode and c is the speed of light in vacuum.

It is possible to set $k_0 = n_g \frac{\omega_b}{c}$.

Consequently, the optical power in the waveguide can be expressed as follows:

$$P(z,t) = P_0[1 + cos\ (\omega_b t - k_o z)]e^{-\alpha_o z} \quad (2.4.3)$$

This equation can be expressed as follows: $P(z,t) = P_{dc}(z) + P_1(z,t)$ where the first term $P_{dc}(z) = P_0 e^{-\alpha_o z}$ is the power that generates the dc part in the current and the second term $P_1(z,t) = P_0 cos\ (\omega_b t - k_o z)e^{-\alpha_o z}$ is the oscillating term at ω_b that will generate the THz wave. $P_1(z,t)$ can also be written in the phase vector notation:

$$P_1(z,t) = Re(P_{ac}(\omega_b, z)e^{j\omega_b t}) \quad (2.4.4)$$

with $P_{ac}(\omega_b, z) = P_0 e^{-\alpha_o z} e^{-jk_o z}$.

-Electrode design:

In the TW-photomixer, the electrodes are designed on top of an LT-GaAs layer, similar to a traditional interdigitated structure, with the exception of possessing a guiding structure. Figure 2.11depicts a cross-sectional view of two electrodes deposited on a semiconductor layer. When carriers are excited and a biasing source is present, they follow semi-elliptical trajectories that reflect the electric field lines within the material. It can be proven that most of the carriers generated in the semiconductor exist on its surface. FromFigure 2.11, it can be inferred that the trajectories of these surface carriers can be approximated by straight lines. Therefore, we will only consider the surface carriers transiting between the electrodes of spacing l, as shown in Figure 1.17 of the previous chapter. We will recall that the transit time of carriers is defined by $\tau_{tr} = \frac{l}{v} = \frac{l}{\mu E}$. The ratio between the carrier lifetime and the carrier transit time $\gamma = \frac{\tau}{\tau_{tr}}$ is defined as the

photoconductive gain, and it describes the number of electrons collected by the electrodes per absorbed photon. The photoconductive gain is proportional to the photoresponse and can be increased by reducing the electrode spacing. However, in the presence of a guiding structure, close electrodes would result in high THz propagation losses. Thus, it is crucial to evaluate the tradeoff between propagation losses and photoconductive gain in TW-photomixers.

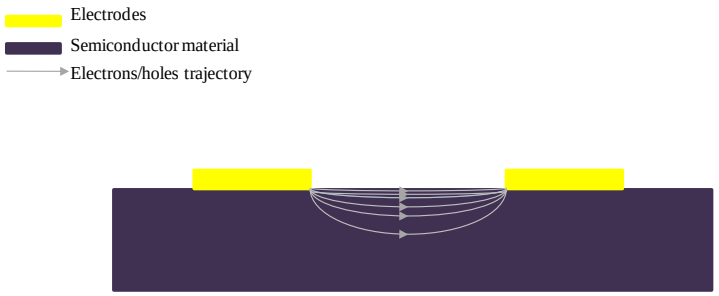

Figure 2.11: Cross-section representation of a electrodes deposited on a semiconductor material showing the semi-elliptical trajectories of the carriers following the electric field lines generated by the dc bias.

-Photocurrent source model: By recalling the photoconduction defined in the first chapter (Figure 1.17) we can presume that we have a photoconductor consisting of two biasing electrodes on a photoconductive material of thickness *t* and having low lifetime carriers τ, a mobility μ and bias electric field much smaller than the saturation velocity electric field ($E_{dc}<<E_s$). The inter-electrode spacing is defined as the distance *l*. By considering that we are in a traveling-wave regime and based on the photoconduction theory for carrier lifetime limited ultrafast devices we can easily express the oscillating current $dI_{ac}(\omega_b, z)$ generated between *z* and *z* + *dz*[62][63]:

$$dI_{ac} = -\frac{q}{\hbar\omega}\frac{(|P_{ac}(z+dz)| - |P_{ac}(z)|)}{w \times \sqrt{1+(\omega_b\tau)^2}} \times \frac{\tau}{\tau_{tr}} e^{-jk_0 z} e^{-j\varphi} \qquad (2.4.5)$$

where $\tau_{tr} = l/\mu E_{dc}$ is the transit time of the carriers between the electrodes (assuming a 1D photoconductor), $\varphi = atan(\omega_b\,\tau)$ and $\omega = \frac{\omega_1+\omega_2}{2}$

For $dz \to 0$ and by applying the first order Taylor expansion we get:

$P_{ac}(z+dz) \to P_{ac}(z) + \frac{dP_{ac}(z)}{dz}dz$ hence, we obtain:

$$\frac{dI_{ac}(\omega_b, z)}{dz} = -\frac{q}{\hbar\omega}\frac{1}{\sqrt{1+(\omega_b\tau)^2}}\frac{|dP_{ac}(z)|}{dz}\frac{\tau}{\tau_{tr}}e^{-j\varphi}e^{-jk_o z} \tag{2.4.6}$$

$$= A(\omega_b)e^{-\gamma_o z}$$

with $A = \alpha_o P_0 \frac{q}{\hbar\omega}\frac{1}{\sqrt{1+(\omega_b\tau)^2}}\frac{\tau}{\tau_{tr}}e^{-j\varphi}$ and $\gamma_o = jk_o + \alpha_o$

Meanwhile, from the small signal electrical model of a photomixing source presented in the first chapter[107] we know that this photocurrent source has an internal admittance $G_0 dz$ expressed as follows:

$$G_0 dz \approx -\frac{q}{\hbar\omega}\frac{\mu\tau}{l^2}(P_{dc}(z+dz) - P_{dc}(z)) \tag{2.4.7}$$

Hence the internal admittance per unit length is:

$$G_0 \approx -\frac{q}{\hbar\omega}\frac{\mu\tau}{l^2}\frac{dP_{dc}}{dz} \approx \alpha_o P_0 \frac{q}{\hbar\omega}\frac{\mu\tau}{l^2}e^{-\alpha_o z} \tag{2.4.8}$$

-Equivalent circuit model: Following [106], we can model the travelling wave photomixer by a standard transmission line having a distributed photocurrent source $\frac{dI_{ac}}{dz}$ and an internal admittance per unit length G_0. However, in this case since the photomixer is distributed over a well-defined length the circuit is analyzed by defining a differential element model. Figure 2.12 shows the equivalent differential circuit model for a distributed photomixer system.

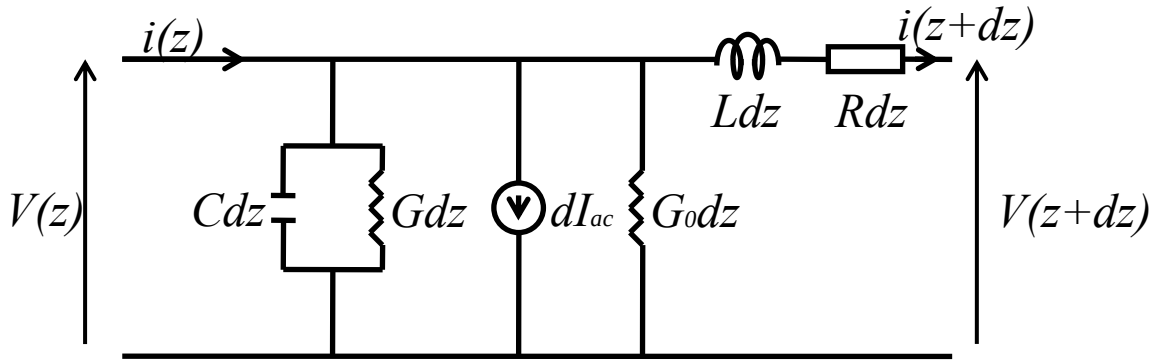

Figure 2.12: Equivalent differential circuit model for a distributed photomixer system.

From reference [106] we assume that the voltage solution is of the form $V_s(z,t) = Re(V(z)e^{j\omega_b t})$ and by using the distributed model of the THz waveguide including the photocurrent source, we can obtain by the Kirchhoff's voltage law:

$$V(z) = V(z+dz) + I(z+dz) \times Zdz \tag{2.4.9}$$

By applying the Taylor expansion, we get:

$$\frac{dV}{dz} = -I(z) \times Z - dI \times Z \tag{2.4.10}$$

then we can neglect the second order terms:

$$\frac{dV}{dz} = -I(z) \times Z \tag{2.4.11}$$

where $Z = R + jL\omega_b$.

Then by applying Kirchhoff's current law on the circuit:

$$\begin{aligned} I(z+dz) &= I(z) - V(z) \times (Ydz + G_0 dz) + \frac{dI_{ac}}{dz}dz \\ \Longrightarrow -\frac{dI}{dz} &= V(z) \times (Y + G_0) + \frac{dI_{ac}}{dz} \end{aligned} \tag{2.4.12}$$

Here $Y = G + jC\omega_b$.

Z and Y are related to a THz waveguide without a source and their calculation will be shown below. Now if we replace equation (2.4.11)in (2.4.12) we get:

$$\frac{d^2V}{dz^2} = V(z) \times Z(Y + G_0) + Z\frac{dI_{ac}}{dz} \tag{2.4.13}$$

If we consider that the propagation is lossless, we get $G \sim 0$ and we assume that $G_0 \ll Y$. Finally, we obtain the standard telegrapher's equation with a current source term:

$$\frac{d^2V}{dz^2} - {\gamma_t}^2 V(z) = +ZAe^{-\gamma_o z} \tag{2.4.14}$$

where $\gamma_t = \sqrt{ZY} = jk_t + \alpha_t/2$, k_t is the THz wave propagation constant and α_t is absorption coefficient of the THz wave. In the following we will consider the solutions of a transmission line without a source. This allows us to express k_t as function of physical parameters of the circuit. Note that the theory of a CPW and a transmission line is briefly emphasized in Appendix B. Consequently, here are the general solutions of voltage and current waves which are propagating on a transmission line:

$$V(z) = V_1 e^{j\omega_b t - \gamma_t z} + V_2 e^{j\omega_b t + \gamma_t z} \tag{2.4.15}$$

$$I(z) = \frac{V_1}{Z_c} e^{j\omega_b t - \gamma_t z} - \frac{V_2}{Z_c} e^{j\omega_b t + \gamma_t z} \tag{2.4.16}$$

where $Z_c = \frac{Z}{\gamma_t} = \sqrt{\frac{Z}{Y}}$

The general solutionsof in voltage and current of thetelegrapher's equation with a current source, are of the following form:

$$V(z) = V_1 e^{-\gamma_t z} + V_2 e^{\gamma_t z} + \frac{ZA}{\gamma_o^2 - \gamma_t^2} e^{-\gamma_o z} \tag{2.4.17}$$

$$I(z) = \frac{V_1}{Z_c} e^{-\gamma_t z} - \frac{V_2}{Z_c} e^{\gamma_t z} + \frac{\gamma_o ZA}{\gamma_o^2 - \gamma_t^2} e^{-\gamma_o z} \tag{2.4.18}$$

To calculate V_1 and V_2 we use the boundary conditions: $z = 0$ and $z = l$ where l is the device length. It is important to note that here we model a device that is not adapted at the input since the fabricated device will be designed in this manner. This gives us $I(0) = 0$ and $\frac{V(l)}{I(l)} = Z_l$. which allows us to calculate $V_1(l)$ and $V_2(l)$:

$$V_1(l) = \frac{A((Z_l\gamma_o - Z_c\gamma_t)e^{-\gamma_o l} - \gamma_o(Z_l + Z_c)e^{\gamma_t l})}{(\gamma_o^2 - \gamma_t^2)\left[\left(1 - \frac{Z_l}{Z_c}\right)e^{-\gamma_t l} + \left(1 + \frac{Z_l}{Z_c}\right)e^{\gamma_t l}\right]} \tag{2.4.19}$$

$$V_2(l) = \frac{A((Z_l\gamma_o - Z_c\gamma_t)e^{-\gamma_0 l} - \gamma_o(Z_l - Z_c)e^{-\gamma_t l})}{(\gamma_o^2 - \gamma_t^2)\left[\left(1 - \frac{Z_l}{Z_c}\right)e^{-\gamma_t l} + \left(1 + \frac{Z_l}{Z_c}\right)e^{\gamma_t l}\right]} \quad (2.4.20)$$

If $Z_l \approx Z_c$ and $k_t \approx k_o$ and the optical losses are way larger than the THz losses $(\frac{\alpha_o}{2} \gg \alpha_t)$

We obtain a very simple form of V_1 and V_2:

$$V_1(l) = \frac{AZ_c(\alpha_0 e^{-\gamma_0 l} - \gamma_o e^{\gamma_t l})}{(\gamma_o^2 - \gamma_t^2)e^{\gamma_t l}}$$

$$V_2(l) = \frac{AZ_c\alpha_0 e^{-\gamma_o l}}{(\gamma_o^2 - \gamma_t^2)e^{\gamma_t l}}$$

By replacing them in (2.4.17)we get:

$$V(l) = \frac{AZ_c}{\gamma_0^2 - \gamma_t^2}[(\frac{\alpha_0}{2}(1 + e^{-2\gamma_t l}) + \gamma_t)e^{-\gamma_o l} - \gamma_o e^{-\gamma_t l}] \quad (2.4.21)$$

Finally, the THz output power at the load impedance Z_l is calculated and expressed as:

$$P_{THz} = \frac{1}{2}Re(\frac{1}{Z_l})|V(l)|^2 \quad (2.4.22)$$

In the first part of this chapter, we showed a simplified model of a TW-photomixer to present the basic limitations of the device. Here we represent a realistic situation where we consider the THz propagation losses, the cutoff due to lifetime and the transit time between the two electrodes. In Table 2-2 we show the realistic physical parameters that we implemented in the equation. These parameters correspond to an LT-GaAs photoconductor having an electrode design similar to the design shown in Figure 2.11with an interelectrode spacing of 2 µm.

Symbols	*Physical meaning*	*Value*
l	Device length	1 mm
w	Inter-electrode spacing	2 µm
τ	Carrier lifetime	500 fs
τ_{tr}	Carrier transit time	200 ps
v_s	Saturation velocity	8×10^6 cm/s **[108]**
E_s	Saturation field	~50 KV/cm
μ	Carrier mobility	~200 $cm^2/(V.s)$ **[109]**
$\hbar\omega$	Photon energy	1.58 eV (λ=780 nm)
α_o	Optical absorption coefficient	2.3 mm^{-1} (~10 dB/mm)
α_t	THz absorption coefficient	0.5 mm^{-1} (3 dB/mm @ 1 THz)
Z_c	Characteristic impedance	50 Ohms
n_{THz}	THz refractive index	1.8

Table 2-2: Numerical values used in the theoretical model.

The propagation losses around 1 THz were extracted from a 2D electromagnetic simulation by FEM method of the fundamental mode of a 50-Ω-CPW on a 1-µm-thick membrane of GaAs that were realized by my supervisor Emilien Peytavit. Here we consider that we pump the device by 2 W optical power. Figure 2.13 plots the expected THz output power as a function of the frequency calculated by using this model. Three different index mismatch values have been considered here with α_o=10 dB/mm: Δn = 0 %, 6.7 % and 10 %. For comparison, we have also plotted the first two Δn values when α_o increases along the device so that the optical power is absorbed linearly, i.e. $\frac{dP}{dz}$ is constant. The other parameters used in the theoretical model are given in Table 2-2 and the device input termination is an open circuit. It can be seen that for perfect phase matching, output powers reaching 200 µW at 1 THz and 3 µW at 4 THz are expected with this device. As previously seen and as shown in the inset of Figure 2.13, the travelling wave signature of a photodetector is a 6-dB loss in the frequency response at "low" frequency as compared with a lumped device photomixer at equal photocurrent.

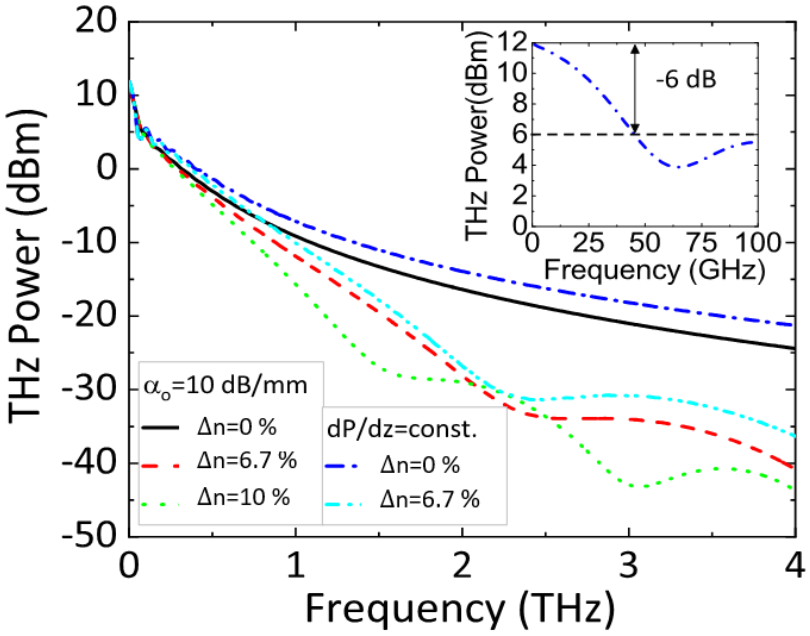

Figure 2.13: Theoretical THz power as a function of the beating frequency provided to a 50 Ohm load by a 1-mm-long TW photomixer pumped by an optical beatnote of power $\boldsymbol{P_0}$=2 W.

Conclusion

In this chapter wepresented the theory of traveling-wave-photomixers, highlighting the fundamental limitations of such devices. While TW-photomixers offer significant theoretical advantages over traditional lumped-element photomixers, practical implementation has been hindered by weak and unsatisfactory results. This can be attributed to several factors, such as the challenge of achieving velocity matching between the THz phase velocity and the optical group velocity. Previous studies have utilized semiconductors as the optical waveguide, which results in a high group index compared to the THz refractive index, making it difficult to achieve velocity matching. To overcome this limitation, a new concept is proposed where a Si_3N_4/SiO_2 waveguide platform is patterned between the electrodes of a CPW on an LT-GaAs membrane. The optical beatnote is absorbed by evanescent couplingin the LT-GaAs membrane and the THz is guided and dissipated in the load or emitted through antennas. This new design introduces an original technique to achieve optimal matching between velocities. The main idea lies on tuning the respective velocities by modifying the respective dimensions of the waveguides and the thickness of the LT-GaAs membrane. Finally, we presented a

theoretical study based on the photoconductive theory and acircuit model of a transmission line with a current source that expect microwatt level output power at 1 THz for velocity matched devices.In conclusion, our proposed solution presents a viable alternative for improving the performance of TW-photomixers. The following chapters will present the modeling and experimental results for two different generation of these TW-photomixers.

Chapter 3: Traveling wave photomixer compatible for 780-nm wavelength illumination

Introduction:

This chapter presents the practical implementation of the previously introduced concept of a TW-photomixer, which is illuminated with an optical beatnote having a wavelength around 780 nm. The novelty of this concept is the integration of a Si_3N_4/SiO_2 waveguide platform and the realization of an LT-GaAs membrane. To optimize the waveguide platform, various simulation methods were used such as Ansys Lumerical tools: MODE-FDE solver and FDTD solver which are based on Finite Difference Eigenmode and Finite Difference Time Domain algorithms respectively. The core dimensions were determined using MODE-FDE to ensure a single TE-mode propagation. Parameters, such as the mode confinement, effective index, and group index, were studied as a function of the core width. The grating design was optimized using a 2D FDTD model, where the lower cladding thickness, grating period, duty cycle, and optimal angle of incidence of the fiber were defined. BPM (Beam Propagation Method) was also used to design the MMI. This technique is based on solving the scalar wave equation, describing the behavior of electromagnetic waves in a given material.Test samples were fabricated to validate the calculated parameters, including coupling losses, propagation losses in waveguides above gold or GaAs and the MMI efficiency. Electromagnetic simulation using HFSS was also performed to evaluate the capability of a CPW design on a LT-GaAs membrane to tune the THz refractive index. Dimensions such as the central strip width, the interelectrode spacing and the membrane thickness were varied allowing the calculation of the index mismatch and the THz propagation losses. That latter was fabricated on an LT-GaAs membrane test sample where electrical measurements were realized. The THz propagation losses and the effective index were measured up to 0.8 THz. After that, the device fabrication process is described. It is worth noting that this section primarily focuses on the fabrication of devices suitable for 780 nm and 1550 nm illumination due to the similarities in the fabrication steps except for the dielectric waveguide dimensions and compositions. Material studies were conducted to optimize the Si_3N_4/SiO_2 waveguide platform for both wavelengths. The optoelectronic characterization of the device is discussed in the last section, which is divided into two sections: dc photoresponse measurements and frequency response measurements.

3. Traveling wave photomixer compatible for 780-nm wavelength illumination: modeling, fabrication and characterization

3.1. Optical modeling and characterization

In section2.3 we presented the concept of coupling through a grating with a back-reflecting mirror. In this section, FDE (Finite Difference Eigenmode) and FDTD (Finite Difference Time Domain) simulations are realized to calculate the specific dimensions of the waveguide such as the SiO_2 and Si_3N_4 thicknessest_{SiO_2} and $t_{Si_3N_4}$, the core widthw_{core} corresponding to a single-mode operation and the grating coupler period p, shown in Figure 3.1 (a) and (b). Additionally, the MMI length L_{MMI} and width w_{MMI}, shown in Figure 3.1 (c),will be defined in order to split the fundamental mode in two modes having each the same power. For more information, Appendix D provide a brief presentation on the three simulation methods.

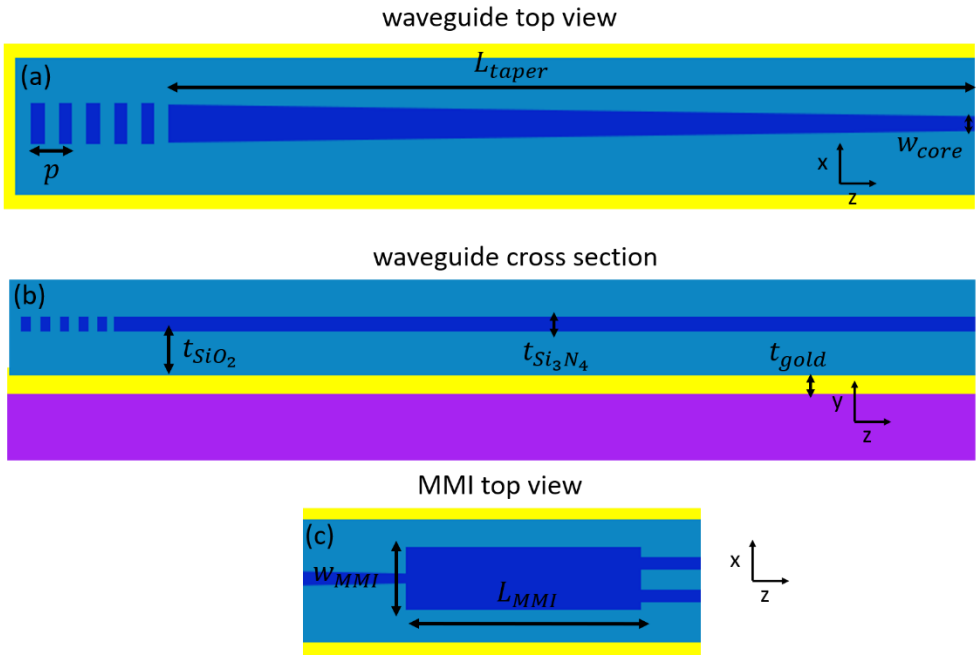

Figure 3.1: Waveguide platform representation showing (a) a top view of the grating and the tapered waveguide, (b) an yz cross section of the same structure and finally (c) a top view of the MMI.

3.1.1. Optical simulation for different waveguide geometries compatible for 780 nm wavelength

3.1.1.1. Single-mode-waveguide design

To optimize the waveguide for single-mode operation, the dimensions of the Si_3N_4 core should be chosen such that only the fundamental transverse electric (TE) mode can propagate since the grating coupler diffracts only the TE modes. This can be achieved by making the thickness and width of the core with the same order of magnitude to the wavelength of the light being used, which in this case is 780 nm. The refractive indices of Si_3N_4 and SiO_2that we used in the simulation model were measured using ellipsometry on test samples at a wavelength of 780 nm and found to be 1.9 and 1.45, respectively. To determine the optimal core width for single-TE-mode operation, we first set the core thickness to 200 nm, which allows for the presence of $TE_{m,0}$ modes. Next, the core width was varied from 200 nm to 2000 nm. The effective index of the possible modes is studied in this core width range. Figure 3.2, indicates that a single-TE-mode operationis achieved for a width lower than 784 nm. Forlower widths, the mode tends to be squeezed out of the core and instead propagates more in the cladding, resulting in lower effective index values.

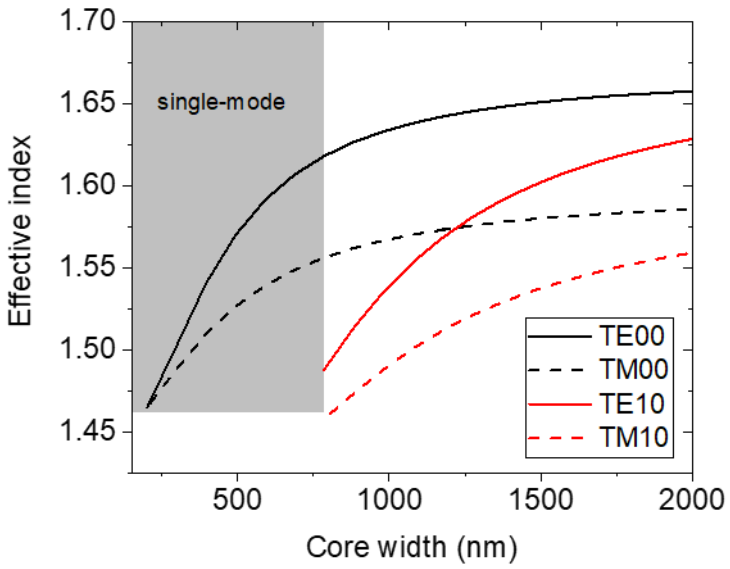

Figure 3.2: Effective index of the TE/TM modes at λ=780 nm in a 200 nm thick Si_3N_4 core as function of the core width.

Figure 3.3 illustrates the transverse electric (TE) profile for two different core widths: 200 nm (a) and 400 nm (b). FDE simulations also provide the effective area of the mode, which is calculated as the ratio of the mode's total energy density per unit area to its peak energy density. As the core width is reduced, the mode is pushed out of the core and the effective area increases. This suggests that the core width is the important parameter to consider when adjusting the distributed absorption in the LT-GaAs material.

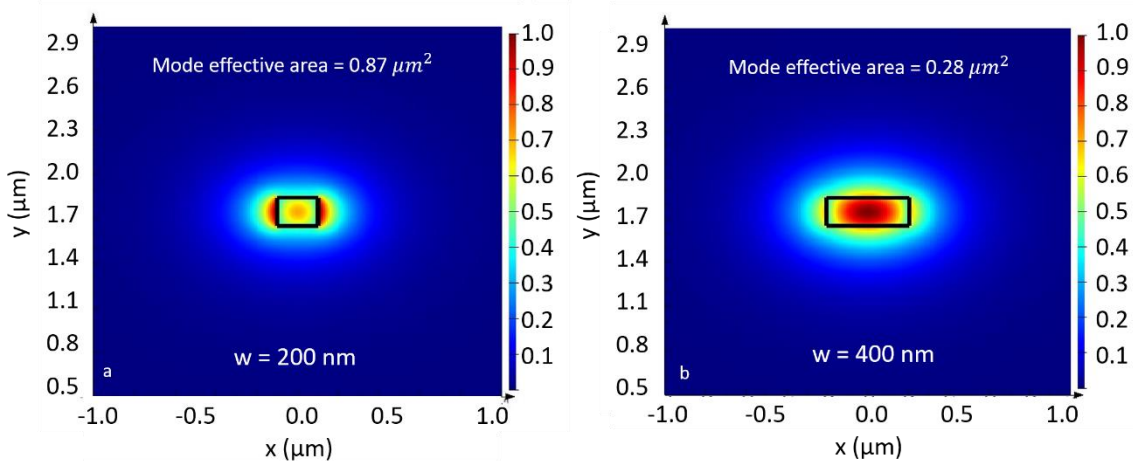

Figure 3.3: FDE solver interface showing the fundamental TE mode profile for (a) a 200 nm wide core and (b) a 400 nm wide core.

To ensure a smooth transition of the fundamental mode to the active region,the gold layer thickness should be minimized. However, if the latter is too thin, this would result in high optical losses due to transmission through the gold layer and absorption in the LT-GaAs before reaching the active region.The suitable thickness was defined basedon the Beer-Lambert law where reflection, transmission and absorption coefficients wereused at 780 nm. By setting a target of 0.002% transmission through the gold layer, we determined that a thickness of 70 nm would be appropriate. Since the core thickness is about three times the thickness of the gold layer, we can expect that the mode in the core will not be significantly affected by scattering due to a discontinuity in the waveguide. This prediction was confirmed through finite-difference time-domain (FDTD) simulations using realistic dimensions based on a test sample fabricated in the clean room.Figure 3.4 shows an SEM image of the core transition to the active region.

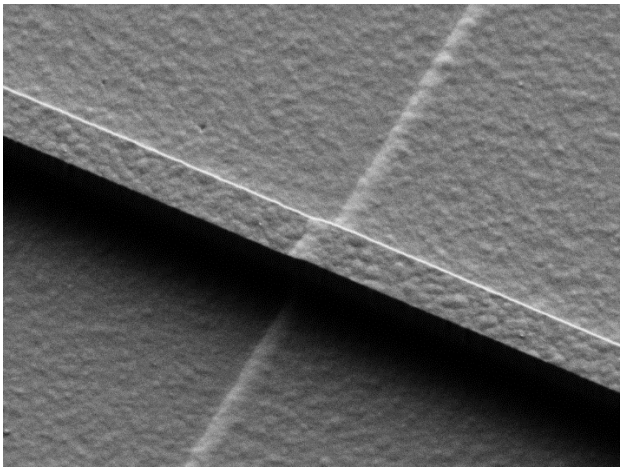

Figure 3.4: SEM image of the core transition from the back reflecting mirror to the active region.

3.1.1.2. Group index

After defining the single-mode operation, we can now use the same simulation model to calculate the group index for different core widths. However, a realistic simulation design is considered where we included theLT-GaAs membrane. Figure 3.5 shows the group index variation as function of the core width. For a core ranging from 150 nm to 500 nm we can see that the group index increases from ~1.55 to ~1.9. These results will be important later in the section 3.2.1 where the optimum designs of the CPW and membrane are studied in order to achieve index matching.

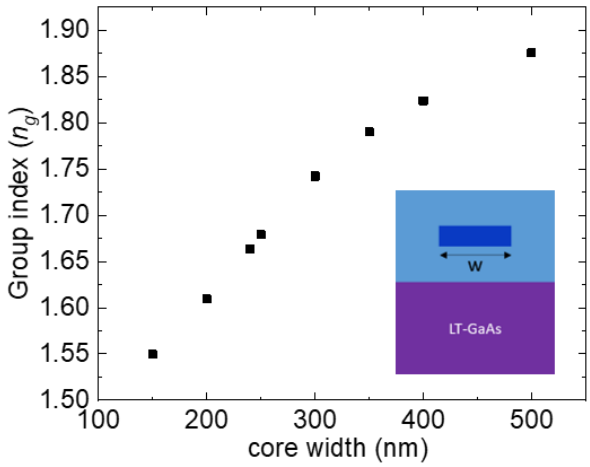

Figure 3.5:.Group index of the fundamental TE mode at λ=780 nm as a function of the core width obtained by 2D FDE MODE solver.

3.1.1.3. Grating coupler design

To determine the optimal design of the grating coupler, we will first calculate initial values for the critical parameters such as the grating period and lower cladding thickness. These values will be based on the requirement for constructive interference between the back reflected light and the input light. The grating period can be calculated using equation (C.2) from Appendix C:

$$p = \frac{m\lambda}{n_{eff} - n_{cladding} \sin\theta}$$

The grating period, denoted as "p", depends on the wavelength λ, the coupling angle θ, the cladding index $n_{cladding}$, and the effective index of the grating mode n_{eff}. Here, we will consider the first order ($m = 1$) and fix θ at 10° to reduce interference between the fiber facet and the device. The cladding index, which corresponds to the index of SiO_2 as measured by ellipsometry, falls in the range of 1.45 to 1.5 at 780 nm depending on the sample. The effective index of the grating mode is not yet defined. As a first approximation, we will consider an effective index between 1.55 and 1.6, which is close to the effective index of the fundamental TE mode in a continuous waveguide as shown in Figure 3.2. Using these values, we calculate the grating period to be between 570 nm and 605 nm, depending on the cladding index and the effective index of the mode. To achieve maximum back coupling, it is necessary to have a constructive interference on the grating. Therefore, the lower cladding thickness t should be a multiple of $t_{m+1} - t_m = \frac{(m+1)\lambda_{SiO_2}}{2} - \frac{m\lambda_{SiO_2}}{2} = \frac{\lambda_{SiO_2}}{2} = \frac{\lambda}{2n_{SiO_2}} \approx 265 \pm 5$ nm, where t_{m+1} and t_m are the consecutive thicknesses corresponding to constructive interference. If the core is too close to the gold layer, large propagation losses will be induced before reaching the active region. Therefore, we choose to work with the thickness corresponding to the third order constructive interference, which is approximately 795 ± 15 nm. This ensures that the core is sufficiently far from the gold layer while still being able to evanescently couple to the LT-GaAs material.

Having established initial estimations for the grating period and lower cladding thickness, we conducted a parameter sweep using these values in a two-dimensional finite-difference time-domain (FDTD) simulation model. To accurately reproduce the

experimental configuration, a model based on a tutorial in the simulation tool underwent several modifications. In, the experimental setup, the fiber was cleaved at a 0° angle, resulting in an air gap between the fiber facet and the sample. This would result in to reduced optical coupling due to reflections from the sample, as well as additional losses due to light scattering entailed from the roughness of the substrate, the gold layer, SiO_2 lower cladding, Si_3N_4 layer, and SiO_2 top cladding. This problem can be partially solved by introducing an index matching gel between the fiber and the sample. To reproduce these conditions in the simulation, the model was modified to include the 0° cleavage angle and the presence of the index matching gel between the fiber and the grating. Test samples were then fabricated with varied lower cladding thicknesses to identify the optimal thickness for maximum coupling.

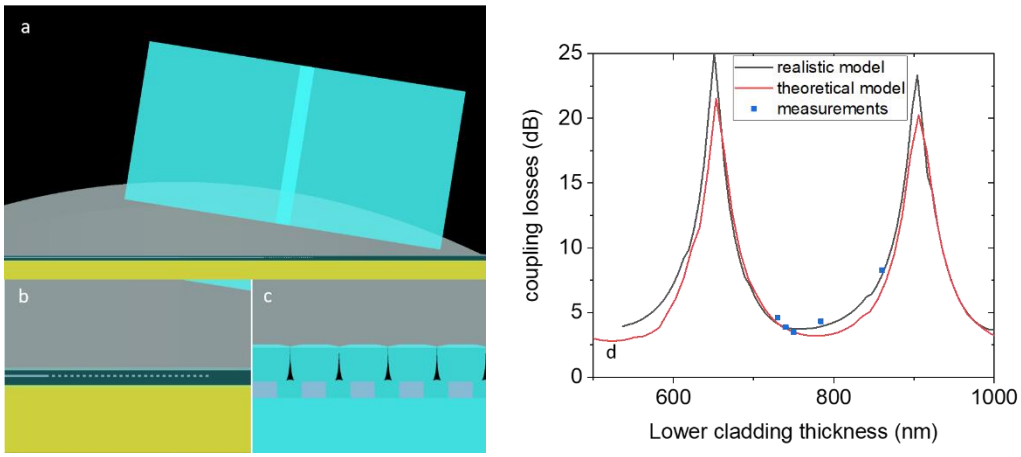

Figure 3.6: (a) simulation interface of the coupling structure. Zoom in on the theoretical (b) and realistic (c) grating coupler design. (d) Coupling losses as function of the lower cladding thickness for the realistic and theoretical design and for measurements on test samples.

Figure 3.6 (a) shows the simulation interface with a 0°cleaved fiber above the grating coupler and an index matching gel between the two. Figure 3.6 (b) and 3.6 (c) show a zoomed-in view of the theoretical and realistic grating designs, respectively. The realistic design is based on a focused ion beam (FIB) cut similar to the one shown later in Figure 3.30. These triangular shaped void gaps are due to non-conformal deposition of the top SiO_2 layer. Figure 3.6 (d) shows the lower cladding thickness as a function of the coupling losses for both the theoretical and realistic designs, as well as experimental results represented by blue scatter points. The SiO_2 index was around 1.5 when the test samples

were fabricated, leading to an optimal thickness of 758 nm (3.7 dB) for the realistic design and 774 nm (3.19 dB) for the theoretical design. The lowest measured coupling losses at the operating wavelength of 780 nm was 3.5 dB (44.6% coupling efficiency) at a lower cladding thickness of 750 nm. These results demonstrate that at λ=780 nm, even small changes in deposition rate or material quality (roughness, index, etc.) can significantly impact the coupling losses. It is worth noting that before each SiO_2 or Si_3N_4 layer was deposited, a test was performed to verify the deposition rate and refractive index. Given that in the worst-case scenario there is a maximum error of 5% on well-defined thicknesses, sometimes it can be challenging to achieve the exact calculated optimal thicknesses.

3.1.1.4. Multimode interferometer (MMI) design

In order for the optical waveguides to fit between the electrodes of a coplanar waveguide, the inter-waveguide spacing at the output of the MMI coupler needs to be determined by the strip width of the coplanar waveguide. The strip is the central metallic line in a coplanar waveguide, and according to electromagnetic simulations performed byEmilien Peytavit, the width of this strip should be around 6 µm to ensure that the refractive index of the THz wave stays within an interval where quasi-phase matching is possible. The interelectrode spacing has been set to 2 µm in order to avoid high THz propagation losses in the waveguide.As a result, a minimum inter-waveguide spacing of 8 µm. Based on a 3D BPM simulation optimization performed by Vincent Magnin, the MMI width was initially set to 5 µm and the length to 285 µm. However, this length isconsidered too large and would result in important optical propagation losses before reaching the active region. To reduce the MMI length to an acceptable level, the inter-waveguide spacing was reduced to 2.5 µm, resulting in an MMI length of 29 µm. The 8 µm inter-waveguide spacing is then achieved through a 150 µm-longtaper, as shown in Figure 3.7. A similar kind of work where they optimized an MMI with a corresponding taper was realized in ref [103]

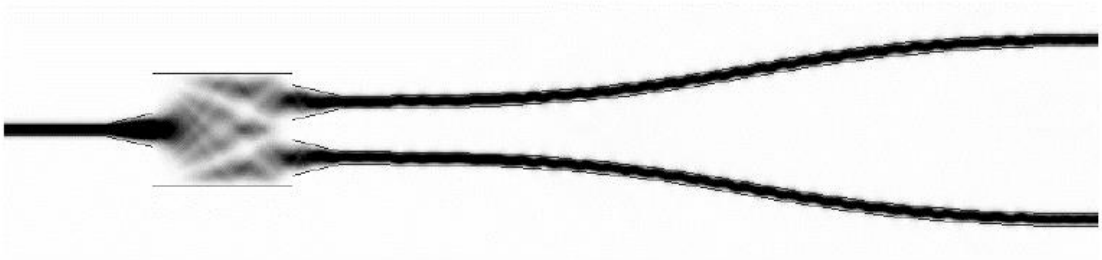

Figure 3.7: Top view of the TE fundamental mode coupled to the 29 µm long and 5 µm large MMI. The vertical dimension is out of scale (enlarged).

3.1.2. Characterization of the Si_3N_4/SiO_2 waveguide platform

In the previous section, we presented measurements of the coupling losses. Here, we describe the cut-back method that we used to estimate these coupling losses as well as the propagation losses in the waveguides. Figure 3.8 shows the experimental setup of the waveguide characterization. To extract the propagation losses, we fit a linear model to the measured optical losses$\left(10log\left(\frac{P_{output}}{P_{input}}\right) \text{in dB}\right)$ of several waveguides as a function of their respective length (in mm). The slope of the resulting line corresponds to the waveguide's propagation losses (in dB/mm) and the intercept of the fit with the y-axis represents the insertion losses. An example of the linear fit is shown later in Figure 3.24.

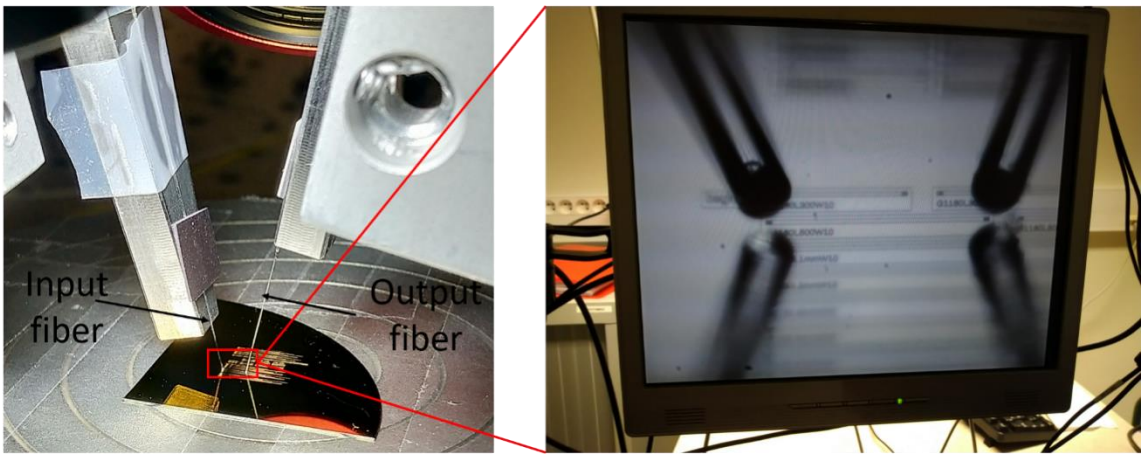

Figure 3.8: Experimental setup for the characterization of the waveguide platform. For a clear photo showing the waveguides and the optical fibers, the index matching gel is not used.

Figure 3.9 shows an example of the mask used to fabricate the waveguides for the cut-back measurements. There are two typical designs used for this purpose. The first design consists of waveguides with a constant core width (5 μm) that are terminated at both ends with grating couplers. The entire waveguide structure is patterned on top of a back-reflecting gold layer. The second design is composed of two parts: (1) a coupling structure that includes a grating coupler and an adiabatic taper designed to follow a third-order polynomial function, gradually decreasing the core width from 5 μm to a few hundred nanometers at the active region and (2) when the core reaches its constant width, it steps from the back-reflecting mirror onto the LT-GaAs active region. The length of the segment above the LT-GaAs is then varied to extract the propagation losses in the semiconductor. In both designs, coupling between the fibers and the planar waveguides occurs through the input and output grating couplers. The only variable dimension is the waveguide length. In the first design, while the slope of the fit corresponds to the propagation losses, the intercept corresponds to the insertion losses which in this case are the coupling losses of the two grating.For the second design (waveguide on LT-GaAs), the insertion losses correspond to the coupling losses of the two grating couplers and the losses in the two tapers.

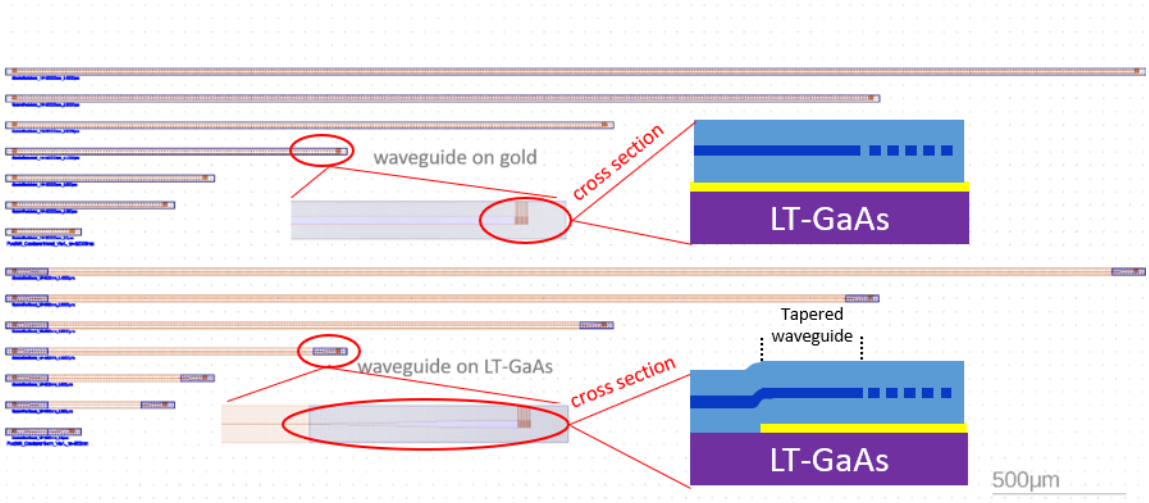

Figure 3.9: Example of the lithographic mask of a test structure presenting straight waveguides on gold and on LT-GaAs used to measure the propagation and coupling losses. Cross section representations in the grating show the main difference between the two designs.

For the first design, the propagation losses for a 5 μm wide core were around 2.9 dB/mm. In this situation, it is considered that the mode is well confined in the core and the losses originatespurely from the Si_3N_4 composition. It is important to note that a material study is realized to optimize the SiO_2roughness and the Si_3N_4 composition for low propagation losses at $\lambda = 780$ nm. The results of this study will be shown later in the section describing the fabrication.

3.1.2.1. Losses in the taper and absorption in the active region

In the course of this work, two types of devices were fabricated: 1) LT-GaAs membraned supported devices, where the active region is transferred to a high resistivity silicon wafer and 2) Devices on GaAs bulk layers which is the substrate at which the LT-GaAs is grown after a thin AlGaAs layer. In this section, all the optical measurements were realized on devices having a GaAs bulk. Layer. Since we already measured the coupling lossesof the grating couplers (3.5 dB/grating)from the first design we can extract the losses in the taper segment. Note that, based on test devices where the taper length was varied it was found that there was no significant difference between the losses of a 300 μm long and 150 μm long taper and they were measured to be around 0.8 dB/taper. As a result, a taper length of 150 μm was defined for the full device.Figure 3.10(a) shows the taper losses for different core widths. We can see that these losses are not the same for all core widths and start to becomesignificant when the core width is under 200 nm. At low core widths,the overlap of the fundamental mode profile with the substrate increases resulting in higher losses due to absorption.Later these taper losses will be considered when measuring the dc photoresponse for devices with different core widths.

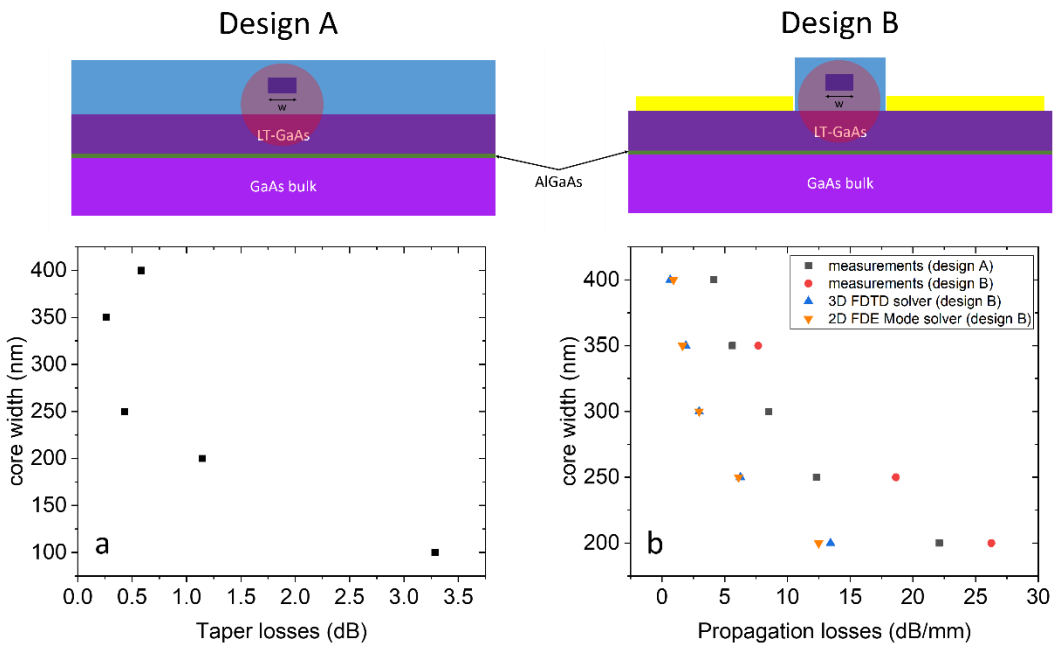

Figure 3.10: (a) Measurements of the losses in the taper before reaching the active region. (b) Measured propagation losses above the LT-GaAs layer in design A (black). Measured propagation losses above the LT-GaAs layer in design B (red). Simulated propagation losses above LT-GaAs using 3D FDTD solver (blue) and 2D FDE Mode solver (orange).

In the case of waveguides above the LT-GaAs, in order to verify if the metallic waveguide result in optical losses, we will consider two designs shown inFigure 3.10. Design A correspond to the same structure shown in Figure 3.9 where there were no electrodes deposited and Design B correspond to realistic design where the metallic waveguide is deposited. In Figure 3.10(b), we present the measurement and simulation results of the core width as a function of the propagation losses/absorption in LT-GaAs. In the 2D FDE MODE solver design, the fundamental mode losses were calculated for different core widths. Note that these losses represent the losses of the mode in full structure while in the FDTD solver a 3D model of the device was designed, where the fundamental mode propagated for 100 µm and the losses were extracted from the absorbed power only in the LT-GaAs layer.It should be noted that in the two simulation designs, all materials were considered lossless except for the LT-GaAs ($n_{GaAs\ @\ 780\ nm} = 3.7 + 0.09j$) and the gold ($n_{Gold\ @\ 780\ nm} = 0.174 + 4.86j$).It is observed that the results of the two simulations are similar suggesting that all the optical power is absorbed in the LT-GaAs and there are no losses due to the metallic waveguides. On the other hand, the

measurements show higher losses for design B compared to design A. It is noteworthy to mention that in design B, it was not possible to measure the propagation losses for all core widths. This was mainly due to the lower process yield of devices having the design B because of their additional fabrication steps. Since the results of the two simulation models are similar, we concluded that the metallic lines do not result in significant optical losses, we can assume that this increase in propagation losses in design B originates from the sidewall roughness of the etched top cladding. Overall, the results of the four curves display a similar exponential-like decay, however, the measurements are slightly higher than what was expected by the two types of simulations. This discrepancy may be attributed the presence of roughness and scattering that was not introduced in the simulation model.

3.1.2.2. Waveguide design allowing linear absorption in the active region

In order to design waveguides allowing linear absorption along the device, first we consider that the optical absorption in the waveguides follows the Beer-Lambert law, the optical power as function of the length z can be written as follows:

$$P(z) = P_0 e^{-\alpha_o z}$$

Where α_o is constant and is the absorption coefficient of LT-GaAs for a given core width and P_0 is the power at $z = 0$. Note that α_o increases for lower core widths since the fundamental mode is squeezed out of the core resulting in higher interaction with the LT-GaAs. In order to increase the emitted THz power, the absorbed power should be distributed linearly along the device length ($P(z) = P_0 - az$). This is shown in Figure 2.13 in the blue dashed plot where the absorption density $p_{abs} = -\frac{dP(z)}{dz} = cte = a$. At $z = L$, $P(L) = 0$ which leads to $a = p_{abs} = \frac{P_0}{L}$. Where L is the waveguide length. Finally, the linearly absorbed power is expressed in the following form:

$$P(z) = P_0 \left(1 - \frac{z}{L}\right) = P_0 e^{-\alpha_o z} \qquad (3.1.2.1)$$

The latter is only possible if α_o is dependent of z. Knowing that α_o is dependent of the core width w, we can assume that by changing the core width along the waveguide α_o can be varied along z. Now we can calculate $\alpha_o(z)$ from (3.1.2.1):

$$\alpha_o(z)[Np/mm] = \ln\left[(1 - z/L)^{\frac{-1}{z}}\right] \quad (3.1.2.2)$$

$$\alpha_o(z)[dB/mm] = -10 \times \log(e) \times \ln\left[(1 - z/L)^{\frac{-1}{z}}\right] \quad (3.1.2.3)$$

Now that we defined a position dependent absorption coefficient in order to create a constant absorption density in the device, we need to define the core design allowing that. To achieve this, we have defined the relation $w(\alpha_o(z))$. Since the absorption coefficient was then measured for each core width utilizing the cut-back method, an exponential fit was performed on the measured data, and the best exponential decay equation that fitted the results is presented as follows:

$$w(\alpha_o) = A_0 + A \times e^{\frac{-\alpha_o}{t_1}} \quad (3.1.2.4)$$

The measurements and the exponential fit are shown in Figure 3.11. A_0, A and t_1 are constant values and are defined by the best fit and are shown in the inset table of Figure 3.11. A_0 represents the core width at the end of the waveguide.

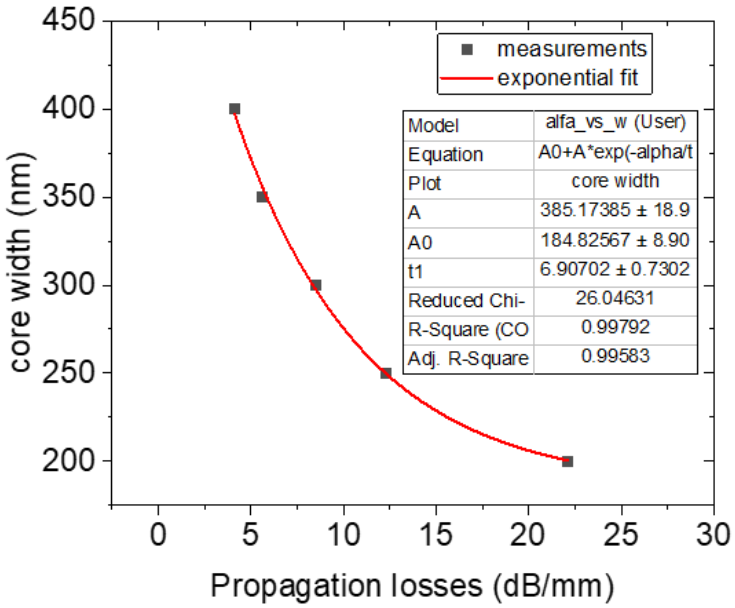

Figure 3.11: Core width as function of the propagation losses above the LT-GaAs layer. In red is shown the exponential fit based on equation (3.1.2.4).

After finding the relation between w and α_o, and since α_o is z-dependent we can now express w as a function of z.

$$w(z) = A_0 + A \times e^{\frac{-10\times\log(e)\times\ln\left[(1-z/L)^{\frac{-1}{z}}\right]}{t_1}} \qquad (3.1.2.5)$$

Equation(3.1.2.5) allows to design a waveguide having a varying core width along the device resulting a constant absorption density along the device. As an example, we consider an optical input of 1 W coupled into a 1 mm long waveguide. Figure 3.12 (a) shows the core width as a function of position (black) and the corresponding absorbed power along the waveguide (red). The core width function is plotted using equation (3.1.2.5). The red plot indicates that the power is absorbed linearly along the device, resulting in a more even distribution of power along the waveguide. Figure 3.12(b), we assume a constant core width of 200 nm throughout the device corresponding to propagation losses of 22.11 dB/mm. In this case, the absorbed power density is nonlinear along the device, with about 90% of the light absorbed before the first half of the

waveguide. This leads to a less even distribution of light in the device, which reduces the device's performance in the traveling-wave regime.

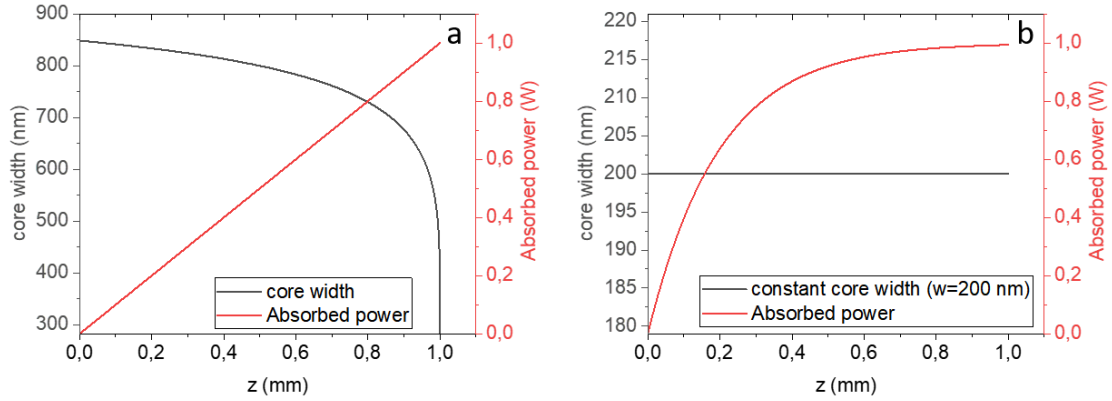

Figure 3.12: (a) Variable core width along the device (black line) allowing a linear absorbed power (in red) in the device. (b) Constant core width (200 nm) along the device (in black) resulting in a fast absorption in a 1 mm long device.

3.1.2.3. MMI characterization

The MMI was also characterized by fabricating test samples where there is one grating coupler for the injecting fiber and two at the output fiber. The MMI length was varied (28, 29 and 30 µm) as it relates to the 50/50 splitting of the mode.Figure 3.13 shows the measurement of the losses and the efficiency of the MMI for the three defined lengths. The efficiency of the MMI is defined by the ratio between the two outputs emitted each by a grating coupler. In this study we chose to use the 29 µm long MMI since it possesses the lowest losses (1.73 dB) and a plausible efficiency (~0.88). Note that these losses correspond to the MMI and the 150 µm-long taper. As for the efficiency, it can be observed that the three lengths have similar efficiencies and the slight difference may be due to measurement errors.

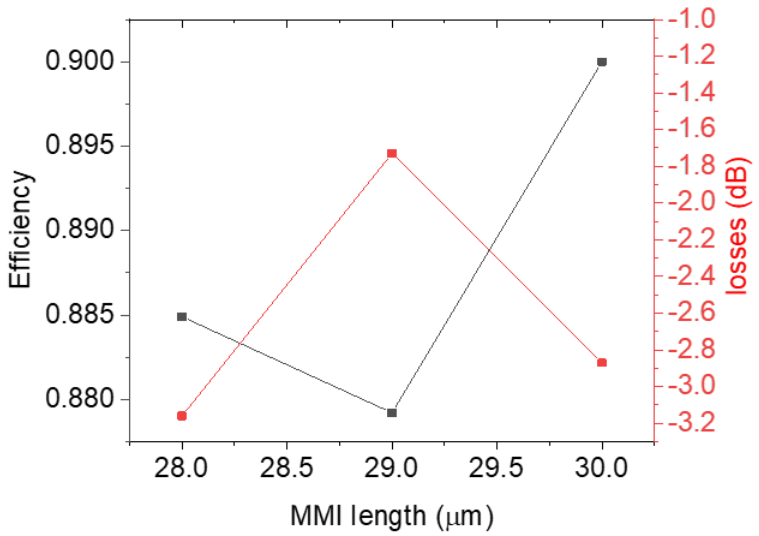

Figure 3.13: MMI efficiency (black) and losses (red) as function of the MMI length.

As a result, in a CPW design, the lowest possible injection losses that could be achieved before reaching the active region ranges between ~5.48 dB and ~8.48 dB depending on the core width. These losses are still considered high and could be reduced by using CPS design where the optical beatnote is coupled to the active region directly after the adiabatic taper allowing to gain 1.73 dB (MMI and taper losses). However, for the CPS design, on bench measurements are only possible up to 67 GHz. Higher frequencies could be characterized by implementing resonant antennas.

3.2. Electromagnetic modeling and characterizations

To determine the optimal configuration for phase matching and to estimate the propagation losses of CPW on the membrane, we used 2D electromagnetic simulations based on the finite element method (FEM) on CPW designs. After that, the simulated parameters were used to fabricate a test sample of an LT-GaAs membrane supported CPW. Measurements of THz effective index and propagation losses were realized up to 0.8 THz.

3.2.1. Modeling of an LT-GaAs membrane-supported CPW

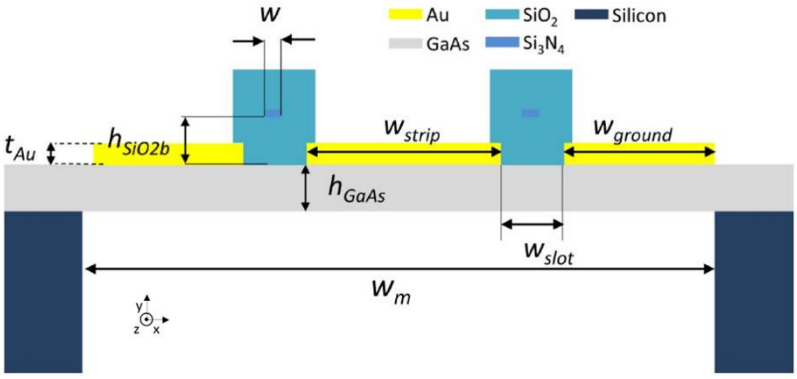

Figure 3.14: 2D representation of the complete structure showing the LT-GaAs membrane, the coplanar waveguide, and the optical waveguides.

- **CPW optimization**

In Figure 3.5, we demonstrated that the optical group index can vary between 1.5 and 1.9 based on the core width of the waveguide. Similarly, the THz refractive index can be determined by the dimensions of the coplanar waveguide. The THz refractive index formula includes both a capacitance and inductance term as shown in Appendix B, and by altering the width of the central strip, the inductance/capacitance will change and therefore the THz refractive index can be modified.Figure 3.14 shows the representation of the LT-GaAs membrane design with the CPW and dielectric waveguides. We fixed the slot width w_{slot}, the ground width w_{ground}, the membrane width w_m, the gold thickness t_{Au}, and the LT-GaAs thickness at 2 µm, 6 µm, 40 µm, 600 nm, and 700 nm respectively. A 2D FEM simulation was conducted for three different strip widths (6 µm, 12 µm, and 18 µm) in the 0.1-1 THz frequency range. Figure 3.15illustrates the THz refractive index (a) and propagation losses (b) for these strip widths as a function of the frequency. We can see that for wider strip widths, the refractive index decreases. Importantly, the values in Figure 3.15 (a) clearly allow for phase matching between the THz and the optical beatnote. The optimal scenario is when the strip width is 18 µm, as the refractive index falls between 1.8 and 1.85 in the frequency band since it is easily achievable in the group index. Additionally, the 18 µm wide strip corresponds to the lowest propagation losses between

the two other values with losses ranging from 2 dB/mm at 0.1 THz to 5 dB/mm at 1 THz. Even for a 1 mm-long device these losses are considered acceptable.

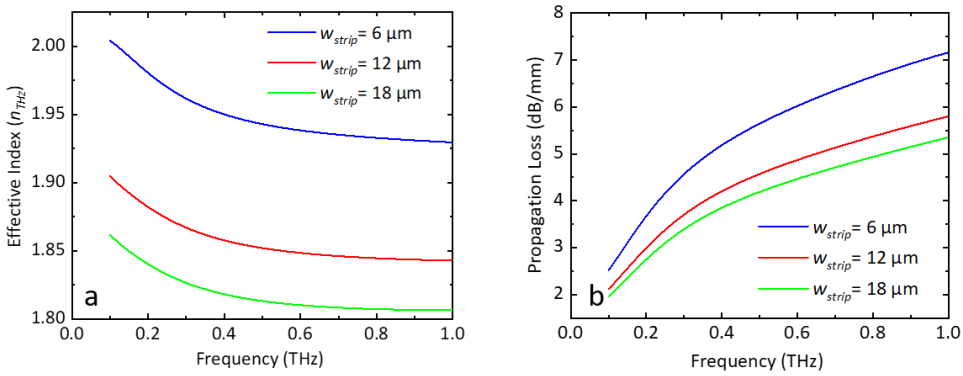

Figure 3.15: THz effective index (a) and THz propagation losses (b) for three strip widths w_{strip}(6 µm, 12 µm and 18 µm) as function of the frequency.

Now, by considering that the optical group index and THz refractive index can be easily adjusted, we will analyze the device performance by computing the phase mismatch resulting in a 3-dB roll-off at three various frequencies. As per the simplified model presented in section 2.1, we can deduce that the THz output power is directly related to $\left|\frac{\sin(\Delta\varphi)}{\Delta\varphi}\right|^2$ wherethe index mismatch is expressed as follows:

$$\Delta\varphi = \frac{(n_g - n_{THz})\pi L f_b}{c}$$

f_b and L are the beating frequency and the device length respectively. We will define $\Delta n = n_g - n_{THz}$. In Figure 3.16 we present the maximum value of $|\Delta n|$ as a function of device length for various 3 dB cut-off frequencies. It can be observed that achieving almost perfect index matching is necessary for high cut-off frequencies and longer devices. However, for a shorter device (500 µm) and a 3dB cut-off frequency of 500 GHz, the index mismatch is slightly higher than 0.5, which can be easily managed. Figure 3.16 serves as a useful guide for determining the parameters that enable quasi-index-matching, as all parameters in $\Delta\varphi$ can be controlled through the device design and the desired generated frequency. Based on these conclusions, the CPW and the membrane design will be examined in the following paragraphs.

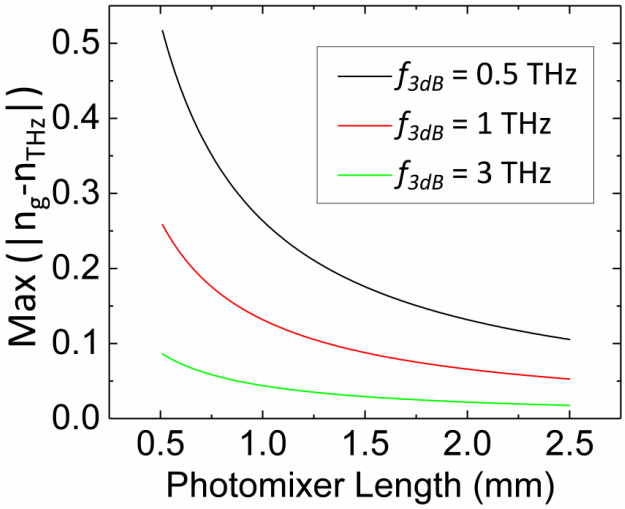

Figure 3.16: Maximum index mismatch as function of the photomixer's length for 3 different 3dB cut-off frequencies: 0.5 THz, 1 THz and 3 THz.

In Figure 3.17we fix the frequency at 1 THz and plot the THz effective index as a function of the central strip width for different LT-GaAs thicknesses and we consider a group index around 1.8. Based onFigure 3.16, in order to achieve$f_{3dB} = 1$ THz for a 1 mm long device the THz effective index should be defined in the range of 1.8 $\pm$ ~0.15.We can see that the THz effective index decreases for thinner LT-GaAs membranes. This is due to the fact that thinner membranesresult in higher overlap of the THz mode with air. On the other hand, thicker LT-GaAs layers have higher thermal conduction, which is necessary for high optical powers. In conclusion, a 700 nm LT-GaAs thickness and a strip width between 10 µm and 18 µm results in a fine balance between the need for high thermal conduction and a plausible index matching leading to a 3-dB cutoff at 1 THz or higher.

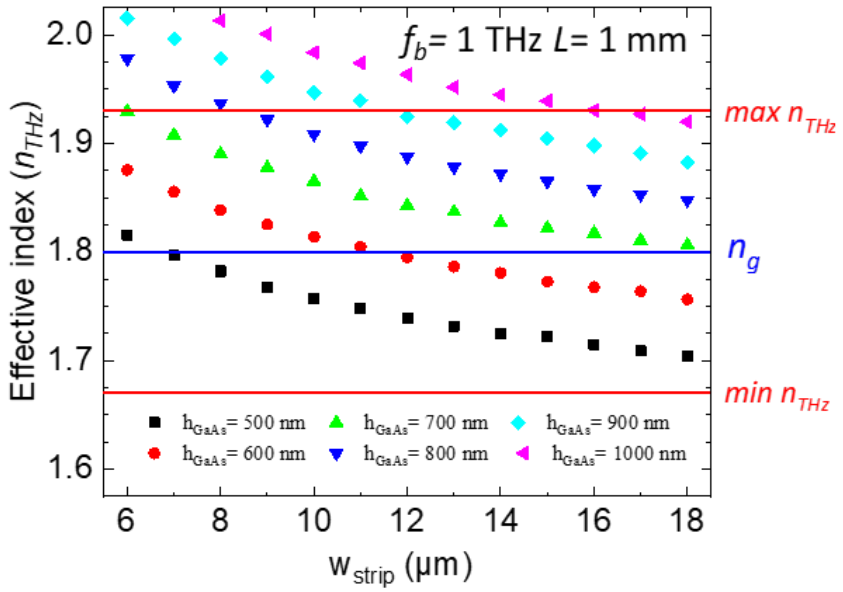

Figure 3.17: THz refractive index at 1 THz as function of the strip width.

We will now examine how changing the slot width affects the refractive index and the propagation losses as function of the strip width at 1THz. h_{GaAs} is set to 900 nm and the other dimensions will remain the same. By increasing the slot width by 1 µm, we can decrease the effective index of the mode by 0.1 and decrease propagation losses at 1THz by 1.5 dB. This is presented in Figure 3.18 (a) and (b). However, this also means that a higher bias voltage is required to achieve the same photoresponse. As previously explained, the closer the electrodes are, the higher the photoconductive gain will be, but at the expense of higher THz propagation losses. In conclusion, while decreasing propagation losses and bringing the THz refractive index closer to the optical group index may seem beneficial, it is not worth the decrease in the photoconductive gain. On the other hand, 1 µm of interelectrode spacing would result in high propagation losses. As a result, a slot of 2 µm is maintained.

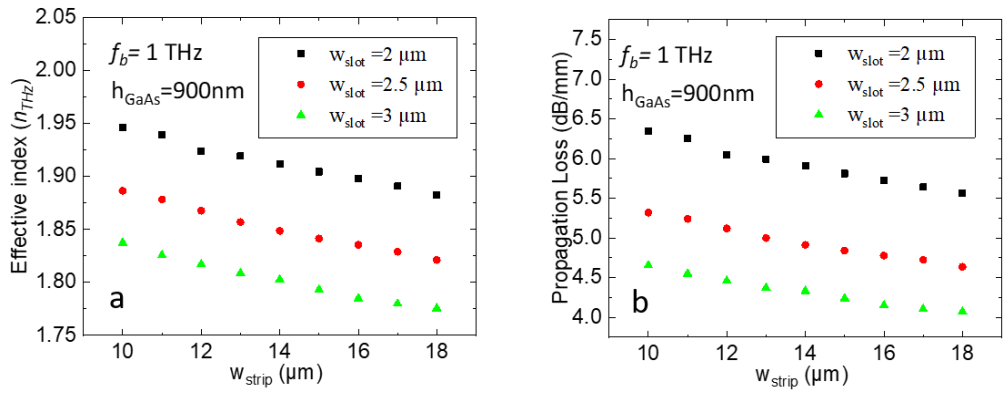

Figure 3.18: THz effective index (a) and THz propagation losses (b) for three strip widths w_{strip}(6 µm, 12 µm and 18 µm) as function of the frequency.

3.2.2. Electrical characterization of the LT-GaAs membrane-supported CPW

On-wafer measurements have been performed up to 750 GHz by means of vector network analyzers (VNA) by using suitable frequency extenders and coplanar probes. We present in Figure 3.19 (a) the experimental attenuation coefficients of a 1-µm-thick LT-GaAs membrane-supported CPW. It can be noticed a rather good agreement with the theoretical results obtained by FEM modelling (assuming an infinitely wide membrane). However, the surface impedance approximation used in the FEM model gives only a rough estimation of ohmic losses which dominate the propagation losses of the membrane supported CPW since the radiation losses are almost canceled. We have also plotted in Figure 3.19, theoretical ohmic losses obtained by using a quasi-TEM model of coplanar waveguides developed by Heinrich [110]. This model assumes an infinitely thick substrate and we mimicked a membrane-supported CPW by setting the dielectric constant of the substrate ϵ_r so that the quasi-TEM effective dielectric constant of the CPW TEM mode $n_{THz}$is close to that obtain by the FEM model ($n_{THz} \approx 2$). In the quasi-static limit, the effective index n_{THz} of a CPW patterned on a substrate of dielectric constant ϵ_r is given by $n_{THz}{}^2 = (\epsilon_r+1)/2$, thereby if $n_{THz} = 2$, $\epsilon_r = 7$. It can be noticed a very good agreement of the propagation loss given by this model with the experimental ones at least from 1 to 500 GHz.

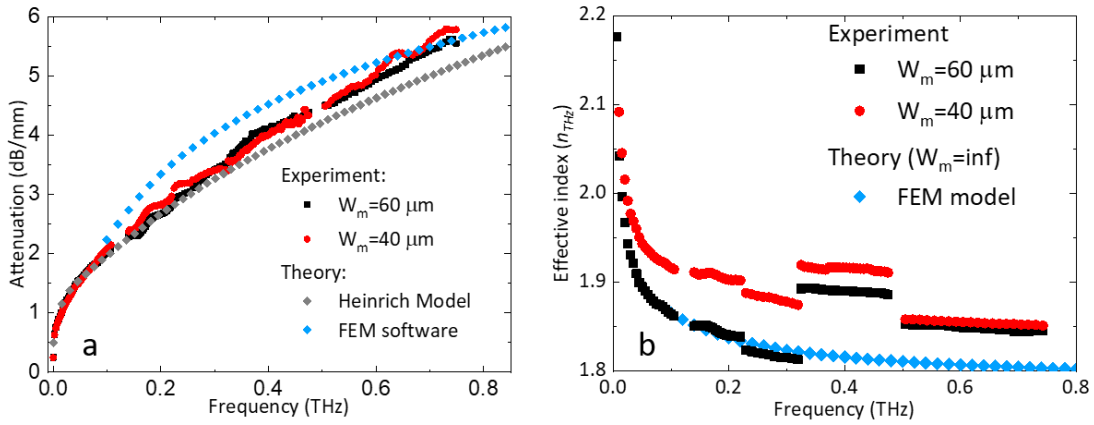

Figure 3.19: THz attenuation α_t and effective index n_{THz}, as function of frequency on a LT-GaAs membrane-supported CPW without optical waveguide. Geometrical parameters: w_m.=40 and 60 µm, w_{strip}=6 µm, w_{ground}=10 µm, and w_{slot}=2 µm. Theoretical values have been obtained by FEM modelling (see inset of Fig. 3 for further details) and by using a quasi_TEM model [110] . Experimental values have been obtained by using scattering parameters measurements on CPW of two different lengths L_1=1 mm and L_2=4 mm [111].

The 40 µm-width membrane show similar attenuation coefficient as the 60µm-width, around 5.5 dB/mm at 750 GHz, values still acceptable for a 1-mm-length TW photomixer. Regarding the effective index n_{THz} plotted Figure 3.19 (b), which is extracted from phase measurements, extremely sensitive to exact probes distances and calibration, experimental values are clearly less reliable at frequency greater than 300 GHz. At higher frequency, we can estimate by comparison with experimental results obtained at lower frequency and also with simulations that the error in phase measurement results in a relative error in the determination of the effective index $\Delta n_{THz}/n_{THz} \approx \pm 3\%$. Though, we can still conclude that effective index well below n_{THz}=1.9 are achievable with this technology but also that narrower membranes exhibit higher effective index which can be explained by a slight overlap of the CPW mode and the silicon substrate.

3.3. Traveling-wave-photomixer: Fabrication process

In this section we describe the fabrication process of a traveling-wave photomixer for the 780 nm and 1550 nm wavelength. The fabrication is summarized ina process flow diagram shown in in Figure 3.20. Initially, an epitaxial layer consisting of a GaAs substrate, a GaInP stop etch layer, and an LT-GaAs layer was transferred to a high-

resistivity silicon (HR-Si) wafer by means of adhesive bonding. The GaAs substrate was then subjected to wet-etching techniques to obtain access to the LT-GaAs layer, and the back reflecting was patterned onto it. Subsequently, a lower SiO_2 cladding layer and a Si_3N_4 layer were deposited, and both layers were patterned to establish the core and to expose the LT-GaAs layer, allowing the deposition of the coplanar waveguide (CPW). Once the CPW had been deposited, a top SiO_2 layer was applied, encasing the entire device. The upper SiO_2 cladding was selectively etched to access the contact pads used to bias the device, and the membrane was fabricated by etching the HR-Si beneath the CPW. Notably, the fabrication process for both wavelengths was almost identical, with only minor disparities concerning the optical waveguide construction. Further details pertaining to the device fabrication and the optimization of the optical waveguide for both wavelengths are provided in subsequent sections of the study.

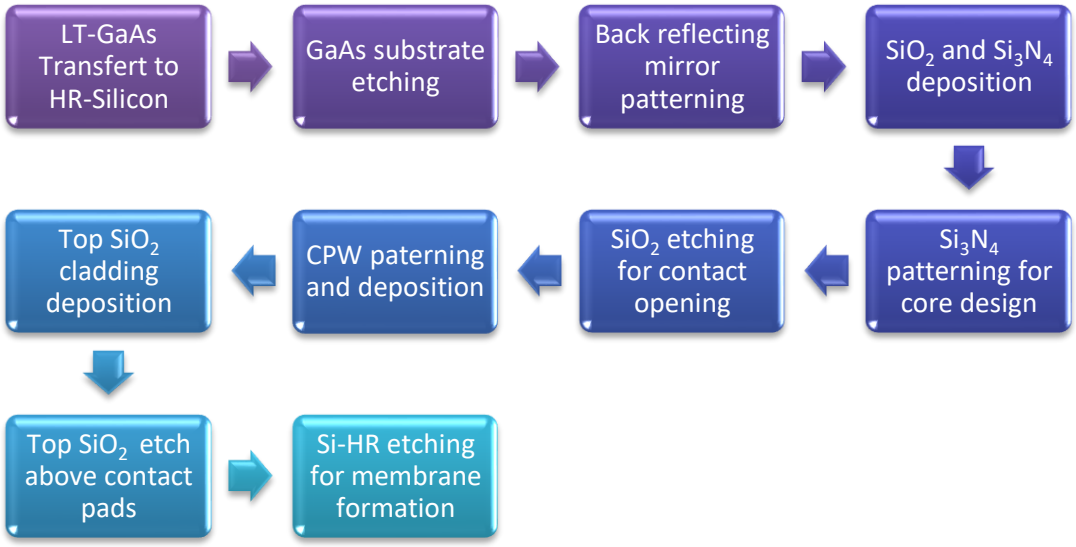

Figure 3.20: Schematic diagram illustrating the fabrication process flow of a traveling-wave photomixer. The process involves transferring the epitaxial layer onto a high resistivity Silicon wafer, etching the bulk substrate to access the LT-GaAs layer, patterning the back-reflecting gold layer, realizing the optical waveguide platform by pattering the Si_3N_4 core and the SiO_2 bottom cladding, depositing electrodes, encapsulating the device with a top SiO_2 cladding, etching the SiO_2 above the contacts, and finally etching the Si-HR membrane

3.3.1. LT-GaAs transfer to high resistive Silicon wafer

In order to realize the LT-GaAs membrane, it is necessary to transfer the LT-GaAs layer to a high resistivity silicon wafer, which can be achieved through wafer bonding. However, to ensure the success of this process, several steps must be taken beforehand. Initially, a layer of GaInP is grown on a 2-inch GaAs substrate, followed by the growth of an LT-GaAs layer. The epilayer is then cleaved to obtain a quarter of the wafer.Following an acid-based cleaning and surface treatment for the high resistivity silicon wafer and the epilayer, a resist (BCB) is spin coated on the two samples. After that the epilayer is transferred to the high resistivity silicon wafer through adhesive bonding. This technique is based on high mechanical pressure and high temperature allowing a bonding between the two BCB layers. A detailed section on this technique is presented in Appendix E-I

-BCB etching: After bonding, it is important to remove any remaining BCB from the HR-Si wafer to prevent contamination during subsequent fabrication steps. This is done using plasma reactive ion etching (RIE) in an OXFORD instruments Plasmalab80Plus system (Appendix E-II).The etching process was realized using a gas mixture of O_2 and CF_3.

-Substrate wet etch: We performed chemical wet etching on the substrate in order to access the LT-GaAs active region. The etching process consists of three steps: 1) A fast etching step based on a mixture H_2O_2, H_2SO_4 and H_2O. The aim of this step is to reach the proximity of the GaInP etch stop layer. 2) A slow etch step based on H_2O, H_2O_2 and NH_4OH. This step allows to etch the remaining several micrometers of GaAs allowing a visual verification of the GaInP. 3) A final step allows the access to the LT-GaAs through a fast etch of the GaInP in a hydrochloric acid solution (HCL). The details of these etching steps are shown in Appendix E-III.Figure 3.21shows a recap on the LT-GaAs transfer to the HR-Si wafer, summarizing the bonding and etching steps of the substrate. Note that the thickness of the layers inFigure 3.21 are not scale.

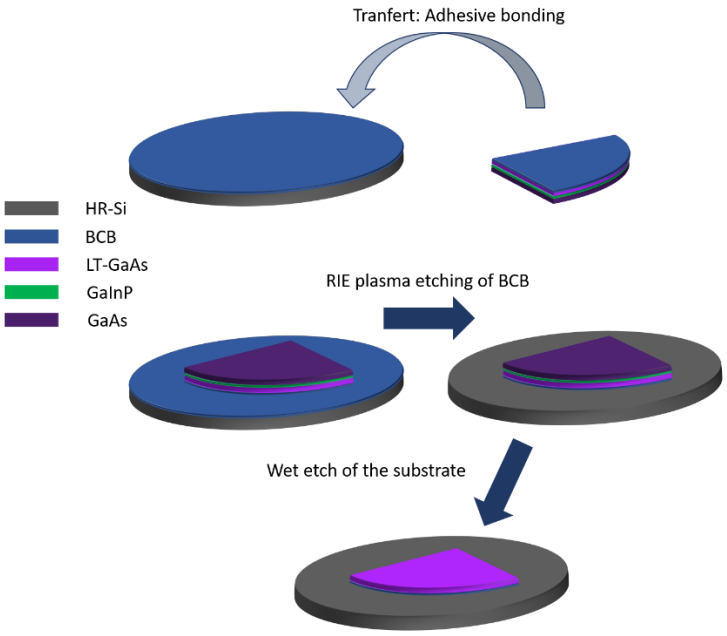

Figure 3.21: Schematic depiction of the LT-GaAs transfer to the HR-Si wafer showing the adhesive bonding step, the RIE etching of the BCB and the chemical of the GaAs/GaInP.

3.3.2. Fabrication of thedielectric waveguide platform

The first step in fabricating the device is the creation of a back-reflecting mirror under the grating coupler. In this process, a bilayer consisting of two different electro-sensitive positive resists (COPO EL13% and PMMA 3% 495 K) is spin coated on the sample and patterned using E-beam lithography (Appendix E-IV) to create a rectangular design for the back-reflecting mirror. COPO EL13 % stands for copolymer Ethyl lactate diluted for 13 % and PMMA 3% 495 K stands for polymethyl methacrylate. The bilayer is then developed in a solution of MIBK developer and IPA. The COPO EL13% resist is more electrosensitive than the PMMA 3% 495 K, resulting in an undercut profile shown in Figure 3.22. Gold is then deposited onto the whole sample using evaporation under vacuum. The principle of gold deposition using evaporation under vacuum involves the heating and vaporization of a high-purity gold target resulting in the condensation of the gold atoms onto a substrate in a low-pressure environment. Finally, the sample is placed in a resist stripper solution allowing to dissolve the resist bilayer and liftoff the gold, leaving only the gold pattern on the sample.

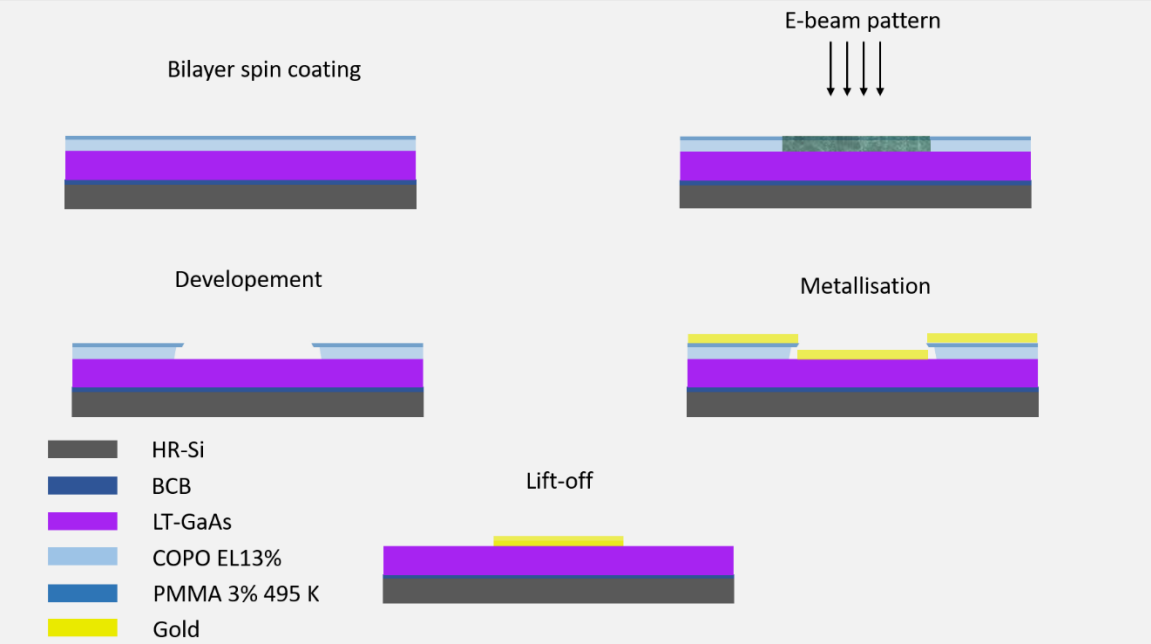

Figure 3.22: Schematic representation of a COPO EL13%/PMMA 3% 495K lithography and lift-off process after metallization.

- **SiO_2/Si_3N_4 deposition for the lower cladding and the core**

To fabricate the waveguide structure, a multilayered stack is formed on the sample using Plasma-enhanced chemical vapor deposition (PECVD) technique. Firstly, an SiO_2 layer is deposited as the lower cladding layer, followed by deposition of a Si_3N_4 layer as the waveguide core material. The PECVD machine used for deposition was from Oxford instruments of type Plasmalab80Plus system. For more information, the principle of Plasma-enhanced chemical vapor deposition is detailed in Appendix E-V. In such tools, in order to realize a deposition recipe, important parameters should be defined such as gas flows, chamber pressure, RF power, lower plate temperature and deposition time. The optimization aimed to achieve the highest material quality by minimizing the roughness and intrinsic optical losses. The propagation losses were measured on test waveguides, where the core was patterned and etched via RIE (Reactive Ion Etching) and followed by a deposition of a top SiO_2 cladding. Further details on the core patterning will be shown in the following section. The succeeding subsections describe the material analysis carried out in the study.

3.3.2.1. SiO_2/Si_3N_4compatible for 780 nm and 1550 nm wavelengths

- **SiO_2 with reduced roughness:**

Surface roughness is a crucial factor that can cause scattering and adversely affect the propagation losses of a material. To address this, a study was conducted by Funaki Bavedila and Christophe Boyaval on SiO_2 to reduce its surface roughness. The roughness is represented by R_q which is the root mean square average of the roughness profile ordinates and was measured using an Atomic Force Microscope (AFM). Roughness can be reduced either by optimizing the deposition parameters or by using CMP (Chemical Mechanical Planarization) which is a technique based on the combination of mechanical and chemical polishing. Generally, it is used to level the surfaces of silicon oxide, polysilicon, and metal layers in preparation for lithography steps. In order to analyze the roughness, an SiO_2 thickness of 1040 nm was defined (optimal coupling). All test samples were realized on a Silicon wafer on which 200 nm of gold were deposited by evaporation. First the power and the gas flows of a standard recipe (P_{RF} = 10 W, SiH_4/N_2O = 700 sccm/150 sccm, T=300ºC and P=1 T) were varied and no significant reduction on the roughness was measured (~ 5 nm). After that the pressure was reduced from 1 T to 0.5 T resulting in a reduction of the roughness from 5.45 nm to 2.3 nm. When treated with CMP the samples corresponding to the two pressures resulted in a roughness around 0.5 nm.

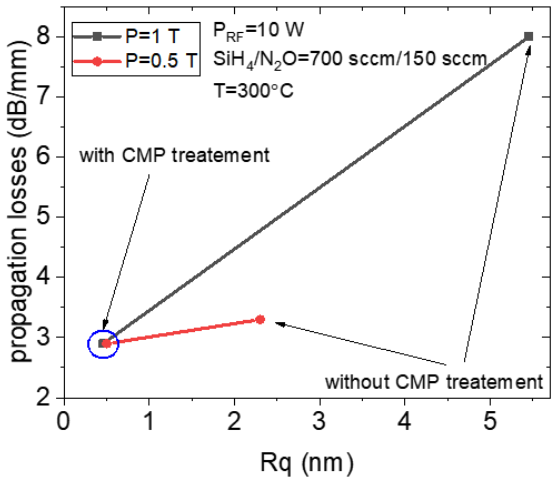

Figure 3.23: Propagation losses in a waveguide as function of the bottom SiO_2 cladding roughness. The SiO_2 was deposited for a pressure of 1 T and 0.5 T. The corresponding layers are also planarized using CMP.

Figure 3.23shows the propagation losses of waveguide fabricated on the previously studied SiO_2 layers. The propagation losses were measured using the cut-back method for the two chamber pressures, with and without CMP treatment. It can be seen that by reducing the chamber pressure from 1 T to 0.5 T, the propagation losses are reduced from 8 dB/mm to almost 3 dB/mm and after planarization, the results are corresponding to the two pressures are similar and close to 3 dB/mm. As a conclusion, no significant change in the propagation losses is observed for SiO_2 roughnesses under 2 nm. On the other hand, the latter are still relatively high which suggests that the losses may originate either from the proximity to the gold substrate or from absorption in the Si_3N_4 core. Note that the parameters of the deposited Si_3N_4 layer are defined as follows: P_{RF} = 10 W, $SiH_4/NH_3/N_2$ = 360 sccm/20 sccm/240 sccm, T=300ºC and P = 1 T.

- **Propagation losses for different SiO_2 thicknesses**

At this stage, the Si_3N_4 recipe is not yet optimized because the goal is to investigate the impact of the proximity of the fundamental mode to the gold layer. To this end, the propagation losses were measured for two different lower cladding thicknesses, namely 2100 nm and 1040 nm. Figure 3.24 displays the cut-back measurements of the optical losses for these two lower cladding thicknesses. Even though there is a significant

difference between the lower cladding thicknesses, the propagation losses of 5 µm wide cores are similar which suggests that the losses due to the gold substrate are negligible and are mainly due to scattering and absorption in the dielectric due to impurities. In both cases, the propagation losses were still high, making these waveguides unsuitable for integration into a TW-photomixer. As a result, further material study on the Si_3N_4 composition will be realized in the following section.

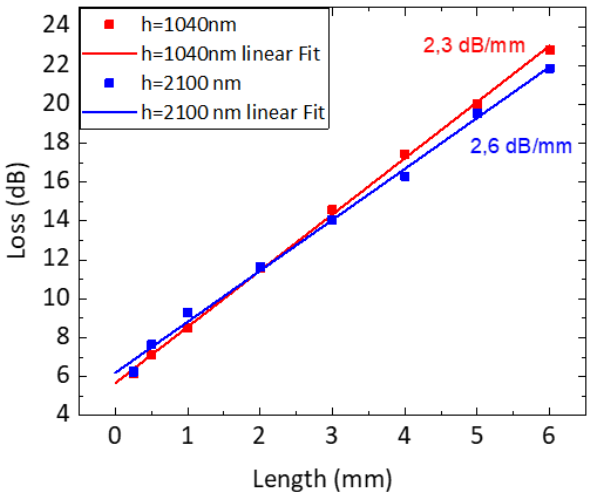

Figure 3.24: Cut-back measurements showing the optical losses as function of the waveguide length for two SiO_2 lower cladding thicknesses (2100 nm and 1040 nm)

- **Low loss Si_3N_4 compatible for 780 nm wavelength**

Once the cladding roughness was minimized (< 2 nm) and the propagation losses were measured to be around 2.3 dB/mm for a 1040 nm thick cladding, a study was conducted on the Si_3N_4 parameters. SiH_4 and NH_3 were used as the two gases. The propagation losses were measured for different SiH_3/NH_3 flow rates. The SiH_4 flow was fixed at 360 sccm and the NH_3 flow was increased from 20 sccm to 50 sccm. It was found that the propagation losses decreased from 2.3 dB/mm to 1.07 dB/mm as the NH_3 was increased as shown in Figure 3.25. Waveguides based on Si-rich materials exhibit higher losses at lower wavelengths due to the microstructure of the layers, which tend to have more defects due to the incorporation of both Si-H and Si-Si bonds[112]. Additionaly, Si-rich materials possess a higher absorption at $\lambda = 780$ compared to $\lambda = 1550$ nm. Conclusively, the

Si_3N_4recipe having higher flows in NH_3 was chosen for λ = 780 nm ($P_{RF} = 10$ W, $P = 1$ T, $T = 300$ºC, SiH_4 = 360 sccm and NH_3 = 50 sccm).

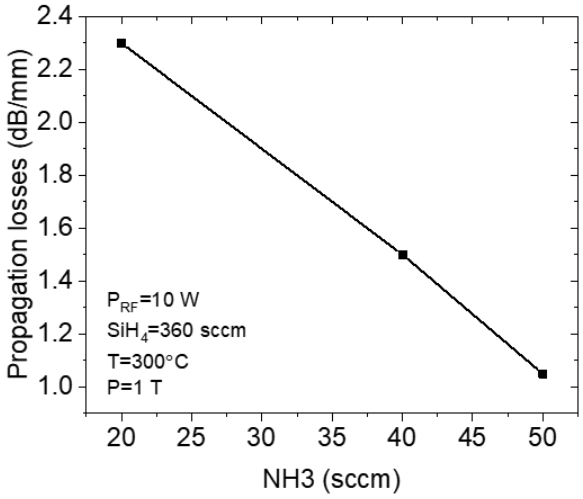

Figure 3.25: Propagation losses as function of the NH_3 gas flow while the SiH_4 flow was fixed to 360 sccm.

- **SiO_2/Si_3N_4 compatible for the telecom wavelength**

An analogous investigation was conducted on Si_3N_4 with the aim of refining the propagation losses in waveguides compatible for λ = 1550 nm. The experimental conditions were maintained at a temperature of 300ºC, an RF power of 10 W, and a chamber pressure of 1 T. The variables that were investigated were the gas flows. Table 3-1presents the propagation losses associated with the two distinct Si_3N_4 formulations. It is worth noting that these two recipes were already optimized for 1550 nm wavelength and the aim of this study is to compare between them.

		Propagation losses (dB/mm)
SiH_4/NH_3	360 sccm/20 sccm	0.61
$SiH_4/NH_3/N_2$	500 sccm/50 sccm/240 sccm	0.73

Table 3-1: Propagation losses for two Si_3N_4 recipes having different gas flows. The chamber pressure, the RF power and plate temperature are 1 T, 10 W and 300ºC respectively

The first formulation involves SiH_4 and NH_4 with respective gas flows of 360 sccm and 20 sccm, while the second formulation involves SiH_4, NH_3 and N_2 with gas flows of 500

sccm, 50 sccm and 240 sccm respectively. Despite the distinctive formulation of the two recipes, the propagation losses are comparable and lower than those at a wavelength of 780 nm. This dissimilarity in losses between the two wavelengths is primarily caused by the higher absorption in the Silicon at λ = 780 nm. Additionally, due to Rayleigh scattering, which is inversely proportional to the fourth power of wavelength $(1/\lambda^4)$[113], waveguides compatible for 780 nm illumination result in higher scattering. This can be seen by comparing the coupling to the waveguides. For λ = 780 nm, it was crucial to use an index matching gel or else the coupling losses would be way higher. Hence, the minimal variation in the composition of the material has a more significant impact on the propagation losses at 780 nm compared to 1550 nm wavelength.

Table 3-2shows a summary of the optimized recipies of SiO_2 and Si_3N_4 for the two wavelengths.

					Gas flows (sccm)		
		Chamber temperature (°C)	**Chamber pressure (Torr)**	**RF Power (W)**	**SiH_4**	**N_2O**	**NH_3**
780-nm device	**SiO_2 top and bottom cladding**	300	0.5	10	150	700	
	Si_3N_4 core	300	1	10	360		50
1550-nm device	**SiO_2 bottom cladding**	300	0.5	10	150	700	
	SiO_2 top cladding	300	1	10	150	700	
	Si_3N_4 core	300	1	10	360		20

Table 3-2: Optimized SiO_2 and Si_3N_4recipes for low losses at 780 nm and 1550 nm wavelengths.

- **Waveguide core patterning**

In this section, the waveguide core and other optical components such as the grating coupler, the MMI and the tapered cores are patterned by E-beam lithography. The pattern is realized on a high-resolution positive resist (CSAR 62). This resist acts as mask having the pattern of the desired designs. When developed, the Si_3N_4 is etched until the SiO_2 lower cladding.

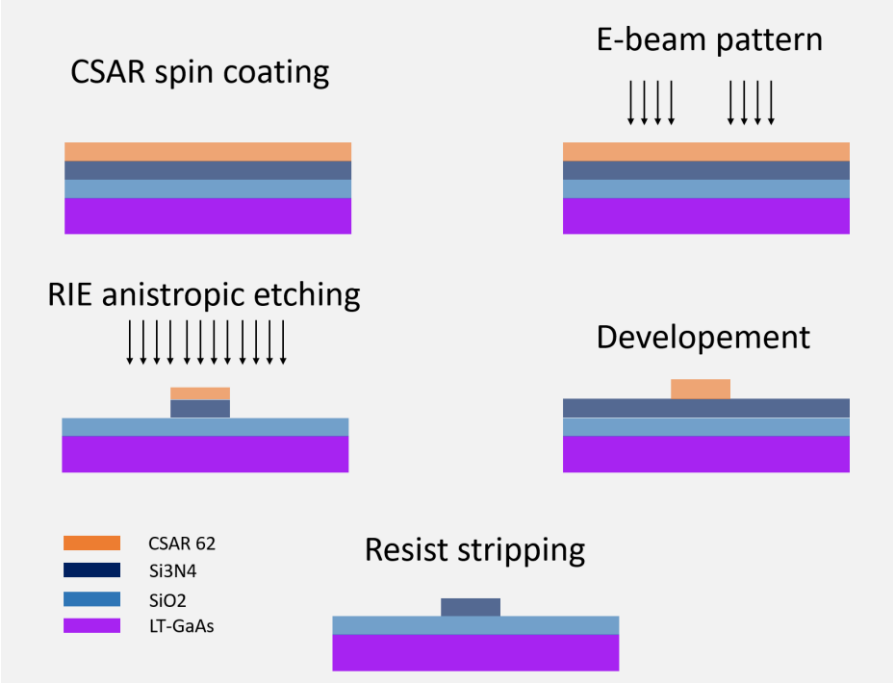

Figure 3.26: Schematic depiction of the core pattering using RIE technique.

Previously, we have seen that it is possible to etch a material using a chemical etching process, also known as wet etching. This type of etching has the advantage of being fast, but the more or less isotropic behavior of this technique can be considered a disadvantage in certain cases, especially for small patterns (on the order of micrometers). In this case, it is preferable to use RIE since this technique results in anisotropic etching due to the physical nature of the etching.Conclusively, the Si_3N_4 is etched using an RIE etching recipe based on CHF_3 and CF_4 gases. A simplified schematic representation of the etching process is shown in Figure 3.26. Figure 3.27 shows SEM images depicting the detailed steps to of the core patterning and etching. The details of the lithographic step and the etching process are presented in Appendix E-VI.As a conclusion, the etching was mainly

anisotropic, as the Si_3N_4 profile is perpendicular to the SiO_2 cladding and there was no significant shrinkage in the design dimensions.

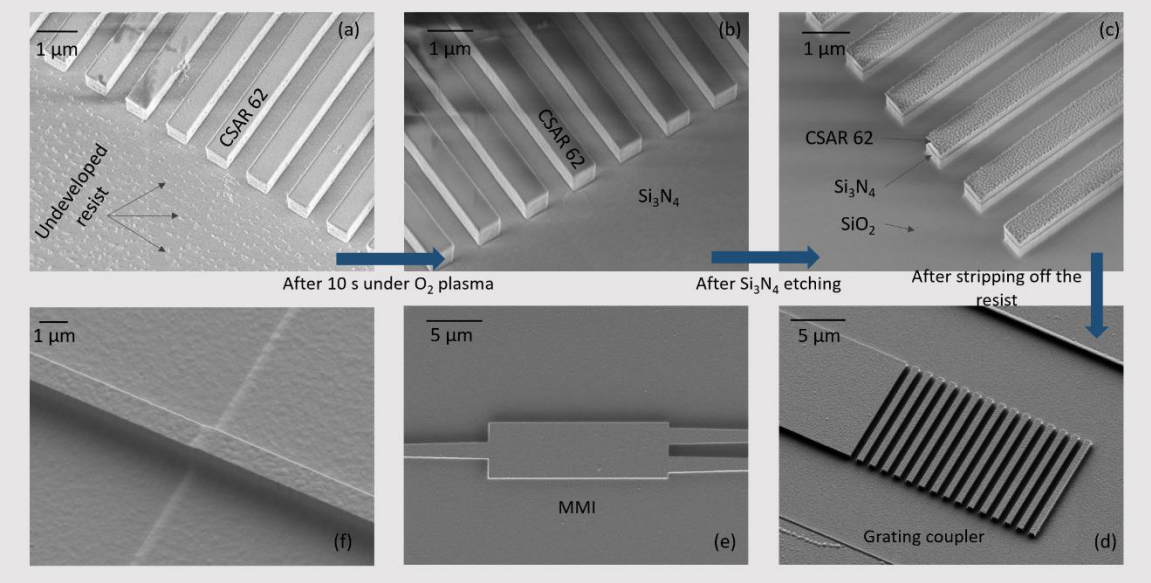

Figure 3.27: (a) and (b) show SEM images of the resist pattern above the Si_3N_4 layer. (c) show an SEM image after etching the Si_3N_4. (d), (e) and (f) show the grating coupler, the MMI and the core transition to active region after the resist stripping.

- **Bottom cladding patterning and etching for contact opening**

The bottom SiO_2 layers in both TW-photomixers designs (780 nm or 1550 nm) possessed a thickness that ranged from 500 nm to 800 nm, which required a high etch selectivity $\left(\frac{material\ etch\ rate}{resist\ etch\ rate}\right)$. The ICP-RIE (inductive coupled plasma - reactive ion etching) technique was chosen over the RIE technique due to its higher selectivity (AppendixE-VII). This etching step is necessary to expose the LT-GaAs active region,allowing for electrode deposition.Figure 3.28 (a) and (b) show the device after etching the bottom cladding at the beginning and end of the active region, respectively. In some cases, as shown inFigure 3.28(b), the sidewalls of the etched SiO_2 may contain byproducts due to chemical reactions between the etchants and the resist[114]. The latter can be cleaned by in an ultrasonic bath, but this may risk damaging some of the devices on the sample. The subsequent lift-off step of electrode metallization can also help clean any remaining debris from this step.

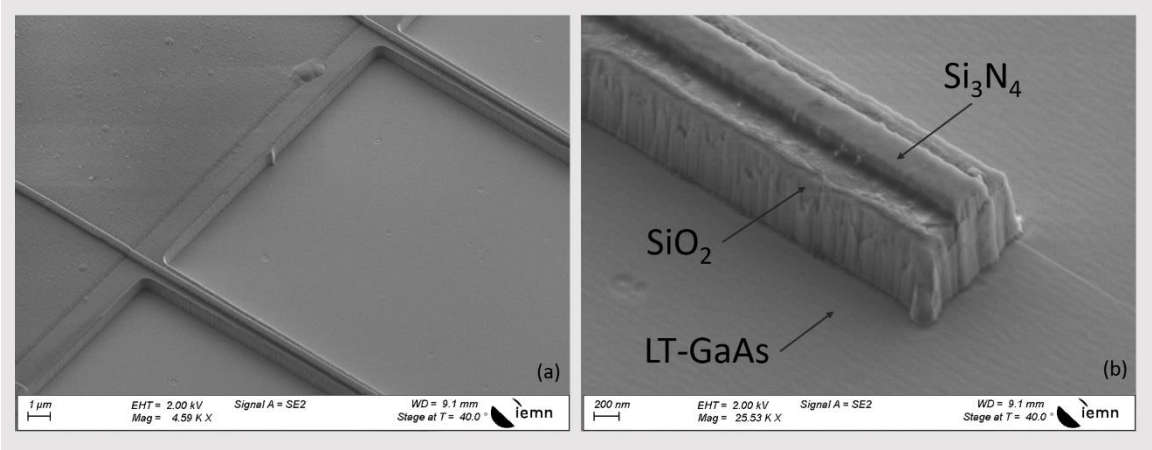

Figure 3.28:(a) SEM images showing the waveguide after etching the bottom SiO_2 at the beginning of the active region and (b) a zoom in at the end of the waveguide.

3.3.3. Electrodes and THz waveguides (CPW and CPS)

In this step, the same lithography and lift-off process that was used for the back-reflecting mirror is repeated. There will be two THz waveguide designs: CPW and strip lines or CPS. The CPS design is introduced since it allows a direct integration of the grating coupler and the tapered waveguide to the active region which results in reduced insertion losses. Before electrode deposition, the LT-GaAs is treated in a HCl 30% (Hydrochloric acid) solution to etch any possible oxides (GaAsO) on the surface.Figure 3.29shows the device after the lift-off step. Figure 3.29 (a) and (e) show an SEM image of the beginning of the active region. There are two different designs for the electrodes, one with the core directly entering between the metallic lines and the other with a tapered design where the core enters smoothly between the metallic lines. The aim of this design is to avoid optical losses due to a direct change in the mode profile when entering the active region. Meanwhile this design was not better than the first since part of the optical source will be absorbed in the LT-GaAs before arriving to the 2 µm interelectrode spacing where carriers are accelerated by the electric field.Figure 3.29 (b) shows the middle part of a device with a CPW design and Figure 3.29 (c) and (d) show contact pads at the end of the device compatible for the two different THz waveguides. Eventually, coplanar or CPS probes will be used to apply the bias voltage and collect the generated RF or THz waves. Note that all of the SEM images shown in this section or in previous sections correspond to either the 1550 nm design or the 780 nm design.

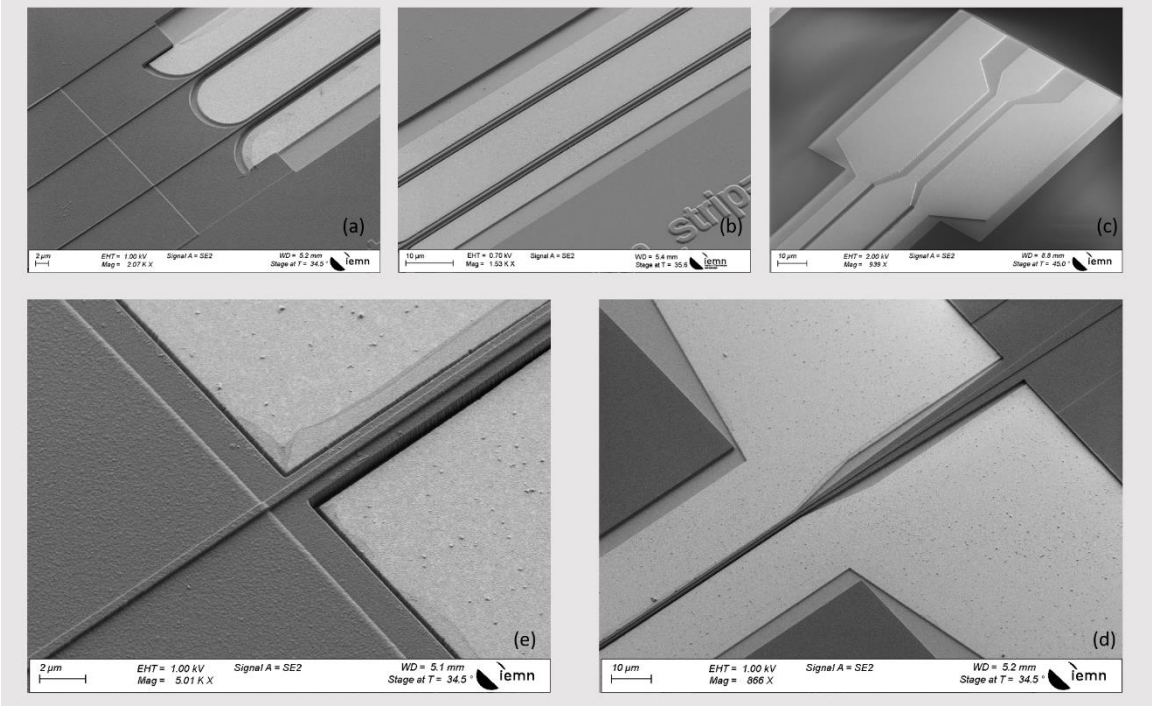

Figure 3.29: SEM images showing the waveguide after the lift-off step. (a), (b) and (d) shows the CPW design and (d) and (e) shows the CPS design.

- **Top cladding deposition**

An SiO_2 layer is deposited above the whole structureFigure 3.30 (a) shows a top view of the grating after the top cladding deposition. It is important to mention that, the spacing between two grating ridges and their thickness are of the same order. As a result, the deposition of the SiO_2 above the grating pattern was not conformal resulting in void gaps between the ridges. Figure 3.30(b) shows an inverted SEM image that corresponds to a FIB (Focused Ion Beam) cut of the grating coupler showing the triangular shaped void gaps in the periodic structure of the grating. Figure 3.30 (d) shows a zoom in on the FIB cut where the notched Si_3N_4 is visible. As presented previously, these void gaps were considered in the simulation of the grating.

After the SiO_2 deposition, an ICP-RIE etching step was realized to expose the contact pads at the end of the device.

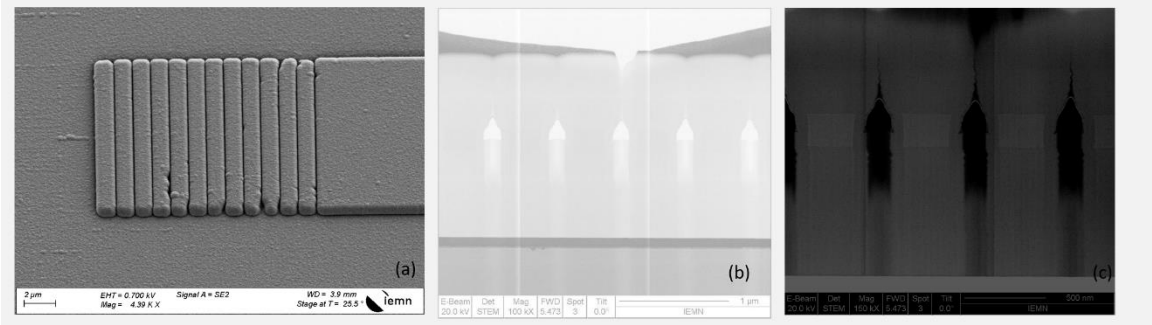

Figure 3.30:(a) SEM images showing a top view of the grating coupler and (b), (c) a side view of a FIB cut of the grating coupler.

3.3.4. HR-Si etching for membrane realization

LT-GaAs membranes are patterned by etching the silicon wafer (thickness~200µm) by means of Bosch process deep reactive ion etching (see [115] for example). This step was realized by Fuanki Bavedila, a process engineer working in the Photonic THz group. In Figure 3.31 is shown a SEM view of a cross section of 45-µm-wide LT-GaAs membrane-supported photomixer including the optical waveguide patterned within the CPW slots.

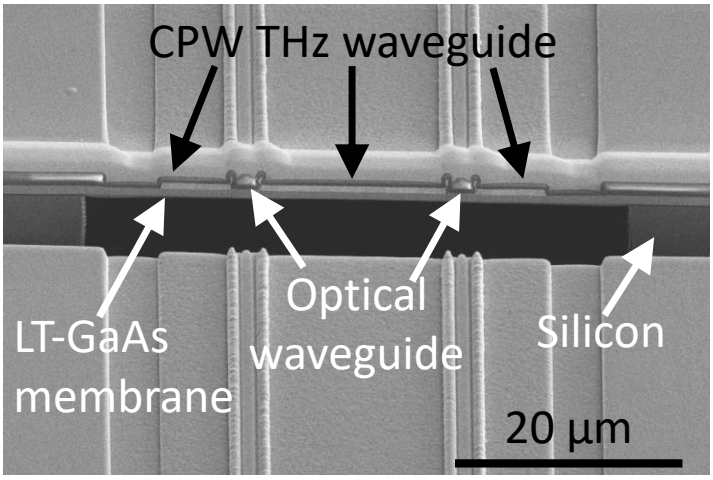

Figure 3.31: SEM view of a FIB-cut cross section of the membrane-supported TW photomixer.

- **Remarks on the device fabrication process**

During the fabrication of the TW-photomixer compatible for 780 nm-illumination, two separate versions were realized. One version was conducted on a bulk

material, while the other was carried out on a membrane. A slight modification was made to the etching pattern of the SiO_2 used to expose the electrodes. For the membrane devices, the top cladding was selectively etchedonly above the contact pads, and the metallic lines were encapsulated with SiO_2 as depicted inFigure 3.32 (a). On the other hand, two runs were fabricated for devices on bulk. The first had a similar configuration to what is shown in Figure 3.32 (a) while second had a top cladding also etched above the metallic lines as shown in Figure 3.32 (b). Theoretically this arrangement allows for better confinement of the fundamental mode above the LT-GaAs region. The etching step was followed by a prolonged over-etch in order to create spacing between the metallic lines and the optical waveguide, as well as to ensure proper etching above the metallic lines (Figure 3.32(c)and (d)). However, this over-etching resulted in the pulverization of gold from the metallic lines on the cladding sidewalls, leading to optical losses due to light scattering and absorption. To address this issue, RIBE (Reactive Ion Beam Etching) was employed as a purely physical etching process that bombarded the etch sidewalls with Argon ions enabling the etching of the thin pulverized gold layer.

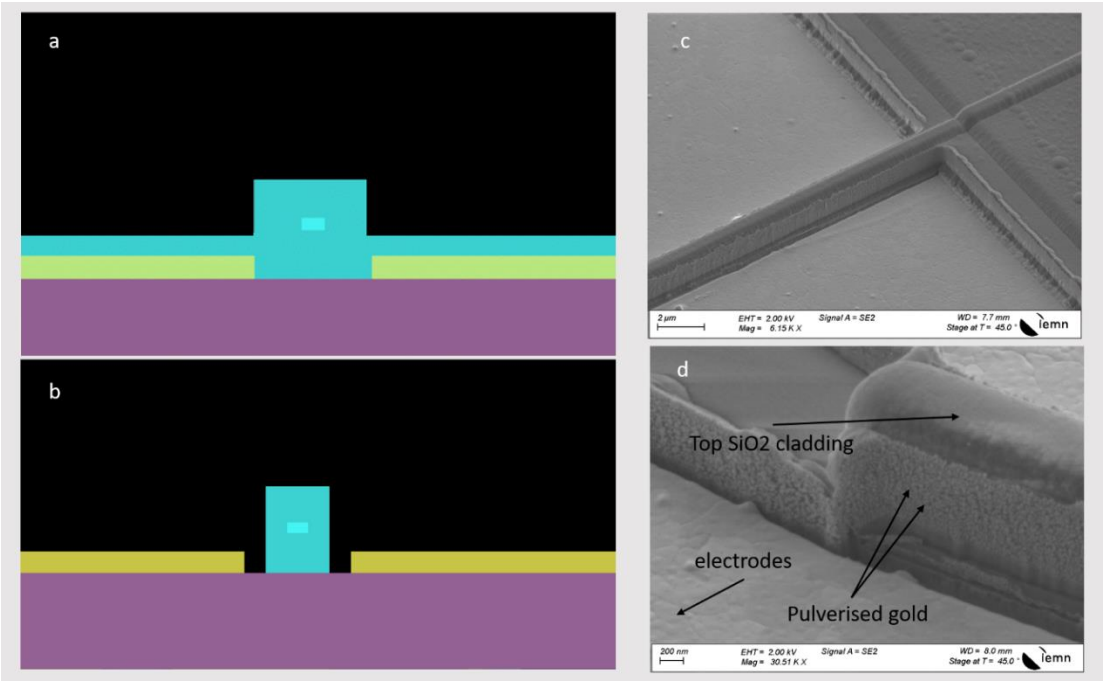

Figure 3.32: Schematic representation of the two top cladding designs. (a) The top cladding was either etched above the contact pads as it encapsulated the metallic line or (b) etched above the contact pads and the metallic lines. (c) and (d) show SEM images of the pulverized gold on the side walls of the etched top cladding.

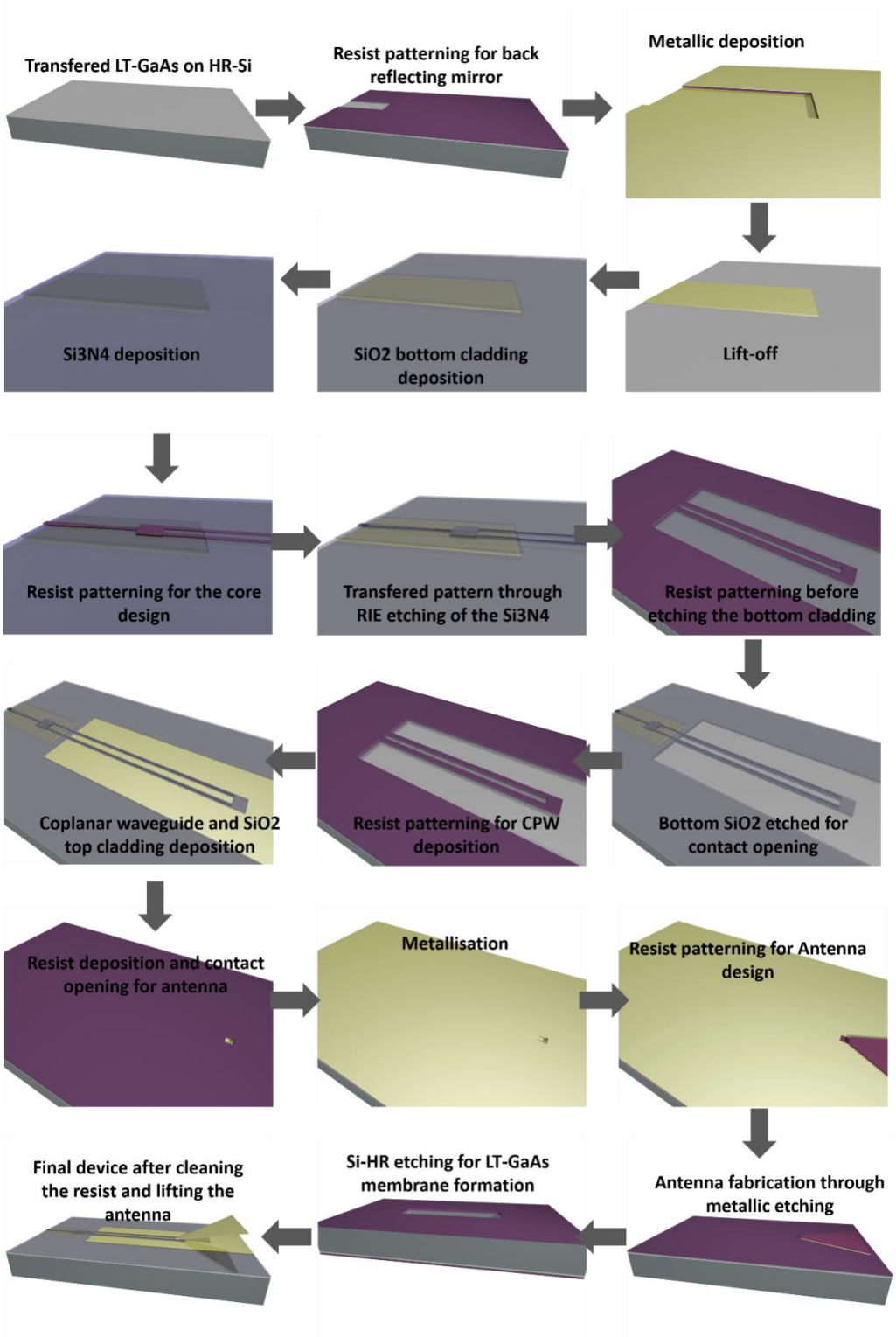

Figure 3.33: Schematic representation showing a summary of the fabrication steps of the device. The possibility of fabricating an antenna is also shown

Figure 3.33 consists of schematic representations showing a summary of the fabrication process. In this figure, we show the possibility of fabricating an antenna at the output of the device allowing the emission into free-space.

3.4. Optoelectronic characterization

Typically, on the same process wafer, test samples are fabricated to measure physical parameters such as propagation losses, coupling losses, taper losses, and MMI efficiency. These parameters are first measured after the process (as described in sections 3.1 and 3.2) and then dc photoresponse measurements are conducted on the devices to evaluate the optical absorption as it relates to different dimensions such as device length, core width, lower cladding thickness, and measurements with or without a top cladding. Finally, frequency response measurements are conducted on the devices that performed best in the dc measurements. In this section, we will present the photoresponse and frequency response measurements for devices on bulk and on membrane.

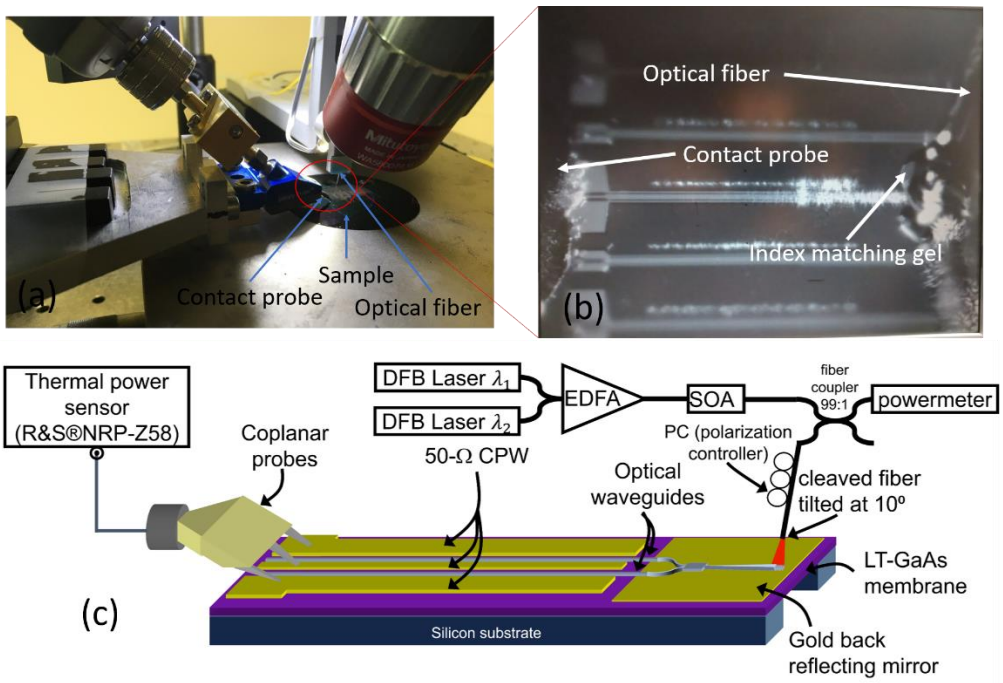

Figure 3.34: (a) Photograph of the sample showing the contact probes and the optical fiber. (b) Photo of a biased CPW-TW photomixer showing the optical fiber, the index matching gel allowing higher optical coupling and the contact probes biasing the device. (c) Representation of the frequency response measurement setup up to 110 GHz. A Labview interface allows a frequency sweep of the lasers and saves the output power from the thermal power sensor for each frequency. The SOA allows an optical amplification up to 400 mW.

The measurement setup for the devices on membrane is presented inFigure 3.34(a) that shows a photo of the sample with the contact probes and the optical fiber. The electrical characterization of a 1 mm-long-TW photomixer has been performed up to 100 GHz by using a 780-nm Toptica TeraScan system and a Toptica 780-nm SOA amplifier. The device is illuminated by the optical beatnote through a cleaved-fiber as shown in Figure 3.34(b).The output power is collected by using a coaxial-coplanar probe and sent to a thermal power sensor (R&S®NRP-Z58).A Labview interface developed by Vanessa Avramovic sweeps the laser beating frequency up to 110 GHz and records the output power from the thermal power sensor as function of the frequency. The interface also saves the photocurrent during the frequency sweep to assess its stability.Figure 3.34 (c) shows a representation of the full measurement setup.It is worth noting that in the measurement setup of the devices on bulk, a spectrum analyzer was used instead of the Thermal sensor.

3.4.1. On Bulk

3.4.1.1. DC photoresponse measurements

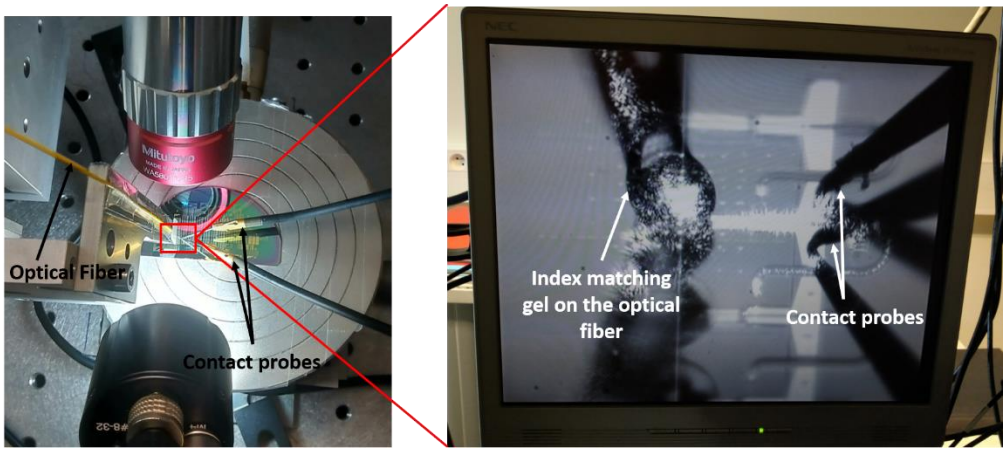

Figure 3.35: DC measurement setup showing a closeup on the biasing probes the fiber and a CPS device. The index matching gel can be seen on the edge of the fiber.

This section discusses the results of dc photoresponse measurements, which were conducted on a variety of cells fabricated on a single ½ 2 inch bulk wafer, and replicated multiple times. As previously mentioned in the fabrication process, two runs of TW-photomixers on bulk were fabricated. Figure 3.36 presents a cross section depiction of the

TW-photomixer in the two runs. In Run 1 the top cladding was only etched above the contact pads at the end of the device to allow device biasing. Note that, in this first run, several complications in the fabrication were encountered such as a huge shift in the lower cladding thickness due to a variation in the PECVD parameters resulting in huge insertion losses. Additionally, misalignments in some lithographic steps were also observed, however we managed to extract valuable information from some devices that were less affected by the misalignment. In this run, the main idea was to verify if thicker metallic waveguidesresult in higher overlap with the optical mode leading to higher optical losses. This was verified by realizing dc photoresponse measurements for devices having different electrode thicknesses. The measurements were performed on CPS designs, as these designs can be easily biased using only two contact electrodes as shown inFigure 3.35which represents the measurement setup.

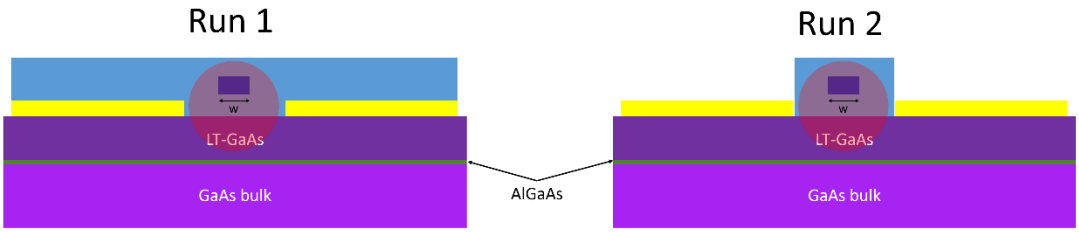

Figure 3.36: Representation of a cross section of two fabricated runs of fabricated TW-photomixers on bulk.

The first step was to measure the photocurrent by illuminating the devices with a cw laser of 8 mW at 780 nm wavelength and applying a bias voltage up to 20 V. The photoresponse can then be calculated in two different ways: 1) by dividing the photocurrent with the optical power at the fiber output (8mW) and 2) by dividing the photocurrent with the resulting optical power after the grating coupler and the taper. Here we consider the second technique since it evaluates the intrinsic behavior of each device without considering the effect of the insertion losses. Figure 3.37 shows the photoresponse of two photomixers having different electrode thicknesses (100 nm and 400 nm) as a function of the core width. It can be observed that the two devices possess a similar photoresponse that reaches a maximum between 30 mA/W and 40 mA/W. These results validate the

negligible effect of the metallic lines on the optical losses as previously shown in FDTD and FDE simulations.

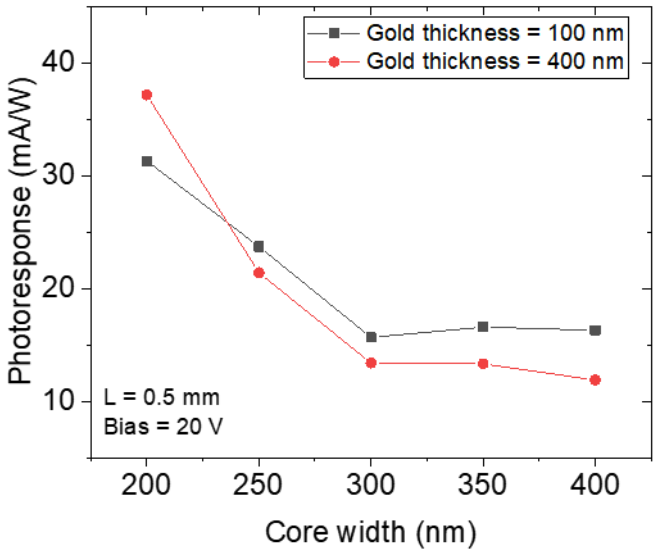

Figure 3.37: Photoresponse of as function of the core width in a photomixer having an electrode thickness of 200 nm (black) and 400 nm (red).

As a result, in the second run the thickness of the metallic lines was set to400 nm in order to reduce ohmic losses and the top cladding was etched above the metallic lines in order to allow better mode confinement only above the LT-GaAs.First, the photocurrent was measured as a function of the bias voltage.Figure 3.38 shows the dark current and the photocurrent of a 0.7 mm long TW-photomixer versus the bias voltage. It can be observed that the I-V behavior of the device is symmetrical with a large contrast between the dark current and the photocurrent which reached a maximum value around 50 µA at a bias voltage of 20 V and an optical power of 8 mW. It can also be seen from the I-V characteristic curve that at high bias voltage, the photocurrent presents a superlinear behavior hinting to a prolonged electron lifetime of the electrons.

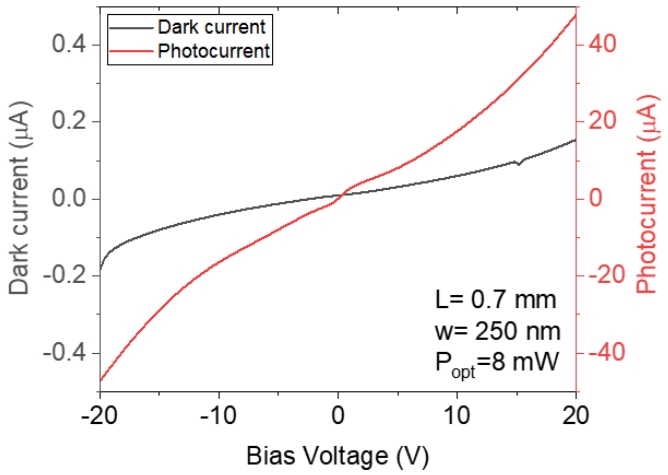

Figure 3.38: I-V characteristics of a 0.7 mm long CPS TW-photomixer having a core width of 200 nm. The device is illuminated by an optical power of 8 mW.

A study is realized on the device's photoresponse in order to validate the optical, measurements and simulations of the absorption in the LT-GaAs realized in section (3.1.2). CPS cells were replicated four times and the fabricated dimensions are shown inTable 3-3.

Core width (nm)	100	150	200	250	300	350	400
Device length (mm)	0.1		0.3	0.5		0.7	1

Table 3-3: Core width and device length of the characterized devices.

The results shown inFigure 3.39, present the mean photoresponse as a function of device length for different core widths, calculated by dividing the photocurrent with the optical power after passing through the grating coupler and the taper. As can be seen, in some cases the error is relatively high, mainly due to the small number of measured samples. It should be noted that even though there were four replicas of each device, for most cases, at least one device was damaged. In some cases where there are no error bars and there is a yellow "x", only one device was measured, since all the other replicas presented fabrication defects. Meanwhile, valuable information can still be obtained despite uncertainty.

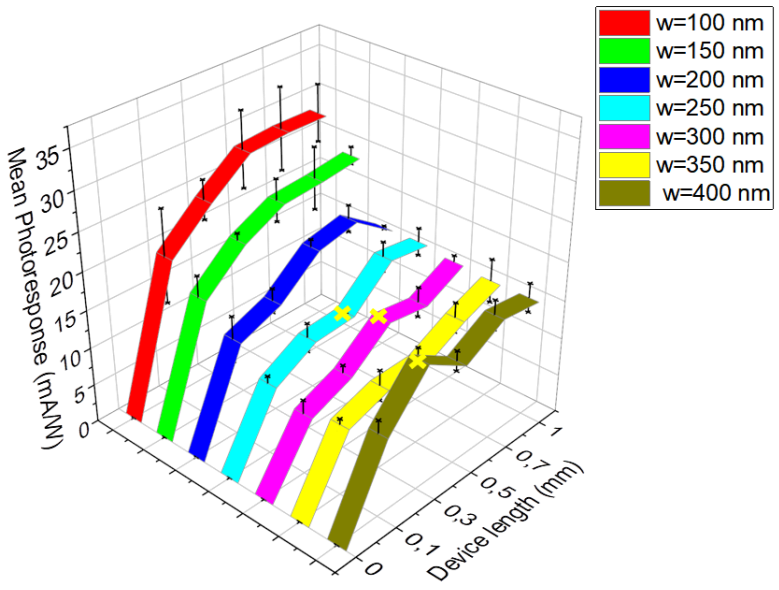

Figure 3.39: The graph shows the average photoresponse of devices with the same core width based on the device length. The photocurrent was divided by the optical power at the active region after it passed through the grating coupler and taper.

Devices with 100 nm and 150 nm core widths present full absorption of the optical mode between 0.3 mm and 0.5 mm. Meanwhile devices with 200 nm and 250 nm core width reaches full absorption between 0.7 mm and 1000 mm. For the core widths 300 nm and 350 nm, it can be seen that there is no full absorption of the optical mode before 1 mm length. For the 400 nm core width, no clear information can be obtained, but based on the two previous core widths, it is expected to behave in the same manner. It can also be observed that the uncertainty (yellow x) decreases as the light is absorbed faster since there is less chance of defects in shorter devices. As expected from the optical measurements of the propagation losses/absorption in section (3.1.2), the highest photoresponse/absorption (~28 mA/W) corresponds to the devices having the lowest core width (100 nm). For higher core widths (except for 150 nm), the photoresponses are around 15 mA/W. These values are comparable to photoresponses calculated from vertically illuminated lumped-element photomixers and represent the best we can get if we manage to design devices having insertion losses that tends to 0. Surprisingly, these results are much lower than the measurements in the first run. For the same device dimensions (L = 0.2 mm and w = 200 nm), a photomixer from the first run possess a

photoresponse around 2 times higher than the second run. In fact, the etching of the top cladding above the metallic lines turned out to be detrimental for the mode propagation and resulted in high losses due to the roughness of the side walls of the etched SiO_2.
Since in this second run, no technological problems were encountered, it is convenient to characterize the full behavior of the device, by calculating the photoresponse based on the power at the optical fiber output (8 mW). As a result, the photoresponse would range between 4 and 6 mA/W which is considered very low due to the huge insertion losses of the device.

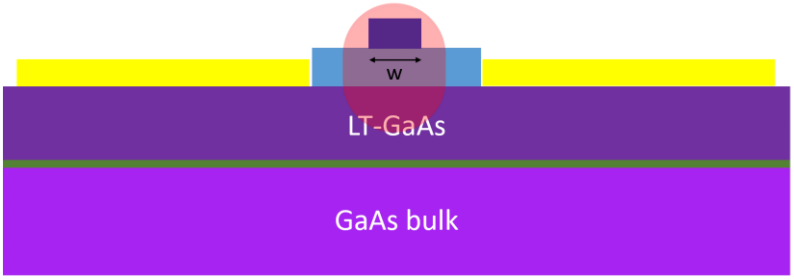

Figure 3.40: TW-photomixer design without a top cladding for the dielectric waveguide.

It is noteworthy to mention that photoresponse measurements were conducted also prior to the top cladding deposition since the electrodes were accessible. The coupling losses are unchanged with or without the cladding since the gel has the same index as the top SiO_2 cladding. However, when the fundamental mode enters the active region it will be in an assymetric structure (air/Si_3N_4/SiO_2) as shown in Figure 3.40. This results in the fundamental mode not being centered in the core and shifting slightly towards the active region, leading to a higher photoresponse reaching a maximum of 18 mA/W (the photoresponse was calculated based on the 8 mW optical power). Regrettably, the photoresponse is not steady and tends to decrease, reaching the same values with the top cladding deposited. This can be explained by the gel moving towards the active region through surface tension, eventually covering the entire waveguide.

To conclude, previously the aim was to design long devices reaching 1 mm however due to the high dependency of the mode propagation on the technological process, it would be more convenient to define lengths under 0.7 mm and core widths

between 200 nm and 300 nm allowing fast absorption and lower insertion losses. Moreover, in order to avoid additional optical losses due to the sidewall roughness of a reduced top cladding, it is preferable to etch the top cladding only above the contact pads. The top cladding thickness can also be reduced. This would result in a fundamental mode that possess higher overlap with the active region.

3.4.1.2. Frequency response measurements:

The frequency response of these devices is characterized in the sub-THz range 0-67 GHz. Due to low photoresponse and to avoid low signal-to-noise ratio (SNR), only the CPS designs were measured to prevent extra optical losses from the MMI and the taper in a CPW design. As a result, the losses in the CPS waveguides were measured by Vanessa Avramovic and were found to be around 1 dB/mm at 67 GHz which is still considered acceptable in this frequency range.The photomixing measurement setup is similar to what ispresented inFigure 3.34, but the output power is measured by a spectrum analyzer. Figure 3.41 displays the generated and calculated output power from the theoretical circuit model for two devices with different dimensions: (a) one having a length of 0.3mm and a 150 nm wide core and (b). another having a length of 0.7 mm and a 250 nm wide core The dimensions were selected based on the photoresponse measurements which showed that both configurations resulted in a total absorption of the optical power at their respective lengths. In order to maximize the generated power, the two devices were biased at 20 V even though an electron velocity saturation was reached.Then they were illuminated at 300 mW resulting in a photocurrent around 1.15 mAfor L = 0.3 mm and 1.3 mAfor L = 0.7 mm. The theoretical model aligns well with the measured results with a deviation of 3 to 4 dB. The optical absorption in the simulation model was defined using the values obtained from the optical transmission between the input and output grating coupler. This discrepancy between the simulation and the experiment may be due to the fact that a part of the optical power was not only absorbed in the LT-GaAs but also scattered by the roughness of the cladding sidewalls. As expected from the simplified model shown in section (2.1), the longer device (0.7mm) exhibits an earlier 6 dB roll-offaround 57 GHz compared to the shorter device (0.3mm) which is expected to reach the 6 dB around 111 GHz. It is important to note that the index of the sub-THz wave in these frequency ranges was measured to be around 2.7 on bulk.

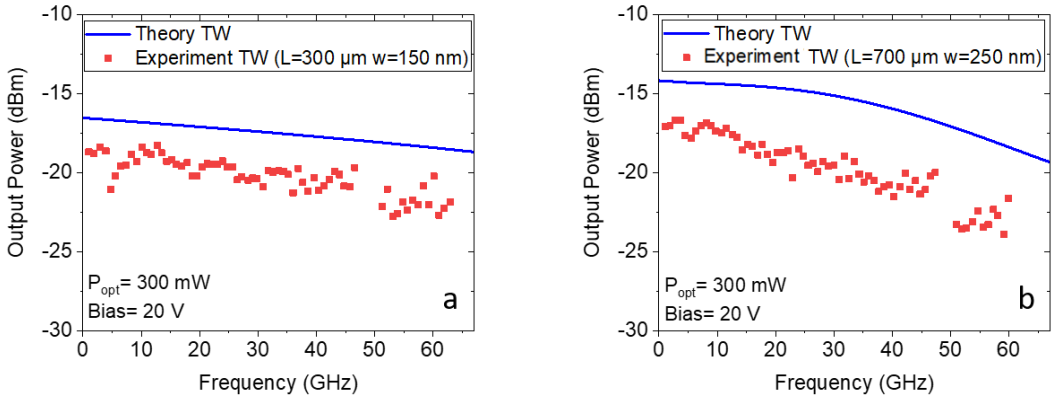

Figure 3.41: Theoretical (line) and experimental (symbols) frequency response of a (a) 0.3 mm long and a (b) 0.7 mm long TW-photomixer. In the two cases the bias was at 20 V and the optical power at 300 mW resulting in a dc photocurrent of I_{dc}=1.15 mA and 1.3 mA for L=0.3 mm and 0.7 mm respectively.

Now that the frequency response characterization was realized, Figure 3.42 presents dynamics of the device in terms of optical power. From this figure we can conclude a linear relation between the photocurrent and the optical power and a quadratic relation between the generated RF power and the optical power. Moreover, this also shows the capability of such devices to absorb high optical powers reaching 300 mW.

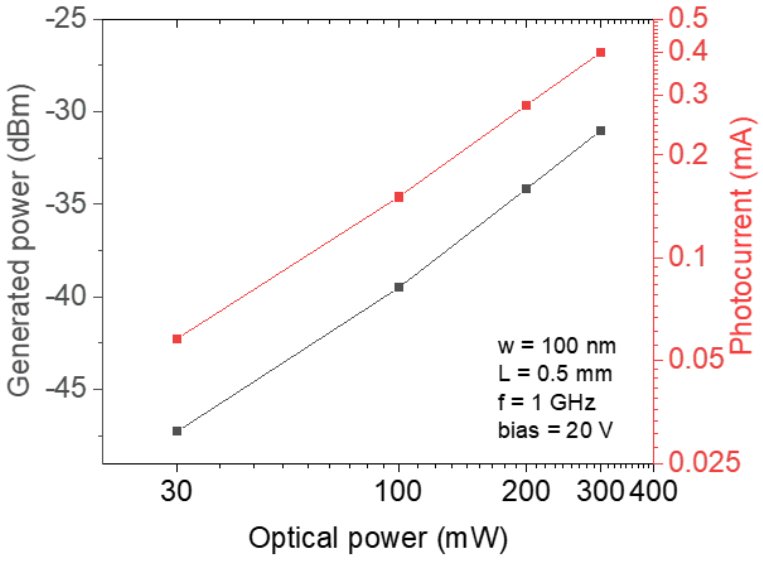

Figure 3.42: Photocurrent and generated power as function of the optical power.

As a conclusion, these results are still weak mainly due to high insertion losses and the optical losses due to the sidewall roughness of the top cladding. However, we managed to prove the necessity of the membrane in the case of TW-photomixer reaching a 1 mm length.

3.4.2. On membrane

3.4.2.1. Frequency response

Figure 3.43illustrates the frequency response of a 1 mm long CPW-TW-photomixer up to 100 GHz. It is worth noting that the top cladding design is similar to run 1 for devices on bulk. It can be seen that the output power is very low despite a large optical pump (maximum P_0 =400 mW, limited by our set-up), due to a low photoresponse and dc photocurrent (I_{dc}=0.5 mA and bias = 10 V) on this sample. However, the experimental frequency response clearly shows a transition between a lumped-element and a traveling behavior around 50 GHz, as predicted by the simplified model. As for the theoretical frequency response for front-side illumination, it is also plotted (in dashed) to highlight the negative effect of phase mismatch between optical and THz waves for large size photomixers. Conclusively, despite the low output powers due to high insertion losses we managed to prove a TW-behavior in these photomixers in the frequency range 0-100 GHz. The following chapter will discuss the adaptation of such devices for 1550 nm wavelength. Normally, the optical waveguide platform is more compatible to the telecom wavelength.

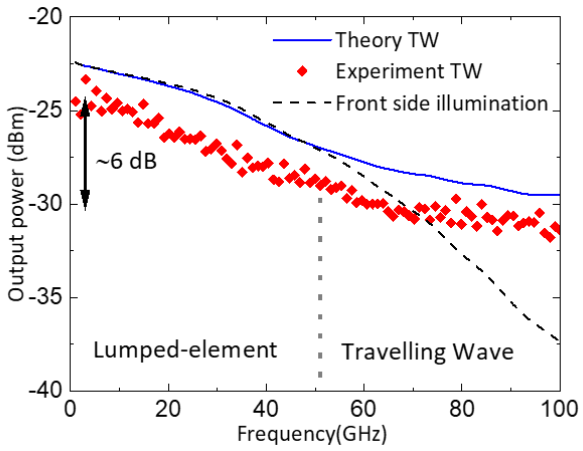

Figure 3.43: Theoretical (line) and experimental (symbols) frequency response of a 1-mm-long TW photomixer at 10 V bias and an optical power P_0=0.4 W resulting in a dc photocurrent I_{dc}=0.5 mA. In dash line is also plotted the theoretical output power assuming a front side illumination (obtained by using our model with $n_{THz} = 0$).

Conclusion

In this chapter, first we presented the optimization of the dielectric and THz waveguides parameters for integration in the TW-photomixer. After that, we presented a detailed study on the complex fabrication process of the device comprised of at least 5 lithographic steps. The optoelectronic characterization showed thatthe major issue of these devices remains in the compatibility of the waveguide platform with the 780 nm wavelength.The optical properties (coupling losses/propagation losses) of the waveguides were not stable between several runs. This was due to the fact that we were using an open service PECVD machine that was not always in stable conditions along the time span of this PhD and there were several delays in the maintenance due to COVID-19 lockdowns. Moreover, the necessity of the index matching gel was one of the most constraining points. However, we have proved that it is possible to reach propagation losses as low as 1 dB/mm through the use of CMP (Chemical Mechanical Planarization) technique.Lower propagation and insertion losses are only possible for PECVD depositions at higher temperature (> 300ºC) which is not compatible with III-V materials. Meanwhile, future devices can be fabricated using the CMP technique only on the SiO_2 layer above LT-GaAs. This would result in plausible insertion losses. It is also worth noting that a new

PECVD machine with industrial properties will arrive at the IEMN next year. This machine will allow the possibility for Si_3N_4 depositions which islikely to reduce the absorption at the 780 nm wavelength. To conclude, even though the generated power was very low due to the reason cited above, the 6-dB roll-off signature of a TW-photomixer have been demonstrated for the first time. We have also shown that if the insertion losses were negligible these devices reach higher photoresponse values (40 mA/W) than those of LT-GaAs based vertically illuminated photomixers. By utilizing a thinner top cladding, it is possible to induce a shift in the position of the fundamental mode towards the active region, leading to an increase in the photoresponse via enhanced absorption. In upcoming devices, the implementation of surface treatment through CMP technique or the utilization of the PECVD apparatus can effectively decrease the insertion losses to attain realistic levels, ranging between 2.5-3.5 dB. With such insertion losses and knowing that these devices exhibit high capability to handle optical power of up to 400 mW and they possess optimal waveguide dimensions allowing index matching, they are able to reach the microwatt level at 1 THz.

Chapter 4: Traveling wave photomixer compatible for 1550-nm wavelength illumination

Introduction:

This chapter presents the same TW-photomixer designs as previously shown, but adapted for 1550-nm wavelength illumination. The modifications will involve adjusting the size of the optical waveguides and the semiconductor choice. The LT-GaAs is one of best candidates since it is well known for its sub-picosecond lifetime and its compatibility for high frequency applications however, in the previous chapter we used LT-GaAs annealed at 580ºC which is optimized for 780-nm illumination and is not suitable for a 1550-nm laser source as its absorption at this wavelength is much lower. The focus of this chapter is on the subject of enhancing the LT-GaAs absorption at 1550 nm by briefly studying the defect dependent sub-band gap absorption in LT-GaAs. This has been tested in micro-cavity photomixers to evaluate its ability to generate high frequency signals, before finally being integrated into TW-photomixers. It is important to mention that at these wavelengths, the availability of a wideband cw laser source (1510 nm-1630 nm) made it easier to study and characterize optical components such as the grating coupler, ring resonators for group index measurements and to investigate the absorption as function of the wavelength for various waveguide configurations. Finally, DC and AC electrical characterization will be analyzed.

4. Traveling wave photomixer compatible for 1550-nm wavelength illumination: modeling and characterization

4.1. Sub-band gap absorption in LT-GaAs ($E_{photon} < E_g$)

In the previous chapter, the LT-GaAs was defined as the active region for the TW-photomixer due to its compatibility to the 780 nm wavelength and especially, due to its high dark resistivity and sub-picosecond lifetime allowing the generation of frequencies up to the THz region. At the telecom wavelength, the absorption in the LT-GaAs is much lower and is only possible through mid-gap energy levels, however this should not change the sub-picosecond carrier nature in the material. As a result, we decided to use the LT-GaAs as the active region for the 1550 nm wavelength TW-photomixer. In this section we will discuss the LT-GaAs absorption at λ = 1550 nm and we will present the main factors allowing to increase this absorption.

In order to follow up the study on LT-GaAs shown in Appendix A, we will refer back to the energy band diagram shown inFigureA.2. In reference [116], an experiment using deep-level transient spectroscopy observed a trap at 0.65 eV below the conduction bandedge and identified it with the As_{Ga} antisite defect. In fact, it turned out that these As_{Ga} antisites exist as neutral deep donors $(As_{Ga})^0$ that cannot capture electrons and they exist also as electron acceptors $(As_{Ga})^+$. Depending on the growth and annealing temperatures, the concentration of active $(As_{Ga})^+$ recombination centers can be $(0.3 - 3) \times 10^{18}$ cm^{-1}[117]. In ref.[118], they show a clear relation between the annealing temperature and the sub-band gap absorption. Figure 4.1 show the absorption spectra of an LT-GaAs layer annealed at different temperatures. It is observed thatthe sub-band gap absorption increases for lower annealing temperatures. In the following, this subject will be part of an optimization of the absorption of LT-GaAs at 1550 nm illumination.

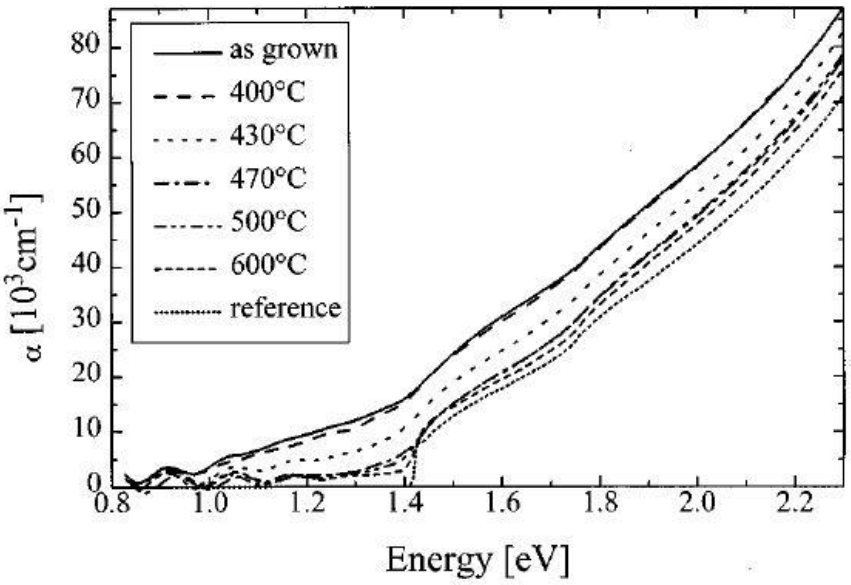

Figure 4.1: Absorption spectra of LT-GaAs annealed at different temperatures compared to a reference sample and an As grown sample [119].

In ref.[120], they excited an LT-GaAs photoconductive antenna with a pulsed 1550 nm laser source and they did a study on the sub-band gap absorption shown in the red arrows in the energy band diagram in FigureA.2. In this case light can be absorbed through several phenomena cited below:

(i) A two-step transition through the mid-gap energy level, where carriers are excited from the valence band to the mid-gap states then excited to the upper conduction band states. (red arrows)

(ii) The excitation of trapped electrons in the mid-gap state into the conduction band. These electrons as in the 870 nm illumination decay (τ_3) from the upper conduction band to the lower one through the liberation of a phonon.

(iii) Two photon absorption which is a process of absorption of two photons simultaneously. Carriers then are excited to the upper conduction band level. Note that this process happens also at 870 nm illumination but is less probable in the two cases.

(iv) The excitation of trapped electrons in As precipitates to the surrounding LT-GaAs. These electrons have an activation energy of 0.7 eV, this implies that for higher sub-band gap absorption at 1550 nm wavelength it is important to increase the As defects present in the material.

As a conclusion, sub-band gap absorption is generally observed in the GaAs grown at low temperatures with an excess of As. This absorption is induced by a significant number of deep defects created by an excess of As atoms. Annealing at lower temperatures, allows the presence of the As-based defects as precipitates and not as larger clusters which results in the higher sub-band gap absorption due to the excitation of trapped electrons in the As precipitates. In this work, the absorption of the LT-GaAs at λ = 1550 nm will be studied by varying the annealing temperatures of the LT-GaAs. The annealed layers will be tested in micro-cavity photomixers in order to evaluate their absorption as well as their carrier lifetime behavior.

4.1.1. LT-GaAs micro-cavity photomixers compatible for 1550 nm-wavelength illumination

Based on the information presented earlier, we have chosen to investigate defect dependent sub-band gap absorption by varying the post-annealing temperature of the LT-GaAs. This was verified by fabricating and characterizing Fabry-Perot micro-cavity photodetectors specifically optimized for 1550 nm operation, already studied by Maximilien Billet during his PhD. This section will briefly outline the design principles and fabrication process of the device. For more in-depth information, refer to Maximilien's PhD manuscript [121]. Additionally, we performed pump-probe measurements on these epitaxial layers to form a notion on the carrier lifetime dynamic with the help of Jean-Francois Lampin.

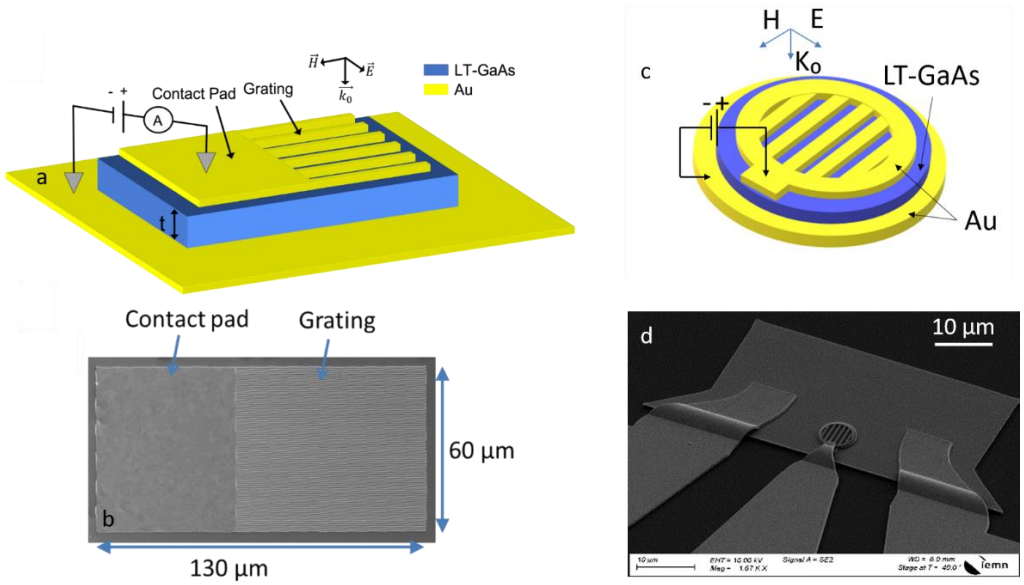

Figure 4.2: (a) Schematic representation of the micro-cavity photodetector designed for DC photoresponse measurements. (b) Top SEM image of the represented device in (a). In (c) is a schematic representation of a micro-cavity photomixer shown in an SEM image in (d) designed for frequency generation.

4.1.1.1. Optical design

The LT-GaAs photoconductors designed for 1550 nm operation, as illustrated in Figure 4.2, are comprised of an optical cavity made up of a 450 nm thick LT-GaAs thin layer sandwiched between two gold layers, which serve as both contact electrodes and cavity mirrors. The top mirror is a 300 nm thick nanostructured optical gold grating with a sub-wavelength periodicity of 900 nm and a slit width of 500 nm. This design was created through rigorous coupled-wave analysis (RCWA) to produce a Fabry–Pérot (FP) resonance for a thickness of 450 nm under 1550 nm illumination, with polarization parallel to the grating direction, as shown in Figure 4.2[122].Figure 4.2 (a) and (c) display schematic illustrations of test samples specifically for dc and ac measurements respectively. Figure 4.2 (b) and (d) shows their respective SEM images. The behavior of these devices is discussed in more detail in the subsequent chapter since the focus of that chapter is on this type of devices.

4.1.1.2. Epitaxial growth and fabrication

The fabrication procedure for the samples involved the following steps: starting with a 450-μm-thick semi-insulating GaAs substrate, a 0.1-μm-thick GaInP etch-stop layer was grown using gas-source molecular beam epitaxy (GS-MBE), followed by the addition of a 500-nm-thick layer of low temperature (250°C) grown GaAs. The GaAs wafer was then divided into four pieces and annealed at temperatures of 450°C, 500°C, 540°C and 580°C, respectively. Four different samples (S1, S2, S3, S4) were processed. The buried gold layer illustrated in Figure 4.2 was created by transferring the LT-GaAs epitaxial layers onto a 2-in.-diameter silicon wafer, using an Au–Au thermocompression layer bonding technique [121]. A gold grating was then patterned on the LT-GaAs layer through the use of electron beam lithography, electron beam evaporation, and lift-off techniques. As depicted in the SEM image in Figure 4.2 (b), the test structures for photocurrent measurement consisted of a 60 × 55 μm^2 optically opaque gold contact pad and a 60 × 75 μm^2 array of 300-nm-thick gold electrodes (p = 900 nm and a = 500 nm). As for devices compatible for photomixing, the diameter of the top sub-wavelength grating was varied in order to locate the best tradeoff between the RC frequency limitation and the optical saturation due to smaller sizes of the device.

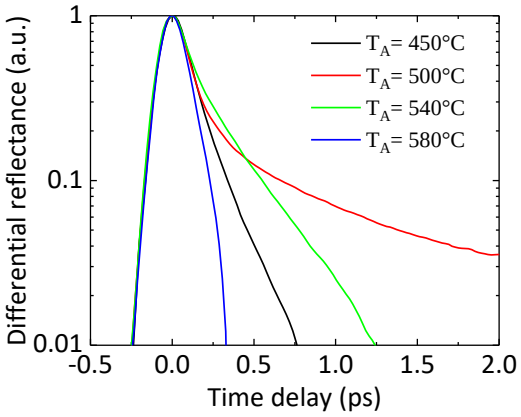

Figure 4.3:.Time-resolved photoreflectance measurements obtained on the LT-GaAs layers grown at 250 °C and annealed at T_A= 450,500,540 and 580°C.

4.1.1.3. Electron dynamic characterization

In Figure 4.3, time-resolved photoreflectance measurements using 200 fs optical pulses with a wavelength of 820 nm from a Ti:Sapphire laser are displayed. These measurements demonstrate clearly the presence of electronic carrier trapping on a sub-picosecond time scale, making them suitable for THz applications. However, it is important to note that extracting accurate carrier lifetime data from the measurements is difficult due to interference from the metallic back mirror. Additionally, it is noteworthy to mention that this measurement technique allows only the measurement the electron lifetime and do not give any information of the hole lifetime. The GaAs annealed at 580°C, which is generally used in 800 nm wavelength applications, is considered as a reference for low carrier lifetime and high frequency generation/detection. Consequently, the black plot (580°C) is considered as a reference for low carrier lifetime, the GaAs annealed at 450°C can be a promising candidate for a sub-picosecond lifetime behavior as it is the closest to the reference sample.

4.1.1.4. Dark resistivity and photoresponse measurements

The effect of post-growth annealing temperature on dark resistivity was analyzed in Figure 4.4. This was done by measuring the dark currents on four samples and plotting it against the bias voltage (inset of Figure 4.4). The slope of the current-voltage relationship was also calculated at zero bias voltage, using the equation $dI/dV = G_0$. The dark resistivity ρ_d was then determined by using the values for a 1D resistor with a thickness of 450 nm and an area of 60×130 μm^2.The dark resistivity ρ_d is calculated as the following:

$$\rho_d = \frac{A}{t \times G_0}$$

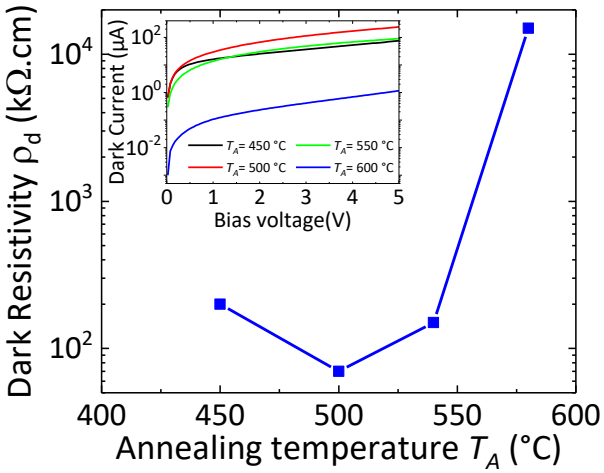

Figure 4.4: Dark resistivity dependence on post-growth annealing temperature T_A. Inset: Dark current versus Bias voltage obtained on the 60×130 μm^2 area test structures.

The photoresponse experiment was performed using a fiber-coupled external cavity laser that emitted light at a wavelength of 1550 nm. The laser light was focused through either a cleaved fiber (for samples S2 and S4) or a lensed fiber (for samples S1 and S3) into a gaussian spot with a mode field diameter of either 10.5 μm or 2.5 μm, respectively. It is worth noting that the spot width variation is unlikely to affect the results of this study since it has been previously shown that under cw illumination, in linear absorption regime, the spot diameter has no influence on the photoresponse of the optical cavity photoconductors as far it is smaller than the active area [122]. The polarization of the laser light was adjusted using a fiber polarization controller to align the electric field perpendicular to the grating electrodes. Figure 4.5 shows the photoresponse (R) as a function of bias voltage obtained for the four different samples, under cw optical power of 5 mW.

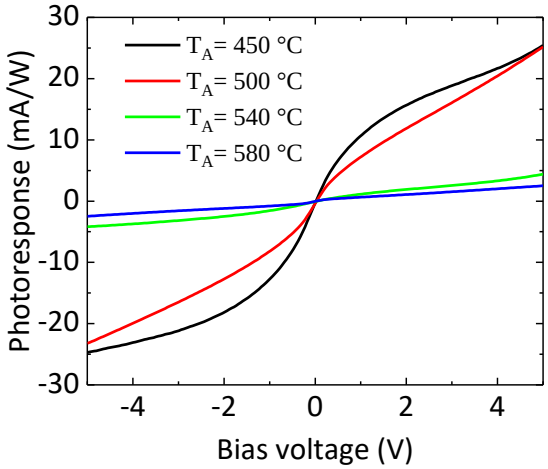

Figure 4.5: Photoresponse-Bias voltage characteristics measured on optical cavity photoconductors fabricated using LT-GaAs layers grown at 250 °C and annealed at T_A= 450,500,540 and 580 °C.

It can be observed that at the maximum bias voltage, both samples S1 (annealed at 450°C) and sample S2 (annealed at 500°C) exhibit a photoresponse that is roughly 10 times greater than that of sample S4 (annealed at 580°C). Furthermore, the slope of the photoresponse-voltage curve for S1 at zero bias voltage was found to be 10 times higher than that of S4 (17 mS/W compared to 1.7 mS/W). This latter figure is critical in THz optoelectronics applications, as it shows the capability of a photoconductor to attain a photoconductance value that is high enough to achieve appropriate impedance matching with free-space antennas or the standard 50-ohms input impedance of RF waveguide instruments. The increase in photoresponse is attributed to a higher defect density in the LT-GaAs layer, which results in increased optical absorption. By comparing the photoresponse obtained in previous studies at 1550 nm and 780 nm [122],[123], it is estimated that around 25% of the incoming light is absorbed in the active layer of S1, and that the absorption depth in the LT-GaAs layer annealed at 450°C is approximately 30 µm. Conclusively, with such results we can consider that the LT-GaAs annealed at 450ºC would be a perfect candidate for a distributed absorption in a TW-photomixer. Meanwhile, the carrier lifetime behavior should be verified in a photomixing experiment.

4.1.1.5. Frequency response measurements

Frequency response measurements were carried out for the four samples (S1, S2, S3 and S4) over the range 0-67 GHz, as depicted in Figure 4.6. Devices with a diameter of 8 µm similar to the one shown in Figure 4.2 (d) were illuminated by a beating optical source having a power of 85 mW, except for T_A = 580ºC where the device had a diameter of 10 µm and was pumped by an optical power of 100 mW. the measured RF power corresponds to a bias voltage of 5V applied to the devices through 50-ohms coplanar probes. It is worth mentioning thatdue to the low absorption of the LT-GaAs in S4, the slight increase in the top grating diameter (10 µm) and the optical power (100 mW)resulted in a generated RF signal slightly above the spectrum analyzer's noise level allowing a frequency response comparison with the other samples.

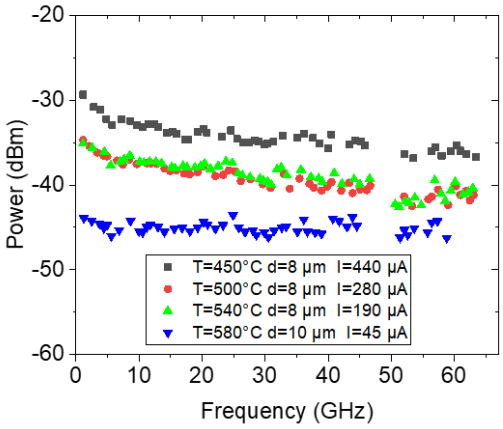

Figure 4.6: Generated RF power for the four samples annealed at T_A= 450,500,540 and 580 °C. The devices were biased at 5V.

Before analysing the result, it is important to note that the RC cutoff frequency of these devices falls outside of the measured frequency range[121]. Upon comparing the frequency response of the four samples, it can be observed that sample S4 has a flat response throughout the entire frequency range. By evaluating the expected power from the dc photocurrent $P_{exp} = 10\log\left(\frac{1}{2}RI^2\right)$ where$R = 50$ ohms and I is the photocurrent shown inFigure 4.6, we obtain a resulting power of -42.9 dBm, which is slightly higher than the measured power (P_{ac}~43.9 dBm). This can be attributed to the sub-picosecond behavior of almost all the excited carriers in the semiconductor, leading to nearly full

conversion of the absorbed optical power into ac current. All the other samples (S1, S2 and S3) present a fast roll-off of ~5 dB in the first 5 GHz and then a flat response up to 63 GHz. If we calculate P_{exp} for samples S1, S2, and S3, we obtain -23.15 dBm, -27.07 dBm, and -30.44 dBm, respectively. This represents significant shifts between P_{exp} and P_{ac} at 40 GHz of ~13 dB for S1 and S2, and ~9 dB for S3. This indicates that reducing the annealing temperature greatly increases absorption, but also changes the carrier dynamics. The photocurrent is mainly dependent on the electron lifetime as well as the hole lifetime. It is believed that at low annealing temperatures, more carriers are excited through mid-gap states and those that decay back to a mid-gap energy level remain blocked in defect traps for longer time (nanoseconds) before the electron-hole recombination. This nanosecond behavior could be attributed to the holes which possess a larger lifetime from electrons resulting in the slower recombination. This also shows that the majority of the photocurrent originates from the holes.

In conclusion, although there is a proof of high lifetime behavior, there are still enough sub-picosecond excited carriers resulting in a flat frequency response that is ~10 dB higher than the reference sample annealed at 580ºC. To the best of our knowledge, theseare the first photomixing measurements achieved with LT-GaAs illuminated at 1550 nm wavelength. As a result, LT-GaAs annealed at 450ºC will be implemented in the 1550 nm-TW-photomixer.

4.2. Optical modeling and characterization

In this chapter, simulations were conducted to fine-tune the dimensions of optical components for use with the 1550 nm wavelength. The advantage of this wavelength was the possibility to analyze optical components due to the existence of a readily accessible wideband continuous wave laser. This made it possible to design ring resonators and measure the optical group index of the mode. Additionally, at 1550 nm, the light scattering caused by surface roughness is minimal, which eliminated the need for using an index matching gel for optical coupling.

4.2.1. Single-mode-waveguide operation

To accommodate the change in wavelength from the previous chapter to 1550 nm (almost twice as much), the core width and thickness of the waveguide were doubled.

This was confirmed through a 2D FDE Mode Solver simulation, which showed that the waveguide was operating in single-mode with a core width reaching 1000 nm and a thickness of 400 nm. Figure 4.7 (a) shows the effective area evolution of the fundamental TE mode as function of the core width. As presented in the previous chapter, for lower core widths the mode is squeezed out of the core explaining the increase in the effective area. This can also be explained in Figure 4.7 (b) by the decrease in its effective index. Note that the simulated design is presented in the inset of Figure 4.7 (a). Finally, with the waveguide now in single-mode regime and having a core width allowing reasonable absorption in the active region, the next step is to fabricate test samples to optimize the other optical components, such as the grating coupler, MMI and the taper and to design ring resonators for group index measurements.

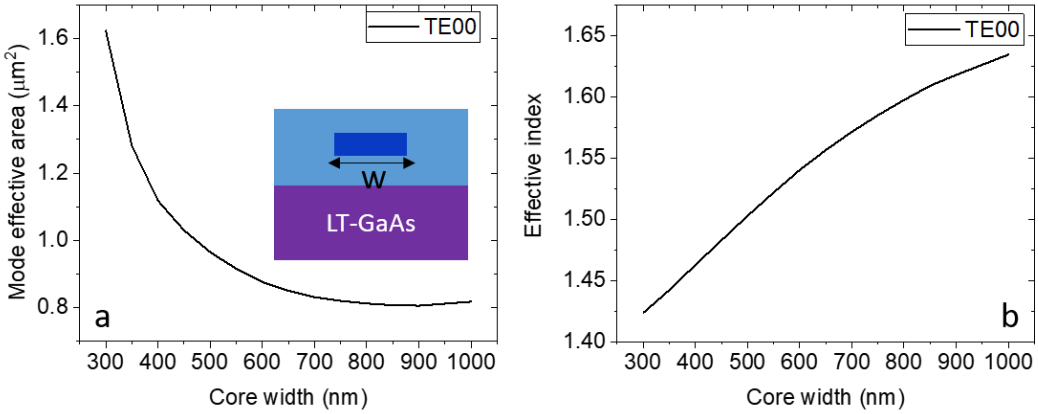

Figure 4.7:(a) Effective area of the fundamental TE mode as function of the core width. (b) Effective index of the fundamental TE mode as function of the core width at $\lambda = 1550$ nm.

4.2.2. Grating coupler characterization

In this section, the optimization of the optical waveguide platform at the 1550 nm wavelength was pursued by fabricating test samples on Si wafers. The test devices consisted of a waveguide on top of a thin gold layer deposited on a Si wafer.Figure 4.8shows a photo of one test sample where the waveguide platform was fabricated on a gold layer deposited on a Silicon wafer. On the right side of the figure is shown a schematic representation of a top view and a cross section of the waveguide.

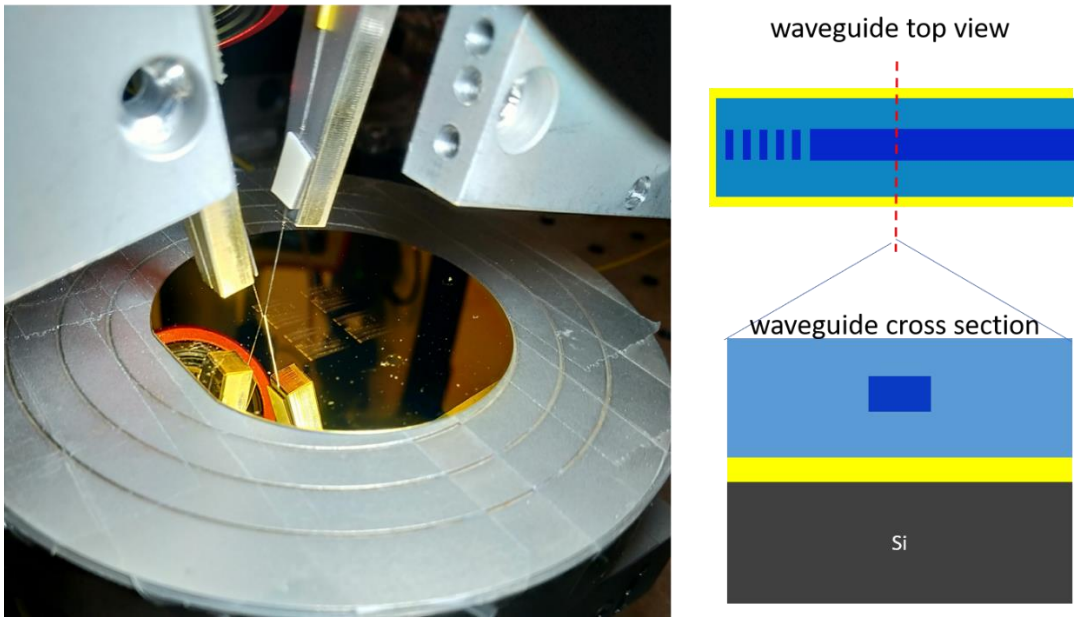

Figure 4.8: Photo of a test sample under optical characterization where the used substrate was Silicon. On the right side, a schematic representation showing a top view and cross section of the waveguide.

The grating period for the 1550 nm wavelength was estimated to be around 1170 nm by adapting the grating period that was designed for the 780 nm wavelength. A preliminary simulation model showed that a maximum coupling should be observed for an injection angle of 13º and a period of 1160 nm. Note that, the measured refractive indices of SiO_2 and Si_3N_4 were 1.45 and 2.01, respectively. As discussed in Chapter 3, the lower cladding thickness is a critical factor in maximizing optical coupling. Therefore, the first two constructive interference peaks at the grating coupler corresponds to an SiO_2 thickness around 500 nm and 1000 nm. Hence, four test samples with a lower cladding thickness varying around 500 nm were fabricated (t = 462, 500, 547, and 615 nm). It is worth noting that a realistic design of the grating was used in the simulation model as shown in Figure 4.9.

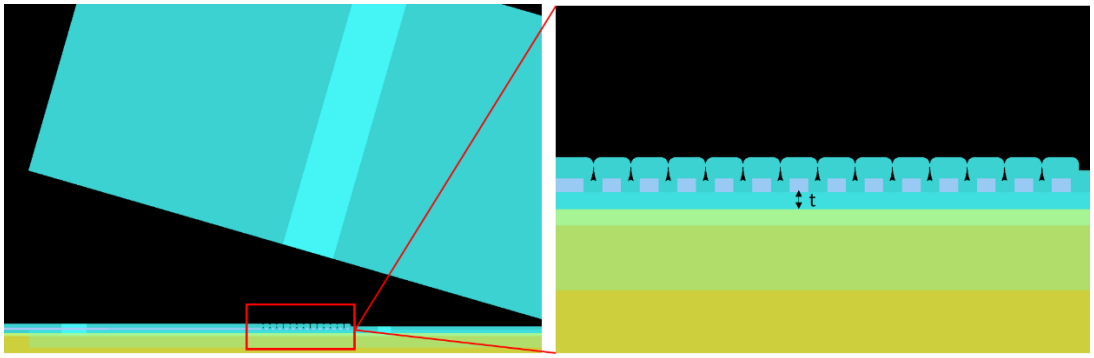

Figure 4.9: Screen capture of the 2D FDTD design showing the optical fiber above the grating coupler and an enlarged image presenting the realistic design.

The grating period was varied around 1160 nm. The results of the 3D FDTD simulation model were in good agreement with the experimental measurements of the coupling losses, as shown in Figure 4.10(a).The minimum coupling losses measured were around 2 dB for a wide range of SiO_2 thicknesses (~200 nm), which drastically increased the error margin when depositing SiO_2. Figure 4.10 (b) shows the coupling losses as a function of the wavelength for the best two grating couplers, with the lowest coupling losses of 1.8 dB achieved at λ=1550 nm for a grating period of 1140 nm and an injection angle of 11º. The corresponding lower cladding thickness was 547 nm. As already mentioned earlier, the measurements were realized without the need of the index matching gel as a result, the optimum top cladding thickness was set to 662 nm based on simulations.

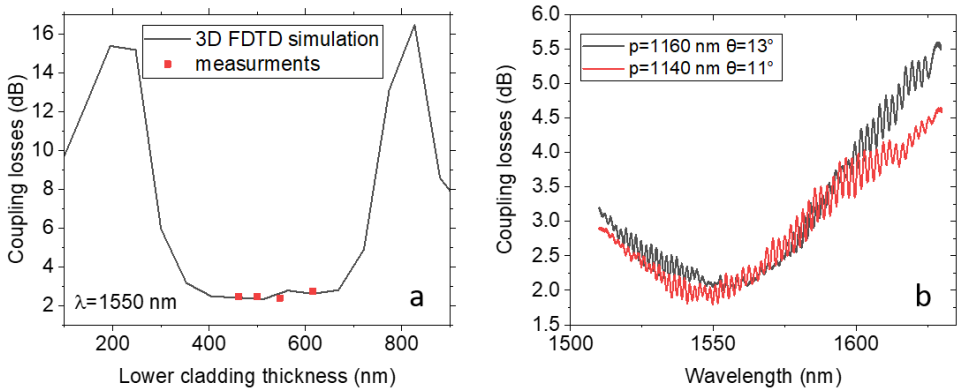

Figure 4.10:(a) Comparison between the measured coupling losses (red) and coupling losses calculated in a 3D FDTD model as function of the lower cladding thickness. The grating period was 1160 nm and the fiber tilted at 13º. (b) Measured coupling losses for two grating couplers having different periods (1160 nm in black and 1140 nm in red). The optimum angle for a minimum coupling loss at 1550 nm is 13º and 11º for p = 1160 nm and 1140 nm respectively.

4.2.3. Propagation losses and absorption in the active region

Regarding the propagation losses, they were first only measured on gold as all the test waveguides were made on this material. The main cause of the propagation losses in these devices is the proximity between the core and the substrate, leading to a significant interaction between the mode and the substrate. This was confirmed by realizing a test sample where the bottom cladding thickness was about 500 nm thicker than the optimal thickness defined before. Figure 4.11 presents a comparison between the propagation losses for these two bottom cladding thicknesses. The propagation losses were measured for three core widths (0.5, 1 and 10 µm). As expected, the propagation losses sharply increase when the core is closer to the gold layer (t=547 nm) and reached a maximum of 9 dB/mm for a core width of 0.5 µm.

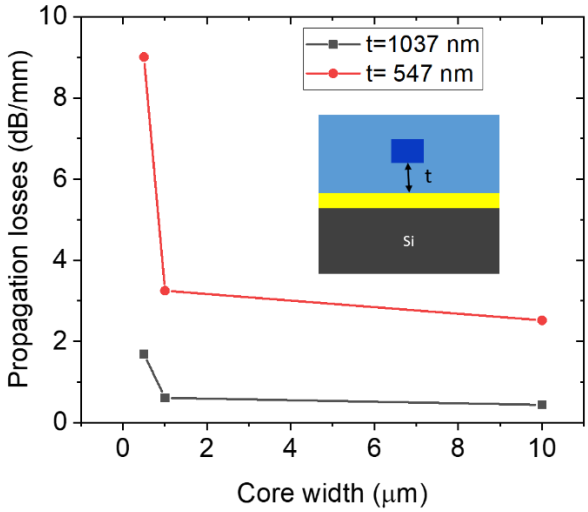

Figure 4.11: Propagation losses as function of three core widths (0.5, 1 and 10 μm) for two thicknesses of the bottom cladding (547 nm and 1037 nm).

As a conclusion, a greater proximity between the substrate and the fundamental mode results in increased propagation losses. Moreover, in cases where the waveguide is positioned above the active region, losses in the optical signal are primarily attributed to absorption in the LT-GaAs material. As a result, the SiO_2 thickness of 547 nm will be used for the TW-photomixer. However, the taper length is optimized to minimize the propagation losses above the gold layer. Here the designed adiabatic taper reduces the core width following a third order polynomial from 10 μm(right after the grating) to a few hundred nanometers (at the active region). On the test sample, several taper lengths were designed and the loss was measured for each length, as shown in Figure 4.12 (b). Note that for all the test tapers, the core width was set to 0.5 μm. These losses mainly originate from two sources: interaction with the gold layer, which was previously explained, and non-adiabatic conditions. In fact, adiabatic tapers are designed to minimize the mode mismatch between the input and output waveguides, which is essential for high transmission efficiency. However, the adiabatic condition becomes increasingly difficult to maintain as the taper length is reduced. This also can be explained by the fact that the taper length determines the size of the tapered region and the rate of change of the waveguide width. A very short taper may not provide sufficient space for the optical mode to smoothly transition between the input and output waveguides, leading to mode

mismatch and low transmission. This can be seen in Figure 4.12 (a), which displays the result of a 3D FDTD simulation for different taper lengths in a lossless medium allowing to quantify the taper adiabaticity. The inset of Figure 4.12 (a) shows a screen capture of the FDTD model. As seen, non-adiabatic regime begins when the length is below 200 µm. Above this length, there is no losses due to non-adiabaticity. In Figure 4.12 (b), it can be seen that for taper lengths less than 100 µm, losses due to non-adiabatic conditions are dominant compared to those in the gold. Meanwhile, for lengths over 100 µm, the taper is considered adiabatic, but the metal losses are not negligible. A length of 100 µm, where the taper is adiabatic and the metal losses are minimal, was found to be an optimal balance. As a result, this taper dimension is validated for the complete TW design.

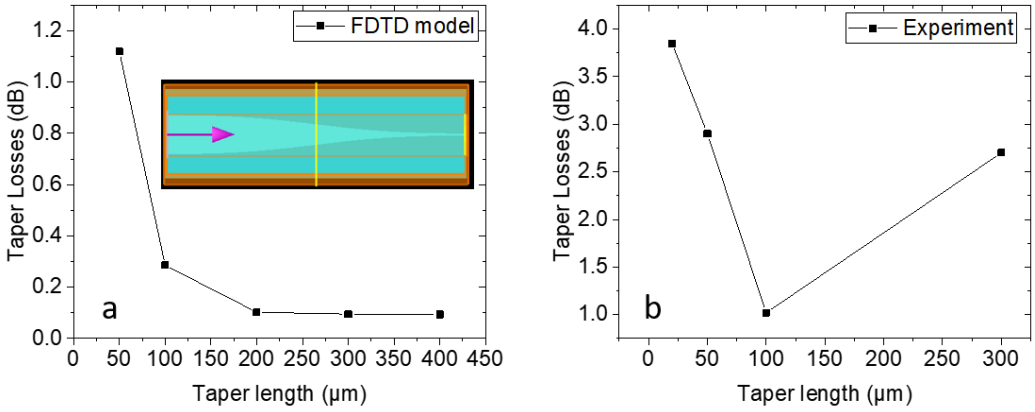

Figure 4.12: (a) Taper losses as function of the taper length. In the simulation model, all the material used were set to be lossless. Here losses are only from the non-adiabaticity of the taper. (b) Measured losses of in tapers as function of their respective length.

Meanwhile, optical losses above the LT-GaAs were only measured for two designed core widths (0.5 µm and 1 µm) due to the lack of space on the sample. Note that these losses were measured on the sample where the LT-GaAs was bonded to the high-resistivity silicon wafer. Unexpectedly, the 1 µmwide core resulted in higher propagation losses (21.72 dB/mm) than the 0.5 µm(18 dB/mm). This was verified in a 3D FDTD simulation model of a 100 µm long device. The propagation losses for the 1 µmand 0.5 µmwide core were 16.57 dB/mm and 13.69 dB/mm respectively. This slight shift between the measurements and the simulation can be attributed to additional losses from other sources that cannot be introduced in the simulation such as the surface and etched sidewalls

roughness. This unexpected result lead us to further investigate the losses in the LT-GaAs. The latter were then measured as function of the wavelength for the two core widths and is presented inFigure 4.13. A top view of the measured waveguide is shown below the measurement plot. The inset depicts a cross section of the structure where the BCB and the HR-Si are visible. As we can see, the absorption peak in the LT-GaAs can be tuned to upper wavelengths when the core width is reduced which explains the higher absorption at 1 µm core width. This behavior hints to a core width dependent directional coupling between the core and the LT-GaAs. Since the core width modulates the fundamental mode properties, it could affect a possible phase matching/overlap with other modes in the LT-GaAs at a defined wavelength resulting in directional coupling between the fundamental mode and these modes. Further studies should be realized to validate this theory. It is worth noting in this chapter, the propagation losses on LT-GaAs may not reflect the optical absorption only under the core as shown in the inset of Figure 4.13. This will be seen later in the dc photoresponse measurements as function of the core width.

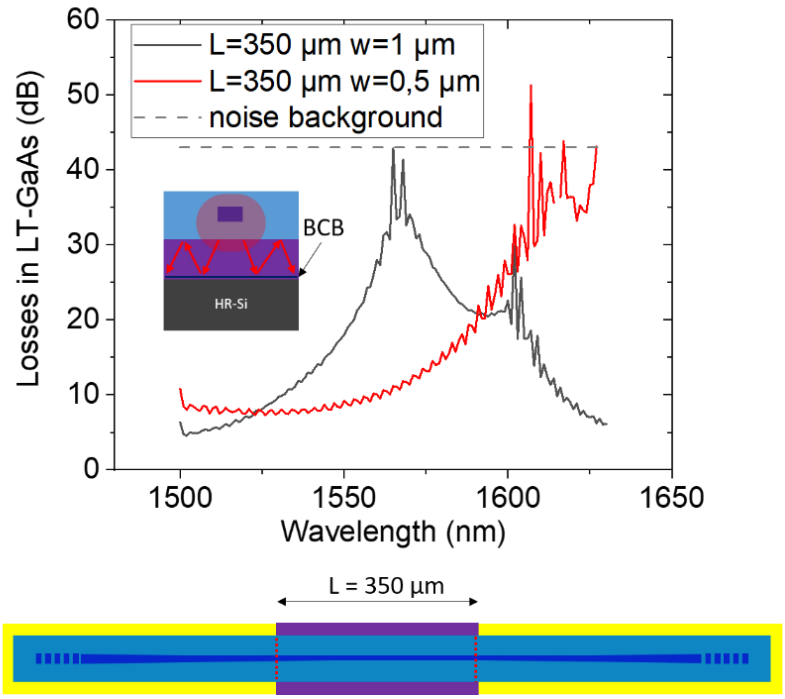

Figure 4.13: propagation losses in a 350 µm long waveguide segment above the LT-GaAs. The black and red curves correspond respectively for a core width of 1000 nm and 500 nm.

4.2.4. MMI characterization

In the same manner, simulations using the BPM method were carried out by Vincent Magnin and the ideal length and width of the MMI were determined to be 16 µm and 5 µm, respectively. The width and length of the MMI were varied on the experimental samples based on these calculated values. The optimal performance of the MMI was achieved with a width of 5 µm. Figure 4.14 displays the efficiency of the MMI (in black) and its losses (in red) as a function of its length. It's worth noting that the losses in the taper connecting the MMI output to the active region are also included. As expected by the the BPM simulations, an efficiency of 1 is achieved at a length of 16 µm and the losses at this length are relatively low, ~0.6 dB. These low losses can be attributed to the optimization of the length of taper, as determined by a 3D FDTD simulation, which showed that a 40 µm long curved segment resulted in losses of ~0.17 dB. Note that in the simulation model, all the materials were assumed to be lossless in order to quantify only the adiabatic condition of the taper. Consequently, the total optimal distance between the grating coupler and the active region was reduced to approximately 170 µm, resulting in total insertion losses of ~3.4 dB (grating coupler losses, taper losses, MMI and taper losses). As a conclusion, the insertion losses at λ = 1550 nm were much lower than the insertion losses at λ = 780 nm. This was mainly due to the higher compatibility of the waveguide platform to the telecom wavelength.

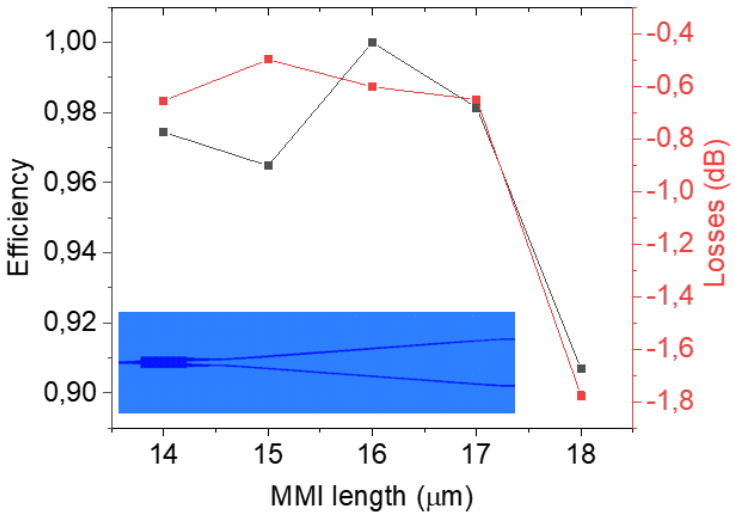

Figure 4.14: MMI efficiency (black) and losses (red) as function of the MMI length.

4.2.5. Group index measurement

Since there are less spectral constraints at this wavelength, it was possible to measure the group index. This was realized through the fabrication of micro-ring resonators shown in Figure 4.15 (a). An optical ring resonator is a type of optical cavity that consists of a closed loop of optical waveguide material. The waveguide is designed so that the round-trip phase shift of the light waves that travel through the resonator is equal to an integer multiple of 2π. This results in constructive interference of the light waves, causing the cavity to resonate at specific frequencies. Optical ring resonators are commonly used in various optical applications, such as laser technology, sensing, and communication systems. In [124], based on a first order approximation of the dispersion in a micro-ring resonator, they express the free-spectral-range (FSR) as the following:

$$FSR = \frac{\lambda^2}{n_g L} \tag{4.2.1}$$

The free spectral range (FSR) is the spacing between two resonance peaks observed after passing through the resonator (as shown in Figure 4.15 (b)). The distance of a roundtrip through the resonator is represented by L, while n_g represents the group index. The FSR was measured for several ring resonator radii, and the group index was calculated by fitting the measured FSR as a function of the roundtrip length based on equation (4.2.1) (as shown in Figure 4.15 (c)). This was done for waveguides on top of gold and on top of LT-GaAs, for four different core widths between 350 nm and 750 nm as shown in Figure 4.15 (d) and (e) respectively. The measured FSR results fit relatively well with the 2D FDE Mode Solver simulations when on top of gold, but there is an overall shift of ~ 5.5 % observed for LT-GaAs, except for the lowest cores where the error is higher. The error bars correspond to the fitting error, which can also reflect lower precision in the measurements. For lower core widths, especially for the waveguides on LT-GaAs, the error bars are larger due to higher uncertainty in measuring the FSR. It is important to note that the overall shift between the simulation and measurement results could be due to not well-defined optical properties of the LT-GaAs. In the simulation model, a constant refractive index of 3.37 was used based on the previous work of Maximilien Billet[121]. However, the modification of the LT-GaAs growth and annealing may result in slight modifications of its optical properties leading to a change in the refractive index defined

in Maximilien Billet's manuscript. Moreover, in the simulation window we considered an infinite LT-GaAs thickness, however in reality, there was the BCB and the Si wafer below the LT-GaAs.

In summary, depending on the core width, it is possible to define a group index between ~2 and 2.3. Based on what was presented in the previous chapter, these values indicate that the membrane is not required at this wavelength, as they are closer to the THz refractive index of the CPW on bulk (2.7). However, the optimal core width should also be selected based on its respective absorption.

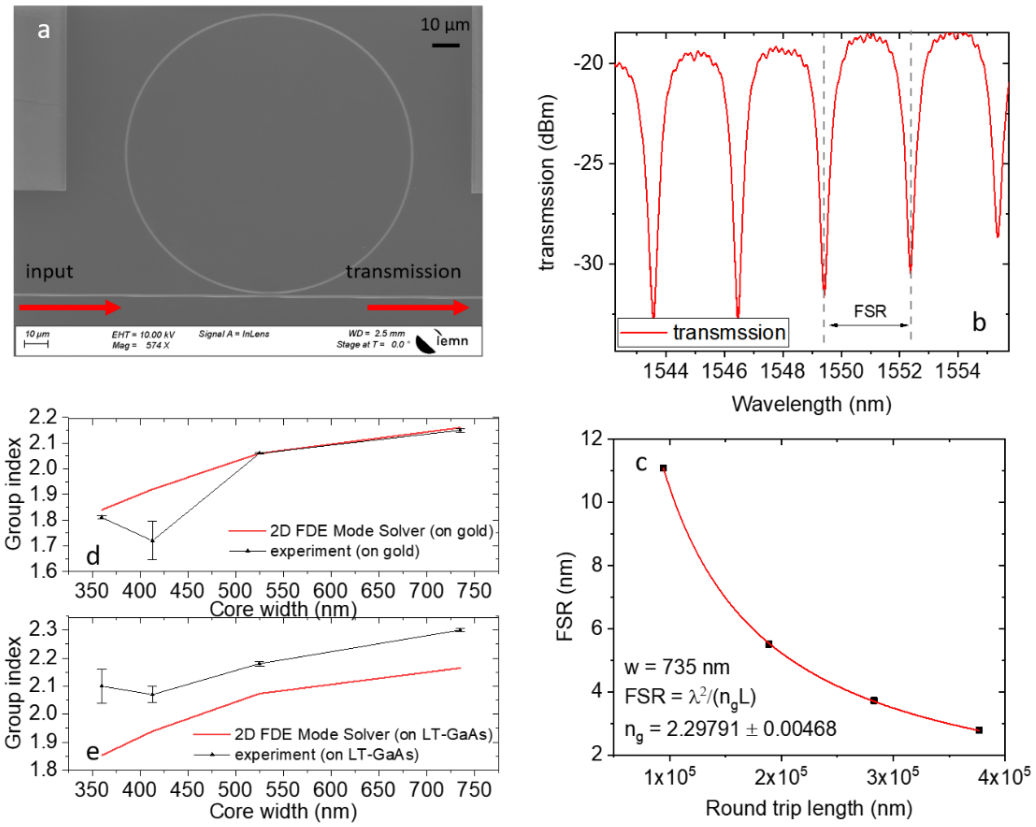

Figure 4.15:(a) SEM image of a micro-ring resonator showing the input and output of the ring. (b) Measured transmission spectrum of the ring resonator showing the FSR. (c) Measured FSR of a micro-ring resonator of core width 735 nm as a function of the roundtrip length (black) fitted to equation (4.2.1) (red). Measured (black) and simulation results (red) ofgroup index as function of the core width of waveguides on gold (d) and on LT-GaAs (e).

4.3. Optoelectronic characterization

4.3.1. DC photoresponse measurements

While the absorption in the LT-GaAs is increased at the wavelength of 1550 nm, it is still lower than that of the 780 nm wavelength illumination. Therefore, we fabricated devices reaching 2 mm length in case the optical power is not completely absorbed before. First, the photocurrent was measured as a function of the bias voltage. shows core widths and the lengths of the measured CPS-TW-photomixers.

Core width (nm)	270	370	420	520	620
Device length (mm)	0.1	0.2	0.5	1	2

Table 4-1: Core width and device length of the characterized devices.

The devices were biased up to 20 V and illuminated with a cw Yenista laser source with a power of 6.4 mW at the fiber output of and at wavelength λ=1550 nm. Figure 4.16 (a) shows an I-V characteristic curve of a 2 mm long TW-photomixer having a core width of 620 nm. It can be observed that the low annealing temperature of the LT-GaAs resulted in relatively high dark currents. Moreover, similarly to what was presented in the previous chapter, at high voltages the photocurrent presents a superlinear behavior that can be attributed to an increase in the electron's lifetime after a saturation in their velocity. The photoresponse was calculated by dividing the measured photocurrent by the fiber output power since there was no information of the taper losses corresponding to each core width. In Figure 4.16 (b), we show that a photoresponse reaching ~50 mA/W was measured for a core width of ~620 nm and a device length of 2 mm. Note that the photoresponse shown in the figure is calculated by dividing by 6.4 mW.These photoresponse values are ~7.5 times higher than the those measured at λ=780 nm. This can be attributed to the compatibility between the waveguide platform and the wavelength which is expressed by lower coupling losses and propagation losses. Additionally, on this sample the photoresponse was measured on the only two identical CPS cells and the results came out almost identical which proves the high process yield of the devices. Moreover, based on the previous study on the annealing of LT-GaAs, it is expected that the primary source of high photoresponse is due to the presence of holes with a high lifetime in the material.

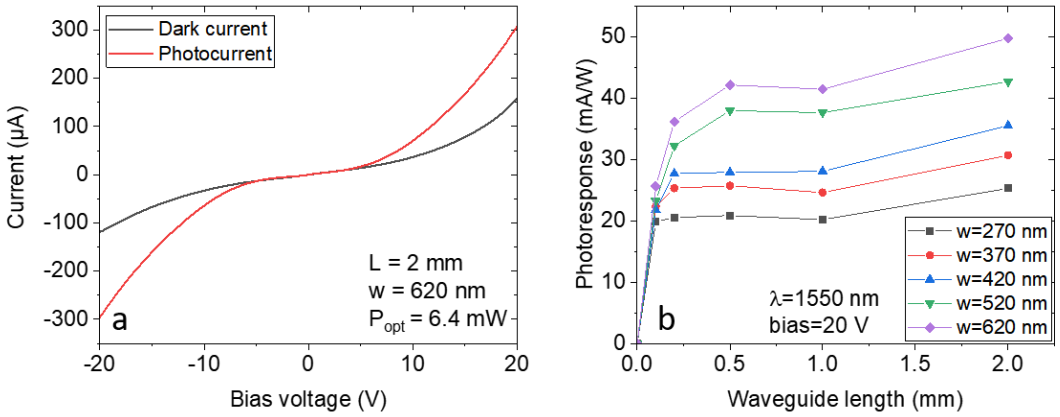

Figure 4.16: (a) I-V characteristic of a CPS-TW photomixer showing the photocurrent and the dark. Photoresponse as function of the device length for different core widths. The wavelength and the bias were set to 1550 nm and 20 V respectively. The photoresponse was calculated based on the optical power at the fiber output (6.4 mW).

As mentioned previously, due to the lack of space on the sample, only two core widths (500 nm and 1000 nm) were designed on test devices with an input and output grating coupler allowing the extraction of the taper losses. For the two core widths, the losses in the taper were around 1 dB. However, on a full design where we have the electrodes, several core widths were designed reaching a maximum value of 620 nm. Note that in a full design, it is not possible to extract the taper losses, as a result, we will consider that the taper losses are similar for all core width widths and are around 1 dB, which are the taper losses measured for w = 500 nm and 1000 nm. Now if we consider the widest core width (620 nm), the photoresponse calculated by considering the effective optical power at the active region would reach 100 mA/W for a device length of 2 mm. Additionally, the absorption of optical power in relation to the core width exhibits a contrary pattern compared to devices illuminated at a wavelength of 780 nm. It is observed that the photoresponse reaches its peak value for the longest device and the wider core. Previous calculations show an absorption depth of about 30 μm for LT-GaAs annealed at 450ºC [125], leading to the assumption that the optical mode is not just absorbed between the electrodes, but also below the electrodes farther than the electric field lines and in the Silicon substrate via radiation, as illustrated in Figure 4.17. By considering that most of the photocurrent is generated by photons absorbed between the electrodes we can deduce

that thinner cores produce a compressed mode leading to higher losses from absorption in the metallic electrodes, absorption far from the electric field generated by the bias, and radiation in the Silicon substrate. In contrast, wider cores exhibit higher mode confinement in the core and slight overlap with the LT-GaAs, resulting in an extended absorption distance and higher absorption between the electrodes, which explains the greater photoresponse.

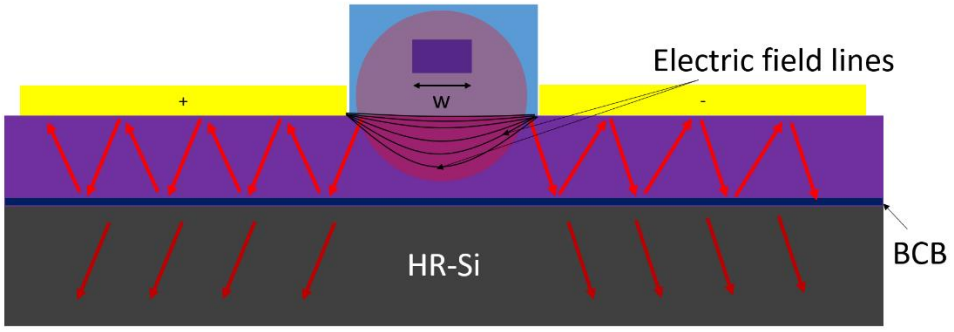

Figure 4.17: Schematic representation of a cross section of the TW-photomixer showing a depiction of the fundamental mode profile and the fraction of light that is lost in the LT-GaAs under the electrodes or radiated in the Silicon. The electric field lines are also shown.

As a conclusion, a 0.5 mm long device and a core width of approximately 600 nm is a suitable candidate for photomixing. At this length, the photoresponse has already reached its maximum value and the group index (~2.3) results in an index mismatch between ~0.2 and ~0.5, which is equivalent to a 3 dB-cutoff between 0.5 THz and 1 THz.

4.3.2. Frequency response measurements

In this section, we will examine the frequency response of CPS devices measured previously in dc. The measurement setup used is similar to the one used in the previous chapter shown inFigure 3.34,where photomixing-generated power in the range of 0-67 GHz was measured using an R&S spectrum analyzer. The devices were illuminated up to 355 mW and even though the superlinear behavior of the the photocurrent at high electric fields, the device was biased at 20 V in order to maximize the generated power allowing the highest signal to noise ratio in the frequency range 0-67 GHz. Based on the highest

photoresponse, which was measured for the core width w=620 nm, photomixing was performed at this core width for three different lengths (L= 0.2, 0.5, and 1 mm), as illustrated inFigure 4.18. For all three devices, the generated power experienced a rapid roll-off of ~20 dB within the first 5 GHz before plateauing. If we compute the expected power based on the dc photocurrent ($^1/_2\, RI_{exp}{}^2$), the resulting powers for L= 0.2, 0.5, and 1 mm are -4.77 dBm, -4.07 dBm, and -2.7 dBm, respectively, which results in a total shift of ~33 dB from the measurements at 40 GHz. To a lesser extent, a similar behavior was previously observed in micro-cavity photomixers. This rapid roll-off may be due to the fact that the interelectrode spacing in the TW-photomixer is 2 μm, whereas in micro-cavity-photomixers, it is 450 nm, which allows for the collection of a majority of low lifetime carriers since the active region is sandwiched between the electrodes. Meanwhile, in the TW-photomixer design, although the bias is at 20 V, the electrodes are not optimized for carrier collection and are considered to be sufficiently far apart to collect all possible low-lifetime carrier.

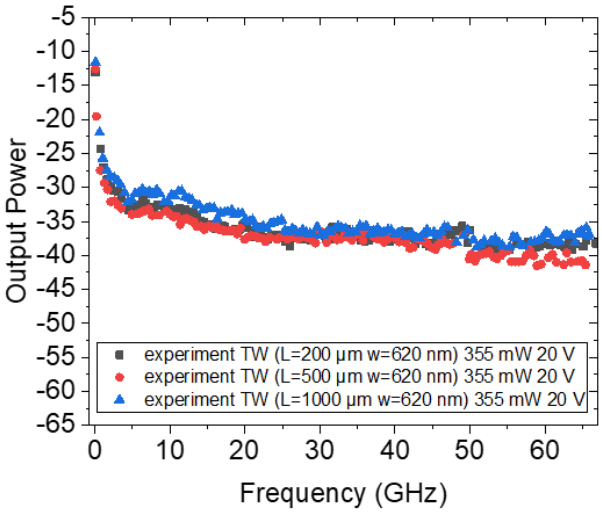

Figure 4.18: experimental frequency response of a 200 μm (black), 500 μm (red) and 1000 μm (blue) long TW photomixer. The bias was at 20 V and the optical power at 0.355 W resulting in a DC photocurrent of 3.65 mA, 3.957 mA and 4.63 mA respectively.

After analyzing the frequency response of the TW-photomixer, we examined the relationship between the optical power and its impact on the device's performance. The

photomixer theory predicts that the dc-photocurrent should have a linear relationship with optical power, provided there are no saturation effects. Additionally, the power generated by the photomixer should increase quadratically with the optical power. These predictions were confirmed by Figure 4.19, which displays the photocurrent and generated power as a function of optical power. Furthermore, Figure 4.19 demonstrates that there was no thermal failure detected up to a maximum optical power of 355 mW.

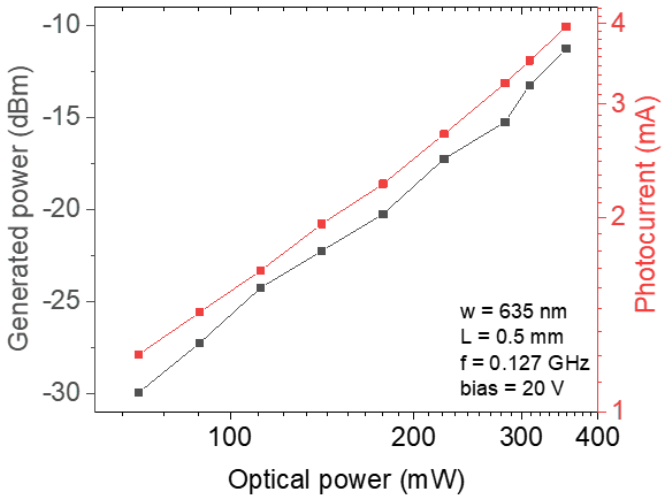

Figure 4.19: Photocurrent and generated power as function of the optical power.

Conclusion

As a conclusion, we managed to fabricate a high efficiency low temperature SiO_2/Si_3N_4 waveguide platform compatible to III-V semiconductor devices with sufficiently low insertion losses reaching a total of 3 dB (grating coupler and taper) in a CPS-TW design and ~4 dB (grating coupler, taper and MMI) for a CPW-TW design. Moreover, an optical power reaching 0.355 W was coupled and absorbed along a 2 mm long waveguide segment above an LT-GaAs layer. The device limits in terms of maximum optical power were not reached since we were constrained by the risk of damaging the fiber connectors at high optical powers. The LT-GaAs carrier behavior turned out to be worse than the expectations since the design was not optimized for a high photoconductive gain and the carrier lifetime behavior was not optimal for high frequency generation. Conclusively, this high-quality waveguide platform could be introduced to

other semiconductors compatible for ultra-fast frequency applicationsatλ=1550 nm such as InGaAa:Fe or LT-InGaAs. On the other hand, as already presented in Figure 4.6, even though the 1550 nm wavelength absorption in the LT-GaAs annealed at 580ºC is low, it possesses only sub-picosecond lifetime behavior. A plausible solution is to use an LT-GaAs annealed at 580ºC and modify the TW-design to increase the absorption in the active region allowing a higher photoconductive gain. For future work, it would be interesting to investigate the behavior of a novel TW-photomixer modified design shown in Figure 4.20. This design consists of fabricating the optical waveguide on top of an LT-GaAs ridge and depositing part of the metallic guiding structure on the sidewalls of the ridge. The ridge allows a better confinement of the light in the LT-GaAs and since the electrodes are in contact with the sidewalls, higher number of carriers could be collected resulting in better photoconductive gain compared with the first TW version. In case of a design on bulk, an AlGaAs layer could be used as lower cladding for the LT-GaAs ridge waveguide. However, it is important to anticipate possible optical losses in the metallic electrodes contacting the sidewalls. In case of a design on bulk, an AlGaAs layer could be used as lower cladding for the LT-GaAs ridge waveguide. Overall, the efficiency of such design should be well studied before its realization.

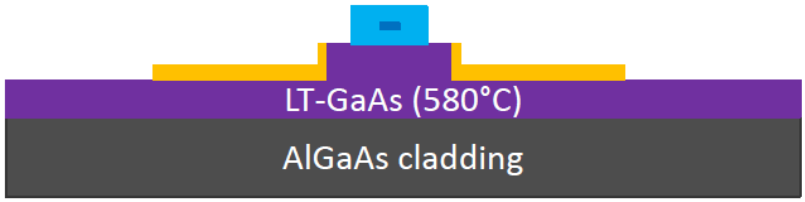

Figure 4.20: Modified design of a TW-photomixer based on 580ºC annealed LT-GaAs illuminated by a 1550 nm wavelength.

Conclusions and perspectives:

This scientific manuscript provides an overview of my research spanning three and a half years focused on the development of optoelectronic devices for THz wave generation. The main idea is to design of a novel TW-photomixer capable of absorbing high levels of optical power and due to its traveling-wave structure it is capable to compete with the existing state-of-the-art photomixers. The novelty of the proposed TW-photomixer lies in the integration of a low temperature SiO_2/Si_3N_4 waveguide platform that is compatible with III-V semiconductors. This waveguide platform is patterned between the slots of a coplanar waveguide (CPW) designed on LT-GaAs membrane supported by a high resistivity silicon substrate. The combination of the dielectric waveguide platform and the CPW supported LT-GaAs membrane allowed for a plausible index matching between the optical and electrical wave for devices reaching a length of 1 mm. The optical beatnote is coupled to the active region through a combination of an original grating coupler design, a taper, an MMI and the absorption in the LT-GaAs was tuned by varying the core width. This waveguide platform was adapted for both 780 nm and 1550 nm wavelengths. The membrane design exhibited high thermal resistivity, enabling optical illumination up to 400 mW, which was limited only by the characterization setup. Moreover, based on our developed theoretical model we show that when an index matching is achieved and for a high optical power these devices would reach the microwatt level at 1 THz.

For devices compatible with 780 nm wavelength illumination, the main issue was the compatibility of the dielectric waveguide with the operating wavelength. Even though, a study was conducted to reduce optical losses by examining the surface roughness of the SiO_2 cladding and the Si_3N_4 material composition, the devices still exhibited high insertion losses ranging from 5.5 dB to 8.5 dB due to scattering, which was detrimental to coupling especially when no index matching gel was used. This was mainly due to the instability of the PECVD machine.These high insertion losses could be easily reduced by using chemical-mechanical planarization technique which showed that 1 dB/mm propagation losses are possible. Meanwhile these devices could reach a maximum photoresponse of 40 mA/W which is higher than those of vertically illuminated MSM LT-GaAs photomixers. Despite the high insertion losses, the frequency response of a 1 mm

long TW-photomixer illuminated by a 400 mW optical power showed a TW-behavior up to 100 GHz. The results were validated using a developed optoelectronic circuit model of the TW-photoconductor.For future projects on TW-photomixers operating at this wavelength, the dielectric waveguide platform could be fabricated using a new PECVD machine which have an industrial production level.As a result of the quality of the dielectric materials deposited by such machine, the insertion losses could be drastically reduced allowing these devices to overcome the lumped-element photomixers in terms of output power and bandwidth and reach an output power around 100 µW at 1 THz.

In the last part of this work, the dielectric waveguide platform was adapted for the telecom wavelength (1550 nm) and test samples were fabricated to evaluate the insertion losses. The grating couplers displayed coupling losses as low as 2 dB, comparable to state-of-the-art grating couplers based on LPCVD processes, resulting in low insertion losses that reached 3.4 dB for the CPW TW-photomixer design. Overall, we managed to fabricate a waveguide platform allowing the access to a III-V active region with insertion losses as low as 2 dB/mm. Such platform, using low temperature depositions (<300°C) represents the best we can get with PECVD tools and is compatible with any other devices based on III-V materials. Additionally, micro-ring resonators were designed to measure the group index of the fundamental mode propagating above gold or LT-GaAs. The results were verified by simulations, indicating group index values ranging between 2 and 2.3, resulting in quasi-perfect index matching with the effective index of the RF/THz wave. Initially, LT-GaAs possess a sub-picosecond lifetime and high dark resistivity, allowing it to be the best candidate photomixers. However, the absorption in LT-GaAs at 1550 nm is low and occurs mainly through mid-gap energy levels directly related to the defect concentration in the material. Mid-gap assisted absorption was optimized by reducing the post annealing temperature of LT-GaAs from 580ºC to 450ºC. The photoresponse measurements on micro-cavity photoconductors showed a seven-fold improvement (25 mA/W) compared to the sample annealed at 580ºC. Even though a 5-dB roll-off before 5 GHz is observed in these devices, the frequency response after 5 GHz was flat up to 67 GHz and still 10 dB higher (-35 dBm) than the sample annealed at 580ºC proving a picosecond-lifetime behavior. These results represent the first photomixing measurements on LT-GaAs-based photomixers illuminated at 1550 nm. However, the electrode design

of the TW-photomixer was not optimal for low-lifetime carrier collection, leading to a larger roll-off (~20 dB) compared to the micro-cavity devices. Therefore, the LT-GaAs annealed at 450ºC was not compatible with TW-photomixers. For future work, it would be interesting to use semiconductors compatible for 1550 nm illumination such as InGaAs or iron doped InGaAs. Even though the dark resistivity in such materials is lower than the LT-GaAs, they possess a higher absorption at λ= 1550 nm and all excited carriers exhibit low lifetime allowing high frequency generation.

Publications in international journals

- **Tannoury, C.**,Billet, M., Coinon, C., Lampin, J.-F. and Peytavit, E. (2020), Low-temperature-grown gallium arsenide photoconductors with subpicosecond carrier lifetime and photoresponse reaching 25 mA/W under 1550 nm CW excitation. Electron. Lett., 56: 897-899. https://doi.org/10.1049/el.2020.1116

- F. Bavedila, **C. Tannoury** *et al*., "Development of a Millimeter-Long Travelling Wave THz Photomixer," in *Journal of Lightwave Technology*, vol. 39, no. 14, pp. 4700-4709, July15, 2021, doi: 10.1109/JLT.2021.3078226.

Communications in international conferences

- **C. Tannoury**, M. Billet, C. Coinon, J. -F. Lampin and E. Peytavit, "Low-Temperature-Grown Gallium Arsenide Photoconductors with Photoresponse reaching 25 mA/W under 1550nm CW excitation," *2020 45th International Conference on Infrared, Millimeter, and Terahertz Waves (IRMMW-THz)*, 2020, pp. 1-1, doi: 10.1109/IRMMW-THz46771.2020.9370757

- **C. Tannoury**, M. Billet, C. Coinon, J. -F. Lampin and E. Peytavit, "Low-Temperature-grown GaAs photoconductors suitable for 1550nm-wavelength illumination," *2021 46th International Conference on Infrared, Millimeter and Terahertz Waves (IRMMW-THz)*, 2021, pp. 1-2, doi: 10.1109/IRMMW-THz50926.2021.9567204.

- F. Bavedila et al., "Millimeter-long travelling wave photoconductors for THz generation by photomixing," 2021 46th International Conference on Infrared, Millimeter and Terahertz Waves (IRMMW-THz), 2021, pp. 1-2, doi: 10.1109/IRMMW-THz50926.2021.9567211.

- C. Tannoury *et al*., "Optoelectronic THz mixer based on iron-doped InGaAs in a plasmonic microcavity," *2022 47th International Conference on Infrared, Millimeter and Terahertz Waves (IRMMW-THz)*, 2022, pp. 1-1, doi: 10.1109/IRMMW-THz50927.2022.9895790.

-C. Tannoury, V. Avramovic, E. Okada, C. Coinon, J. -F. Lampin and E. Peytavit, "Traveling wave photomixers based on low-temperature-grown Gallium Arsenide reaching 50 mA/W under 1550 nm CW illumination," 2022 47th International Conference on Infrared, Millimeter and Terahertz Waves (IRMMW-THz), 2022, pp. 1-2, doi: 10.1109/IRMMW-THz50927.2022.9895804.

Appendix

A. Low-temperature-grown Gallium Arsenide:

Low carrier lifetime operating semiconductors were realized by non-crystalline material growth or by inducing damage to another crystalline material. In 1980 Auston et al.[126], demonstrated one of the first experimental results of a picosecond lifetime regime by amorphous grown silicon in a photoconductor. In this demonstration the carrier lifetime was reduced to 40 ps, whichis explained by the fast relaxation time of the photoexcited carriers to localized states. Later in the 1980s, lower lifetimes were achieved reaching 600 fs by oxygen implantation into silicon on sapphire [127]. Low temperature grown Gallium Arsenide was also studied as it was used as buffer layer in transistor and other field-effect devices since it showed very high resistiviy[128]. This led to several investigations on the properties of these LT-GaAs buffer layers. One of the early theoretical results, predicted that arsenic antisites produced deep level donors [129] as well as metastable states [130]. In 1990, Melloch et al. were the first to prove experimentally the presence of the arsenic precipitate whose size ranged from 2 to 10 nm [131]. Following the earlier experiments using defects in silicon, the same method was applied to LT-GaAs. This resulted in photoexcited carriers having a lifetime less than 400 fs [132]. Additionally, the LT-GaAs exhibited sub-bandgap photoresponse at 1300 nm [133]. The sub-bandgap absorption will be detailed in the sections below. In the mid to late 1990s was the rise of ultrafast LT-GaAs photodetectors. 1-THz imaging systems were realized thanks to fast LT-GaAs photoconductive switches PCSs [134] and LT-GaAs is still the best candidate for ultra-fast photoconductive devices. In the following we will present the main parameters that define the carrier lifetime, the resistivity and the carrier mobility in the LT-GaAs.

In the GaAs case the normal growth temperature ranges between 580^{o}C and 600^{o}C [116]. It has been shown that when GaAs is grown by molecular beam epitaxy (MBE) at low temperatures (250^{o}C), its crystallin structure is non-stochiometric with around 1% of Arsenic excess. This excess induces point defects (El2) in the material and the density of these point defects vary with the annealing or growth temperature [131]. From Figure A.1, it is shown that at low growth temperatures and before annealing, the point defects are distributed in all the crystallin structure in several forms such as

vacancies in the Ga positions (V_{Ga}), As antisites (As_{Ga}) which are Arsenic atoms replacing Gallium atoms and As interstitial (As_i) which are Arsenic atoms present between two atoms in the normal structure of the lattice.

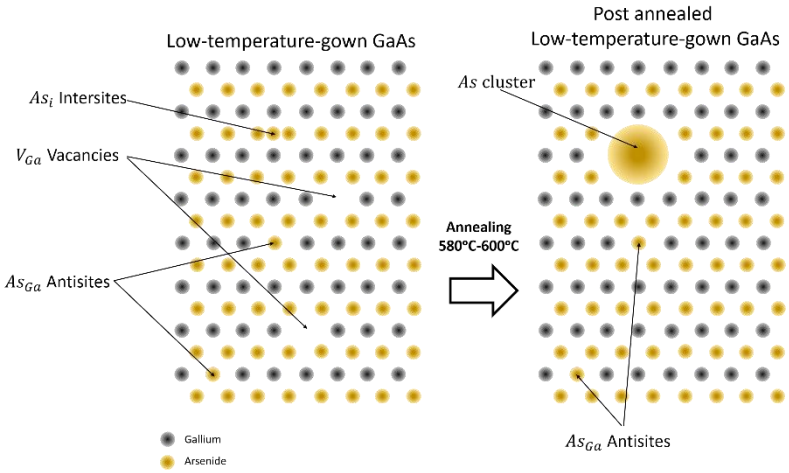

Figure A.1 representation of the LT-GaAs crystal before and after annealing

Annealing was observed to convert these point defects (mainly the As interstitial) into Arsenic clusters [135]. As a result, the crystallin structure tends to be more stochiometric as in the case of high temperature grown GaAs with clusters of As. Carrier lifetimes were shown to be proportional to the clusters spacing and inversely proportional to the clusters size. It is also important to note that when annealed, the number of As-clusters increases resulting in an increase in the material dark resistivity (>10^3KΩ.cm) [136]. To sum up, the carrier lifetime is reduced for higher growth temperatures and higher annealing temperatures. Meanwhile, in fast photoconductive devices, high dark resistivities are required for higher photoresponses. In 2003, Gregory et al. [137] observed that these do not occur at the same rate, that is, the lifetime remains fairly constant up to anneal temperatures of 500°C allowing a good combination of fairly low carrier lifetime and high dark resistivity. In a femtosecond pump-probe reflectivity measurements, the shortest measured lifetime (90 fs) corresponds to a sample grown at 195°C and annealed at 580°C for 10 min [136].

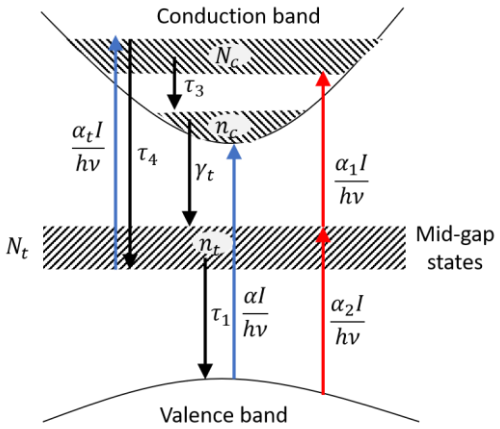

FigureA.2: Energy band diagram of LT-GaAs

Excitation with $E_{photon} \geq E_g$

For a better understanding, FigureA.2 shows the energy-band diagram of LT-GaAs with all the possible optical carrier excitations and relaxations. The blue arrows correspond to pump photon energies greater or equal to the bandgap energy. Eventually, the density of the of the point defects plays an important role in defining this energy-band diagram. If the LT-GaAs crystallin is rich with the EL2 point defects (defect concentration $10^{20} cm^{-3}$), mid-gap energy levels are created allowing different type of transitions depending on the photon energy. Initially, the energy gap between the valence band and the bottom of the conduction band is 1.42 eV corresponding to an optical wavelength of 870 nm. This is represented by a direct transition shown in FigureA.2 by the first blue arrow $\frac{\alpha I}{h\nu}$ where α is the band-to-band absorption coefficient, I is the incident intensity of light with a photon energy $h\nu$. In fact, after the electrons are excited directly from the valence band to the conduction band, carrier populations in the bottom of the conduction band relax to form populations in the trap states that decays back to the valence band to recombine with holes. This two-step recombination is called Shockley-Read-Hall (SRH). Carriers that are still trapped in the mid-gap states allow transitions to higher excited states in the conduction band. This can be shown by the second blue arrow transition $\frac{\alpha_t I}{h\nu}$, where α_t is the absorption coefficient from the traps to excited states in the conduction band.

Carrier lifetime measurement: In order to understand the carrier relaxation dynamics in semiconductors, a common technique is the transient differential transmission/reflection

pump-probe experiment. This involves splitting a pulsed laser beam into a high-power pump signal and a low-power probe signal, and then measuring the reflection/transmission of the probe signal as the time delay between the two signals is varied. The setup for the used experiment (reflection) is shown in Figure A.3. By using a delay line to adjust the path length of the pump, it can be made to arrive before, after, or simultaneously with the probe at the sample. Figure A.4 (a) and (b) shows the time-resolved photoreflectance ($\Delta R/R$) measurements in linear and logarithmic scale respectively as function of the delay time (Δt). This measurement was performed using a 200 fs optical pulses at $\lambda = 820$ nm provided by a Ti: Sapphire laser. The studied LT-GaAs sample was grown at 250 ± 5°C and annealed at 580°C during 60s. When the pump and probe are synchronized, a maximum differential reflectance is measured as shown in figure A.4.

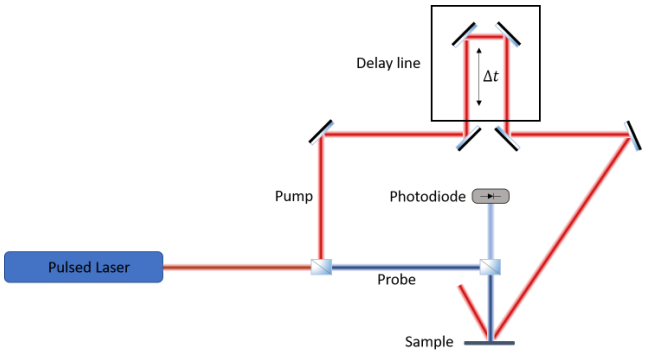

Figure A.3: Pump-probe setup for carrier lifetime measurements

At this point, the absorption of the material is saturated and all carriers have been excited to the conduction band. As a result, it is less likely that additional photons will be absorbed, which is depicted in the peak in the differential reflectance. This peak is plotted on a logarithmic scale in Figure A.4 (b) for easier analysis. After the saturation point, the carriers begin to decay following the processes described above and depicted in different colors in Figure A.4. The rapid decrease in the red curve represents the thermalization of carriers from higher energy states in the conduction band to the band edge (τ_3). The lifetime of the carriers can be determined from the blue curve, which represents the SRH recombination of carriers from the conduction band to the valence band through mid-gap states. The presence of As antisites causes some carriers to become trapped in the mid-

gap states for longer periods of time before eventually decaying back to the valence band, as indicated by the green curve.

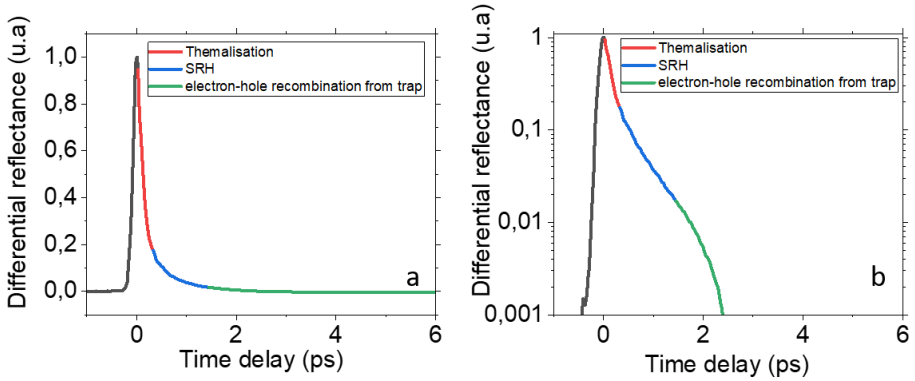

Figure A.4:(a) Differential photoreflectance as function of the pump delay time in linear and (b) logarithmic scale

B. Coplanar waveguides (CPW):

In an ideal CPW, the metal is deposited on a semi-insolating substrate of infinite thickness and the ground planes are semi-infinite. This results in the presence of two fundamental modes having no cutoff frequency [138][139]:

- Uneven quasi-TEM mode, also called coplanar mode.
- Even quasi-TE mode, also called slit mode.

The parities are defined based on the considerations of the longitudinal components of the electromagnetic field relative to the Oy axis. We then qualify the mode for which $E_z(-x,y) = E_z(x,y)$ as an even mode and the mode for which $E_z(-x,y) = -E_z(x,y)$ as an odd mode. The uneven mode (coplanar mode) is generally the desired propagating mode in the transmission line [140]. Meanwhile, the even mode is highly dispersive mode and is excited due to the discontinuity in the ground plane. The latter can be filtered out by connecting the two ground planes by an air bridge [138][139][140][141].

In reality, the substrate thickness and the width ground line are finite. As a result, other modes appear in the structure that we will call parasitic modes. In this case we consider the approximation of a quasi-TEM mode. By definition, a TEM mode can only exist in the presence of at least two disjoint metallic conductors immersed in a homogeneous medium. It is a non-dispersive and cutoff-free propagation mode. The coplanar line being an open propagation structure, the electromagnetic fields propagate

both in the substrate and in the air. As a result, there are non-zero longitudinal components of E_z and H_z. However, their amplitudes remain relatively low and we speak of a quasi-TEM mode. The dispersive nature of the line comes from one part of this inhomogeneity of structure (possible propagation of parasitic modes) and on the other hand, the skin effect which causes a frequency-dependent variation of the effective permittivity. These parasitic modes (slit modes, micro-strip modes, higher order coplanar modes) can be minimized by applying the following criteriums on the design:

$$h_s < 0.12\lambda_d \tag{B.1}$$

$$d \leq \frac{\lambda_d}{10} \tag{B.2}$$

$$d \ll h_s \tag{B.3}$$

$$d \ll W_g \tag{B.4}$$

h_s, d, λ_d and W_g are respectively the substrate thickness, the distance between the ground lines, the wavelength in the dielectric and the ground line width. By applying a higher constraint on equation (B.2) such that $d < \frac{\lambda_d}{20}$, this can effectively eliminate radiation losses. When designing the transmission line, it is important to ensure that established above standards are met in order to reduce the presence of parasitic modes and to support only the odd mode. For example, in millimeter wave range, it is hard to meet condition (B.1) when using substrates such as GaAs or InP, which usually have a thickness of 400 µm. Adhering to this rule would result in very small distance between ground lines, d, and this would lead to significant increase in ohmic losses in the transmission line. In situations where the substrate thickness is much greater than d, surface waves are unavoidable, but they do not have any significant impact, as long as condition (B.2) is met. Note that conditions (B.3) and (B.4) are also important to reduce the microstrip modes. Now that we presented the main conditions to design a coplanar waveguide

allowing the propagation of a quasi-TEM coplanar mode, we can consider the transmission line theory to model the propagation of such mode in the structure. Figure B.1 shows the equivalent circuit model of a transmission line which can be used to model the propagation along the line. From the circuit below, we can conclude the following:

- The characteristic impedence Z_c:

$$Z_c = \sqrt{\frac{R + jL\omega}{G + jC\omega}} \tag{B.5}$$

- The propagation constant γ:

$$\gamma = \sqrt{(R + jL\omega)(G + jC\omega)} = \alpha + j\beta \tag{B.6}$$

α: absorption coefficient (Np/mm or dB/mm)

β: propagation constant of the guided mode ($\beta = \frac{2\pi}{\lambda}$)

- The phase velocity v_φ and the refractive index of the mode n_{eff}:

$$v_\varphi = \frac{\omega}{\beta} \tag{B.7}$$

$$n_{eff} = \frac{c_0}{v_\varphi} \tag{B.8}$$

Now we will assume that we have negligible losses which leads us to calculate β as function of L, C and ω. As a result, the refractive index can be written as the following:

$$n_{eff} = c_0\sqrt{LC}$$

Since the capacitance and inductance of a CPW are determined by the dimensions of the central strip line we can now define the effective index of the mode of propagation based on the dimensions of the CPW and the membrane. However, it is important to note that these results come with a trade-off with the propagation losses.

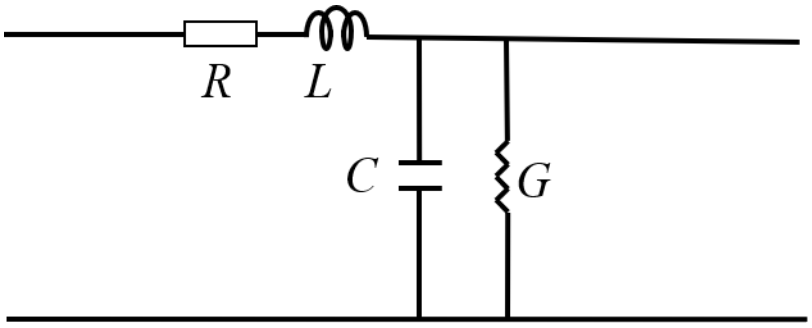

Figure B.1: Equivalent circuit model of a TEM transmission line.

C. Grating couplers:

State of the art:

Paper	SiN type	Designed Wave-length (nm)	SiN layer thickness (nm)	SMF-28 angle from normal (°)	Measured Maximum Fiber-to-Chip Coupling Efficiency	1 dB Bandwidth (nm)	Remarks
[142],[143]	LPCVD Si_3N_4 n = 2.022	1550	700	8	-3.7 dB (42.7%)	54	For non-linear applications in 700 nm Si_3N_4
[144]	PECVD SiN	1550 / 1310	700	8	-6.35 dB (23.2%) / -9.2 dB (12.0%)	~39 / ~31	Unidirectional, single-polarization dual-band GC
[145],[146]	Si_3N_4 n = 2.0	1550	600	16.5	-1.5 dB (70.8%)	35	No top oxide to increase grating strength; SMF-28 112µm above chip surface to diffract over 25 periods
[147]	PVD SiN_x n = 1.980	1550	550	0	-4.9 dB (32%) (simulated)	~1 nm	SiN_x GC between DBR-pair cavity
[148]	Si_3N_4 n = 1.9827	1550	550	-2.9	-2.66 dB (54.2%) (simulated)	80	SMF Gaussian MFD is 20.8µm
[149]	LPCVD Si_3N_4 n = 2.0	1550	400	8	-4.2 dB (38.0%)	67	Through-etch Si_3N_4 GC with 2.25µm BOX
[150],[151]	LPCVD Si_3N_4	1550	400	10	-5.4 dB (28.8%)	~18	SiN GC array for multicore optical fiber
[152]	Si_3N_4	1550	400	7	-6.58 dB (22%)	~29	Gold mirror; grating not etched

[153]	Liquid source CVD Si_3N_4 n = 1.80	1550	325	0	-4.5 dB (35.5%)	~35	Si_3N_4 GC with 10 Si_3N_4/SiO_2 DBR layers
[154]	PECVD SiN_x n = 1.9894	1550	220	9	-2.73 dB (53.3%)	47.9	Through-etched displaced SiN_x bilayer

Table C.1 State of the art of Si_3N_4 grating couplers for telecom wavelength.

Table C.1 from reference [154] is a state of the art if SiN_x grating couplers for 1550 nm illumination. It shows that couplers with a basic design achieve coupling losses between 2 dB and 3 dB, whereas 1 dB can be reached only at the expense of very complex design and fabrication. But in general, we could consider that a simple grating design could reach around 3 dB coupling losses. Another interesting parameter is the 1-dB bandwidth of the grating. In our case, this parameter is not much important since the two wavelengths λ_1 and λ_2 generating the beating source will be a couple of nanometers around the peak wavelength 1550 nm where the grating is still sufficiently broadband. For example, if $f_{THz} = 1$ THz and $\lambda_1 = 1550$ nm then $\lambda_2 =$1558 nm and from the table below we can see that for the majority of cases the grating coupler possess a 1-dB bandwidth of tens of nanometers.

Grating theory:

Next, we will provide a basic model of the grating theory. In FigureC.1, we will consider an optical mode propagating in a planar waveguide having a propagation constant k_{mz} where m is the order of the mode. By periodically notching the waveguide core we can make a diffraction grating such that light that is diffracted off the rulings will constructively interfere toward the direction of the optical fiber core. The diffraction period is chosen such that the scattering from individual rulings constructively interferes at a desired angle.

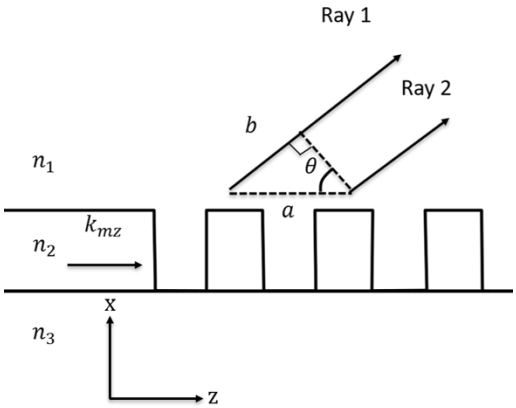

Figure C.1: Schematic representation of the grating coupler showing the diffracted rays

From Figure C.1 we can write a relation between the diffraction angle θ and the periodicity a. For a given period, the path length difference (b) results in constructive interference between ray 1 and ray 2. This will happen when the phase difference between ray 1 and ray 2 are integer multiples of 2π. If we define the phases of ray 1 and ray 2 as $k_1 b$and $k_{mz} a$ respectively, the phase matching condition can be written as follows:

$$k_{mz} a - k_1 b = 2\pi m \tag{C.1}$$

where $m = \pm 1, \pm 2, \pm 3 \ldots$

if we develop the equation (C.1) we get:

$$\frac{2\pi}{\lambda} n_{eff} a - \frac{2\pi}{\lambda} n_1 b = 2\pi m$$

$$\Longrightarrow n_{eff} a - n_1 b = m\lambda$$

$$\Longrightarrow \sin(\theta) = \frac{n_{eff} - \frac{m\lambda}{a}}{n_1} \tag{C.2}$$

Generally, when a grating is designed, equation (C.2) is a simple way to find the diffraction angle or the period since all the other parameters are already defined.

D. Simulation methods:

1) MODE – FDE (Finite Difference Eigenmode) solver

This technique basically calculates the spatial profile and the frequency dependence of the mode in the structure by solving Maxwell's equations on a cross sectional mesh of the

waveguide. This solver calculates the electric field mode profiles, the effective index, the group index, the dispersion etc. In general, a 3D design is constructed and the calculation is realized in a 2D chosen cross section of the design.

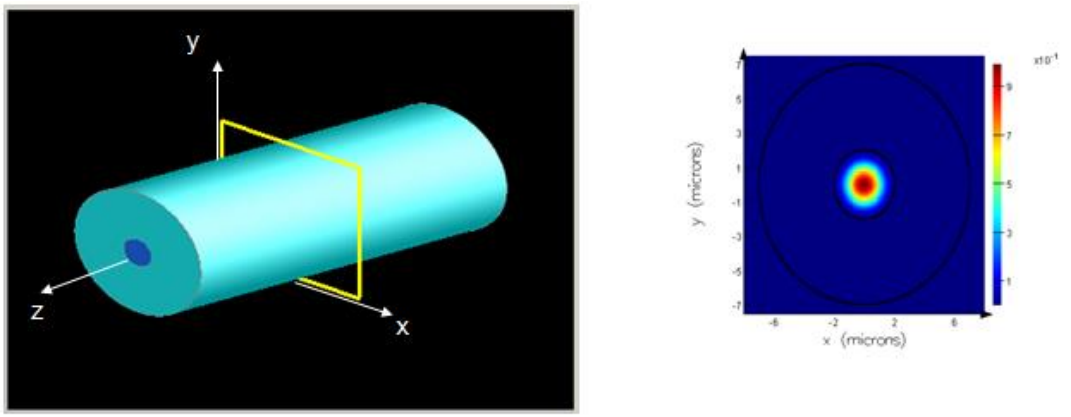

Figure D.1: FDE solver interface showing an example of a cross section of a fiber with the calculated mode profile in this cross section.

Figure D.1 illustrates a fiber design in which the core mode profile is determined using a solver called MODE-FDE. This solver employs a finite-difference algorithm to create a mesh of the waveguide geometry, which allows it to handle a wide range of waveguide structures. Once the structure is meshed, the solver uses sparse matrix techniques to solve a matrix eigenvalue problem based on Maxwell's equations, yielding information about the various modes present in the system and their characteristics, such as the effective index, group index, propagation losses, polarization, and effective mode area. The MODE-FDE solver is based on the work of Zhu and Brown [155], with additional modifications and enhancements, and more details about its meshing and computation techniques can be found in the following reference [156].

2) Finite Difference Time Domain (FDTD) solver [157][158][159]

The FDTD (Finite-Difference Time-Domain) technique is a method for analyzing the behavior of electromagnetic fields in 3D or 2D geometries over time. It involves solving Maxwell's curl equations, which describe the relationships between electric and magnetic fields in non-magnetic materials, using a finite-difference approach. This technique allows for the calculation of various physical parameters, including the complex pointing vector and the transmission, reflection, and absorption of electromagnetic waves in a specific

section or volume. The FDTD algorithm implemented in the Lumerical tool is described in more detail in the referenced publication [160].

The FDE solver shown in Figure D.1 is limited to calculating the electric field profile of the fiber mode and its optical properties within a 2D cross section of the fiber structure. In contrast, the FDTD method allows a 3D simulation region in which the mode can propagate for a specified distance. By placing monitors at specific positions within the simulated structure, it is possible to extract information about the mode's properties, such as transmission, polarization, and losses, as it propagates through the fiber.

3) 3D BPM (3D finite difference beam propagation method)[161]

The 3D finite difference beam propagation method is a computational method used to solve the scalar wave equation, which describes the behavior of electromagnetic waves in a given material. The method involves dividing the waveguide into a grid of small cells, and solving the wave equation at each cell to determine the electric field amplitude and phase of the light at that point. The finite difference approximation is used to discretize the wave equation, which allows for its numerical solution using standard computational techniques. The method can be used to study the propagation of light through complex optical waveguides, and to understand how the wave characteristics are affected by factors such as the material properties, geometry, and boundary conditions of the waveguide.

E. Device fabrication:

I. Adhesive Bonding

Both the HR-Si wafer and the quarter wafer of the epilayer are cleaned in an ultrasonic acetone bath. The active layer is treated with diluted hydrochloric acid (HCl) to remove any oxides. The HR-Si wafer undergoes surface treatment using hydrofluoric acid (HF), followed by a mixture of sulfuric acid (H_2SO_4) and hydrogen peroxide (H_2O_2).Finally, a layer of diluted benzocyclobutene (BCB) is spin-coated onto both the LT-GaAs and HR-Si surfaces. BCB is a hydrocarbon that is commonly used in adhesive bonding due to its low moisture absorption (0.12% by weight) and low absorption losses in the THz region [162].

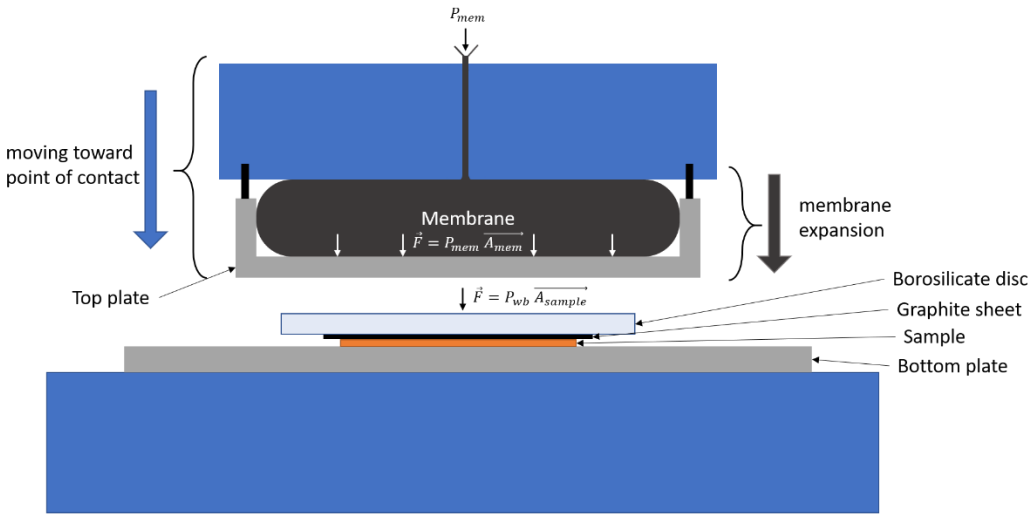

Figure E.1: Schematic representation of the bonding process inside the chamber.

-Adhesive Bonding:

The bonding process is carried out using a commercial Süss SB6e machine. The process is largely automated and follows a predetermined recipe that is programmed into the machine's software. The recipe includes parameters such as chamber pressure, bonding pressure, chamber temperature, temperature ramps, and time. The quarter wafer is placed on top of the HR-Si wafer and the stack is placed on a bottom plate that can be detached from the machine. A 500 µm thick graphite sheet and a 3-inch diameter borosilicate disc are then placed on top of the stack. The 4 mm thick borosilicate helps to apply a uniform pressure to the entire structure, while the graphite sheet protects the edges of the quarter wafer from excessive pressure to prevent cracking. The bottom plate with the stack is then loaded into a holder and placed in the chamber to begin the bonding process. During the process, a top structure consisting of the top plate and a membrane will move towards the contact point with the stack. When the top structure reaches the contact point, a pressure P_{mem} is applied to inflate the membrane and press down on the top plate and the sample. Figure E.1 shows a simplified depiction of the bonding process, and Figure E.2shows the trend of the chamber temperature and the membrane pressure in the first 300 min of the recipe. The bonding process starts by applying a constant pressure to the membrane, increasing it to 615 mbar, and raising the temperature of the top and bottom plates to 250°C. This step takes 1 hour and 12 minutes. The temperature of the plates and the

pressure on the membrane are then maintained at this level for another 1 hour and 12 minutes. Finally, the pressure is released and the temperature is gradually lowered to room temperature (this step is not shown inFigure E.2). The wafer is then removed from the machine.

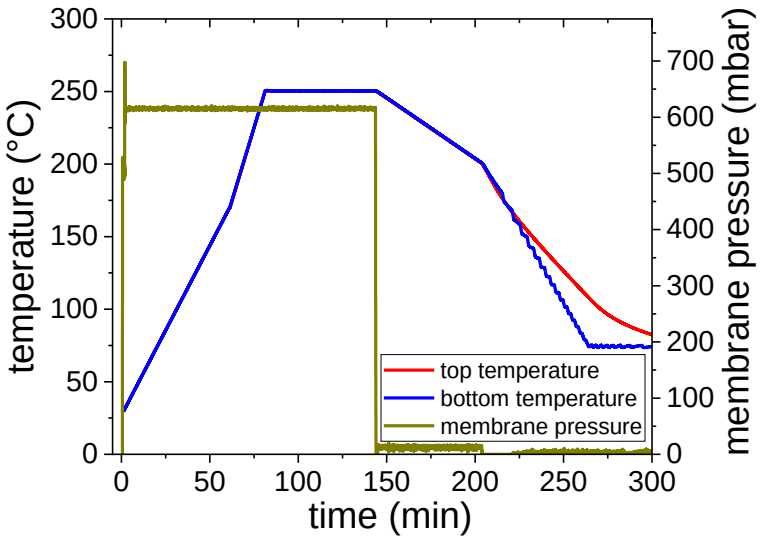

Figure E.2: Chamber temperature and membrane pressure of the adhesive bonding as function of time.

II. Reactive Ion Etching (RIE):

In a reactive ion etching (RIE) process, a vacuum is created by removing air from the chamber to allow plasma to ignite. Plasma is generated through the application of a strong radio frequency (RF) electromagnetic field to the wafer platter, which ionizes the gas molecules in the chamber by removing their electrons. The oscillating electric field accelerates the electrons up and down in the chamber, occasionally causing collisions with the chamber's upper wall or wafer platter. In contrast, the ions, being heavier, respond less to the RF field. Electrons that are absorbed into the chamber walls are discharged to ground and do not alter the electronic state of the system, while those deposited on the wafer platter can cause a charge buildup due to its DC isolation, leading to a negative voltage of several hundred volts. The plasma has a slight positive charge, resulting from the higher concentration of positive ions relative to free electrons. Positive ions tend to drift towards the wafer platter and react chemically with the surface materials of the samples. They can also remove material by sputtering through transferring their kinetic

energy. The vertical delivery of reactive ions in RIE can produce highly anisotropic etch profiles, unlike the typically isotropic profiles generated by wet chemical etching. The etching conditions in an RIE system depend on a number of process parameters, such as chamber pressure, gas flows, and RF power. shows a simplified representation of an RIE process. Figure E.3 shows a schematic representation of an RIE chamber.

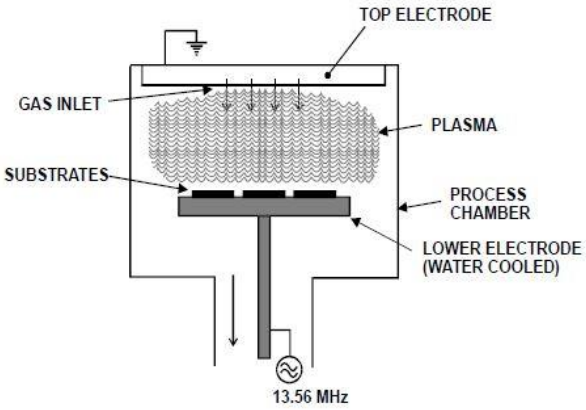

Figure E.3: Schematic representation of the chamber of an RIE tool.

III. GaAs substrate Etch:

The details of the etching process of the GaAs substrate and the GaInP stop etch layer are described as follows:

1. The first step involves using a mixture of H_2O_2:H_2SO_4:H_2O in a ratio of 8:1:1 to etch the majority of the 400 µm of GaAs. H_2O_2 oxidizes the GaAs, enabling it to be dissolved by the H_2SO_4. The addition of H_2O slows down the etching rate, allowing us to periodically check the thickness of the GaAs and ensure the etching is homogeneous. To further improve the homogeneity, the sample is placed on a rotating holder and immersed in the acid solution, with a magnetic stirrer mixing the solution. Figure E.4 shows a time track of the GaAs thickness during the etching in several regions of the wafer. The etch rate during this step is approximately 18 µm/min, and after 20 minutes, the GaAs thickness is around 30 µm with an acceptable homogeneity of ± ~5 µm. It is worth noting that the etch rate in the middle of the wafer is slightly higher than at the edges. Once this fast etch step is complete, we change the etching solution in order to continue etching until we reach the etch stop layer.

Etch time (min)	Thickness (µm)			
	A	B	C	D
0	391	386	396	391
10	202	170	168	172
18	63	51	44	49
20	37	34	23	28

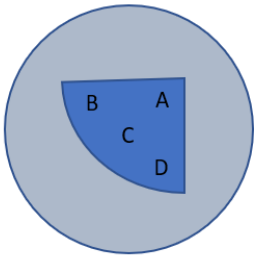

Figure E.4: Track of the GaAs substrate thickness as function of time in different region of the sample.

2. In the second step of the etching process, a slow etching step was used to etch the remaining GaAs. This involved using a mixture of H_2O:H_2O_2:NH_4OH in a 1:1:2 ratio to etch the remaining ~30 µm of GaAs over a period of 28 minutes. This mixture resulted in a relatively low etch rate of ~1.09 µm/min, allowing for better visual control of the final micrometers of the GaAs substrate.
3. In the third and final step of the etching process, the 100 nm GaInP etch stop layer is etched in a single step. The sample is placed in a solution of 30% HCl for 30 seconds, until a color change is observed on the quarter wafer. This indicates that the LT-GaAs layer is reached. The sample is then rinsed in isopropyl alcohol (IPA) and is ready for device fabrication.

IV. E-beam lithography:

In the engineering community, the term "E-beam lithography" is commonly used to refer to the technique of using a focused beam of electrons to create micrometric and nanometric patterns on a sensitive, resistive polymer. This process is typically carried out using an electron beam lithography system, which employs an electromagnetic deflection system to scan the beam across the substrate. In the present study, we used a Raith nanofabrication machine (type ebpg5000Plus) for this purpose, as shown in Figure E.5. This particular machine utilizes a vector scan system that only deflects the beam to areas where part of the pattern is being exposed, rather than scanning the entire surface. This allows for high resolution, placement accuracy, and flexibility in patterning designs with length scales that may not be achievable with other lithography techniques. It also enables the overlap of different levels of lithography with high alignment accuracy, reaching less than 20 nm. One advantage of using a software mask to define the pattern is that it is easy

to change designs without having to create a new physical mask. However, other techniques such as photolithography are generally faster than E-beam lithography, as they utilize a physical mask that is exposed to UV light in a single step, rather than the serial process used in E-beam lithography, where the pattern is exposed one pixel at a time. The minimum pixel size for the Raith machine can reach 1.25 nm.

Figure E.5: ebpg 5000Plus E-beam lithography machine from RAITH nanofabrication company.

After exposing the resist material to the desired pattern using the electron beam lithography system, the next step is to perform a development process. This involves placing the sample in a specific chemical solution that allows the pattern to be created in the resist material. There are two main types of resists: positive and negative. When developed, a positive resist results in the dissolution of the patterned areas, creating a mold that can be filled with metal to create electrodes or other metallic structures. A negative resist, on the other hand, hardens the patterned areas and dissolves the unpatterned regions when developed, leaving behind only the hardened resist with the desired shape. Negative resists are often used in etching processes to protect areas that should not be etched. The development time is determined by the electron dose D (μC/cm²), which is defined in the software of the electron beam lithography machine. Another important parameter to consider is the writing frequency F, which is the rate at which the beam moves from one pixel to the next. In the machine used in this process, the writing frequency can range from

0.5 KHz to 50 MHz. It is calculated based on the measured beam current C (nA), the known pixel size r, and the dose required to properly expose the resist. The appropriate dose is typically determined through testing, in which the development time is fixed and patterns are repeated at different doses. The writing frequency can then be expressed as:

$$F[MHz] = 0.1 \times \frac{C[nA]}{D[\mu C/cm^2] \times r[\mu m]} \quad \text{(E.1)}$$

V. Plasma Enhanced Vapor Deposition (PECVD):

The principle of plasma-enhanced chemical vapor deposition (PECVD) involves the use of a low-pressure plasma to enhance the chemical reaction between precursor gases and a substrate. During the PECVD process, precursor gases are introduced into a vacuum chamber containing a substrate to be coated. A low-pressure plasma is then created using an electric field, which generates a high-energy environment that promotes the dissociation of the precursor molecules into reactive species such as radicals and ions. These reactive species react with the surface of the substrate and each other, leading to the formation of a thin film. The thickness and composition of the film can be controlled by adjusting the process parameters, such as the flow rate and composition of the precursor gases, the power and frequency of the electric field, and the pressure and temperature of the chamber. Overall, the principle of PECVD deposition involves the use of a low-pressure plasma to enhance the chemical reactions between precursor gases and a substrate, resulting in the formation of a thin film with controlled thickness and composition.

The PECVD tool used in this work is similar to the one used for RIE, but it is configured for deposition. In the latter, the RF modulation is applied to the top electrode instead of the lower electrode which in this case is heated up to 340°C.The process of depositing the layers using the PECVD machine involves several steps:

1. A sufficient vacuum is achieved and the lower electrode is heated up to the desired temperature in a pumping step.
2. The chamber is conditioned with 400 sccm of N_2 for 5 minutes in a purge step.

3. The deposition step involves defining a chamber pressure, an RF power, and different gas flows depending on the deposited material. The step time is determined based on the desired thickness, and the maximum error in the deposited thickness is typically less than ± 5% of the desired value.

Figure E.6 shows a schematic representation of the PECVD deposition process.

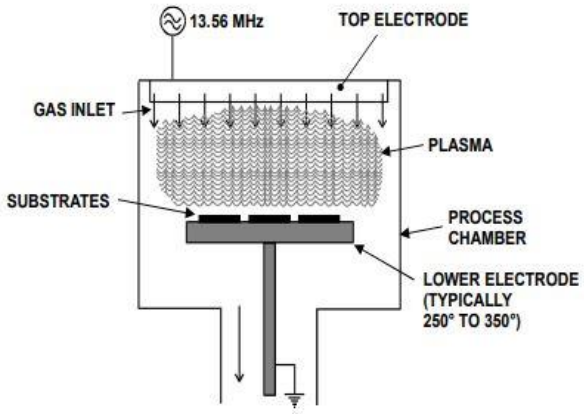

Figure E.6: Schematic representation of the PECVD deposition process.

In order to get a solid-state material from the gases, the following chemical reactions happen in the chamber:

- In the case of SiO_2, the reaction involves the combination of SiH_4 gas with N_2O gas to produce SiO_2 solid, as well as N_2 and H_2 gases as byproducts. N_2O is often used in the PECVD process for SiO_2 due to its ability to produce higher quality films compared to O_2.
- For the formation of Si_3N_4, the reaction involves the combination of SiH_4 gas with NH_3 gas to produce Si_3N_4 solid, along with H_2 gas as a byproduct.

It is worth noting that these reactions typically take place in a plasma environment, where the gases are ionized and can more easily react with each other to form solid materials.

VI. **Core patterning:**

The sample is first coated with a high-resolution positive resist, CSAR 62, and then patterned using E-beam lithography. The exposed areas are then developed using the AR600 546 developer, wherein the remaining resist protects the Si_3N_4 and represents the pattern of the core. Figure 3.27(a) shows the resist pattern of the grating coupler design with its dimensions matching those defined in the e-beam software. However, there may

still be some undeveloped resist around the grating, which can result in loss of design dimensions and non-straight resist profile if left for too long in the developer solution. To overcome this, a 10-second RIE based on oxygen plasma is used, which ensures a clean surface without significant changes in dimensions (Figure 3.27 (b)). A part of the grating is shown in Figure 3.27(c), which is etched using plasma RIE. The etching parameters are shown in Table E.1. The calculated etch rate is approximately 0.92 nm/s. The remaining resist is dissolved by soaking in a resist stripper bath at 70°C for 2 hours. Figure 3.27(d), (e), and (f) show the complete grating coupler, a top image of an MMI, and the transition of the waveguide from the back-reflecting mirror to the LT-GaAs active region, respectively.

RF power (W)	180
Chamber pressure (mT)	50
CHF_3 (sccm)	40
CF_4 (sccm)	40

Table E.1 Si_3N_4 etching parameters.

VII. **Bottom cladding patterning:**

ICP-RIE is a technique that involves the use of a coil surrounding the chamber that generates an alternating RF magnetic field. This magnetic field ionizes the gas molecules and atoms present in the chamber, resulting in a low-pressure plasma that can effectively etch the material. The absence of an electric field near the walls of the reactor ensures that there is no erosion or bombardment of the walls, leading to a higher level of anisotropy in the etching process. The induction phenomenon allows more particles to participate in the material etch, leading to a more efficient and precise fabrication process.

The SiO_2 etching parameters are shown in Table E.2.

RF power (W)	50
ICP power (W)	100
Chamber pressure (mT)	2
CHF_3 (sccm)	40

Table E.2 SiO_2 etching parameters.

References

[1] V. Lashkaryov Institute of Semiconductor Physics, NAS of Ukraine, 41, prospect Nauky, 03680 Kyiv, Ukraine and F. F. Sizov, "Brief history of THz and IR technologies," *Semicond. Phys. Quantum Electron. Optoelectron.*, vol. 22, no. 1, pp. 67–79, Mar. 2019, doi: 10.15407/spqeo22.01.067.

[2] M. Walther, B. M. Fischer, A. Ortner, A. Bitzer, A. Thoman, and H. Helm, "Chemical sensing and imaging with pulsed terahertz radiation," *Anal. Bioanal. Chem.*, vol. 397, no. 3, pp. 1009–1017, Jun. 2010, doi: 10.1007/s00216-010-3672-1.

[3] P. de Maagt, "Terahertz technology for space and earth applications," in *2006 First European Conference on Antennas and Propagation*, Nice, France: IEEE, Nov. 2006, pp. 1–4. doi: 10.1109/EUCAP.2006.4585001.

[4] R. Appleby, "Passive millimetre–wave imaging and how it differs from terahertz imaging," *Philos. Trans. R. Soc. Lond. Ser. Math. Phys. Eng. Sci.*, vol. 362, no. 1815, pp. 379–393, Feb. 2004, doi: 10.1098/rsta.2003.1323.

[5] R. Beigang, "Industrial Applications of Terahertz Technology: From Layer Thickness Measurements to Mail Screening," in *Imaging and Applied Optics 2014*, Washington, D.C.: OSA, Jul. 2014, p. AW1A.2. doi: 10.1364/AIO.2014.AW1A.2.

[6] G. Ducournau *et al.*, "Ultrawide-Bandwidth Single-Channel 0.4-THz Wireless Link Combining Broadband Quasi-Optic Photomixer and Coherent Detection," *IEEE Trans. Terahertz Sci. Technol.*, vol. 4, no. 3, pp. 328–337, May 2014, doi: 10.1109/TTHZ.2014.2309006.

[7] S. Sy *et al.*, "Terahertz spectroscopy of liver cirrhosis: investigating the origin of contrast," *Phys. Med. Biol.*, vol. 55, no. 24, pp. 7587–7596, Dec. 2010, doi: 10.1088/0031-9155/55/24/013.

[8] T. Ouchi *et al.*, "Terahertz Imaging System for Medical Applications and Related High Efficiency Terahertz Devices," *J. Infrared Millim. Terahertz Waves*, vol. 35, no. 1, pp. 118–130, Jul. 2013, doi: 10.1007/s10762-013-0004-5.

[9] J. Takayanagi *et al.*, "High-resolution time-of-flight terahertz tomography using a femtosecond fiber laser," *Opt. Express*, vol. 17, no. 9, p. 7533, Apr. 2009, doi: 10.1364/OE.17.007533.

[10] V. N. G. & C. KG, "Non-destructive terahertz sensor for coatings," *European Coatings*. http://www.european-coatings.com/Raw-materials-technologies/Production-and-testing/Non-destructive-terahertz-sensor-for-coatings (accessed Mar. 30, 2020).

[11] "COBE | Science Mission Directorate." https://science.nasa.gov/missions/cobe (accessed Apr. 02, 2020).

[12] "Opton Laser International - Laser sub-THz IMPATT." https://www.optonlaser.com/laser/laser-sub-thz-impatt (accessed Apr. 02, 2020).

[13] A. S. Hajo, O. Yilmazoglu, A. Dadgar, and F. Kuppers, "Reliability Improvement of High-Power THz GaN Gunn Sources for Active Imaging Systems," in *2018 43rd International Conference on Infrared, Millimeter, and Terahertz Waves (IRMMW-THz)*, Nagoya: IEEE, Sep. 2018, pp. 1–2. doi: 10.1109/IRMMW-THz.2018.8510363.

[14] R. Tsu and L. Esaki, "Tunneling in a finite superlattice," *Appl. Phys. Lett.*, vol. 22, no. 11, pp. 562–564, Jun. 1973, doi: 10.1063/1.1654509.

[15] L. L. Chang, L. Esaki, and R. Tsu, "Resonant tunneling in semiconductor double barriers," *Appl. Phys. Lett.*, vol. 24, no. 12, pp. 593–595, Jun. 1974, doi: 10.1063/1.1655067.

[16] A. V. Raisanen, "Frequency multipliers for millimeter and submillimeter wavelengths," *Proc. IEEE*, vol. 80, no. 11, pp. 1842–1852, Nov. 1992, doi: 10.1109/5.175259.

[17] S. Schiller, B. Roth, F. Lewen, O. Ricken, and M. C. Wiedner, “Ultra-narrow-linewidth continuous-wave THz sources based on multiplier chains,” *Appl. Phys. B*, vol. 95, no. 1, pp. 55–61, Apr. 2009, doi: 10.1007/s00340-008-3279-9.
[18] A. Siligaris *et al.*, “A 270-to-300 GHz Sub-Harmonic Injection Locked Oscillator for Frequency Synthesis in Sub-mmW Systems,” *IEEE Microw. Wirel. Compon. Lett.*, vol. 25, no. 4, pp. 259–261, Apr. 2015, doi: 10.1109/LMWC.2015.2401980.
[19] R. Warnecke and P. Guenard, “Some recent work in France on new types of valves for the highest radio frequencies,” *Proc. IEE - Part III Radio Commun. Eng.*, vol. 100, no. 68, pp. 351–362, Nov. 1953, doi: 10.1049/pi-3.1953.0073.
[20] J. H. Booske, “Plasma physics and related challenges of millimeter-wave-to-terahertz and high power microwave generation,” *Phys. Plasmas*, vol. 15, no. 5, p. 055502, May 2008, doi: 10.1063/1.2838240.
[21] S. S. Dhillon *et al.*, “The 2017 terahertz science and technology roadmap,” *J. Phys. Appl. Phys.*, vol. 50, no. 4, Art. no. 4, Feb. 2017, doi: 10.1088/1361-6463/50/4/043001.
[22] L. Esaki and R. Tsu, “Superlattice and Negative Differential Conductivity in Semiconductors,” *IBM J. Res. Dev.*, vol. 14, no. 1, pp. 61–65, Jan. 1970, doi: 10.1147/rd.141.0061.
[23] J. Faist, F. Capasso, D. L. Sivco, C. Sirtori, A. L. Hutchinson, and A. Y. Cho, “Quantum Cascade Laser,” *Science*, vol. 264, no. 5158, pp. 553–556, Apr. 1994, doi: 10.1126/science.264.5158.553.
[24] R. Köhler *et al.*, “Terahertz semiconductor-heterostructure laser,” *Nature*, vol. 417, no. 6885, pp. 156–159, May 2002, doi: 10.1038/417156a.
[25] S. Khanal, L. Gao, L. Zhao, J. L. Reno, and S. Kumar, “High-temperature operation of broadband bidirectional terahertz quantum-cascade lasers,” *Sci. Rep.*, vol. 6, no. 1, p. 32978, Dec. 2016, doi: 10.1038/srep32978.
[26] Q. Lu, D. Wu, S. Sengupta, S. Slivken, and M. Razeghi, “Room temperature continuous wave, monolithic tunable THz sources based on highly efficient mid-infrared quantum cascade lasers,” *Sci. Rep.*, vol. 6, no. 1, p. 23595, Jul. 2016, doi: 10.1038/srep23595.
[27] Y. Jiang *et al.*, “Spectroscopic Study of Terahertz Generation in Mid-Infrared Quantum Cascade Lasers,” *Sci. Rep.*, vol. 6, no. 1, p. 21169, Aug. 2016, doi: 10.1038/srep21169.
[28] Y. Irimajiri *et al.*, “Precise Evaluation of a Phase-Locked THz Quantum Cascade Laser,” *IEEE Trans. Terahertz Sci. Technol.*, vol. 6, no. 1, pp. 115–120, Jan. 2016, doi: 10.1109/TTHZ.2015.2504792.
[29] H. Richter *et al.*, “Performance of a compact, continuous-wave terahertz source based on a quantum-cascade laser,” in *35th International Conference on Infrared, Millimeter, and Terahertz Waves*, Rome, Italy: IEEE, Sep. 2010, pp. 1–1. doi: 10.1109/ICIMW.2010.5612338.
[30] A. Valavanis *et al.*, “Terahertz quantum cascade lasers with >1 W output powers,” *Electron. Lett.*, vol. 50, no. 4, pp. 309–311, Feb. 2014, doi: 10.1049/el.2013.4035.
[31] A. Albo and Y. V. Flores, “Temperature-Driven Enhancement of the Stimulated Emission Rate in Terahertz Quantum Cascade Lasers,” *IEEE J. Quantum Electron.*, vol. 53, no. 1, pp. 1–5, Feb. 2017, doi: 10.1109/JQE.2016.2631899.
[32] G. Xu *et al.*, “Efficient power extraction in surface-emitting semiconductor lasers using graded photonic heterostructures,” *Nat. Commun.*, vol. 3, no. 1, p. 952, Jan. 2012, doi: 10.1038/ncomms1958.
[33] A. Yazgan, L. Jofre, and J. Romeu, “The state of art of terahertz sources: A communication perspective at a glance,” in *2017 40th International Conference on Telecommunications and Signal Processing (TSP)*, Barcelona, Spain: IEEE, Jul. 2017, pp. 810–816. doi: 10.1109/TSP.2017.8076101.

[34] Y. Bai, N. Bandyopadhyay, S. Tsao, S. Slivken, and M. Razeghi, “Room temperature quantum cascade lasers with 27% wall plug efficiency,” *Appl. Phys. Lett.*, vol. 98, no. 18, p. 181102, May 2011, doi: 10.1063/1.3586773.
[35] L. Li *et al.*, “Terahertz quantum cascade lasers with >1 W output powers,” *Electron. Lett.*, vol. 50, no. 4, pp. 309–311, Feb. 2014, doi: 10.1049/el.2013.4035.
[36] B. S. Williams, “Terahertz quantum-cascade lasers,” *Nat. Photonics*, vol. 1, no. 9, pp. 517–525, Sep. 2007, doi: 10.1038/nphoton.2007.166.
[37] Y. Chassagneux *et al.*, “Limiting Factors to the Temperature Performance of THz Quantum Cascade Lasers Based on the Resonant-Phonon Depopulation Scheme,” *IEEE Trans. Terahertz Sci. Technol.*, vol. 2, no. 1, pp. 83–92, Jan. 2012, doi: 10.1109/TTHZ.2011.2177176.
[38] “Robert W. Boyd-Nonlinear optics-Academic Press (2008).pdf.”
[39] J. R. Paul, M. Scheller, A. Laurain, A. Young, S. W. Koch, and J. Moloney, “Narrow linewidth single-frequency terahertz source based on difference frequency generation of vertical-external-cavity source-emitting lasers in an external resonance cavity,” *Opt. Lett.*, vol. 38, no. 18, p. 3654, Sep. 2013, doi: 10.1364/OL.38.003654.
[40] K. Fujita *et al.*, “Recent progress in terahertz difference-frequency quantum cascade laser sources,” *Nanophotonics*, vol. 7, no. 11, pp. 1795–1817, Oct. 2018, doi: 10.1515/nanoph-2018-0093.
[41] A. Crocker, H. A. Gebbie, M. F. Kimmitt, and L. E. S. Mathias, “Stimulated Emission in the Far Infra-Red,” *Nature*, vol. 201, no. 4916, pp. 250–251, Jan. 1964, doi: 10.1038/201250a0.
[42] Y.-S. Lee, *Principles of terahertz science and technology*. New York, NY: Springer, 2009.
[43] A. Pagies, G. Ducournau, and J.-F. Lampin, “Low-threshold terahertz molecular laser optically pumped by a quantum cascade laser,” *APL Photonics*, vol. 1, no. 3, p. 031302, Jun. 2016, doi: 10.1063/1.4945355.
[44] J.-F. Lampin *et al.*, “Quantum cascade laser-pumped terahertz molecular lasers: frequency noise and phase-locking using a 1560 nm frequency comb,” *Opt. Express*, vol. 28, no. 2, p. 2091, Jan. 2020, doi: 10.1364/OE.379960.
[45] A. Javan, E. A. Ballik, and W. L. Bond, “Frequency Characteristics of a Continuous-Wave He–Ne Optical Maser,” *J. Opt. Soc. Am.*, vol. 52, no. 1, p. 96, Jan. 1962, doi: 10.1364/JOSA.52.000096.
[46] E. R. Brown, F. W. Smith, and K. A. McIntosh, “Coherent millimeter-wave generation by heterodyne conversion in low-temperature-grown GaAs photoconductors,” *J. Appl. Phys.*, vol. 73, no. 3, pp. 1480–1484, Feb. 1993, doi: 10.1063/1.353222.
[47] E. R. Brown, K. A. McIntosh, K. B. Nichols, and C. L. Dennis, “Photomixing up to 3.8 THz in low-temperature-grown GaAs,” *Appl. Phys. Lett.*, vol. 66, no. 3, pp. 285–287, Jan. 1995, doi: 10.1063/1.113519.
[48] A. Deninger, “State-of-the-art in terahertz continuous-wave photomixer systems,” in *Handbook of Terahertz Technology for Imaging, Sensing and Communications*, Elsevier, 2013, pp. 327–373. doi: 10.1533/9780857096494.2.327.
[49] T. Ishibashi, T. Furuta, N. Shimizu, K. Nagata, Y. Matsuoka, and M. Tomizawa, “Pin photodiode with improved frequency response and saturation output,” Oct. 1998.
[50] E. Schlecht *et al.*, “Schottky Diode Based 1.2 THz Receivers Operating at Room-Temperature and Below for Planetary Atmospheric Sounding,” *IEEE Trans. Terahertz Sci. Technol.*, vol. 4, no. 6, pp. 661–669, Nov. 2014, doi: 10.1109/TTHZ.2014.2361621.
[51] P. H. Siegel, “Terahertz technology,” *IEEE Trans. Microw. Theory Tech.*, vol. 50, no. 3, pp. 910–928, Mar. 2002, doi: 10.1109/22.989974.
[52] P. H. Siegel, “THz Instruments for Space,” *IEEE Trans. Antennas Propag.*, vol. 55, no. 11, pp. 2957–2965, Nov. 2007, doi: 10.1109/TAP.2007.908557.

[53] L. Liebermeister, S. Nellen, R. Kohlhaas, S. Breuer, M. Schell, and B. Globisch, "Ultra-fast, High-Bandwidth Coherent cw THz Spectrometer for Non-destructive Testing," *J. Infrared Millim. Terahertz Waves*, vol. 40, no. 3, pp. 288–296, Mar. 2019, doi: 10.1007/s10762-018-0563-6.
[54] A. Roggenbuck *et al.*, "Coherent broadband continuous-wave terahertz spectroscopy on solid-state samples," *New J. Phys.*, vol. 12, no. 4, p. 043017, Apr. 2010, doi: 10.1088/1367-2630/12/4/043017.
[55] T. Nagatsuma, G. Ducournau, and C. C. Renaud, "Advances in terahertz communications accelerated by photonics," *Nat. Photonics*, vol. 10, no. 6, pp. 371–379, Jun. 2016, doi: 10.1038/nphoton.2016.65.
[56] S. Verghese, K. A. McIntosh, S. Calawa, W. F. Dinatale, E. K. Duerr, and K. A. Molvar, "Generation and detection of coherent terahertz waves using two photomixers," *Appl. Phys. Lett.*, vol. 73, no. 26, pp. 3824–3826, Dec. 1998, doi: 10.1063/1.122906.
[57] A. Khilo *et al.*, "Photonic ADC: overcoming the bottleneck of electronic jitter," *Opt. Express*, vol. 20, no. 4, p. 4454, Feb. 2012, doi: 10.1364/OE.20.004454.
[58] P. A. Gamage, A. Nirmalathas, C. Lim, D. Novak, and R. Waterhouse, "Design and Analysis of Digitized RF-Over-Fiber Links," *J. Light. Technol.*, vol. 27, no. 12, pp. 2052–2061, Jun. 2009, doi: 10.1109/JLT.2008.2006689.
[59] R. G. Vaughan, N. L. Scott, and D. R. White, "The theory of bandpass sampling," *IEEE Trans. Signal Process.*, vol. 39, no. 9, pp. 1973–1984, Sep. 1991, doi: 10.1109/78.134430.
[60] H. F. Taylor, O. Eknoyan, C. S. Park, K. N. Choi, and K. Chang, "Traveling wave photodetectors," vol. 1217, pp. 59–63, 1990.
[61] D. Pasalic, "M A Sc, B Eng, University of Victoria, Canada," p. 189, 1972.
[62] E. Rosencher and B. Vinter, *Optoelectronics*, 1st ed. Cambridge University Press, 2002. doi: 10.1017/CBO9780511754647.
[63] E. R. Brown, F. W. Smith, and K. A. McIntosh, "Coherent millimeter-wave generation by heterodyne conversion in low-temperature-grown GaAs photoconductors," *J. Appl. Phys.*, vol. 73, no. 3, Art. no. 3, Feb. 1993, doi: 10.1063/1.353222.
[64] E. R. Brown, S. Verghese, and K. A. McIntosh, "Terahertz photomixing in low-temperature-grown GaAs," presented at the Astronomical Telescopes & Instrumentation, T. G. Phillips, Ed., Kona, HI, Jul. 1998, pp. 132–142. doi: 10.1117/12.317346.
[65] E. Peytavit *et al.*, "Milliwatt-level output power in the sub-terahertz range generated by photomixing in a GaAs photoconductor," *Appl. Phys. Lett.*, vol. 99, no. 22, p. 223508, Nov. 2011, doi: 10.1063/1.3664635.
[66] F. Bavedila, E. Okada, J.-F. Lampin, G. Ducournau, and E. Peytavit, "LT-GaAs-Based Photomixers With >2 mW Peak Output Power Up to 320 GHz," in *2019 44th International Conference on Infrared, Millimeter, and Terahertz Waves (IRMMW-THz)*, Paris, France: IEEE, Sep. 2019, pp. 1–2. doi: 10.1109/IRMMW-THz.2019.8874037.
[67] E. Peytavit, P. Latzel, F. Pavanello, G. Ducournau, and J.-F. Lampin, "Milliwatt output power generated in the J-Band by a GaAs photomixer," in *2013 38th International Conference on Infrared, Millimeter, and Terahertz Waves (IRMMW-THz)*, Mainz, Germany: IEEE, Sep. 2013, pp. 1–3. doi: 10.1109/IRMMW-THz.2013.6665739.
[68] T. Umezawa, A. Kanno, K. Akahane, A. Matsumoto, N. Yamamoto, and T. Kawanishi, "Study of high power generation in UTC-PD at 110-210 GHz," in *Terahertz, RF, Millimeter, and Submillimeter-Wave Technology and Applications XI*, L. P. Sadwick and T. Yang, Eds., San Francisco, United States: SPIE, Feb. 2018, p. 41. doi: 10.1117/12.2287589.
[69] H. Ito, T. Ito, Y. Muramoto, T. Furuta, and T. Ishibashi, "Rectangular waveguide output unitraveling-carrier photodiode module for high-power photonic millimeter-wave

generation in the F-band," *J. Light. Technol.*, vol. 21, no. 12, pp. 3456–3462, Dec. 2003, doi: 10.1109/JLT.2003.821747.
[70] H. Ito and T. Ishibashi, "Terahertz-wave generation using resonant-antenna-integrated uni-traveling-carrier photodiodes," presented at the SPIE Commercial + Scientific Sensing and Imaging, N. K. Dhar and A. K. Dutta, Eds., Anaheim, California, United States, Apr. 2017, p. 102090R. doi: 10.1117/12.2262764.
[71] F. Nakajima, T. Furuta, and H. Ito, "High-power continuous-terahertz-wave generation using resonant-antenna-integrated uni-travelling-carrier photodiode," *Electron. Lett.*, vol. 40, no. 20, p. 1297, 2004, doi: 10.1049/el:20046431.
[72] A. Wakatsuki, T. Furuta, Y. Muramoto, T. Yoshimatsu, and H. Ito, "High-power and broadband sub-terahertz wave generation using a J-band photomixer module with rectangular-waveguide output port," in *2008 33rd International Conference on Infrared, Millimeter and Terahertz Waves*, Pasadena, CA: IEEE, Sep. 2008, pp. 1–2. doi: 10.1109/ICIMW.2008.4665566.
[73] P. Latzel *et al.*, "Generation of mW Level in the 300-GHz Band Using Resonant-Cavity-Enhanced Unitraveling Carrier Photodiodes," *IEEE Trans. Terahertz Sci. Technol.*, vol. 7, no. 6, pp. 800–807, Nov. 2017, doi: 10.1109/TTHZ.2017.2756059.
[74] J.-M. Wun, Y.-W. Wang, and J.-W. Shi, "Ultrafast Uni-Traveling Carrier Photodiodes With GaAs0.5Sb0.5/In0.53 Ga0.47As Type-II Hybrid Absorbers for High-Power Operation at THz Frequencies," *IEEE J. Sel. Top. Quantum Electron.*, vol. 24, no. 2, pp. 1–7, Mar. 2018, doi: 10.1109/JSTQE.2017.2741106.
[75] H.-J. Song, K. Ajito, Y. Muramoto, A. Wakatsuki, T. Nagatsuma, and N. Kukutsu, "Uni-Travelling-Carrier Photodiode Module Generating 300 GHz Power Greater Than 1 mW," *IEEE Microw. Wirel. Compon. Lett.*, vol. 22, no. 7, pp. 363–365, Jul. 2012, doi: 10.1109/LMWC.2012.2201460.
[76] X. Lin *et al.*, "High performance waveguide uni-travelling carrier photodiode grown by solid source molecular beam epitaxy," *Opt. Express*, vol. 27, no. 25, p. 37065, Dec. 2019, doi: 10.1364/OE.27.037065.
[77] E. Rouvalis, C. C. Renaud, D. G. Moodie, M. J. Robertson, and A. J. Seeds, "Traveling-wave Uni-Traveling Carrier Photodiodes for continuous wave THz generation," *Opt. Express*, vol. 18, no. 11, p. 11105, May 2010, doi: 10.1364/OE.18.011105.
[78] E. Rouvalis, C. C. Renaud, D. G. Moodie, M. J. Robertson, and A. J. Seeds, "Continuous Wave Terahertz Generation From Ultra-Fast InP-Based Photodiodes," *IEEE Trans. Microw. Theory Tech.*, vol. 60, no. 3, pp. 509–517, Mar. 2012, doi: 10.1109/TMTT.2011.2178858.
[79] D. Lasaosa *et al.*, "Traveling-Wave Photodetectors With High Power–Bandwidth and Gain–Bandwidth Product Performance," *IEEE J. Sel. Top. Quantum Electron.*, vol. 10, no. 4, pp. 728–741, Jul. 2004, doi: 10.1109/JSTQE.2004.833963.
[80] J.-W. Shi, S.-W. Chu, M.-C. Tien, C.-K. Sun, Y.-J. Chiu, and J. E. Bowers, "Edge-coupled membrane terahertz photonic transmitters based on metal–semiconductor–metal traveling-wave photodetectors," *Appl. Phys. Lett.*, vol. 81, no. 27, pp. 5108–5110, Dec. 2002, doi: 10.1063/1.1533846.
[81] E. A. Michael, I. Cámara Mayorga, R. Güsten, A. Dewald, and R. Schieder, "Terahertz continuous-wave large-area traveling-wave photomixers on high-energy low-dose ion-implanted GaAs," *Appl. Phys. Lett.*, vol. 90, no. 17, p. 171109, Apr. 2007, doi: 10.1063/1.2722235.
[82] E. R. Brown, F. W. Smith, and K. A. McIntosh, "Coherent millimeter-wave generation by heterodyne conversion in low-temperature-grown GaAs photoconductors," *J. Appl. Phys.*, vol. 73, no. 3, pp. 1480–1484, Feb. 1993, doi: 10.1063/1.353222.
[83] E. R. Brown, "A photoconductive model for superior GaAs THz photomixers," *Appl. Phys. Lett.*, vol. 75, no. 6, pp. 769–771, Aug. 1999, doi: 10.1063/1.124507.

[84] L. Y. Lin *et al.*, “Velocity-matched distributed photodetectors with high-saturation power and large bandwidth,” *IEEE Photonics Technol. Lett.*, vol. 8, no. 10, pp. 1376–1378, Oct. 1996, doi: 10.1109/68.536660.

[85] S. Jasmin, N. Vodjdani, J.-C. Renaud, and A. Enard, “Diluted- and distributed-absorption microwave waveguide photodiodes for high efficiency and high power,” *IEEE Trans. Microw. Theory Tech.*, vol. 45, no. 8, pp. 1337–1341, Aug. 1997, doi: 10.1109/22.618432.

[86] V. M. Hietala, G. A. Vawter, T. M. Brennan, and B. E. Hammons, “Traveling-wave photodetectors for high-power, large-bandwidth applications,” *IEEE Trans. Microw. Theory Tech.*, vol. 43, no. 9, pp. 2291–2298, Sep. 1995, doi: 10.1109/22.414580.

[87] Jin-Wei Shi and Chi-Kuang Sun, “Design and analysis of long absorption-length traveling-wave photodetectors,” *J. Light. Technol.*, vol. 18, no. 12, pp. 2176–2187, 2000, doi: 10.1109/50.908830.

[88] Jin-Wei Shi, Kian-Giap Gan, Yen-Hung Chen, Chi-Kuang Sun, Yi-Jen Chiu, and J. E. Bowers, “Ultrahigh-power-bandwidth product and nonlinear photoconductance performances of low-temperature-grown GaAs-based metal-semiconductor-metal traveling-wave photodetectors,” *IEEE Photonics Technol. Lett.*, vol. 14, no. 11, Art. no. 11, Nov. 2002, doi: 10.1109/LPT.2002.803374.

[89] Jin-Wei Shi *et al.*, “Metal-semiconductor-metal traveling wave photodetectors,” in *The 15th Annual Meeting of the IEEE Lasers and Electro-Optics Society*, Glasgow, UK: IEEE, 2002, pp. 445–446. doi: 10.1109/LEOS.2002.1159372.

[90] Yi-Jen Chiu, S. B. Fleischer, and J. E. Bowers, “High-speed low-temperature-grown GaAs p-i-n traveling-wave photodetector,” *IEEE Photonics Technol. Lett.*, vol. 10, no. 7, pp. 1012–1014, Jul. 1998, doi: 10.1109/68.681301.

[91] D. B. Rutledge, D. P. Neikirk, and D. P. Kasilingam, “Integrated circuits antennas,” in *Infrared and millimeter waves, Vol.10*, K. J. Button, Ed., New York: Academic Press, 1983, pp. 1–90.

[92] V. M. Hietala, G. A. Vawter, T. M. Brennan, and B. E. Hammons, “Traveling-wave photodetectors for high-power, large-bandwidth applications,” *IEEE Trans. Microw. Theory Tech.*, vol. 43, no. 9, pp. 2291–2298, 1995, doi: 10.1109/22.414580.

[93] E. A. Michael, “Travelling-wave photonic mixers for increased continuous-wave power beyond 1 THz,” *Semicond. Sci. Technol.*, vol. 20, no. 7, pp. 164–177, Jul. 2005, doi: 10.1088/0268-1242/20/7/006.

[94] H. Cheng, J. F. Whitaker, T. M. Weller, and L. P. B. Katehi, “Terahertz-bandwidth pulse propagation on a coplanar stripline fabricated on a thin membrane,” *IEEE Microw. Guid. Wave Lett.*, vol. 4, no. 3, pp. 89–91, Mar. 1994, doi: 10.1109/75.275590.

[95] D. B. Rutledge, D. P. Neikirk, and D. Kasilingam, “INTEGRATED-CIRCUIT ANTENNAS.,” 1983.

[96] D. R. Grischkowsky, “Optoelectronic characterization of transmission lines and waveguides by terahertz time-domain spectroscopy,” *IEEE J. Sel. Top. Quantum Electron.*, vol. 6, no. 6, pp. 1122–1135, Nov. 2000, doi: 10.1109/2944.902161.

[97] Y. Maegami *et al.*, “Simple and fully CMOS-compatible low-loss fiber coupling structure for a silicon photonics platform,” *Opt. Lett.*, vol. 45, no. 7, p. 2095, Apr. 2020, doi: 10.1364/OL.388267.

[98] Y. Luo *et al.*, “Polarization Splitter-Rotator Based on Multimode Waveguide Grating,” *Crystals*, vol. 11, no. 10, p. 1170, Sep. 2021, doi: 10.3390/cryst11101170.

[99] Y.-D. Yang, Y. Li, Y.-Z. Huang, and A. W. Poon, “Silicon nitride three-mode division multiplexing and wavelength-division multiplexing using asymmetrical directional couplers and microring resonators,” *Opt. Express*, vol. 22, no. 18, p. 22172, Sep. 2014, doi: 10.1364/OE.22.022172.

[100] Z. Weissman, D. Nir, S. Ruschin, and A. Hardy, “Asymmetric *Y* -junction wavelength demultiplexer based on segmented waveguides,” *Appl. Phys. Lett.*, vol. 67, no. 3, pp. 302–304, Jul. 1995, doi: 10.1063/1.115425.
[101] G. Zhang, S. Honkanen, A. Tervonen, C.-M. Wu, and S. I. Najafi, “Glass integrated optics circuit for 148/155- and 130/155-μm-wavelength division multiplexing and 1/8 splitting,” *Appl. Opt.*, vol. 33, no. 16, p. 3371, Jun. 1994, doi: 10.1364/AO.33.003371.
[102] M. R. Paiam, C. F. Janz, R. I. MacDonald, and J. N. Broughton, “Compact planar 980/1550-nm wavelength multi/demultiplexer based on multimode interference,” *IEEE Photonics Technol. Lett.*, vol. 7, no. 10, pp. 1180–1182, Oct. 1995, doi: 10.1109/68.466583.
[103] J. Mu, S. A. Vazquez-Cordova, M. A. Sefunc, Y.-S. Yong, and S. M. Garcia-Blanco, “A Low-Loss and Broadband MMI-Based Multi/Demultiplexer in Si_3N_4/SiO_2 Technology,” *J. Light. Technol.*, vol. 34, no. 15, pp. 3603–3609, Aug. 2016, doi: 10.1109/JLT.2016.2578463.
[104] G. Chattopadhyay, “Technology, Capabilities, and Performance of Low Power Terahertz Sources,” *IEEE Trans. Terahertz Sci. Technol.*, vol. 1, no. 1, pp. 33–53, Sep. 2011, doi: 10.1109/TTHZ.2011.2159561.
[105] A. W. Jackson, J. P. Ibbetson, A. C. Gossard, and U. K. Mishra, “Reduced thermal conductivity in low-temperature-grown GaAs,” *Appl. Phys. Lett.*, vol. 74, no. 16, pp. 2325–2327, Apr. 1999, doi: 10.1063/1.123839.
[106] V. M. Hietala, G. A. Vawter, T. M. Brennan, and B. E. Hammons, “Traveling-wave photodetectors for high-power, large-bandwidth applications,” *IEEE Trans. Microw. Theory Tech.*, vol. 43, no. 9, Art. no. 9, Sep. 1995, doi: 10.1109/22.414580.
[107] E. Peytavit, M. Billet, Y. Desmet, G. Ducournau, D. Yarekha, and J.-F. Lampin, “Nitrogen-ion-implanted GaAs Fabry-Pérot cavity photoconductor for THz photonics,” in *2015 40th International Conference on Infrared, Millimeter, and Terahertz waves (IRMMW-THz)*, Hong Kong, China: IEEE, Aug. 2015, pp. 1–2. doi: 10.1109/IRMMW-THz.2015.7327720.
[108] E. Y. Wu and B. H. Yu, “High-field electron transport in compensated GaAs,” *Appl. Phys. Lett.*, vol. 58, no. 14, pp. 1503–1505, Apr. 1991, doi: 10.1063/1.105159.
[109] M. B. Kuppam, J.-F. Lampin, E. Peytavit, J.-F. Roux, and J.-L. Coutaz, “Study of Ultrafast Semiconductor Photoswitches for CW RF Signal Sampling and Modulation,” *J. Light. Technol.*, vol. 32, no. 20, pp. 3839–3845, Oct. 2014, doi: 10.1109/JLT.2014.2334063.
[110] W. Heinrich, “Quasi-TEM description of MMIC coplanar lines including conductor-loss effects,” *IEEE Trans. Microw. Theory Tech.*, vol. 41, no. 1, pp. 45–52, Jan. 1993, doi: 10.1109/22.210228.
[111] G. F. Engen and C. A. Hoer, “Thru-Reflect-Line: An Improved Technique for Calibrating the Dual Six-Port Automatic Network Analyzer,” *IEEE Trans. Microw. Theory Tech.*, vol. 27, no. 12, pp. 987–993, Dec. 1979, doi: 10.1109/TMTT.1979.1129778.
[112] T. Domínguez Bucio *et al.*, “Material and optical properties of low-temperature NH_3 -free PECVD SiN_x layers for photonic applications,” *J. Phys. Appl. Phys.*, vol. 50, no. 2, p. 025106, Jan. 2017, doi: 10.1088/1361-6463/50/2/025106.
[113] Y. M. Obeidat and K. L. Lear, “Mathematical Modeling for Losses in Optical Waveguides With Porous Silica Cladding,” *IEEE Sens. J.*, vol. 21, no. 4, pp. 4747–4754, Feb. 2021, doi: 10.1109/JSEN.2020.3035515.
[114] M. Huff, “Recent Advances in Reactive Ion Etching and Applications of High-Aspect-Ratio Microfabrication,” *Micromachines*, vol. 12, no. 8, p. 991, Aug. 2021, doi: 10.3390/mi12080991.

[115] F. Laermer and A. Urban, “Challenges, developments and applications of silicon deep reactive ion etching,” in *Microelectronic Engineering*, Elsevier, Jun. 2003, pp. 349–355. doi: 10.1016/S0167-9317(03)00089-3.
[116] D. C. Look, Z. -Q. Fang, H. Yamamoto, J. R. Sizelove, M. G. Mier, and C. E. Stutz, “Deep traps in molecular-beam-epitaxial GaAs grown at low temperatures,” *J. Appl. Phys.*, vol. 76, no. 2, pp. 1029–1032, Jul. 1994, doi: 10.1063/1.357846.
[117] A. A. Pastor, U. V. Prokhorova, P. Yu. Serdobintsev, V. V. Chaldyshev, and M. A. Yagovkina, “Effect of annealing on the nonequilibrium carrier lifetime in GaAs grown at low temperatures,” *Semiconductors*, vol. 47, no. 8, pp. 1137–1140, Aug. 2013, doi: 10.1134/S1063782613080150.
[118] S. U. Dankowski *et al.*, “Above band gap absorption spectra of the arsenic antisite defect in low temperature grown GaAs and AlGaAs,” *Appl. Phys. Lett.*, vol. 68, no. 1, pp. 37–39, Jan. 1996, doi: 10.1063/1.116748.
[119] S. U. Dankowski *et al.*, “Above band gap absorption spectra of the arsenic antisite defect in low temperature grown GaAs and AlGaAs,” *Appl. Phys. Lett.*, vol. 68, no. 1, pp. 37–39, Jan. 1996, doi: 10.1063/1.116748.
[120] M. Tani, K.-S. Lee, and X.-C. Zhang, “Detection of terahertz radiation with low-temperature-grown GaAs-based photoconductive antenna using 1.55 μm probe,” *Appl. Phys. Lett.*, vol. 77, no. 9, pp. 1396–1398, Aug. 2000, doi: 10.1063/1.1289914.
[121] M. Billet, “Photodétecteurs rapides à la longueur d’onde de 1550 nm pour la génération et la détection d’ondes sub-THz et THz,” p. 236.
[122] M. Billet, P. Latzel, F. Pavanello, G. Ducournau, J.-F. Lampin, and E. Peytavit, “Resonant cavities for efficient LT-GaAs photoconductors operating at λ = 1550 nm,” *APL Photonics*, vol. 1, no. 7, p. 076102, Oct. 2016, doi: 10.1063/1.4954771.
[123] E. Peytavit, C. Coinon, and J.-F. Lampin, “A metal-metal Fabry–Pérot cavity photoconductor for efficient GaAs terahertz photomixers,” *J. Appl. Phys.*, vol. 109, no. 1, p. 016101, Jan. 2011, doi: 10.1063/1.3525709.
[124] W. Bogaerts *et al.*, “Silicon microring resonators,” *Laser Photonics Rev.*, vol. 6, no. 1, pp. 47–73, Jan. 2012, doi: 10.1002/lpor.201100017.
[125] C. Tannoury, M. Billet, C. Coinon, J. Lampin, and E. Peytavit, “Low-temperature-grown gallium arsenide photoconductors with subpicosecond carrier lifetime and photoresponse reaching 25 mA/W under 1550 nm CW excitation,” *Electron. Lett.*, vol. 56, no. 17, pp. 897–899, Aug. 2020, doi: 10.1049/el.2020.1116.
[126] D. H. Auston, P. Lavallard, N. Sol, and D. Kaplan, “An amorphous silicon photodetector for picosecond pulses,” *Appl. Phys. Lett.*, vol. 36, no. 1, pp. 66–68, Jan. 1980, doi: 10.1063/1.91276.
[127] F. E. Doany, D. Grischkowsky, and C. -C. Chi, “Carrier lifetime versus ion-implantation dose in silicon on sapphire,” *Appl. Phys. Lett.*, vol. 50, no. 8, pp. 460–462, Feb. 1987, doi: 10.1063/1.98173.
[128] F. W. Smith, A. R. Calawa, C.-L. Chen, M. J. Manfra, and L. J. Mahoney, “New MBE buffer used to eliminate backgating in GaAs MESFETs,” *IEEE Electron Device Lett.*, vol. 9, no. 2, pp. 77–80, Feb. 1988, doi: 10.1109/55.2046.
[129] G. B. Bachelet, M. Schlüter, and G. A. Baraff, “As Ga antisite defect in GaAs,” *Phys. Rev. B*, vol. 27, no. 4, pp. 2545–2547, Feb. 1983, doi: 10.1103/PhysRevB.27.2545.
[130] J. Dabrowski and M. Scheffler, “Isolated arsenic-antisite defect in GaAs and the properties of *EL* 2,” *Phys. Rev. B*, vol. 40, no. 15, pp. 10391–10401, Nov. 1989, doi: 10.1103/PhysRevB.40.10391.
[131] M. R. Melloch, N. Otsuka, J. M. Woodall, A. C. Warren, and J. L. Freeouf, “Formation of arsenic precipitates in GaAs buffer layers grown by molecular beam epitaxy at low substrate temperatures,” *Appl. Phys. Lett.*, vol. 57, no. 15, pp. 1531–1533, Oct. 1990, doi: 10.1063/1.103343.

[132] S. Gupta *et al.*, “Subpicosecond carrier lifetime in GaAs grown by molecular beam epitaxy at low temperatures,” *Appl. Phys. Lett.*, vol. 59, no. 25, pp. 3276–3278, Dec. 1991, doi: 10.1063/1.105729.
[133] A. C. Warren, J. H. Burroughes, J. M. Woodall, D. T. McInturff, R. T. Hodgson, and M. R. Melloch, “1.3- mu m P-i-N photodetector using GaAs with As precipitates (GaAs:As),” *IEEE Electron Device Lett.*, vol. 12, no. 10, pp. 527–529, Oct. 1991, doi: 10.1109/55.119178.
[134] K. J. Siebert *et al.*, “Continuous-wave all-optoelectronic terahertz imaging,” *Appl. Phys. Lett.*, vol. 80, no. 16, pp. 3003–3005, Apr. 2002, doi: 10.1063/1.1469679.
[135] P. A. Loukakos, C. Kalpouzos, I. E. Perakis, Z. Hatzopoulos, M. Logaki, and C. Fotakis, “Ultrafast electron trapping times in low-temperature-grown gallium arsenide: The effect of the arsenic precipitate spacing and size,” *Appl. Phys. Lett.*, vol. 79, no. 18, pp. 2883–2885, Oct. 2001, doi: 10.1063/1.1413219.
[136] K. A. McIntosh, K. B. Nichols, S. Verghese, and E. R. Brown, “Investigation of ultrashort photocarrier relaxation times in low-temperature-grown GaAs,” *Appl. Phys. Lett.*, vol. 70, no. 3, pp. 354–356, Jan. 1997, doi: 10.1063/1.118412.
[137] I. S. Gregory *et al.*, “High resistivity annealed low-temperature GaAs with 100 fs lifetimes,” *Appl. Phys. Lett.*, vol. 83, no. 20, pp. 4199–4201, Nov. 2003, doi: 10.1063/1.1628389.
[138] N. H. L. Koster, S. Koblowski, R. Bertenburg, S. Heinen, and I. Wolff, “Investigations on Air Bridges Used for MMICs in CPW Technique,” in *19th European Microwave Conference, 1989*, London, UK: IEEE, Oct. 1989, pp. 666–671. doi: 10.1109/EUMA.1989.334045.
[139] C. P. Wen, “Coplanar Waveguide, a Surface Strip Transmission Line Suitable for Nonreciprocal Gyromagnetic Device Applications,” in *1969 G-MTT International Microwave Symposium*, Dallas TX, USA: IEEE, 1969, pp. 110–115. doi: 10.1109/GMTT.1969.1122668.
[140] M. Riaziat, R. Majidi-Ahy, and I.-J. Feng, “Propagation modes and dispersion characteristics of coplanar waveguides,” *IEEE Trans. Microw. Theory Tech.*, vol. 38, no. 3, pp. 245–251, Mar. 1990, doi: 10.1109/22.45333.
[141] R. W. Jackson, “Mode conversion at discontinuities in finite-width conductor-backed coplanar waveguide,” *IEEE Trans. Microw. Theory Tech.*, vol. 37, no. 10, pp. 1582–1589, Oct. 1989, doi: 10.1109/22.41005.
[142] D. Li, X. Zhao, C. Zeng, G. Gao, Z. Huang, and J. Xia, “Compact grating coupler for thick silicon nitride,” in *Optical Fiber Communication Conference*, Anaheim, California: OSA, 2016, p. W2A.20. doi: 10.1364/OFC.2016.W2A.20.
[143] X. Zhao *et al.*, “Compact Grating Coupler for 700-nm Silicon Nitride Strip Waveguides,” *J. Light. Technol.*, vol. 34, no. 4, pp. 1322–1327, Feb. 2016, doi: 10.1109/JLT.2015.2510025.
[144] S. Nambiar, M. Hemalatha, T. Sharma, and S. K. Selvaraja, “Integrated silicon nitride based TE dual-band grating coupler,” in *2017 Conference on Lasers and Electro-Optics Europe & European Quantum Electronics Conference (CLEO/Europe-EQEC)*, Munich, Germany: IEEE, Jun. 2017, pp. 1–1. doi: 10.1109/CLEOE-EQEC.2017.8086967.
[145] Y. Chen *et al.*, “Experimental demonstration of an apodized-imaging chip-fiber grating coupler for Si_3N_4 waveguides,” *Opt. Lett.*, vol. 42, no. 18, p. 3566, Sep. 2017, doi: 10.1364/OL.42.003566.
[146] Y. Chen, R. Halir, Í. Molina-Fernández, P. Cheben, and J.-J. He, “High-efficiency apodized-imaging chip-fiber grating coupler for silicon nitride waveguides,” *Opt. Lett.*, vol. 41, no. 21, p. 5059, Nov. 2016, doi: 10.1364/OL.41.005059.
[147] S. Ura, K. Mori, R. Tsujimoto, J. Inoue, and K. Kintaka, “Position Dependence of Coupling Efficiency of Grating Coupler in Waveguide Cavity,” in *2017 IEEE 67th*

Electronic Components and Technology Conference (ECTC), Orlando, FL, USA: IEEE, May 2017, pp. 1619–1626. doi: 10.1109/ECTC.2017.60.
[148] J. Litvik, I. Dolnak, and M. Dado, "Waveguide silicon nitride grating coupler," presented at the 20th Slovak-Czech-Polish Optical Conference on Wave and Quantum Aspects of Contemporary Optics, J. Müllerová, D. Senderáková, L. Ladányi, and Ľ. Scholtz, Eds., Jasna, Slovakia, Dec. 2016, p. 1014213. doi: 10.1117/12.2263183.
[149] C. R. Doerr, L. Chen, Y.-K. Chen, and L. L. Buhl, "Wide Bandwidth Silicon Nitride Grating Coupler," *IEEE Photonics Technol. Lett.*, vol. 22, no. 19, pp. 1461–1463, Oct. 2010, doi: 10.1109/LPT.2010.2062497.
[150] S. Dwivedi *et al.*, "Integrated Silicon Nitride Fan-in/Fan-out for Multi-Core Fiber Interconnects," in *Advanced Photonics 2017 (IPR, NOMA, Sensors, Networks, SPPCom, PS)*, New Orleans, Louisiana: OSA, 2017, p. IW2A.3. doi: 10.1364/IPRSN.2017.IW2A.3.
[151] S. Dwivedi, B. Song, Y. Liu, R. Moreira, L. Johanson, and J. Klamkin, "Demonstration of compact silicon nitride grating coupler arrays for fan-out of multicore fibers," in *2017 Conference on Lasers and Electro-Optics (CLEO)*, 2017, pp. 1–2.
[152] C. Xu, M. Khajavikhan, and P. LiKamWa, "A silicon nitride grating coupler for efficent coupling bewteen waveguide and fiber," in *2017 IEEE Photonics Conference (IPC)*, Orlando, FL, USA: IEEE, Oct. 2017, pp. 425–426. doi: 10.1109/IPCon.2017.8116170.
[153] J. Hong and S. Yokoyama, "Efficient silicon nitride grating coupler with a dielectric multilayer reflector," in *2017 22nd Microoptics Conference (MOC)*, Tokyo: IEEE, Nov. 2017, pp. 58–59. doi: 10.23919/MOC.2017.8244493.
[154] E. W. Ong, N. M. Fahrenkopf, and D. D. Coolbaugh, "SiN $_x$ bilayer grating coupler for photonic systems," *OSA Contin.*, vol. 1, no. 1, p. 13, Sep. 2018, doi: 10.1364/OSAC.1.000013.
[155] Z. Zhu and T. Brown, "Full-vectorial finite-difference analysis of microstructured optical fibers," *Opt. Express*, vol. 10, no. 17, p. 853, Aug. 2002, doi: 10.1364/OE.10.000853.
[156] "MODE - Finite Difference Eigenmode (FDE) solver." Accessed: Oct. 27, 2022. [Online]. Available: https://optics.ansys.com/hc/en-us/articles/360034917233-MODE-Finite-Difference-Eigenmode-FDE-solver-introduction#:~:text=The%20Finite%2DDifference%20Eigenmode%20(FDE,%2C%20effective%20index%2C%20and%20loss.
[157] D. M. Sullivan, *Electromagnetic simulation using the FDTD method*. New York: IEEE Press, 2015.
[158] M. J. Rycroft, "Computational electrodynamics, the finite-difference time-domain method," *J. Atmospheric Terr. Phys.*, vol. 58, no. 15, pp. 1817–1818, Nov. 1996, doi: 10.1016/0021-9169(96)80449-1.
[159] S. D. Gedney, *Introduction to the Finite-DifferenceTime-Domain (FDTD) Method for Electromagnetics*. in Synthesis Lectures on Computational Electromagnetics. Cham: Springer International Publishing, 2011. doi: 10.1007/978-3-031-01712-4.
[160] "Finite Difference Time Domain (FDTD) solver." Accessed: Oct. 27, 2022. [Online]. Available: https://optics.ansys.com/hc/en-us/articles/360034914633-FDTD-solver
[161] H. Deng, G. H. Jin, J. Harari, J. P. Vilcot, and D. Decoster, "Investigation of 3D semivectorial finite-difference beam propagation method for bent waveguides," *J. Light. Technol.*, vol. 16, no. 5, pp. 915–922, May 1998, doi: 10.1109/50.669039.
[162] L. Cao, A.-S. Grimault-Jacquin, and F. Aniel, "COMPARISON AND OPTIMIZATION OF DISPERSION, AND LOSSES OF PLANAR WAVEGUIDES ON BENZOCYCLOBUTENE (BCB) AT THZ FREQUENCIES: COPLANAR WAVEGUIDE (CPW), MICROSTRIP, STRIPLINE AND SLOTLINE," *Prog. Electromagn. Res. B*, vol. 56, pp. 161–183, 2013, doi: 10.2528/PIERB13072603.